

UNIVERSITÀ DEGLI STUDI  
DI PAVIA, ITALY



**IUSS**

Scuola Universitaria Superiore Pavia

ISTITUTO UNIVERSITARIO  
DI STUDI SUPERIORI DI PAVIA, ITALY

---

A thesis submitted in fulfillment of the requirements for the

**PhD program in**

**Computational Mechanics and Advanced Materials**

XXVIII cycle  
(years 2012 – 2015)

# **SHAPE-MEMORY MATERIALS:**

## **CONSTITUTIVE MODELING FOR ADVANCED APPLICATIONS**

Author: **ELISA BOATTI**

Supervisor and PhD program coordinator: PROF. FERDINANDO AURICCHIO

---



# Acknowledgments

The present dissertation was written during my PhD in Computational Mechanics and Advanced Materials at IUSS Pavia and University of Pavia (from November 1st, 2012 to October 31st, 2015). I would like to acknowledge everyone who helped me in completing this path.

In particular, I would like to thank Prof. F. Auricchio and Prof. A. Reali for giving me the possibility to work in the Computational Mechanics research group at University of Pavia. I also gratefully acknowledge the IUSS Pavia grant which funded my PhD.

During my studies, I spent 3 months at Harvard University and 2 months at Universität Wien: I would like to express my thanks to Prof. K. Bertoldi from Harvard University and Prof. U. Stefanelli from Universität Wien for their useful guidance and kind hospitality, which I greatly appreciated.

Moreover, I would like to thank my colleagues and friends in University of Pavia, Universität Wien, and Harvard University, for all the time spent in learning, working and also having fun together.

Finally, I would like to thank my wonderful husband, my family and my dearest friends, who supported me during my studies.

Pavia, October 2015

Elisa Boatti





# Abstract

In a world where human needs are continuously evolving, science and technology are unceasingly pushed to advance beyond their limits. Shape-memory materials, i.e. peculiar materials which can recover their shape when exposed to a certain external stimulus, are an advanced answer to the highly demanding today's market. Indeed, their amazing *shape-memory effect*, together with other advantages such as, e.g., high workability for shape-memory polymers and superelasticity for shape-memory alloys, offers a wide variety of opportunities in many fields, as aerospace (morphing wings, deployable structures), biomedicine (stents, catheters, flexible surgical instruments, filters), construction (sensors, dampers), mechanics and automotive (actuators, switches, valves, grippers). For this reason, research studies and applications on shape-memory materials are continuously increasing.

A widely adopted instrument used to chase the frontiers of engineering is represented by virtual simulations. In fact numerical tools allow to decrease the product development and manufacturing time and cost, for instance replacing expensive prototyping and testing campaigns. Therefore, effective constitutive models able to accurately reproduce the new various industrial and biomedical applications are gaining more and more importance. This is the reason why I devoted my PhD studies mostly to the development and numerical testing of advanced constitutive models for shape-memory alloys and shape-memory polymers. The models are here reported in both a continuous and a discrete time framework; the correspondent implementation in the FEM environment is also presented, with several computational simulations run using commercial and academic software.

After an introduction in Chapter 1, the present dissertation is divided in two parts, the first one devoted to shape-memory alloys and the second one dealing with shape-memory

polymers. Chapter 2 presents a detailed review of the biomedical applications of shape-memory alloys; Chapter 3 describes the *Souza-Auricchio model*, a macroscopic constitutive material model which represents one of the starting points of my work; Chapter 4 reports a study on the explicit numerical implementation of the *Souza-Auricchio model*; Chapter 5 investigates the variational structure of the *Souza-Auricchio model*; Chapter 6 presents a new constitutive model for shape-memory polymers which I developed during the last year of my PhD; Chapter 7 reports a procedure for the semi-automatic generation of UMAT/VUMAT subroutines for the software Abaqus. Finally, Appendix A includes a study which I began during my stay at Harvard University, on obtaining tunable phononic crystals made from shape-memory polymers, and Appendix B reports the description of experimental tests on the self-sensing phenomenon in shape-memory alloys.

# Sommario

In un mondo in cui i bisogni dell'uomo sono in continua evoluzione, la scienza e la tecnologia sono costantemente chiamate a superare i propri limiti. I materiali a memoria di forma, ovvero materiali che possono recuperare una particolare forma quando sottoposti a determinati stimoli esterni, sono una risposta tecnologicamente avanzata a un mercato sempre più esigente. Infatti il loro stupefacente effetto a memoria di forma unito ad altri vantaggi tecnologici, quali alta lavorabilità per i polimeri a memoria di forma e superelasticità per le leghe a memoria di forma, offre una vasta gamma di opportunità in svariati campi, ad esempio aerospaziale (ali trasformabili, strutture ripiegabili), biomedico (stents, cateteri, strumenti chirurgici flessibili, filtri), edilizia (sensori, smorzatori), meccanica ed automotive (attuatori, interruttori, valvole, manipolatori). Per tutte queste ragioni, le attività di ricerca e le applicazioni riguardanti le leghe a memoria di forma sono in continuo aumento.

Uno strumento ampiamente utilizzato per spingersi ai limiti delle frontiere dell'ingegneria è rappresentato dalle simulazioni numeriche in ambiente virtuale. Infatti gli strumenti numerici permettono di abbattere i tempi ed i costi di sviluppo e realizzazione dei prodotti, ad esempio sostituendosi a costosi test e prototipazioni. Pertanto i modelli costitutivi che siano in grado di riprodurre in maniera accurata le nuove e sempre più varie applicazioni industriali e biomediche stanno acquisendo un'importanza crescente. Queste sono le ragioni per le quali ho dedicato i miei studi di Dottorato allo sviluppo ed ai test numerici in ambiente virtuale di modelli costitutivi per le leghe ed i polimeri a memoria di forma. I modelli di seguito riportati sono stati sviluppati sia in tempo continuo che in tempo discreto; è inoltre presentata la corrispondente implementazione in ambiente FEM, con varie simulazioni computazionali svolte utilizzando software commerciali ed accademici.

Dopo un'introduzione nel Capitolo 1, la dissertazione si suddivide in due parti, la prima incentrata sulle leghe a memoria di forma e la seconda riguardante i polimeri a

memoria di forma. Il Capitolo 2 presenta una spiegazione dettagliata delle applicazioni in campo biomedico delle leghe a memoria di forma; il Capitolo 3 descrive il modello di *Souza-Auricchio*, un modello costitutivo macroscopico per i materiali a memoria di forma, che rappresenta uno dei punti di partenza del mio lavoro; il Capitolo 4 riporta un'implementazione numerica esplicita del modello Souza-Auricchio; il Capitolo 5 investiga la struttura variazionale del modello Souza-Auricchio; il Capitolo 6 presenta un nuovo modello costitutivo per i polimeri a memoria di forma, che ho sviluppato durante il mio ultimo anno di Dottorato; il Capitolo 7 contiene una procedura per la generazione semi-automatica delle UMAT/VUMAT subroutines per il software Abaqus. Per finire, l'Appendice A include uno studio, che ho iniziato durante la mia permanenza all'Università di Harvard, relativo a cristalli fononici regolabilirealizzati con polimeri a memoria di forma; l'Appendice B riporta la descrizione di prove sperimentali sul fenomeno del self-sensing nelle leghe a memoria di forma.

# Contents

<b>List of Tables</b>	<b>XII</b>
<b>List of Figures</b>	<b>XVII</b>
<b>1 Introduction</b>	<b>1</b>
1.1 Shape-memory alloys: phenomenology and applications . . . . .	2
1.2 Shape-memory polymers: phenomenology and applications . . . . .	8
<b>2 Review of SMA applications for human health</b>	<b>13</b>
2.1 SMA biomedical applications . . . . .	13
2.1.1 Preliminaries . . . . .	13
2.1.2 Orthodontics . . . . .	17
2.1.3 Orthopedics . . . . .	19
2.1.4 General surgery . . . . .	26
2.1.5 Colorectal surgery . . . . .	33
2.1.6 Otolaryngology . . . . .	35
2.1.7 Neurosurgery . . . . .	37
2.1.8 Ophtalmology . . . . .	38
2.1.9 Urology . . . . .	40
2.1.10 Gynecology and andrology . . . . .	41
2.1.11 Physiotherapy . . . . .	42
2.1.12 Other applications: active prostheses and robot-assisted surgery . .	42
2.2 SMA cardiovascular applications and computer-based design . . . . .	44
2.2.1 Cardiovascular devices: an overview . . . . .	46
2.2.2 Examples of computer-based design . . . . .	57

2.2.3	Carotid artery . . . . .	61
2.2.4	Aorta . . . . .	61
2.2.5	Intracranial artery . . . . .	63
2.2.6	Superficial femoral artery (SFA) and renal artery . . . . .	65
2.2.7	Heart valves . . . . .	66
2.3	Conclusions . . . . .	67
<b>3</b>	<b>Constitutive modeling of SMAs</b>	<b>69</b>
3.1	Introduction . . . . .	69
3.2	Souza-Auricchio model . . . . .	70
<b>4</b>	<b>Explicit formulation of Souza-Auricchio model</b>	<b>75</b>
4.1	Introduction . . . . .	75
4.2	Souza-Auricchio model: time-discrete framework . . . . .	78
4.2.1	Implicit backward Euler algorithm . . . . .	79
4.2.2	Explicit forward Euler algorithm . . . . .	84
4.3	Numerical simulations . . . . .	86
4.3.1	Preliminary tests . . . . .	89
4.3.2	Uniaxial tests . . . . .	90
4.3.3	Biaxial test . . . . .	91
4.3.4	Pseudoelastic cardiovascular stent strut . . . . .	92
4.3.5	Pseudoelastic helical spring . . . . .	95
4.3.6	Actuation of a micro-gripper . . . . .	97
4.3.7	Analysis of a pseudoelastic SMA strand . . . . .	101
4.4	Conclusions . . . . .	107
<b>5</b>	<b>Gradient structures for the thermomechanics of shape-memory materials</b>	<b>109</b>
5.1	Introduction . . . . .	109
5.2	Preliminaries . . . . .	111
5.2.1	Choice of $f$ . . . . .	112
5.2.2	Dissipation and flow rule . . . . .	113
5.2.3	Momentum balance and energy conservation . . . . .	113
5.2.4	Full system . . . . .	114
5.2.5	Dissipativity . . . . .	115

5.3	Gradient structures . . . . .	115
5.3.1	Resolution of the quasistatic equilibrium . . . . .	116
5.3.2	Gradient structure of the isothermal problem . . . . .	117
5.3.3	Gradient structure in the general case . . . . .	118
5.3.4	Gradient structures for space-homogeneous fields . . . . .	120
5.4	Time discretization . . . . .	122
5.5	Semi-implicit scheme for the space-homogeneous case . . . . .	123
5.5.1	Mechanical subproblem . . . . .	126
5.5.2	Thermal subproblem . . . . .	127
5.5.3	Existence for the discrete problem . . . . .	129
5.5.4	Unconditional stability . . . . .	129
5.5.5	Convergence . . . . .	131
5.6	Numerical results . . . . .	133
5.6.1	Nonregularized case in (5.32) . . . . .	134
5.6.2	Implementation . . . . .	136
5.6.3	Material parameters . . . . .	137
5.6.4	Proportional tests . . . . .	137
5.6.5	Non-proportional tests . . . . .	145
5.6.6	Thermal tests . . . . .	150
5.7	Conclusions . . . . .	150
<b>6</b>	<b>A three-dimensional finite-strain phenomenological model for shape-memory polymers</b>	<b>153</b>
6.1	Introduction . . . . .	153
6.2	Time-continuous model formulation . . . . .	155
6.2.1	State and internal variables . . . . .	155
6.2.2	Helmholtz free-energy function . . . . .	158
6.2.3	Clausius-Duhem inequality and dissipativity . . . . .	160
6.2.4	Constitutive equations . . . . .	163
6.2.5	Evolution equations . . . . .	164
6.2.6	Model parameters . . . . .	166
6.3	Time-discrete model formulation . . . . .	167
6.4	Numerical tests . . . . .	168

6.4.1	Uniaxial and biaxial tests . . . . .	172
6.4.2	Comparison between numerical and experimental data . . . . .	176
6.4.3	Simulation of biomedical devices . . . . .	184
6.5	Conclusions . . . . .	188
<b>7</b>	<b>Semi-automatic UMAT/VUMAT subroutines generation</b>	<b>191</b>
7.1	Introduction . . . . .	191
7.2	From AceGen to FORTRAN . . . . .	192
7.3	From FORTRAN to UMAT/VUMAT . . . . .	193
7.4	Application example . . . . .	193
<b>A</b>	<b>Obtaining tunable phononic crystals from shape-memory polymers</b>	<b>197</b>
A.1	Introduction . . . . .	197
A.2	Results and discussion . . . . .	198
A.2.1	Numerical simulations . . . . .	198
A.2.2	Experimental testing . . . . .	203
<b>B</b>	<b>Self-sensing ability of SMA actuators</b>	<b>205</b>
B.1	Introduction . . . . .	205
B.2	Materials and methods . . . . .	206
B.3	Experimental results . . . . .	208
B.4	Constitutive model . . . . .	209



# List of Tables

2.1	Properties of different biocompatible materials. . . . .	14
4.1	Implicit backward Euler algorithm. . . . .	81
4.2	Implicit backward Euler algorithm PT1 step. . . . .	82
4.3	Implicit backward Euler algorithm PT2 step. . . . .	83
4.4	Explicit forward Euler algorithm. . . . .	87
4.5	Material parameters for the Souza-Auricchio model adopted in all the simulations after [30]. . . . .	88
4.6	Computational times, in seconds, of explicit and implicit material constitutive drivers. . . . .	91
5.1	Implementation algorithm. . . . .	137
5.2	Algorithm for the thermal subproblem. . . . .	138
5.3	Algorithm for the mechanical subproblem. . . . .	138
5.4	Test for Case (1). . . . .	139
5.5	Test for Case (2). . . . .	139
5.6	Test for Case (3). . . . .	139
5.7	Test for Case (4). . . . .	139
5.8	Material and numerical parameters for the implicit algorithm. . . . .	140
6.1	Numerical algorithm for the proposed SMP model. . . . .	169
6.2	Numerical algorithm for CASE 1. . . . .	169
6.3	Numerical algorithm for CASE 2. . . . .	170
6.4	Numerical algorithm for CASE 3. . . . .	170
6.5	Return-mapping algorithm for glassy phase plasticity. . . . .	171
6.6	Model parameters. . . . .	175

6.7	Model parameters adopted for the comparison with experimental data by [337]. . . . .	180
6.8	Material parameters adopted for the comparison with experimental data by [107]. . . . .	184
7.1	Semi-automatic UMAT/VUMAT generation procedure. . . . .	193
A.1	Material parameters used in the simulations. . . . .	199

# List of Figures

1.1	Publications histogram. . . . .	3
1.2	Patents histogram. . . . .	3
1.3	Superelasticity (a) and shape-memory effect (b). . . . .	4
1.4	Martensite fraction $\xi$ versus temperature. . . . .	5
1.5	NiTi thermovariale rate (TVR) springs [142]. . . . .	7
1.6	Boeing's variable geometry chevron [142]. . . . .	7
1.7	SMA-actuated autofocus . . . . .	7
1.8	BionicOpter by Festo. . . . .	8
1.9	Fastener made with Diaplex. . . . .	9
1.10	SMP morphing wing. . . . .	9
1.11	SMP composite reflector. . . . .	9
1.12	SMP stent. . . . .	9
1.13	High-temperature shape fixing and recovery upon heating. . . . .	10
1.14	Low-temperature shape fixing and recovery upon heating. . . . .	11
1.15	Classification of SMPs by their shape-fixing and shape-recovery abilities. . . . .	12
2.1	Orthodontic NiTi archwires: treatment sequence, [338]. . . . .	19
2.2	Orthodontic palatal expander, [259]. . . . .	20
2.3	Flexibility of NiTi dental drills. . . . .	20
2.4	NiTi fixator for mounting bridgework. . . . .	21
2.5	SMA endosseous implants, [338]. . . . .	21
2.6	Perio root type implant, [338]. . . . .	22
2.7	Superelastic staple, [338]. . . . .	26
2.8	Superelastic plates, [338]. . . . .	26
2.9	Nitinol surgical fixators. . . . .	27

2.10	Nitinol embracing fixator. . . . .	27
2.11	DynaNail <sup>TM</sup> (courtesy of MedShape Inc., Atlanta), [204]. . . . .	28
2.12	SMA vertebrae spacer, [338]. . . . .	28
2.13	Cranioplasty with NiTi ring, [222]. . . . .	28
2.14	Sequence of deployment of a Nitinol retrieval basket, [194]. . . . .	32
2.15	ColonRing compression anastomosis device. . . . .	35
2.16	Nitinol stapes piston. . . . .	37
2.17	Microforceps for brain surgery, [296]. . . . .	39
2.18	Shape-memory eyeglass frame. . . . .	40
2.19	RPS Allium (Round Posterior Stent) urethral stent. . . . .	41
2.20	Shape-memory glove for physiotherapy. . . . .	43
2.21	Superelastic device for spastic elbow relaxation, [336]. . . . .	45
2.22	Guidewire route through aorta. . . . .	49
2.23	Carotid embolic filters. . . . .	50
2.24	Example of Nitinol self-expanding stent. . . . .	53
2.25	Transcatheter aortic valve prostheses. . . . .	54
2.26	Simulation of self-expanding Nitinol stent expansion. . . . .	60
2.27	Elaboration of Computed Tomography Angiography images. . . . .	62
2.28	Segmentation of pre- and post-operative images. . . . .	64
2.29	Elaboration of Computed Tomography Angiography of the lower limbs. . .	66
4.1	One-dimensional phase diagram generated with material parameters of Table 4.5. . . . .	89
4.2	Trend of the input variables. . . . .	90
4.3	Model response for superelastic and thermal-cycling uniaxial tests. . . . .	91
4.4	Model response for shape-memory uniaxial tests. . . . .	92
4.5	Model response for biaxial test. . . . .	92
4.6	SMA cardiovascular stent strut. . . . .	93
4.7	SMA cardiovascular stent strut. . . . .	94
4.8	SMA cardiovascular stent strut. . . . .	94
4.9	SMA cardiovascular stent strut. . . . .	95
4.10	SMA cardiovascular stent strut. . . . .	96

4.11	SMA helical spring: (a) adopted mesh; (b) initial geometry, boundary conditions, and deformed shape under the maximum displacement. . . . .	97
4.12	SMA helical spring: applied vertical displacement vs. reaction force of the fixed end diagram. . . . .	98
4.13	SMA helical spring: implicit (a) and explicit (b) transformation strain norm distributions. . . . .	99
4.14	SMA helical spring: implicit (a) and explicit (b) Von Mises stress distributions.	100
4.15	SMA helical spring: plot of the internal and kinetic energies vs. total analysis time. . . . .	100
4.16	SMA micro-gripper: mesh and initial geometry. . . . .	101
4.17	Working principle of the micro-gripper. . . . .	101
4.18	SMA micro-gripper: temperature trends. . . . .	102
4.19	Deformed shape of the gripper. . . . .	103
4.20	SMA micro-gripper. . . . .	104
4.21	SMA cable: (a) three layers straight cable cross section; (b) angles of outer helical wires rotation. . . . .	104
4.22	SMA cable: adopted mesh. . . . .	105
4.23	SMA strand: (a) applied boundary conditions and (b) loading history in terms of displacements. A total of 0.2364336 time units are used. . . . .	106
4.24	SMA strand: plot of (a) internal, kinetic, and frictional dissipation energies related to the explicit analysis (b) Hysteric force-displacement diagram. . .	107
4.25	SMA strand: contour plot of the Von Mises stress for points (a) A (b) B, and (c) C of Figure 4.23(b). . . . .	108
5.1	First strain history. . . . .	142
5.2	First strain history. . . . .	142
5.3	First strain history. . . . .	143
5.4	First strain history. . . . .	143
5.5	First strain history. . . . .	144
5.6	First strain history. . . . .	144
5.7	First strain history. . . . .	145
5.8	Second strain history. . . . .	146
5.9	First hourglass strain history. . . . .	147

5.10	Second hourglass strain history. . . . .	148
5.11	Square strain history. . . . .	149
5.12	Thermal tests. . . . .	150
6.1	Uniaxial test. . . . .	173
6.2	Biaxial test. . . . .	174
6.3	Tests 1, 2 and 3. . . . .	175
6.4	Test 1. . . . .	177
6.5	Test 2. . . . .	178
6.6	Test 3. . . . .	179
6.7	Comparison with experimental data by [337]: free-recovery test. . . . .	181
6.8	Comparison with experimental data by [337]: constrained-recovery test. . .	182
6.9	Comparison with experimental data by [107]. . . . .	183
6.10	Stent simulation: scheme. . . . .	185
6.11	Stent simulation: (a) force versus displacement curve; (b) displacement ver- sus temperature curve; (c) force versus temperature curve. . . . .	186
6.12	Stent simulation: Von Mises stress distribution. . . . .	187
6.13	Contraceptive device test: scheme. . . . .	187
6.14	Contraceptive device test. . . . .	188
6.15	Contraceptive device test: Von Mises stress distribution . . . . .	189
7.1	Simple example of AceGen code for linear elastic material model. As men- tioned, AceGen offers an optimized translation of numerical procedures into other languages, FORTRAN among them. . . . .	194
7.2	Generated UMAT for linear elastic material model. . . . .	195
7.3	Linear FEA and higher order FEA comparison. . . . .	196
A.1	Geometry considered for the phononic crystal. . . . .	199
A.2	Shape-memory cycle simulation on the phononic crystal. . . . .	200
A.3	(a) RVE and (b) Brillouin zone in the reciprocal lattice. . . . .	201
A.4	Dispersion diagrams. . . . .	202
A.5	SMP material used in the experimental testing. . . . .	203
A.6	Manufacturing procedure. . . . .	204
A.7	Shape-memory cycle. . . . .	204

B.1	SMA electrical actuation. . . . .	206
B.2	Smartflex (SAES Getters) wires technical data. . . . .	207
B.3	Testing equipment. . . . .	207
B.4	Electrical circuit. . . . .	208
B.5	Experimental data. . . . .	209





# Chapter 1

## Introduction

Shape-memory materials display the peculiar property to recover the original shape after deformation, in presence of the proper external stimulus: this feature is called shape-memory effect. Such behavior is often sided by other useful characteristics and responses, varying from one material to another, which make shape-memory materials good candidates for cutting edge applications in different engineering areas.

Probably the most studied shape-memory materials are shape-memory alloys (SMAs) and shape-memory polymers (SMPs); the present work is devoted to these two groups. In particular, the main portion of this thesis reports the results of my studies and research projects on SMA modeling and applications: Chapter 2 presents a review on the biomedical application of SMAs; Chapter 3 describes a widely used phenomenological constitutive model for SMAs, which has been improved and enhanced: in Chapter 4, an explicit algorithm for such model is presented, and in Chapter 5, a variational reformulation of the fully coupled thermomechanical problem is proposed. Chapter 6 deals with SMPs and presents a new three-dimensional phenomenological model for thermo-responsive SMPs. Finally, in Chapter 7 I propose a procedure to generate in a semi-automatic way UMAT and VUMAT subroutines for Abaqus. An Appendix is also provided, including part A, where the model proposed in Chapter 6 is used to simulate SMP phononic crystals with the aim to obtain tunable frequency band gaps, and part B, which reports the results of experimental tests on SMAs self-sensing abilities.

## 1.1 Shape-memory alloys: phenomenology and applications

SMAAs are a group of metallic materials exhibiting unique properties and, accordingly, drawing the interest of scientific communities and of industries. Following References [291, 203], the first study that opened the door to the future discovery of SMAAs was made in 1932, when a Swedish researcher, Arne Ölander, observed superelasticity in Au-Cd alloys. In the end of the 30ies, Greninger and Mooradian [116] described the formation and disappearance of a martensitic phase, by respectively decreasing and increasing the temperature in Cu-Zn and Cu-Sn alloys. It is, however, only a decade later that the shape-memory effect, and its dependency on the thermo-mechanical material conditions, were finally reported and widely described by Kurdjumov and Khandros in 1949 [173] and by Chang and Read in 1951 [64]. Nonetheless, the first effective step toward industrial use of SMA was the discovery of shape-memory effect in equiatomic NiTi alloys, performed in 1962 by Buehler and its team at the U.S. Naval Ordnance Laboratory, naming, therefore, the alloy as Nitinol (Nickel Titanium Naval Ordnance Laboratory, patent US 3174851 - 1965). Moreover, Raychem Corporation manufactured the first Nitinol industrial application during the 60ies in aeronautics, consisting in hydraulic tube couplers for F-14 fighter planes.

Similarly, the earliest use of Nitinol for medical purposes was reported in the 70ies, when Andreasen made the first implant of a superelastic orthodontic device (patent US 4037324 - 1977). Unfortunately, high production costs and biocompatibility concerns prevented commercial spreading of Nitinol medical devices until the 80ies [223], while nowadays Nitinol, thanks also to the fact that it was the first available functional biomaterial, is a widely accepted material for medical use. The ever-increasing exploitation of SMAAs in medical devices is proved by the strong ascending trend of publications and patents produced on the subject during the last decades, as it is easy to verify through statistic data concerning publication and patent evolution through classical databases such as "Scopus" (see Figure 1.1) and "QPAT" (see Figure 1.2).

The two main effects presented by SMAAs are superelasticity (SE) and shape-memory effect (SME). Superelasticity, also known as pseudoelasticity, is the capability of undergoing large deformations during mechanical loading and of recovering the original shape during unloading; shape-memory effect is, instead, the ability of a deformed SMA material to

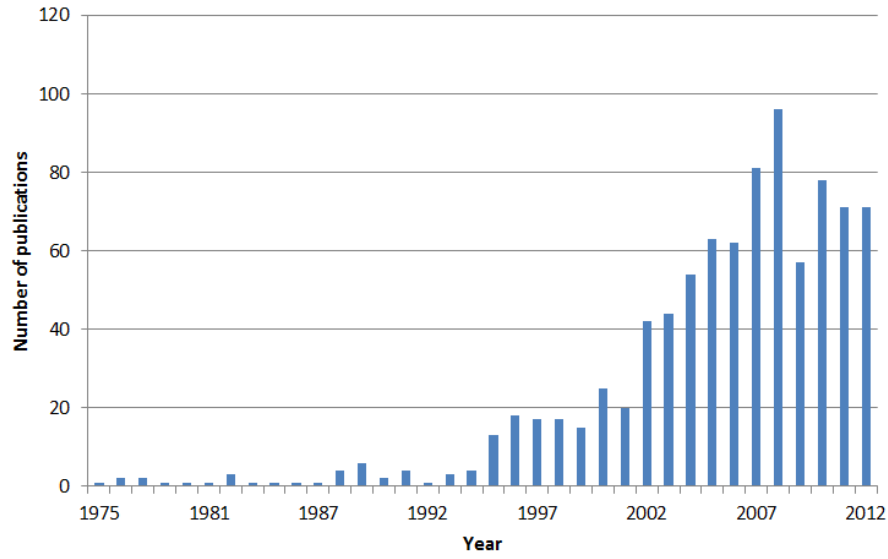


Figure 1.1: Histogram representing the number of publications per year, since 1975 to 2012. The research was performed using the keywords "shape AND memory AND alloy AND \*medical" in Scopus database (consultation: February 2013). The trend is strongly increasing, demonstrating the great interest in SMAs raised in the medical field during the last decades.

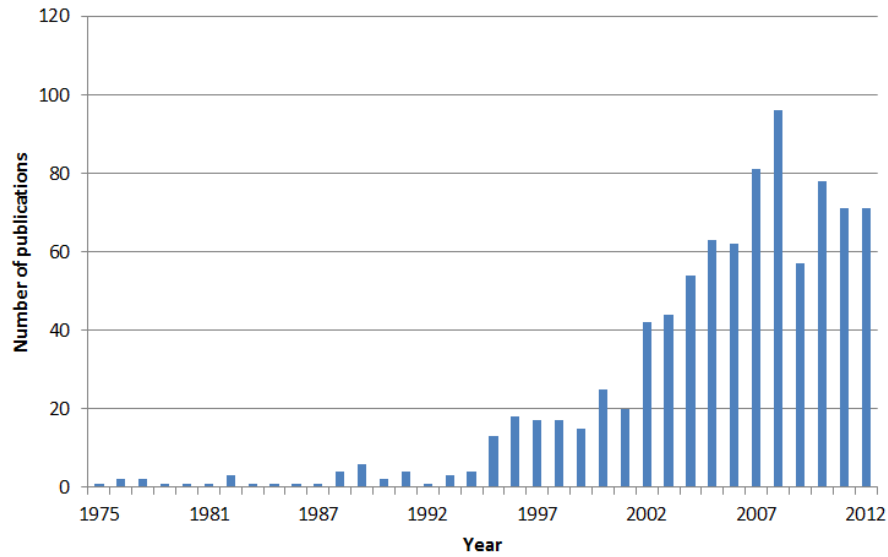


Figure 1.2: Histogram representing the number of patents per year, since 1975 to 2012. The research was performed using the keywords "shape AND memory AND alloy AND \*medical" in QPAT patents database (consultation: February 2013). Also for the patents, the trend is ever increasing.

recover the original shape upon heating. A graphical representation of the two behaviors is provided in Figure 1.3 (left side).

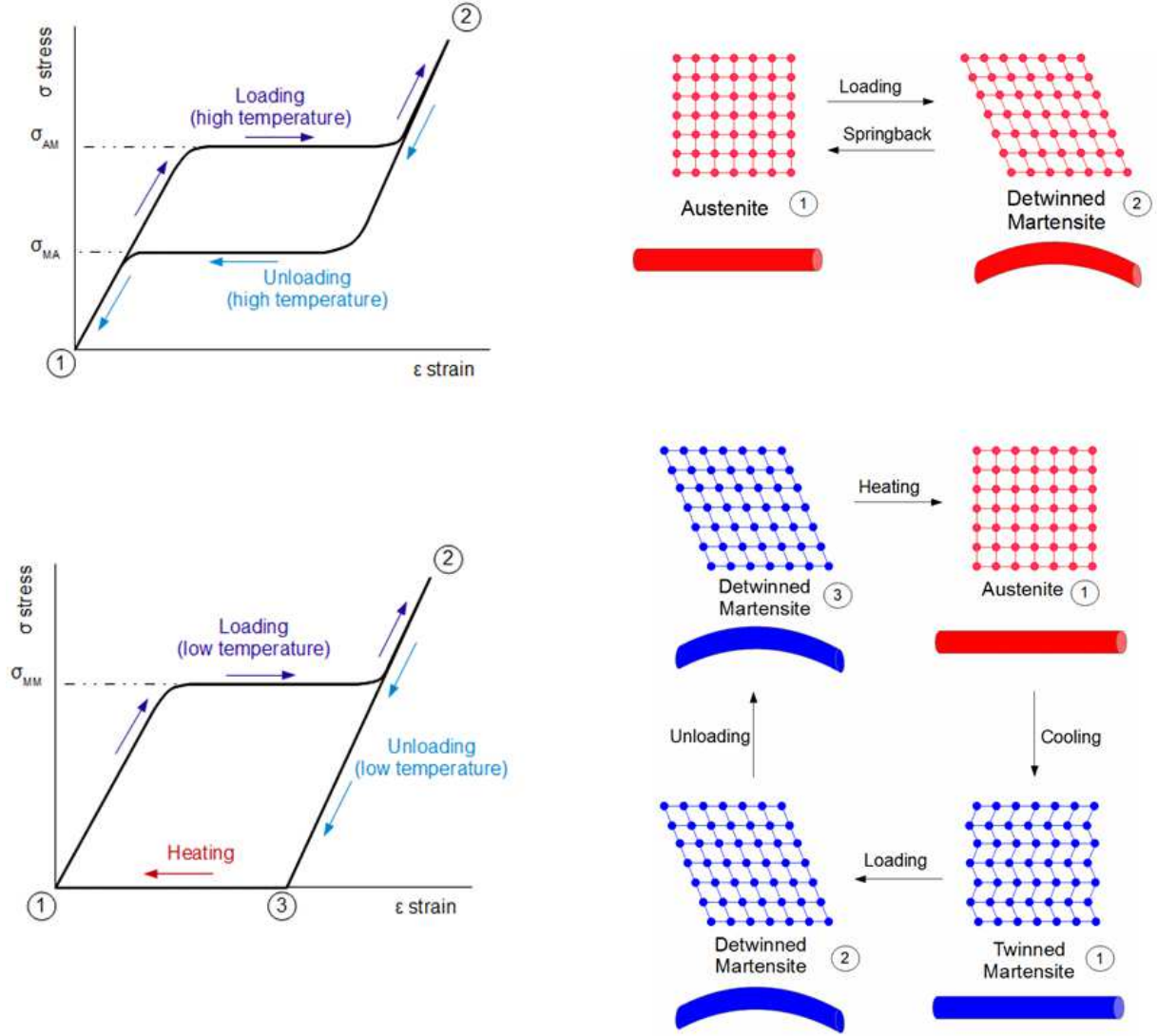


Figure 1.3: Superelasticity (a) and shape-memory effect (b).

The explanation of such unique properties relies on the crystallographic structure of SMA. Two distinct phases can, in fact, be identified: the austenite (or parent) phase, which is stable at higher temperature and has higher symmetry; the martensite (or daughter phase), which is stable at lower temperature and has lower symmetry. Moreover, the martensite can be present in different variants, which can be organized either in the form of twinned or multi-variant martensite or in the form of detwinned or single-variant marten-

site, with a graphical sketch of the possible crystallographic situations provided in Figure 1.3 (right side).

A phase transformation between the two described phases can be induced controlling the material temperature and the state of stress. For the case of no stress, the temperature over which the conversion of martensite into austenite is complete is the so-called austenite finish temperature, traditionally indicated as  $A_f$ , while the temperature below which the conversion of austenite into martensite is complete is the so-called martensite finish temperature, traditionally indicated as  $M_f$  (Figure 1.4). The phase transformation temperature range is comprised between these two values.

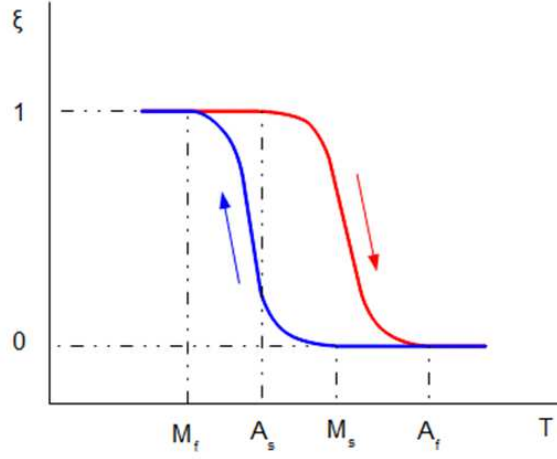


Figure 1.4: Martensite fraction  $\xi$  versus temperature.  $M_f$  is the martensite finish temperature,  $M_s$  is the martensite start temperature,  $A_f$  is the austenite finish temperature and  $A_s$  is the austenite start temperature.

With the few basic concepts introduced so far, it is possible to give a full explanation of the SE and SME properties and a clear connection between the macroscopic effect and the crystallographic features. When the alloy is mechanically loaded at a temperature higher than the austenite finish temperature  $A_f$  and the value of the applied stress is sufficiently high (i.e. over a value indicated as  $\sigma_{AM}$  in Figure 1.3), austenite to martensite transformation is induced. Upon unloading, inverse martensite to austenite transformation occurs (because the austenite is the only stable phase at temperature above  $A_f$ ), and the original shape is recovered, therefore inducing the superelastic effect. It can be noted that when the direct and inverse transformations take place, the stress remains mainly constant over a wide range of deformations, originating respectively an upper plateau and a lower

plateau, which are of high interest in several biomedical applications, as discussed later on.

When the material is mechanically deformed at a temperature lower than the martensite finish temperature  $M_f$ , a transformation from multi-variant to single-variant martensite occurs, if the stress is higher than a determinate value (i.e. over a value indicated as  $\sigma_{MM}$  in Figure 1.3). Upon unloading, a residual deformation is produced. When the material is heated above the austenite finish temperature  $A_f$ , the transformation from martensite to austenite allows shape recovery, inducing the shape-memory effect.

Another unique material feature, which makes SMA extremely attractive in terms of practical applications, is the possibility to modify and adjust the material phase transformation regions and thermo-mechanical characteristic parameters through variations in the alloy composition and/or through proper thermo-mechanical treatments [70, 235]. As an example, the material can remember a desired manufactured shape, which can be set to be different from the original or natural shape. In fact, following Reference [46], SMAs can be processed by "rolling or forging the alloy under heat, then by a series of cold working phases, and finally by a carefully controlled heat treatment to 450 – 550 °C for 1 – 5 min during which the alloy is constrained on a mandrel or fixture to form desired shapes. This process is referred to as shape training". Once the shape training has been performed, whenever the material is heated over the transformation temperature range, it recovers the manufactured shape.

Moreover, under specific and more complex thermo-mechanical treatments, SMAs may also show a two-way shape-memory effect [191], i.e., the ability to thermally cycle between two different induced shapes, also if the amount of shape recovery upon cooling is usually significantly lower with respect to the effect obtained upon heating.

Among the wide variety of SMA applications, there are, for instance [142]: NiTi thermovaryable rate (TVR) springs (Figure 1.5), where the material is used as both sensor and actuator; Boeing's variable geometry chevron (Figure 1.6); SMA-actuated autofocus for a miniature camera by Actuator Solutions GmbH; a flying robot by Festo AG & Co. KG [105], including NiTi muscles.



Figure 1.5: NiTi thermovisible rate (TVR) springs [142].

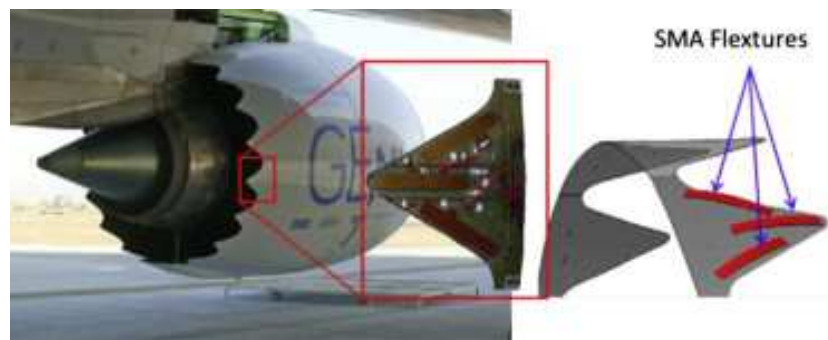


Figure 1.6: Boeing's variable geometry chevron [142].



Figure 1.7: SMA-actuated autofocus for a miniature camera by Actuator Solutions GmbH [38].

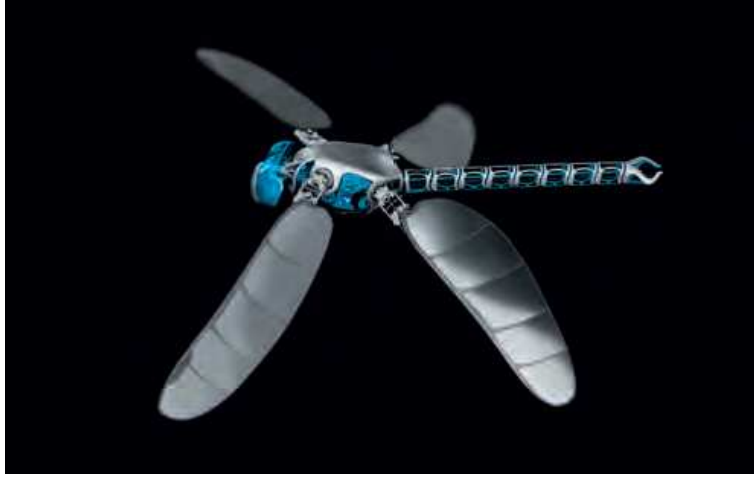


Figure 1.8: BionicOpter is a flying robot manufactured by Festo AG & Co. KG [105], with 4 out of 13 degrees of freedom actuated with SMA muscles.

## 1.2 Shape-memory polymers: phenomenology and applications

SMPs are named after their ability to store a temporary shape and recover their original (parent, or permanent) shape upon an external stimulus. The permanent shape is given to the polymer during processing (e.g. injection moulding and extrusion) and is determined by the crosslinks (i.e. the junctions) in the macromolecular network that are not affected by variations of the external environment conditions; whereas the temporary shape is a deformation imposed to the component which is retained thanks to physical or chemical links, depending on the polymer type [342].

Thanks to their peculiar features, SMPs are good candidates to be used in advanced applications. They are currently utilized for, e.g., heat-shrinkable tubes, wraps, foams, self-adjustable utensils [342], and they are addressed in numerous research studies on biomedical devices, on deployable space structures and microsystems [186, 341], on smart sensors and actuators [41]. In fact, even if SMPs present lower recovery stresses, they display higher recoverable deformation than metallic and ceramic shape-memory materials. Other advantages of SMPs with respect to other shape-memory materials are lower cost, easier manufacturing process, with a consequent higher possibility of creating devices with complex geometries, material lower density, and possible biodegradability [186].

Shape recovery in SMPs can be induced by different mechanisms: thermally, electri-



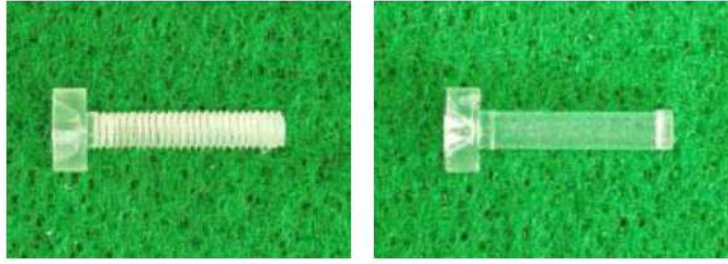


Figure 1.9: Fastener made with Diaplex, by SMP Technologies [309].

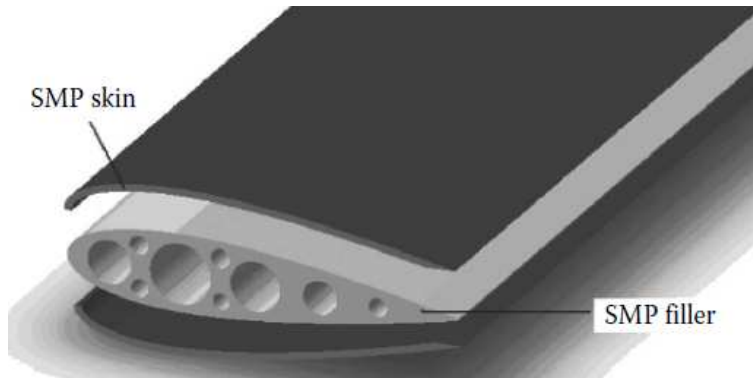


Figure 1.10: SMP morphing wing [342].

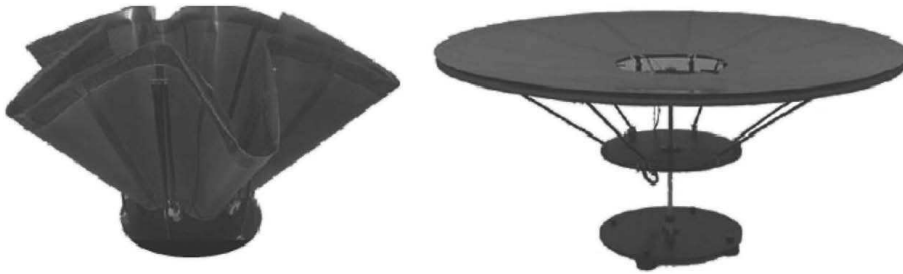


Figure 1.11: SMP composite reflector [342].

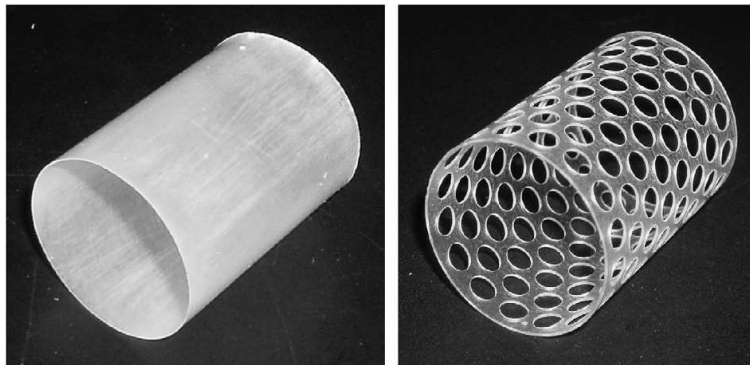


Figure 1.12: Design of a SMP stent [359].

cally, chemically (through immersion in water or other solvent), through light, through electric/magnetic field; however, the most common are thermo-responsive SMPs. The thermally-induced shape-memory effect is associated with a transition temperature which depends on the type of the polymer; the appropriate SMP material to use is therefore chosen according on the temperature range of the application [65].

The typical shape-memory cycle in thermo-responsive SMPs generally consists of a shape-fixing (or shape-programming) procedure, followed by a shape-recovery upon heating. Particularly, two types of shape-fixing protocols can be performed [179, 341]: (i) a heating-stretching-cooling process or (ii) a cold drawing; in the following, we will refer to as *high-temperature* and *low-temperature* shape-fixing, respectively. In case of a shape-memory cycle with high-temperature shape-fixing, the material is first heated above the transition temperature range, then deformed, cooled while keeping the constraint to maintain the deformed shape, and finally re-heated, after the constraint release, to recover the original shape (see Figure 1.13). In case of a shape-memory cycle with low-temperature shape-fixing, the polymer is first deformed while at lower temperatures than the transition range, then unloaded, and finally heated to recover the original shape (see Figure 1.14). The high-temperature shape-fixing is the most common procedure and is applied, for instance, to polyurethane-based polymers [287]; however, the low-temperature shape-fixing is advantageous since it does not require an additional heating-cooling step to achieve the temporary shape [276]. It is performed on polymers with suited mechanical properties for loading at low temperatures (e.g., a low enough modulus at room temperature to ensure deformation by cold-drawing), such as poly(DL-lactic acid)-based poly(urethane urea) [323] or poly( $\epsilon$ -caprolactone) polyurethane [182] SMPs.

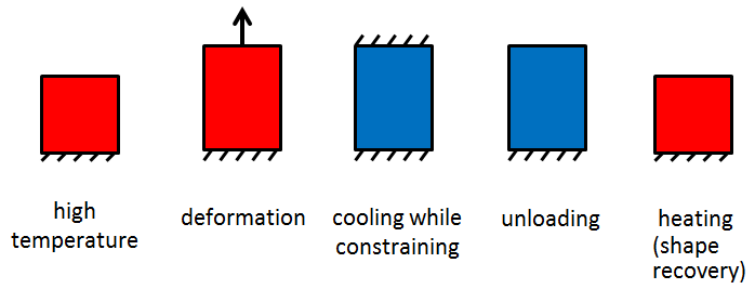


Figure 1.13: High-temperature shape fixing and recovery upon heating.

SMPs can be classified according to their shape-fixing and shape-recovery abilities [187],

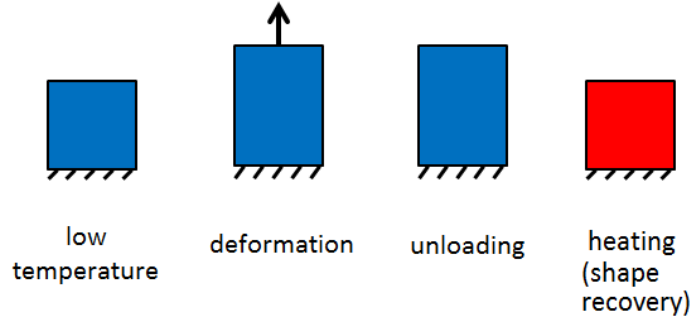


Figure 1.14: Low-temperature shape fixing and recovery upon heating.

as displayed in Figure 1.15, where schematic shape-memory cycles are shown in extension (or strain) versus temperature diagrams. For an ideal material, the recovery happens exactly in correspondence of a single temperature value, so that the recovery curve is sharp, as shown in Figure 1.15a. In the reality, the recovery is not instantaneous and takes place over a wider temperature range, so that the recovery curve is smooth, as represented in Figure 1.15b. If the shape-fixing is not ideal, a certain amount of deformation will be "lost" upon unloading (see Figure 1.15c); if the shape-recovery is not ideal, the original shape will not be recovered completely (see Figure 1.15d). Imperfect shape-fixing and incomplete shape recovery can also take place together. Experimental evidences showing imperfect shape-fixity and incomplete shape-recovery in SMPs can be found, for instance, in [337, 332, 330]. As an example, researches on the long-term characteristics of polyurethane SMP foams reported that the shape-fixity and shape-recovery become imperfect [331].

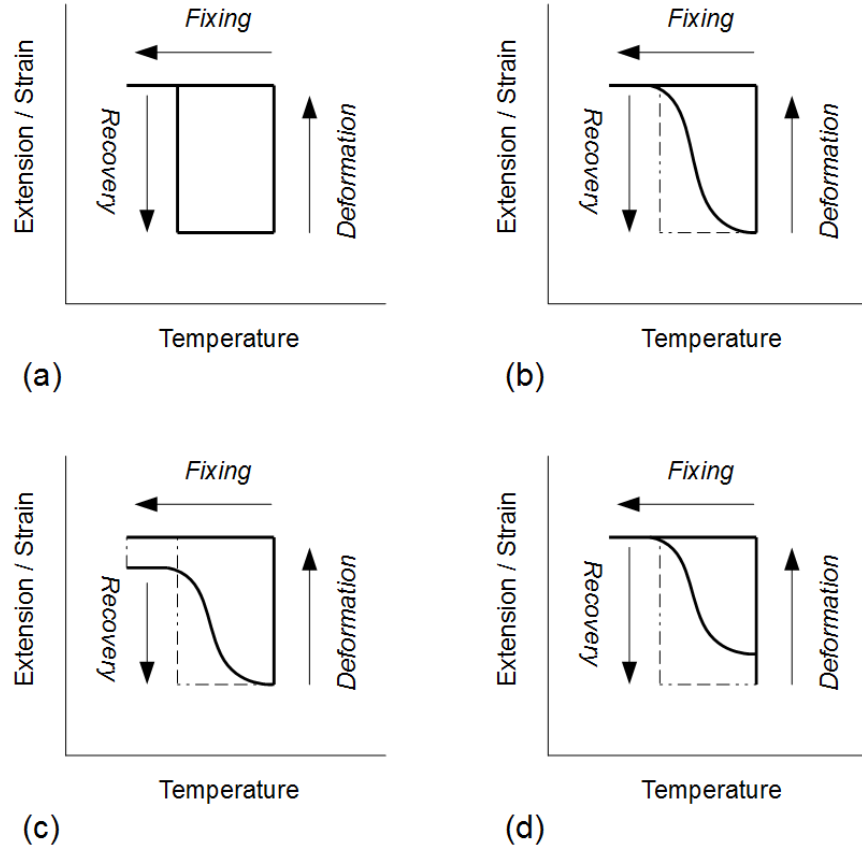


Figure 1.15: Classification of SMPs by their shape-fixing and shape-recovery abilities. (a) Ideal SMP. (b) Non-ideal SMP, with perfect shape-fixing and complete shape-recovery, but finite sharpness of the recovery curve. (c) Non-ideal SMP, with imperfect shape-fixing and complete shape-recovery. (d) Non-ideal SMP, with perfect shape-fixing and incomplete shape-recovery. Figure inspired to [187].

## Chapter 2

# Review of SMA applications for human health

In the first period of my PhD studies, I collected detailed information on the biomedical applications of SMAs. The result of such activity has been the publication of two chapters in a book devoted to the description of the characteristics and of the uses of SMAs in engineering [33, 34]. The two reviews are reported (in an adapted version) in the following. The first one contains a wide review of all the biomedical applications of SMAs in some of the main fields of medicine. The second one is instead focused on the cardiovascular applications of SMAs and on the computer-based design of such devices, which has encountered strong advancements in the last decades.

## 2.1 SMA biomedical applications

### 2.1.1 Preliminaries

Nowadays, the great majority of SMA medical devices are produced using NiTi alloys, thanks to the material good workability in the martensite phase, good resistance to corrosion and fatigue, Food and Drug Administration (FDA) approval, good compatibility with magnetic resonance imaging and computer tomography scanning, [92].

Besides exploiting either superelastic or shape-memory effects depending on the specific biomedical application, NiTi is also frequently adopted due to a closer similarity to biological tissue mechanical response than conventional medical materials, such as stainless

Table 2.1: Properties of different biocompatible materials.

Material	Density [ $g/cm^3$ ]	Young's modulus [ $GPa$ ]
NiTi	6.45	$E_A = 53.5; E_M = 29.2$
Stainless Steel (316 L)	7.95	193
Ti-6Al-4V	4.43	113.8
Bone	1.7 – 2	0.2 – 19.4

steel; for example, NiTi is less dense and with a lower elastic modulus if compared to other standard biomedical materials (see Table 2.1). Moreover, human body offers an isothermal environment, perfectly centered on the necessary conditions for superelastic behavior or shape-memory effect to occur.

Despite NiTi alloys usually consist of a binary nearly equiatomic concentration of Ni and Ti, the possibility of adding ternary elements (e.g., Fe, Cu and Nb) is often explored to influence the material behavior, for example in terms of hysteresis (shallower hysteresis for Fe and Cu, wider for Nb), transformation temperatures and mechanical properties, particularly fatigue response [99]. Clearly, a careful control of the austenite finish temperature is crucial to commercial and medical applications [46].

### Nitinol biocompatibility

Biocompatibility is obviously a critical aspect for any material to be used in medical applications, especially in the case of NiTi, which brings the fear of possible Ni release, proven to cause toxic, carcinogen and immune-sensitizing effects. Potential users of NiTi in medical applications have in fact often rejected their use, being afraid of high Ni release in corrosive environments, such as the human body. This concern was just due to poor knowledge on NiTi alloys; indeed, biocompatibility properties of NiTi alloy are very different if compared to Ni alone, being instead comparable to Ti alloys, which are extremely stable. In fact, starting from the work of Wever, [350], the biocompatibility of NiTi was assessed and compared to materials conventionally adopted in clinical applications (e.g., stainless steel and pure titanium), proving the NiTi good corrosion resistance and good tissue compatibility. In particular, the extensive study of Ryh nen in 2000, [291], used human osteoblast and fibroblast cell cultures to assess NiTi primary cytotoxicity and corrosion rate, showing no toxic effects and no inhibition of cells growth and proliferation. Furthermore, NiTi and stainless steel intramedullary nails were also used to fix femoral osteotomies in rats and

bone healing was evaluated, not only with NiTi nails showing better performance in terms of higher number of healed bone unions than stainless steel, but also with corrosion material alterations more evident in stainless steel than NiTi. Accordingly, Ryhanen's study started to fully demonstrate that NiTi is suitable for medical uses, performing similarly or better than stainless steel and Ti-6Al-4V alloy.

Moreover, as reported by Jackson in 2007, [344], also several in vivo studies conducted in the last decade "disclosed no allergic reactions, no traces of alloy constituents in the surrounding tissue and no corrosion of implants".

In Reference [118], experimental investigations showed that Nitinol genotoxicity is equivalent to the one relative to 316L stainless steel, and is less severe than the one produced by cigarette smoking.

Es-Souni [99] overviews the biocompatibility studies on NiTi and affirms that that "NiTi shape-memory alloys are generally characterized by good corrosion properties, in most cases superior to those of conventional stainless steel or Co-Cr-Mo based biomedical materials. The majority of biocompatibility studies suggest that these alloys have low cytotoxicity (both in vitro and in vivo) as well as low genotoxicity. The release of Ni ions depends on the surface state and the surface chemistry. Smooth surfaces with well-controlled structures and chemistries of the outermost protective TiO<sub>2</sub> layer lead to negligible release of Ni ions, with concentrations below the normal human daily intake".

Clearly, biocompatibility is an important issue for all orthodontic-based applications, since the mouth offers a particularly corrosive environment [44]. Corrosion of metals in the oral cavity depends upon various factors, among which device morphology, saliva pH value, alloy composition. Researchers have often used different procedures to assess biocompatibility in vitro and in vivo for dental applications, so quantitative results are not comparable [218]. However, many studies have been carried out in the last decades to evaluate biocompatibility and corrosion characteristics of SMAs in orthodontic applications (e.g. [144], [44], [168]). These studies demonstrated that Nitinol is in general even more biocompatible than stainless steel, also for orthodontic appliances [218].

### **Nitinol surface properties**

One of the reasons for the good biocompatibility of NiTi alloys relies on the fact that Ti is more rapidly oxidized than Ni, with positive consequences on surface properties: generally, the outer protective TiO<sub>2</sub> film formed by Ti passivation is sufficient to provide

corrosion resistance, acting as an effective barrier to Ni ions release [99]. In other cases, since the surface exposed to body fluids is much higher (such as in porous NiTi biomedical applications), or is exposed to highly corrosive environments, formation of Ti oxide layer may not be enough and corrosion may bring to Ni ions release. In these cases NiTi devices need to be treated with ad-hoc surface modification techniques, to provide more effective barriers and, thus, enhance surface protection from corrosion, leading to implant safe conditions. Surface modification can have various depths, from nanometers to micrometers, and they can be performed through various procedures; among them, we recall mechanical treatments, etching in solutions, electropolishing, heat treatments, ion beam treatments, conventional and plasma ion immersion implantations, laser melting, bioactive coating deposition [300]. Recently TiN (already successfully used in biomedical applications) has been proposed for the improvement of biocompatibility of orthodontic archwires, showing good results in the experimental environment [144].

### **Nitinol fatigue**

A last feature of SMAs, worth mentioning in terms of biomedical application, is the material ability to outperform other conventional metals in strain-controlled environments, whereas, in stress controlled environments, SMAs may fatigue rapidly. Most fatigue environments in the body are a combination of the two conditions, creating difficulties in making previsions about fatigue behavior. However, Duerig affirms that, usually, "the very compliant nature of biological materials tends to push in the direction of strain-controlled fatigue, where Nitinol will excel", [91]. A drawback concerning fatigue is represented by the fact that NiTi alloys exhibit non-standard fracture and fatigue responses, if compared with common engineering metals, due to their stress-induced and/or thermally induced microstructural evolutions and to the complexity of the various phases [286]. As a consequence, well known theoretical models and standard fatigue testing procedures cannot be applied, and a universal description of Nitinol fatigue behavior remains an open issue even today (see [286], [133], [255]). As a consequence, no standard fatigue tests for Nitinol have been defined yet [261]. However, advancements in Nitinol processing [303], [285] and recent studies aimed at optimization of the appliance geometry (for example [135]), allowed latest applications to be more fracture-resistant than in the past and to present a satisfactory HCF (High Cycle Fatigue) behavior. An important example of cyclic strain-controlled Nitinol application is the self-expanding stent, used to treat body conduit stenosis of various types,



whose fatigue life is strongly influenced by the pulsating blood response and by everyday life activities [135] as well as by the small sizes of the devices [286]. In fact, stents can experience up to 40 million loading cycles each year, making the fatigue lifetime a major design criterion of the stent. To this purpose, some experimental campaigns on stent components are available in open literature, e.g. [334, 254, 255, 367]. Another example is represented by the pace-maker leads, requiring a conductive material that can undergo very high numbers of strain-controlled flexing motions without failing. The superiority of Nitinol with respect to other materials was demonstrated for this application [91].

### 2.1.2 Orthodontics

As reported by Thompson in 1999, [327], the first medical use of Nitinol was in the orthodontic field. In fact, in 1971 Andreasen and Hilleman introduced for the first time NiTi orthodontic archwires, [208], observing that Nitinol was able to produce constant and lighter forces, being therefore much more effective than traditional stainless steel wires. Accordingly, since the seventies, extensive research has been published in materials science and orthodontics journals, spreading knowledge on Nitinol properties and allowing effective clinical uses of such a material, see e.g. [327, 103]. Nowadays, even if SMAs are more difficult and expensive to manufacture than conventional materials, they are among the most common materials used for orthodontic devices and several producers are active in the dental market, providing a large variety of appliance choices for many different application fields. Currently, archwires (Figure 2.1) and palatal expanders (Figure 2.2) are the most important SMA-based orthodontic applications, taking advantage of superelasticity features. The motivation for such a successful exploitation of SMA materials is connected to the material ability to apply to the teeth almost constant forces during dental repositioning, obtained as a consequence of the bone remodeling process. In fact, the optimal way to induce physiological dental movements without damaging the underlying tissues and with the minimum patient discomfort, i.e., the optimal tooth movement, is achieved by applying forces low in magnitude and continuous in time, while forces with high magnitude and discontinuous in time can cause hyalinization, a deleterious process caused by tissue disintegration. These considerations exactly explain the success of SMAs in orthodontic applications; in fact, due to the almost constant oral cavity temperature, SMAs can produce proper constant springback forces over a large range of deformations,

making these materials more effective compared to classical alloys, [327]. Such a high biological and clinical effectiveness allows also for less frequent re-adjustments by the attending orthodontist, who may perform few visits per year instead of one visit each 3-4 weeks usually needed for re-tensioning of stainless steel wires as well as for a reduction of patient pain during the whole treatment period. The phase transformation temperature range is clearly very important when assessing the quality of an archwire for a specific orthodontic treatment; for a good clinical application, the temperature range of the material transformation should oscillate between slightly below or close to the temperature in the oral cavity, i.e. from 35°C to 37°C. Clearly, different SMA archwires can be used during the various phases of the orthodontic treatment, to achieve a better forces control. Although archwires represent the most known Nitinol application in orthodontics, other devices are equally useful in simplifying and improving orthodontic clinical practice. Another example is represented by dental drills for root canal procedures (Figure 2.3), [220]. In fact, Nitinol performs exceptionally well at high strains in strain-controlled environments and this ability is exploited in dental drills, which can undergo quite severe bending and still accommodate high cyclic rotations, with good fatigue resistance and high elasticity preventing undesirable failure during root canal procedures, [252]. Another significant orthodontic application is represented by fixators for mounting bridgework (Figure 2.4), [344]. Fixators are in general based on a small SMA element, notched on both sides; as the temperature rises, the notched area expands, causing a permanent hold of bridgework. These fixators can also be used to prevent a loose tooth from falling out. Following a concept similar to the one just described, SMAs have also been exploited for dental prostheses and implants, for example, in the form of endosseous blade type implants (Figure 2.5). The implants are manufactured to have open blades when in the austenite phase, i.e. over the transformation temperature; at room temperature, when the material is in the martensite phase, the implants are deformed to obtain flat blades, to be installed with a simple incision, thus facilitating insertion. After installation, thanks to body temperature, the implant is heated up over austenite transformation temperature, to allow the recovering of a customized shape and the anchoring into the bone. When a single tooth has to be replaced, Nitinol perio-root-type dental implants are also available (Figure 2.6): they are cylinders which, installed in replacement of a missing tooth and heated above transformation temperature, perfectly fit the seat without the need for adhesives, [340]. The opportunity to re-use dental devices has also been investigated, since Nitinol is more

expensive than conventional materials, due to higher production costs; an obstacle for this possibility is created by the higher ions release of recycled devices with respect to brand new ones. Anyway, various contributions highlighted that the amount of ions release is far below the toxic limit, [218]. In the literature it is also possible to find attempts to provide orthodontists with tools able to help in the choice of the proper type of appliance and in therapy planning; these are in general tools based on the development of computational mechanics software, able to virtually reproduce the behavior of SMA orthodontic devices (e.g., see [10, 352]). The continuously changing conditions into the mouth and the fact that geometric parameters are strongly patient specific make it difficult to forecast the orthodontic appliance behavior, so the role of simulations can be very important in the design as well as in the therapy planning.

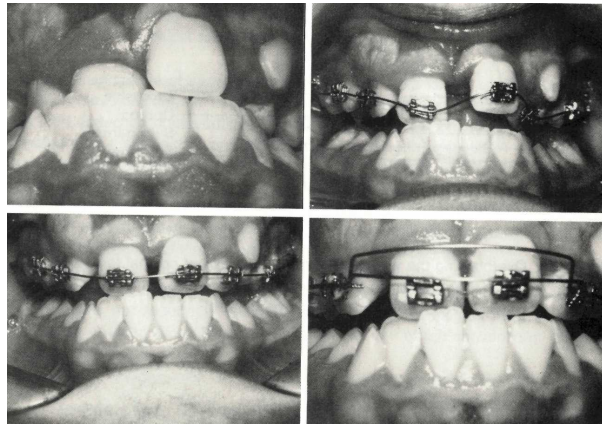


Figure 2.1: Orthodontic NiTi archwires: treatment sequence, [338].

### 2.1.3 Orthopedics

To obtain an effective soldering or union between two disjoint bone segments, essential aspects are a stable fixation and a proper compression action between the two segments. Accordingly, fractured bones are treated with a fixation device, which should strengthen the bone and keep the correct alignment during healing, being at the same time sufficiently stable; moreover, the fixation should be minimally invasive, biocompatible, and induce a biologically-appropriate compression to enhance optimal fracture healing, [324]. SMAs can provide all these requirements in a very efficient way, as demonstrated by several papers present in literature as well as by many SMA-based orthopedic devices as discussed in the

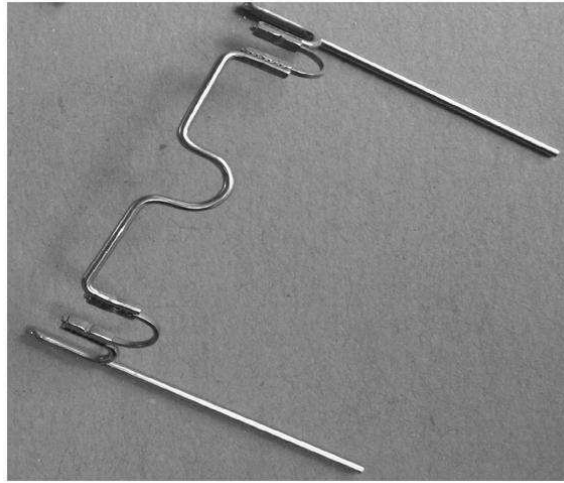


Figure 2.2: Orthodontic palatal expander, [259].

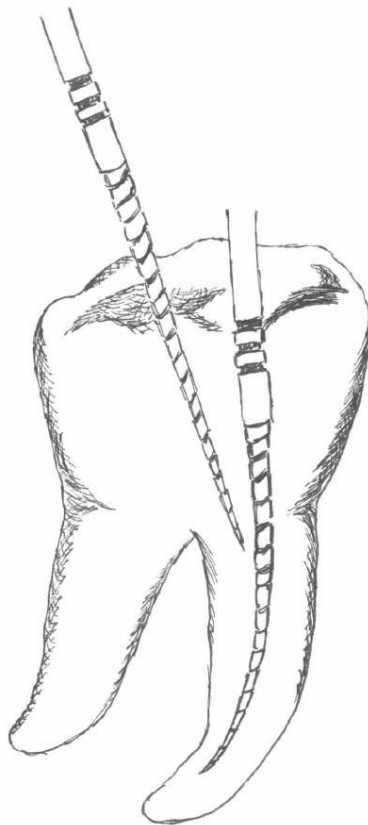


Figure 2.3: Flexibility of NiTi dental drills.

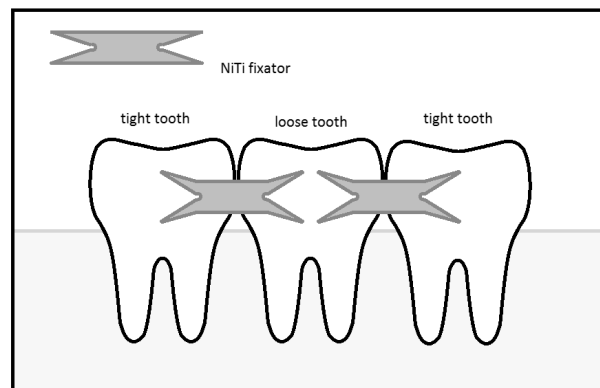


Figure 2.4: NiTi fixator for mounting bridgework.

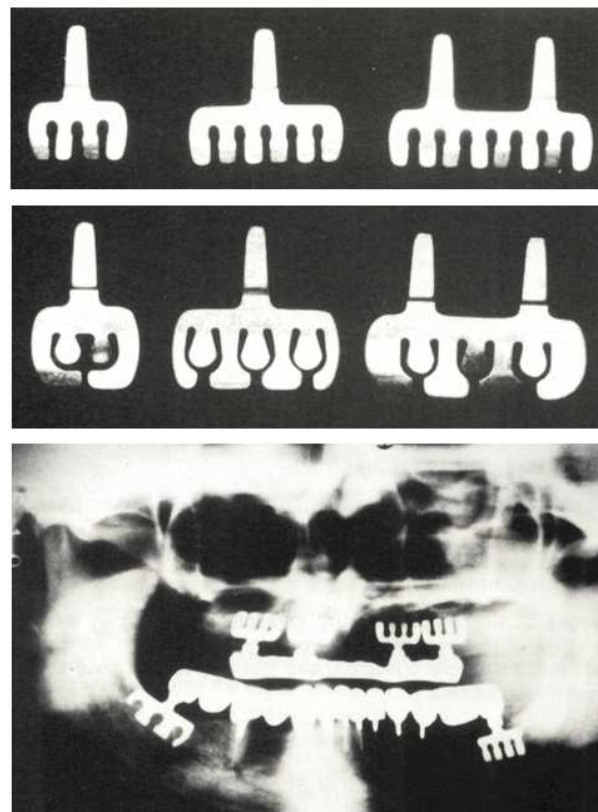


Figure 2.5: SMA endosseous implants, [338].

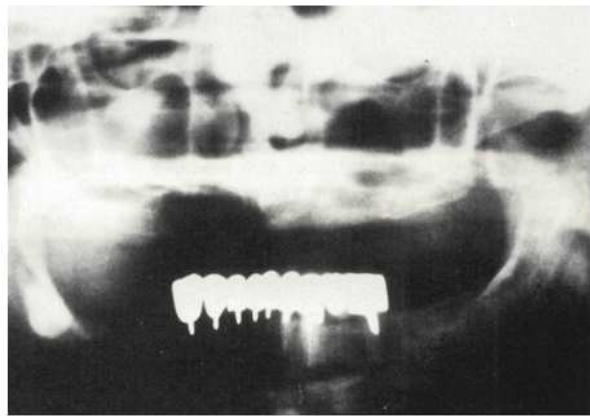
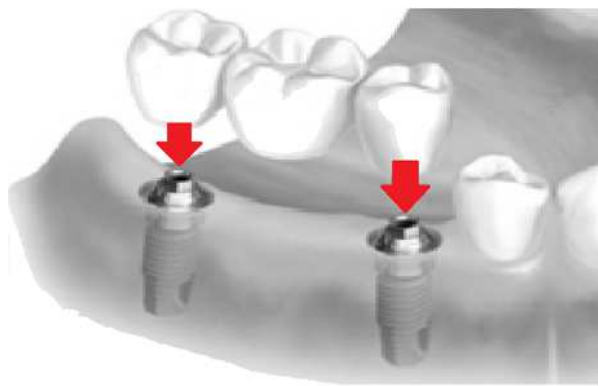


Figure 2.6: Perio root type implant, [338].

following. The simplest fixation device is the SMA staple (Figure 2.7). At room temperature, being the material in the martensitic phase, the staple can be easily shaped to facilitate insertion; when installed and maintained at body temperature, the staple tends to close and to compress the two disjoint bones (i.e., inducing a constrained shape recovery), taking advantage from the material transformation into austenite, hence from the presence of an unloading stress-strain plateau. Clear clinical evidences are discussed in several medical papers, concerning, e.g., the treatment of intra-articular fractures, [77], mandible and face bone fractures, [178], spinal deformities treatments, [302]. In particular, the device simplicity allows a reduction in operation time with apparent advantage also from the clinical perspective (e.g., [178]). Similar conceptual devices are exploited in SMA plates (Figure 2.8), fixed with screws to maintain bone alignment and placed on fractured regions where external cast cannot be easily performed (e.g., facial area, nose, jaws), [123]. Many other surgical Nitinol fixators with different shapes have been also investigated and produced for the treatment of bone fractures (Figure 2.9). For example, the embracing fixator, [361], has been clinically investigated since the 90ies to treat fractures of femur, humerus, radius and ulna. It consists of a body with saw tooth arms (Figure 2.10) and a configuration allowing, upon heating, to embrace the bone about  $2/3$  of the circumference. Moreover, this device applies an axial compression stress which, as already pointed out, is beneficial for healing. Reference [361] reports seventeen long bone fracture cases treated with the embracing fixator from 1990 to 1993, showing satisfactory results. Another shape-memory orthopedic fixation device is represented by the intramedullary nail, a metal rod fixed into the medullary cavity of the bone, used to treat long bones fractures, [139]. Shape-memory effect is exploited to facilitate insertion: indeed, the implant is deformed in the desired shape when in martensite phase and after implantation it is heated over austenite transformation temperature, to obtain tight fixing. A particular type of NiTi intramedullary nail, evaluated in a rat model, was presented in Reference [169], exploiting superelasticity after implantation to produce controlled force acting on the bone. An intramedullary NiTi nail for ankle surgery, called DynaNail<sup>TM</sup> (Figure 2.11), has been introduced by MedShape Inc. (Atlanta), [204]; it contains an internal NiTi element and it can be used to help patients suffering from soft-tissue damage in their lower extremities, resulting in debilitating ankle pain (e.g., diabetic patients). A device worth mentioning is the Nitinol Patellar Concentrator, [69], which is an internal fixator, modeled to be as similar as possible to a human patella, both from the anatomical and the biomechanical

point of view, and "consisting of two basis patellae claws, three apex patellae claws, and a conjunctive waist", as reported by Chuncai and colleagues in [69]. The device is designed for the treatment of every type of patellar fracture, especially for severely comminuted fractures, and clinical studies, [69], have shown that it is a good alternative to partial and total patellectomy. Special NiTi devices have also been designed for the treatment of spine damage or deformities. In Reference [157], a technique based on a Nitinol fixation device is introduced by Kim and colleagues, as an option for the treatment of atlantoaxial instability, a condition in which there is abnormal movement or instability in the cervical spine. The instability derives by laxity of muscles and ligaments around atlas and axis and allows abnormal bending between the two bones, which causes compression of the spinal cord. The Nitinol fixation device is a simple treatment, technically less demanding when compared to more traditional screw and rod fixation, as well as less dangerous in terms of vertebral artery or nerve injury risk. As an example, the spinal vertebrae spacer (Figure 2.12) is a device for the treatment of scoliosis, inserted between two vertebrae to assure spine local reinforcement and to prevent traumatic motion during the healing process. The material superelastic response allows the application of a constant load regardless of the patient position, so that the patient preserves some degrees of motion, [194]. For the case of severe and progressive scoliosis occurring in still growing young patients (with the clear need of preserving bone growth due to the young age), Reference [292] explores, through experiments on rats, the use of a NiTi wire, which is attached to the spine and acts as a correction device, by applying a constant springback force. Another spinal device used for the treatment of scoliosis is represented by the Nitinol correcting rod. Kuong and colleagues performed in [172] a comparison between traditional titanium and novel NiTi rods on 23 patients with adolescent idiopathic scoliosis; the result showed a safe, gradual correction performed by Nitinol rods, which produced "better coronal and sagittal alignments compared to traditional rods". In Reference [345], an evaluation is presented of Nitinol rod ability in correcting different scoliosis types, by the follow-up of 38 scoliosis patients treated with Nitinol rod-assisted scoliosis correction. The reviewed patients showed no neurologic or vascular complications and no abnormalities due to the correction device, such as screw pullout, loosening or metal fracture; therefore, it was concluded that this technique is safe and excellent for three-dimensional scoliosis correction. Among its advantages there are use easiness, decreased screw failure and possibility to be utilized for severe scoliosis. Taking again advantage of the fact that healing of bone fracture can be



enhanced by mechanical stimulation, [43], in 2013 Pfeifer, [264], presented a novel idea to obtain mechanical stimulation using a shape-memory implant, proposing to use contact-less induction heating in order to modify the features (such as the stiffness) of a metallic shape-memory implant within the human body. In 2008, Morawiek and colleagues, [222], presented NiTi rings (Figure 2.13) used to model malformed cranium. After being fixed to the osseous margins, the superelastic rings expand, reshaping the cranium vault; very good clinical results were obtained on very young children. Up to this point, we only considered bulk NiTi devices, but also porous NiTi should be taken into account as a promising candidate for orthopedics. In fact, porous NiTis combine the benefits of shape-memory and superelasticity effects and of its porous structure, providing high osseointegration and osteoconductivity. As a consequence, shape-memory and superelastic properties provide all the already described installation and functional advantages, while the open-porosity structure provides low density, high permeability and high surface area, thus enhancing bone ingrowth and fluids transportation. Moreover, porous NiTi acts as a receptive scaffold for tissue ingrowth, so it can be considered a bioactive material. Researches on porous NiTi as bone implant material began in 1995 in Russia, [307], using an animal model to assess the material behavior in vivo. According to [169], the first application of porous NiTi is a device for intervertebral fusion, introduced by Silberstein in 1997. In Reference [7], a sheep model was used to make a comparison between a new porous NiTi device for intervertebral fusion and traditional intervertebral fusion cages packed with autologous bone. It was reported that the ungrafted porous NiTi implant had significantly better fusion characteristics than conventional intervertebral fusion cages. Moreover, nickel content in tissue adjacent to porous NiTi was equivalent to the control group value and no significant increase in blood nickel content was reported. All the studies carried out on porous NiTi demonstrated good biocompatibility properties, without any cytotoxicity and genotoxicity reaction: it was reported that its biocompatibility is comparable to conventional implant materials (e.g. Ti), [43, 169]. Among its advantages for medical use there are also high strength, important to prevent deformation or fracture, and relatively low stiffness (Young's modulus lower than 20 GPa), useful to minimize stress shielding risk. Shape recovery behavior, as already mentioned, facilitates implant insertion and ensures good mechanical stability within the host tissue: it was shown, indeed, that NiTi foams show better osseointegration than titanium, [183]. Another useful feature is the excellent compatibility of porous NiTi with magnetic resonance imaging and computer tomography

scanning, compared e.g. to Co and stainless steel. Moreover, Zhu and colleagues, [365], reported that porous NiTi shows better osteoconductivity and osseointegration than bulk NiTi. Disadvantages are instead represented, for example, by the need for surface treatments to avoid Ni release (toxic), since nickel release is unavoidable when high surface area is exposed to biological corrosive environment, leading to high production cost. Intervertebral fusion devices, used in spine surgery, are one of the possible applications for porous NiTi. A commercial application of this kind is Actipore (by Biorthex, Canada), an interbody fusion material that allows bone cell growth and fluid transportation into the isotropic interconnected pores for a rapid and solid integration with bone structure without the need for bone grafting or cement, [240].

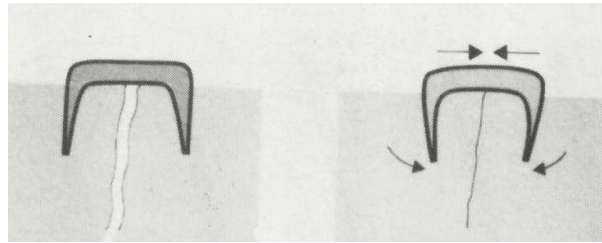


Figure 2.7: Superelastic staple, [338].

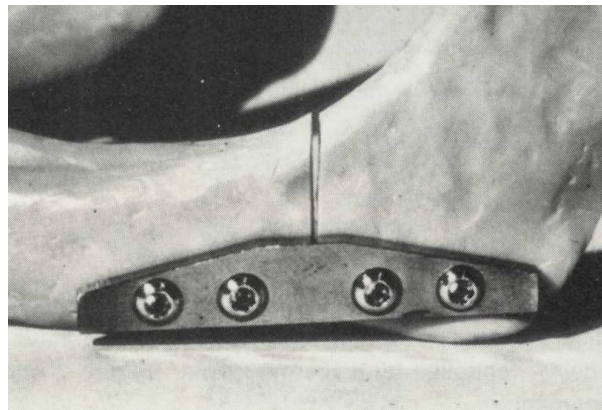


Figure 2.8: Superelastic plates, [338].

#### 2.1.4 General surgery

Another field taking significant advantage of SMA unique features is endoscopic surgery. Endoscopic surgery, also called Minimally Invasive Surgery (MIS), is a modern surgical



Figure 2.9: Nitinol surgical fixators.

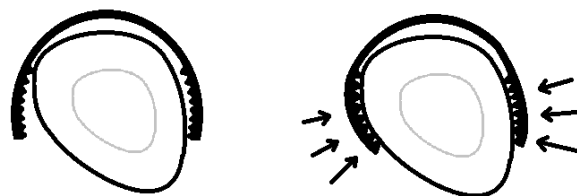


Figure 2.10: Nitinol embracing fixator.

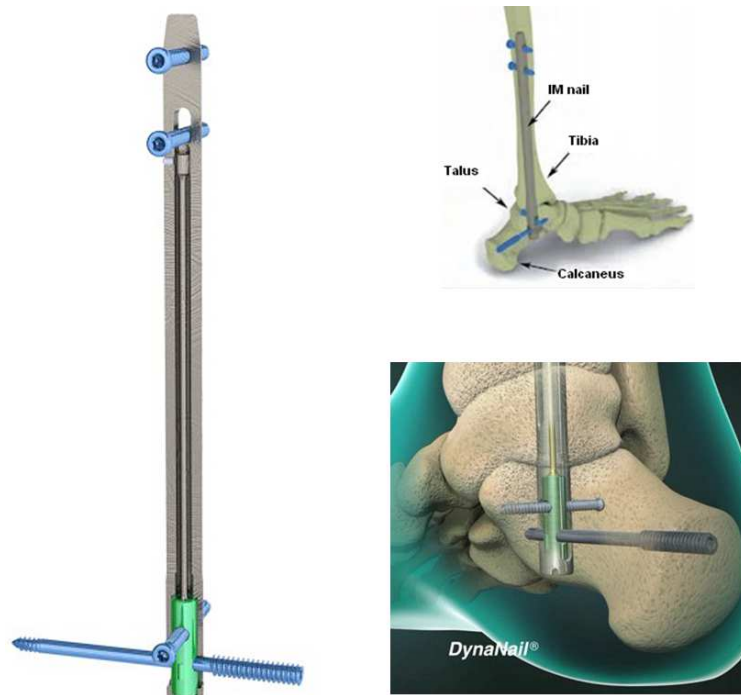


Figure 2.11: DynaNail™ (courtesy of MedShape Inc., Atlanta), [204].

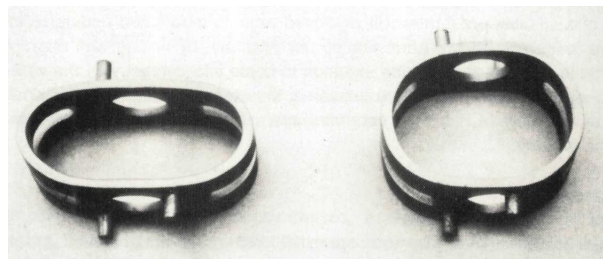


Figure 2.12: SMA vertebrae spacer, [338].

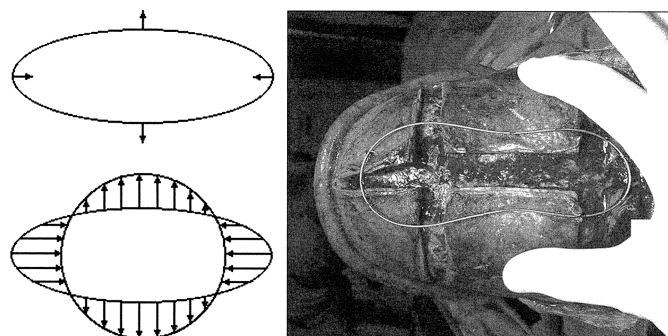


Figure 2.13: Cranioplasty with NiTi ring, [222].

technique in which diagnosis and disease treatment are performed through small incisions or natural body openings. As easily inferable, minimally invasive procedures provide patients with several benefits, such as less post-operational complications, reduced pain, faster recovery, reduction of infection risk, [154]. However, surgical endoscopic procedures require devices able to access and operate into intricate regions, i.e., instruments which are, as much as possible, stretchable, kink resistant, hinge-less and able to apply constant forces over a large deformation range. In this respect, a great advantage of SMAs with respect to stainless steel and other conventional materials is that lower size of the components is needed, since superelastic and shape-memory effects provide higher flexibility, improving effectiveness in narrow cavities. Furthermore, superelasticity provides high strain recovery and a wide constant stress plateau over a large range of strains. These unique SMA characteristics have led, during the last decades, to the design and manufacturing of novel optimized instruments, especially suited for minimally invasive surgery, examples of which are ablation devices, tongs, suture passers, grippers, deflectable graspers and scissors. Such improvements in surgical instruments have also led to configurations which are even more versatile than the one obtainable with conventional endoscopic tools, thus providing more dexterity and ease to the surgeon, even enhancing surgery accuracy. Among the first applications of SMA devices in endoscopic surgery, there are for example various NiTi tools for laparoscopy, which began to be developed since the early 90ies. As an example, Cuschieri, [76], discussed a new generation of SMA instruments, whose functioning goal was to curve in a controlled fashion after introduction into the operating field as well as to be straightened or retracted inside a restraining cannula before withdrawal from the peritoneal cavity. As an example, a curved spatula was manufactured and evaluated; during the spatula production, the operating end of the instrument was "memorized" to outline a semicircle by shape-setting the alloy at high temperature. The "deformed" curved functional end could be retracted inside a stainless steel tube exhibiting an external diameter of 5 mm. The operating end had a sharp, curved cutting tip and blunt sides. A small perforation near the tip enabled the instrument to be used to pass a suture or ligature around tubular structures. The closed instrument can be introduced, through a standard cannula with a 5 mm inside diameter, inside the peritoneal cavity; once it is within the operative field, the functional end can be extruded to the desired curvature, which can be adjusted in order to suit the individual requirements of a particular operation. The pseudoelastic curved spatula was evaluated in six experiments conducted on cross-bred Large White/Landrace pigs and the

conclusion was that the use of the superelastic curved spatula had considerably facilitated dissection of the cystic artery, cystic duct and common bile duct, and that shape-memory pseudoelastic instruments provide a considerable advantage over pre-curved stainless steel instruments. An early application of NiTi in general surgery is represented by the RITA radiofrequency tissue ablation device. This instrument is composed of a straight trocar and Nitinol tubes. The tubes are shape set into a curved configuration and are kept inside the cannula until the correct position for operation is reached. Then the Nitinol tubes are deployed and the ablation procedure is performed. Nitinol components can be withdrawn into the cannula, moved to another position and deployed again as many times as required, [252]. Another SMA surgical instrument is the retrieval basket (Figure 2.14) used to remove stones from bile ducts and kidneys: it is inserted into the conduit in a constrained form and it is opened through heating only when the proper position is reached. Many such products are available on the market, such as ZeroTip<sup>TM</sup> and Escape<sup>TM</sup> (by Boston Scientific, Natick, MA, USA). Similar to baskets, in terms of functionality, are the Nitinol snares, used to retrieve foreign bodies from internal ducts, in a quick, good controlled and safe fashion, [62]. In the paper by Nakamura and colleagues, [227], a new type of active forceps for laparoscopy was proposed. The presented forceps consisted of SMA pipes, whose temperature was controlled by water circulation within the gaps between the pipes. In Reference [195] an active bending electric endoscope powered by SMA coil actuators has been presented. The difference between the proposed design and the traditional one is that the entire shaft is soft, since it uses a SMA actuator instead of a traction wire. As a consequence, accurate observation of deep small intestine area can be easily performed without the patient suffering pain. SMAs have also found application in single-incision laparoscopic surgery (SILS), another area of active research, which has gained extensive interest in recent years; it is a novel minimally invasive surgical procedure through which surgeons operate exclusively through a single entry point. Being one of the less invasive technique, SILS decreases even more post-operative pain and complications, reduces recovery time and provides better cosmetics, [67]. Traditional instrumentations are very hard to form suitable operational triangle during SILS and risk to obstruct each other. Surgeons can have difficulty to distinguish depth and distances during the operation because the instruments are parallel to the light axis, a fact that can cause surgeon weariness. Moreover, existing articulated instruments can be difficult to assemble and can be difficult to clean and sterilize. Therefore, new ergonomic instruments with more degrees of freedom and

simpler design are needed to satisfy SILS requirements. SMA surgical instruments allow multi degrees of freedom transmission with only one component, so that multiple devices can go in and out a single incision simultaneously, achieving at the same time better resistance of the instruments and dexterity of the surgeons. A proposal for such an application is given by Cheng and Song, [67], who presented a virtual prototype of a flexible driving mechanism to create instruments with multiple degrees of freedom, able to meet the flexible requirements of SILS operation and to promote the development of minimally invasive technologies. The idea was to replace the conventional transmission type consisting of rope and pulley with a new driving mechanism consisting of a small diameter cylinder with double helix grooves, able to undergo severe bending during transmission of motion. Another example has been presented by Tognarelli and colleagues, [333], who developed and tested a novel endoluminal robotic platform designed for Natural Orifice Translumenal Endoscopic Surgery. The platform is composed of a miniaturized camera robot coupled with a SMA actuated anchoring frame, attached to the abdominal wall through the use of permanent magnets, conceived to assure appropriate stability of the robotic system inside the abdominal cavity during surgical operation. Speaking about surgery, it is necessary to mention Nitinol guidewires, another fundamental and widely used SMA application, which provides a more versatile and effective deployment of a medical device with respect to conventional devices, made for example of stainless steel. Their kink-resistance and steerability allow for accurate and safe positioning inside narrow cavities, enhancing dexterity of the surgeon and reducing the operation time. As an example, we may cite Nitrex<sup>TM</sup> guidewires (by Covidien, Dublin, Ireland). Also SMA actuated active catheters are available, for a more versatile inspection of human cavities. More detailed information about guidewires and catheters will be provided in the next chapter, dedicated to cardiovascular SMA applications, since the use of such devices is mostly related to cardiovascular field. The most celebrated medical applications of Nitinol are probably the self-expandable stents: they consist of a tubular Nitinol mesh, possibly coated, which can be introduced in body conduits to treat dangerous obstructions. Nitinol self-expandable stents find their major application in cardiovascular surgery, so they will be diffusely described in the next chapter, but they are also successfully used for the treatment of obstructions in various body canals, such as biliary, intestinal and esophageal conduits, [75, 289, 322, 170]. When ducts are strongly damaged, a stent graft may often be necessary: it is a prosthetic device consisting of a stent covered by a polymeric material, with the function of replacing

the damaged conduit, [259]. In the course of years, several evaluation studies on stent treatment of digestive system obstructions were carried out. For example, in Reference [289] a multicenter study on 240 patients demonstrated the long term effectiveness of Nitinol stents in the treatment of malignant biliary obstructions. Again, in Reference [322] a multicenter study on 37 patients suffering from malignant strictures of the esophagus was carried out, using Nitinol self-expanding stents as a treatment. Results showed that fully covered Nitinol self-expanding stents exhibit an improvement in dysphagia scores, but also caused various complications, such as stent malfunction or migration, therefore showing that further improvements in stent design are necessary to limit long term failure of the treatment in esophageal applications. Finally, the study carried out by Kujawski, [170], can be cited; 46 patients suffering from esophageal cancer and treated with coated Nitinol stents were followed up, resulting in the conclusion that covered self-expandable stent offers a safe, fast and effective palliative dysphagia treatment of neoplastic esophageal stenosis. A last simple but important SMA application which is worth citing is represented by Nitinol clips. Self-closing NiTi clips for suturing tissues in minimal-access surgery were introduced in 1999, [169], initially having the function to enhance suturing in cardiovascular surgery (U-CLIP™, Medtronic, Minneapolis, MN, USA), but then their use extended to the other surgery fields. An application in laparoscopic surgery, concerning sutures of the anterior wrap in laparoscopic gastric banding, is reported by Lirici, [184]. Another example is reported in Reference [176], where Nitinol compression clips were used for gastrointestinal anastomosis. Authors agree on the conclusion that Nitinol clips allow faster suturing, since the time consuming task of knot tying can be avoided, and moreover they provide continuous homogeneous pressure upon the joint tissues.

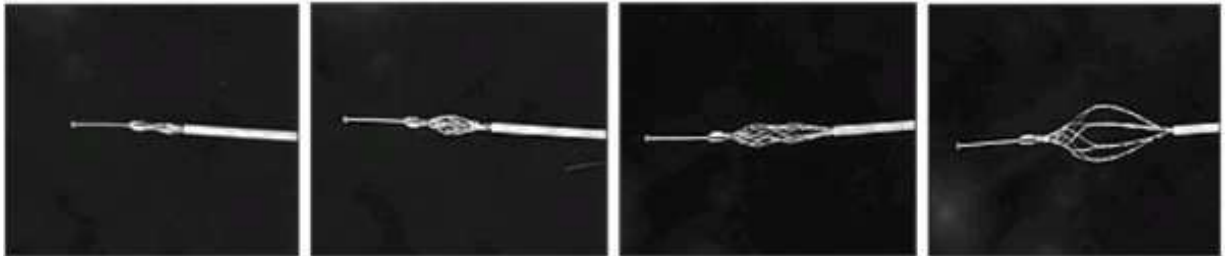


Figure 2.14: Sequence of deployment of a Nitinol retrieval basket, [194].



### 2.1.5 Colorectal surgery

In surgery there is often the need to expand soft tissue without causing any damages. For example, Liu, [185], explains that, in transanal endoscopic microsurgery, expansion of the cavities is required in order to clearly expose the lesions. CO<sub>2</sub> insufflation was initially proposed, but the medical community has not accepted it due to the peritoneal cavity contamination risk; accordingly, other insufflation techniques not involving CO<sub>2</sub> and at atmospheric pressure were studied and reported by many research groups. However, these methods allowed only small expansion and were just manually controllable, causing the risk to perforate the rectal wall. An alternative possible solution could be represented by NiTi, which is a promising material for cavities expansion, since it is biocompatible, highly flexible and controllable. Liu and colleagues, [185], indeed, presented an expansion device, developed for transanal endoscopic surgery, consisting of a drive part and an execute part. After having inserted the device in the rectum, the drive part, consisting of a NiTi spring, exploits the shape-memory effect to compress and generate a recovery stress which bends six superelastic strips. The execute part is actually represented by the superelastic strips, which pushes against the rectal wall, causing tissue expansion. Finally, when the drive part is powered off, it cools down and the superelastic strips push back the spring regaining a straight configuration, which allows extraction of the device from the rectum, [185]. Another recent application of NiTi in colorectal surgery is represented by a device for sutureless anastomosis, which is, as explained by Zbar, [363], a technique aimed at creating "gastrointestinal anastomosis with serosal apposition without the long-term insertion of foreign material transgressing the bowel wall", [363]. The advantages that SMA technology can bring to sutureless anastomosis are due to its greater flexibility and stability in design, introducing the capability to automatically adjust for variable tissue thickness of the bowel wall ends. The SMA based device for compression anastomosis (Figure 2.15), accepted by the FDA since 2006, is called ColonRing (Innomedica AG, Cham, Switzerland), [138], and is used in the colon and rectum for the creation of end-to-end and end-to-side anastomoses in both open and laparoscopic colorectal surgeries. ColonRing is similar to a circular traditional stapler, but it relies on a ring and anvil mechanism, well described in Reference [198]. Masoomi clearly explains that ColonRing "is comprised of 2 main parts: an applier and an implanted compression element. The compression element is composed of a plastic anvil ring and a metal ring including Nitinol leaf springs. When fired, the device holds

the 2 ends of tissue together with circumferentially placed barbed points, which penetrate through the tissue, holding it to the plastic ring. The NiTi ring is released, creating equal compression both radially and longitudinally around the ring. The device has a circular blade that cuts the tissue within the ring, creating patent anastomosis. The tissue heals around the circular edges that are held within the ring, and the device along with the compressed tissue is intended to slough off over the following 8 to 10 days, at which point the ring is expelled from the body with a later bowel movement. The result is a full circumferential, hemostatic-sealed anastomosis without any retained foreign material". Furthermore, Masoomi presented the clinical data of 1180 patients who underwent end-to-end anastomosis using the ColonRing device, taken from a multinational (16 countries) and multicenter (178 centers) data registry provided by NiTi Surgical Solutions (Netanya, Israel). The examined data demonstrated that the use of the ColonRing device is feasible and safe and represents a good alternative technology for end-to-end colorectal anastomosis. A post-marketing study on the ColonRing was also made by D'Hoore, [87], based on evaluations performed by 266 patients, between 2009 and 2011. The device was rated very easy and easy in 97.4 % of cases and the study also allowed to conclude that the Nitinol compression anastomosis device is effective and safe, [87]. As a last example, we may cite one of the few NiTi medical applications exploiting two-way shape-memory effect. Two way shape-memory effect can be for example applied to situations in which a valve-like behavior is necessary, such as in artificial sphincter design. In case of severe muscle dysfunction, transplantation can be attempted, but the success rate is still not high enough. The possibility to replace the damaged tissue with artificial muscles is a valuable alternative which may be offered by SMAs and may provide relief for patients with fecal incontinence, who suffer from both physical and psychosocial problems. Fecal incontinence may be caused by puborectalis muscle dysfunction: Wu and colleagues, [355], presented a design of a NiTi actuated device, with the function to assist human puborectalis. The authors also conducted preliminary experiments at body temperature in order to evaluate the deformation and mechanical properties of the prototype and he demonstrated the promising effectiveness of the proposed device.



Figure 2.15: ColonRing compression anastomosis device (courtesy of InnoMedicus AG, Cham, Switzerland), [138].

### 2.1.6 Otolarngology

SMA's have been also investigated in otolaryngology, a surgery field which involves operation in deep cavities with complex shape, e.g. ear canals. A successful application is represented by stapes prosthesis (Figure 2.16), used to replace natural stapes when stapes footplate is fixed in position, rather than being normally mobile, resulting in a conductive hearing loss. Many stapes prosthesis have been proposed and assessed in last decades, [147, 160, 277, 39, 171, 134]: all the authors agree that Nitinol prostheses are superior to conventional ones because they improve the quality of the interface with the long process of incus and allow to reduce the duration of the implanting procedure. Thanks to shape-memory effect, Nitinol stapes pistons allow to eliminate manual crimping, which is thought to be a major cause of incomplete postoperative elimination of conductive hearing loss and postoperative recurrences of conductive hearing loss. For example, in Reference [277] preliminary results are collected through evaluation of Nitinol stapes prosthesis implanted in patients with otosclerosis and it is suggested that self-crimping Nitinol prosthesis overcomes the drawbacks of manual crimping of conventional procedures. Another evidence of the benefits of SMA prosthesis is given in Hornung's paper, [134], where a new NiTi prosthesis for stapes surgery (Smart<sup>TM</sup> Piston, Gyrus ENT, Bartlett, TN, USA) is presented and assessed through implantation in 85 ears. When heated over 45°C, the prosthesis crimps itself around the long process of the incus, allowing to eliminate manual manipulation, thus facilitating implantation procedure and providing repeatability of the qualitatively

high results. NiTi has another application in the treatment of patients suffering from microtia, which is a defect of a smaller than normal and usually malformed auricle and affects, according to Chi, [68], "approximately one in every 7000 to 8000 infants in the general population". Since the auricle is one of the most complex three-dimensional structures of the body, reconstruction of a congenitally absent ear is a great challenge to the plastic surgeon. Chi used fifteen New Zealand white rabbits as animal models to explore the possibility of a NiTi SMA framework in ear reconstruction in vivo. The author reports that NiTi SMA implant was well tolerated with fewer complications. The NiTi frame exhibits, indeed, a mesh structure which facilitates fibrovascular ingrowth, providing good results and demonstrating that NiTi alloy can represent a valid alternative for ear reconstruction implants. A certainly more critical supporting frame, which can represent a further possible field of application for SMAs, is trachea cartilaginous framework, which is fundamental in maintaining structural integrity of airway: "when it is damaged, airway can collapse during breathing, leading to dyspnea", [192]. Surgical reconstruction of trachea is a challenging operation, since end-to-end anastomosis technique is not always possible, for example in cases when the resected segment would involve more than half the total length of the trachea, cases in which the lesion involves both the larynx and trachea, cases in which the defect is very close to the glottal area, and cases in which previously attempted resection and end-to-end anastomosis has failed. An alternative method to treat tracheal stenosis is homografting (i.e. use of autologous materials such as costal or nasal cartilage), but, as Luo, [192], explains, "the process of obtaining the graft introduces a new site of injury and, furthermore, the shape of the cartilage is often not ideal for the recipient site; so homografting is not recommended as a primary treatment", [192]. So other materials to replace trachea framework are required: Nitinol stents, already mentioned for the treatment of other body canals injuries, are then proposed for trachea reconstruction. Luo, [192], used mesh patch of NiTi as extraluminal stents in 8 experimental animals for reconstruction of a surgically created trachea stenosis. Since the operation had good results in animals, it was then successfully used by Luo to repair a tracheal wall defect in a human victim of a traffic accident.

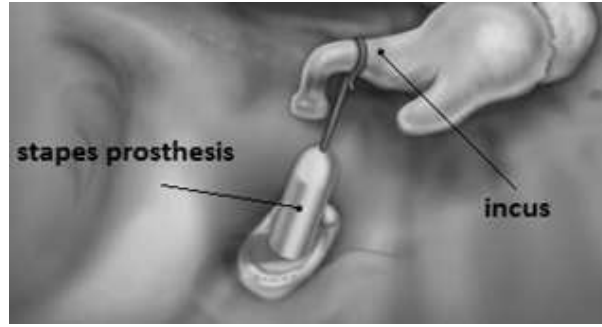


Figure 2.16: Nitinol stapes piston.

### 2.1.7 Neurosurgery

Since the middle 90ies, SMAs found various applications in neurosurgery, mainly in the form of stents, coils, microguidewires and optimized surgical microinstruments. Small dimension requirements of neurosurgical settings are permanently pushing researchers towards investigation of new materials and novel instruments design: among the benefits provided by SMAs there is the possibility to miniaturize the instruments and to reduce the number of the components needed, since simpler design can be performed. In Reference [117] the need for small and flexible surgical instruments for the strongly confined and complex operation environment of neurosurgery is addressed. The paper described the designing and manufacturing of NiTi based microforceps (Figure 2.17) for endoscopic neurosurgery, with no need for mechanical joints, thanks to the superelastic behavior. Another SMA neurosurgical instrument description is provided by Reference [158], where the bending characteristics and fatigue properties of two SMA brain spatulas and a conventional copper spatula were compared. The two SMA spatulas resulted to be less stiff and more fatigue-resistant than the existing copper spatula. At present, challenging conditions of intracranial surgery make it difficult for the surgeon to remove brain tumors completely using traditional surgical tools. In References [131] and [132] a highly dexterous, small cross section, MRI-compatible robot is proposed, using two antagonistic SMA wires for the motion of each joint, so that each joint can be controlled separately through a temperature feedback which produces relative SMA wire bending. Magnetic resonance compatibility of the designed tool is really important because intraoperative magnetic resonance imaging improves the surgeon's capabilities by providing an excellent soft-tissue contrast, traducing in less damage to surrounding healthy tissue. Since aneurysm rupture and consequent cerebral hemorrhage are among the major causes of death in the occidental

countries, many studies have addressed SMA devices able to treat aneurysm, [358], [53], [108]. Among the devices for aneurysm treatment there are coils, ball-shaped wires positioned into the aneurysm to induce clotting, in order to avoid rupture. Coils are usually made of platinum, but recently a mixture of platinum and Nitinol has been used by Ev3 Neurovascular (Irvine, CA), in order to achieve less stretching and better resistance to compaction, [259], [358]. In addition to coils, Nitinol stents can be used for the treatment of intracranial aneurysms, especially when the aneurysm has a large neck: once the coil has been located into the aneurysm, a stent can be released in the corresponding zone of the artery to prevent coil migration, [53, 259]. Moreover, in 1996 a tiny SMA-actuated microgripper, as small as a grain of sand, has been developed, [316], intended to be used as a grasping device in brain aneurysms treatment. Nitinol micro-guidewires are another example of a SMA device successfully exploited in the intricate spaces of neurosurgery environment. In aneurysm treatments and in angioplasty flexible Nitinol micro-guidewires even smaller than 0.5 mm are required to form a guide for the advancement and positioning of other devices (such as angioplasty balloons, stents, filters), by following tortuous paths without kinking. Because of their high steerability and torquability, high strain recovery and resistance to torsion and kinking, NiTi wires cause fewer problems in bending than conventional materials, [259], reducing the operation time and improving the ease of the surgeon. SMA guidewires have been also investigated for the possible use in minimally invasive electrocorticogram recording, a test which provides beneficial information for clinical diagnosis, in particular in neurosurgery, but which still requires invasive procedures such as craniotomy in order to be performed on the wide brain area, [360]. A minimally invasive method to deploy the electrodes, based on a SMA guidewire, is indeed proposed in Reference [360]. A monkey was used for testing: the electrode array was inserted in the subdural space from an 8 mm hole made on the skull, and the electrodes were deployed to the desired position, performing a minimally invasive procedure allowing correct measurement of the somatosensory evoked potential.

### 2.1.8 Ophtalmology

Since advances towards MIS are particularly strong in ophthalmic surgery, especially in cataract surgery, [238], several SMA applications have been investigated. In Reference [239] a preliminary study is made to demonstrate the ocular biocompatibility of Nitinol.

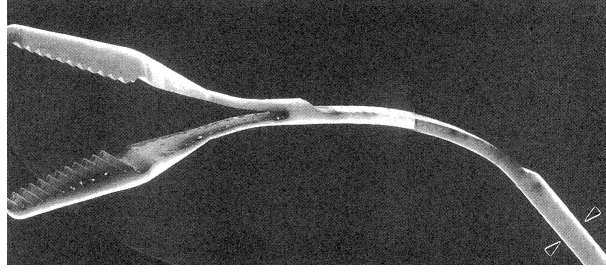


Figure 2.17: Microforceps for brain surgery, [296].

The experiments were performed on Yucatan mini-pigs, using a 30-gauge prototype injector to attach the Nitinol clips to the iris. The Nitinol clip prototype was well tolerated and showed no toxicity in the short-term. Moreover, the injectable delivery system was 15 times faster and technically less challenging than conventional suture techniques. Furthermore, Olson, [238], details the design and testing of a microsurgical injector which delivers a SMA clip for wound closure. Testing was performed on enucleated porcine eyes, simulating different surgical settings, where new SMA clip suture demonstrated a clear advantage over conventional suturing techniques (using Nylon stitches), both in terms of surgical time and wound strength. In terms of suturing performance in space-confined surgical settings, deployment of the SMA clip was 16 times more rapid in pupilloplasty and 20 times more rapid in intraocular lens fixation surgery; moreover, the apposition of the tissue was qualitatively equal or superior to traditional suturing in all the performed procedures. Since usually shorter surgical times correlate with less endothelial damage, NiTi clips can be considered less invasive with respect to conventional suturing. Moreover, NiTi clips demonstrated to be more resilient and reliable than conventional ones; indeed, a recovery of the original shape occurred even when pushed to leak, unlike conventional suture which, if pushed to failure, breaks irreparably. Through other experiments performed on porcine eyes, Olson, [238], also concluded that the injectable shape-memory suture clips assure a decreased risk of late suture failure, which is a main cause of complications occurrence in intraocular lens fixation. The author points out that a possible use of this new suturing procedure is in surgical settings where suturing is "difficult and time intensive, such as during glaucoma extraocular drainage device placement". Another example of a novel SMA device for ophthalmology is presented in Reference [153], where a biocompatible synthetic implant for the surgical treatment of high-complicated myopia, called dynamic plug, is presented. NiTi based alloy is a well suited choice for the implant, which has to

be non-traumatic, easy to use and provide a determinate level of compression over a long period of time. The author explains in the paper that "the application of this device allows low-traumatic correction of the shape of the posterior eye pole and strengthening of the sclera" and describes tests performed over 20 eyes of chinchilla rabbits, showing promising results. A commonly known SMA application is superelastic eyeglass frames (Figure 2.18); differently from conventional frames, they press against the head with constant and comfortable stress, thanks to the constant stress exhibited by the alloy over a large range of strains. Moreover, they can be twisted and deformed, undergoing an unconstrained recovery of their original shape upon unloading.



Figure 2.18: Shape-memory eyeglass frame.

### 2.1.9 Urology

Among SMA applications in urology, flexible, steerable and kink-resistant urethral and prostatic stents (Figure 2.19) for treatment of urinary duct occlusions have been investigated and proposed. In Reference [202], 15 patients with prostatic hyperplasia, who showed no recovery upon administration of  $\alpha$ -1 blockers, were treated with a urethral stent (MEMOKATH<sup>®</sup>) made of NiTi. Exams showed that the MEMOKATH<sup>®</sup> was effective and improved the quality of life in all patients in the early phase of treatment. An open issue is present regarding urethral sphincters: Muller, [224], affirms that "the commercially available artificial urethral sphincters do not mimic natural muscle function and therefore have met with only limited success". As already mentioned in the case of the puborectalis assisting device, SMAs have been investigated to fill this gap: at present, advanced prototypes of SMA activated sphincters are available for animal experiments,



[224].



Figure 2.19: RPS Allium (Round Posterior Stent) urethral stent, made of a Nitinol framework with a polymeric coating (courtesy of Allium Medical Ltd., Caesarea Industrial Park South, Israel), [3].

### 2.1.10 Gynecology and andrology

Probably the first SMA minimally invasive product to be put on the market is the Homer Mammalok, used by radiologists to locate breast tumors. It consists of a Nitinol wire hook and a stainless steel cannulated needle: before insertion, the hook is withdrawn into the cannula, then the needle is inserted into the breast through a small opening and adjusted until its tip is at the site of the tumor; afterwards, the Nitinol wire is advanced, regaining a tight hook configuration and allowing the marking of the tumor. If needed, the hook can be retired and the needle repositioned, [92]. Another application of Nitinol in gynecological field is a permanent birth control device, named Conceptus (by Essure). It is a superelastic Nitinol coil which, inserted into the fallopian tubes through the cervix without incisions, encourage tissue ingrowth and acts like a barrier, with a success rate of 99.8 % in preventing pregnancy. The first patent where Nitinol was used in contraceptive applications was released in 1971, [140]. The TUNA prostate ablation device is a SMA device used in andrology, presenting a cannula with a curved tip, from which straight Nitinol needles are elastically deployed. The needles can be deployed for use, withdrawn into the cannula, moved to another site and deployed again as many times as necessary, [252]. A further clinical application of SMAs in andrology is related to penile implants,

[189], where Nitinol is used in the form of rod or wires. Shape-memory effect is exploited in these devices in order to restore erection ability in damaged organs.

### **2.1.11 Physiotherapy**

Shape-memory effect is used also in physiotherapy of atrophied muscles. An example is a glove activated by shape-memory wires, reproducing the activity of the muscles and simulating the original hand motion (Figure 2.20). In this case, we have two-way shape-memory effect: when the glove is heated, wires become shorter, while when the glove is cooled the wires regain the former shape, opening the glove, [259]. Viscuso and colleagues, [336], presented a device promoting spastic elbow relaxation, based on two superelastic NiTi elements put on the opposite sides of the elbow joint and connecting two shells to be fixed to the upper arm and forearm (Figure 2.21). The novelty of the mechanism is that, differently from conventional devices which fix the arm in a stable position, the NiTi element imposes a stable torque to promote stretching of the muscles. First clinical outcomes showed promising results, with improvements in patients postures and high acceptability of the device by the patients. Another example is provided by Pittaccio and Vicuso, [267], who presented a passive assistive device for ankle dorsiflexion, to be used in case of immobility or spasticity of the ankle after stroke. The device is based on SMA actuation and its aim is to train passively the immobilized joint, providing a repeatable movement able to help maintaining joint flexibility and normal muscle tone. A robot mask to assist physiotherapy of a hemifacial paralyzed patient is presented in Reference [143]. This idea may open the door to a novel range of physiotherapy devices, but significant differences in the proportions of human head among different people demands customized design.

### **2.1.12 Other applications: active prostheses and robot-assisted surgery**

Shape-memory characteristics of SMAs are promising for the creation of a light weight, silent, dexterous anthropomorphic hand. Much work has been done in the last years towards this objective, to provide motion and dimensions as close as possible to human hand ones. At present, there are numerous commercially available prosthetic hands, such as the i-Limb<sup>TM</sup> Hand, which was first launched in 2007 by Touch Bionics, the Otto Bock's SensorHand<sup>TM</sup> Speed, and the Motion Control Hand, [146]. Usually DC motors are used in

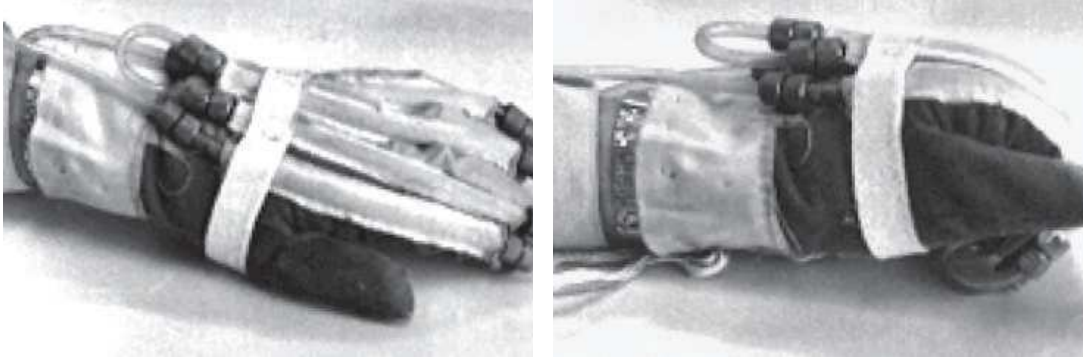


Figure 2.20: Shape-memory glove for physiotherapy respectively at low temperature and at high temperature, [259].

these applications, but the dimensions and weight of this kind of motors don't match with human proportions, compelling to decrease the number of degrees of freedom and making the prosthesis uncomfortable for the end user. This gap encourages the development of new design techniques, such as SMA actuation mechanism, which takes advantage of shape-memory effect, providing a motion similar to muscle behavior. Moreover, SMA actuators show high power to weight ratio, therefore allowing for smaller dimensions of the prosthesis, [146]. Several studies have reported efforts towards the creation of an effective prosthetic hand involving SMA actuators or wires, [310, 152, 201]. In Reference [146] the design of a tendon-driven SMA actuated finger is presented, with the aim to obtain a prosthetic hand exploiting SMA actuation under an EMG (electromyography) signal. In Reference [201] a new light and quiet prosthetic hand using SMA type artificial muscles has been presented. The experiments which were performed to examine the motion of the initial prosthetic finger demonstrated that it could grasp an object, so a hand configuration was set up and tested, with the alimentation provided by a lithium battery, showing finally that the prosthetic hand could grasp different kinds of objects and providing promising results for further research on this topic. As previously described, SMAs have strongly promoted minimally invasive surgery, thanks to the possibility to develop smaller and more effective surgical instruments. Impressive achievements in minimally invasive surgery have been also allowed by the persistent advances in robotics, [113]. Shape-memory effect has indeed been exploited using SMA wires and actuators to optimize robotic arms operation. In MIS, the robot is required to provide a big output with the smallest volume. Having local, lightweight and powerful actuators at end-effectors could help to simplify surgical

robot design and to optimize the number of degrees of freedom: SMA actuator meets these requirements because it has high energy density, exhibits large recoverable strain and is miniaturizable, [304]. Moreover, Shi, [304], showed that the electric resistance of SMAs has approximate linear relationship with the strain, a fact which makes accurate self-sensing possible. In the last years, many studies have been carried out on the use of SMAs in robot-assisted minimally invasive surgery. For example, in Reference [161] a novel hybrid actuator is presented, in order to increase the number of degrees of freedom in MIS, through the idea of a local actuation of the end-effector, which consists, in this case, of a 5-mm-diameter laparoscopic needle driver. As already pointed out, in the state of the art of robotic tools for minimally invasive surgery (MIS), the number of degrees of freedom is limited by the fact that the actuators used to activate the end-effectors are located outside the patient's body, with the power transmitted by means of sliding link or tendon-driven mechanisms: in these conditions the design of the wrist gets complicated. The proposed millimeter-scale hybrid actuator design consists of two stages: a dc micromotor stage and an SMA actuator stage, whose limited dimensions allow local actuation of the end-effector, thus simplifying the design of the spherical wrists and increasing the number of DOFs. In Reference [113] another SMA actuated robotic application is presented, consisting of a prototype MIS-robotic tool, using SMA-wires in an antagonistic tendon configuration, which results in low stiffness. Moreover, the low weight (150 gr) of this tool "makes it suitable for most surgical operations".

## **2.2 SMA cardiovascular applications and computer-based design**

The aim of this chapter is to provide a comprehensive overview of the application of SMAs in the field of cardiovascular surgery, which represents the most significant share of the SMA medical market. In fact, the unique features of SMAs, and in particular of Nitinol, which is the most used SMA in the biomechanical field, well fit with the needs of current trend in cardiovascular surgery, i.e., the minimization of the device size and, at the same time, the reduction of the procedural impact on the patient's recovery time. Such an approach, commonly called minimally invasive surgery, is usually based on operations performed through small artificial incisions or natural body openings. In particular, for



Figure 2.21: Superelastic device for spastic elbow relaxation, [336].

cardiovascular applications, minimally invasive surgery is usually labeled as endovascular surgery, because the miniaturized devices are delivered by low-profile catheters, introduced through narrow vascular accesses running inside the cardiovascular system. The outlook of SMA-based cardiovascular devices is promising not only because medical procedures are becoming less and less invasive, [115], but also because the impact of cardiovascular diseases (CVDs), which is the generic name given to the dysfunctions of the cardiovascular system such as atherosclerosis, hypertension, coronary heart disease, heart failure or stroke, steadily increases. In fact, CVDs are nowadays the leading cause of death in the Western countries: a recent report of American Heart Association (2011) states that, on the basis of 2007 mortality rate data, more than 2200 Americans die of CVD each day, an average of 1 death every 39 seconds, [339]. The same trend is also present in Europe, where CVDs are the major death cause in almost every European country, causing over 4 mln deaths, [232]. These data, integrated by a constant increase of the average life expectancy, well explain the high impact of such pathologies on the economy of Western countries: in Europe, the estimated direct and indirect cost of CVDs are 196 bln EUR per year, [326], while the total direct and indirect cost of CVDs and stroke in the United States for 2008 is estimated to be \$297.7 bln, [339]. Given these considerations, in this chapter we review the application of SMAs in the field of cardiovascular devices, with a special focus on the device design and, in particular, on how advanced computer-based modeling is used in this context. For this reason the chapter will firstly give a brief overview of the different types of SMA cardiovascular devices and then, for each of them, a literature review of the related numerical simulation is proposed.

### **2.2.1 Cardiovascular devices: an overview**

Historically, of vascular diseases have been treated combining open surgery with medical management. Since the first description of a percutaneous procedure, the use of endovascular approaches has revolutionized the treatment of vascular disease. In the last decades, endoluminal therapy of vascular diseases has expanded from simple dilatation of atherosclerotic lesions to more complex acute lesions, assuming also a significant role in the management of aortic aneurysms or dissections. As already stated, these broadened indications for endovascular therapy have been supported by technological improvements in the concept, design, and technologic content of endovascular devices. Among this advancement, the

contribution of SMAs, and in particular of Nitinol, cannot be ignored. The goal of this section is to provide an overview of the SMA-based applications in cardiovascular surgery. Given the constant growth of such a type of applications, the present review would not be exhaustive but it aims at assessing the main applicative sectors and the clinical tasks targeted by the SMA features embedded in the device. It is worth noting that most of the applications described in the following can be used for endovascular surgery because, thanks to the pseudoelastic effect, they present as a primary feature the capability to be highly compressed within a low-profile delivery system and to recover the desired shape after the deployment. We have categorized the SMA cardiovascular devices in three main families: i) catheters and guidewires; ii) embolic filters; iii) stents and stent-grafts. While the first category represents the basic elements of endovascular approach, embolic filters were the first SMA-based devices in cardiovascular field, [259]; finally, stents and stent-grafts represent the major share of the SMA cardiovascular market, [92, 115]. Nevertheless, we have collected in a supplementary, generic category (i.e., Other cardiovascular devices) all the remaining applications.

### **Catheters and guidewires**

The pseudo-elastic effect of Nitinol is exploited in two fundamental components of the endovascular procedure toolkit: the guidewire and the catheter. As easily understandable from its name, the purpose of a guidewire is to create a pathway in the vascular system up to the target lesion (Figure 2.22). The guidewire can be thought as the rail on which the catheter runs. The catheter is basically a low-profile hollow tube, aimed at delivering in the target lesion a miniaturized device. The operator has an indirect view of the system through real-time X-ray images where the vascular tree visibility is enhanced by the injection of a contrast dye. In most endovascular procedures, guidewires have to achieve and to keep the critical access across the target lesion along the entire procedure and must be significantly long in order to reach vascular districts which are far from the endovascular access. For instance, the carotid artery, which is located in the neck, may be reached from a femoral access point, which is instead located in the upper part of the leg. Moreover, the vascular path could be characterized by a severe tortuosity and numerous side branches; this is the reason why wires have to be steerable and torquable, [92]. This issue also clearly explains why even a small permanent deformation is undesired. In order to accomplish such requirements, current guidewires are usually made of an inner core wire (mandrel)

surrounded by an outer coil wrap. The core wire has a tapered shape in the distal part which does not extend to the guidewire tip, where a more flexible and ideally atraumatic distal coil tip is instead positioned. Moreover, in order to improve lubricity, the guidewire surface is coated with a hydrophilic polymer. As already pointed out by Duerig and colleagues in 1999, [92], guidewires were the first applications to take advantage of the kink resistance (i.e., resistance of the wire to deformation) of Nitinol. In fact, the inner core of guidewires was originally made of stainless steel. Later on, flexibility provided by the unique properties of SMAs allowed the development of novel guidewires, able to enhance the dexterity of the surgeon. Nowadays, both stainless steel and Nitinol are used for the inner part of guidewires. Stainless steel provides the advantage of a good torque controllability, while Nitinol is more stretchable and steerable. Moreover, Nitinol is used also for its "soft" end-user feel which allows precise placement and delivery through very tortuous paths without losing a good torqueability and pushability of the device, [268]. Future developments are expected on micro-guidewires (diameter less than 0.5 mm), to be used for abdominal blood vessels, peripheral and cerebral arteries, in view of less and less invasive surgical techniques, [236, 259]. Nitinol is also used to produce active catheter shafts: high deformability, kink resistance, and capability to recover the original shape make them far more controllable than conventional devices and allow easy insertion and inspection inside the human body. One of the appealing applications of SMAs in this sector is the actuation of the catheter, which can be based on different types of NiTi microactuators, providing various motions, such as bending, torsion and extension/contraction, and presenting different deformation mechanisms according to the requirements of the device. For example, thin NiTi plates fixed along the side of the catheter, or NiTi wires embedded in the catheter body, can provide the bending motion when heated. Whereas, NiTi coils designed to twist or untwist according to temperature variation can provide torsional motion. Extension motion can be instead provided by NiTi coils acting as an extending or contracting spring. Moreover, stiffness control can also be provided by equipping the catheter with further SMA coils, which become stiffer when heated, thanks to the phase change from martensite to austenite. The activation mechanism usually relies on Joule effect, producing heat by the application of an electric current, [125].



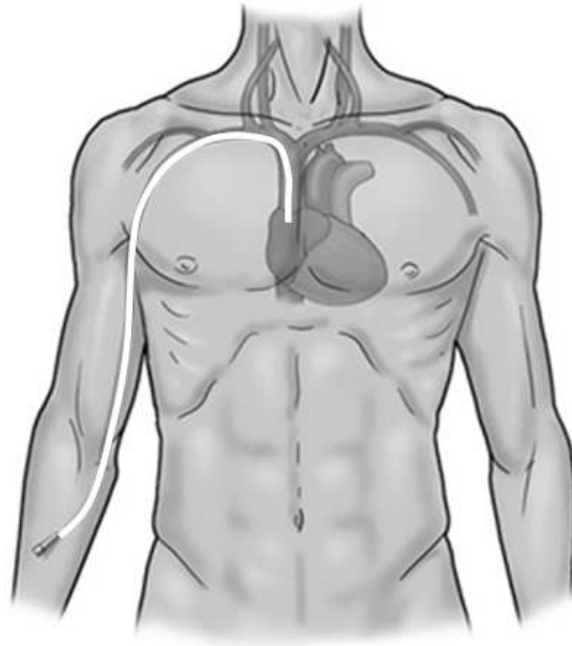


Figure 2.22: Guidewire route through aorta.

## Embolic filters

Embolic filters (Figure 2.23) are another successful example of the use of pseudoelastic effect for endovascular surgery. In fact, the basic mechanism exploited in such a type of application is the capability to expand inside the lumen, starting from a low-profile shape. The device, compressed within the catheter, is delivered inside the vessels and deployed thanks to pseudoelastic effect. Once the filter is open, it has the aim of capturing small clots floating within the blood stream. When the basket filter is full, it is retrieved usually by a pull-back mechanism, which reduces the device profile to the compressed configuration allowing thus the endovascular navigation. A number of design variants have been proposed for this class of SMA-based devices, [148, 193], but their efficacy is still a matter of clinical debate, [225, 137]. In this context, a special mention should be given to the venous Simon filter, which can be considered the first vascular SMA application, [306, 259]. This pioneering filter, still used in the clinical practice, [278], is used to prevent emboli in patients unable to tolerate anticoagulants and exploits the shape-memory effect. The device, manufactured in the open configuration with a NiTi alloy having austenite finish temperature ( $A_f$ ) equal to the body temperature, is preloaded into a catheter while in the martensitic state. The device is then easily crimped on the catheter thanks to the

residual deformation due to the martensitic transformation, which is kept through a chilled saline solution flowing in the catheter during the insertion of the filter into the body. Once the catheter is in place, the filter is released, the flow of chilled saline solution is stopped, and the device is warmed by the surrounding blood, thus recovering its pre-defined flower-like shape.

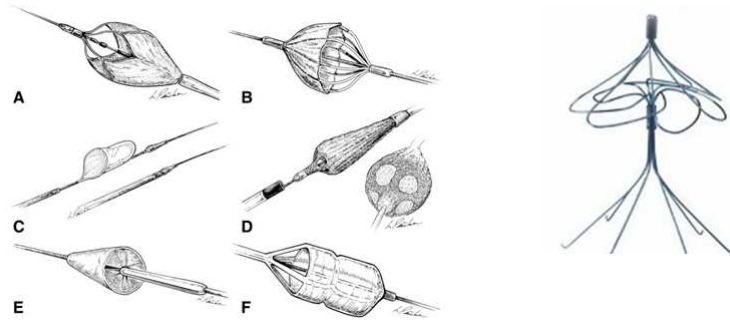


Figure 2.23: On the left, illustrative sketch of different carotid embolic filters adapted from Kasirjian et al., [148], (A) AccuNet, (B) AngioGuard, (C) Filter-Wire EX, (D) Interceptor, (E) IntraGuard, (F) NEURhield (EmboShield). On the right, Simon Nitinol Vena Cava Filter manufactured by Bard.

## Stents and stent grafts

The term stent derives from Dr. C.T. Stent, a dentist who in the late 1800's developed an orthodontic device to assist in fanning an impression of teeth, [288]. Such a term is nowadays generally given to an expandable tube-like device, which is inserted into a natural conduit of the body to mechanically enlarge a disease-induced localized narrowing of the duct (Figure 2.24). Although some stents are made by polymers, most of them are metallic. In endovascular surgery, stents are usually used to enlarge the so-called stenosis, i.e., an abnormal narrowing of arterial lumen due to a local disease-induced thickening of the vessel wall. The metallic frame of the device can be (partially) covered by a polymeric skirt to form a hybrid vascular prosthesis called stent-graft. Such devices are normally used to diverge the arterial blood flow within pathologic vascular anatomies; for instance, stent-grafts are used to reduce the pressurization of aneurysmatic sac or to exclude the perfusion of false lumen in a dissected artery, [205]. The real success of stents rose from their use in the treatment of coronary stenosis. In fact, the intravascular stent drew the interest of the medical community from 1994, when the stainless steel Palmaz-Schatz Coro-

nary Stent was launched, [150], to integrate percutaneous transluminal angioplasty (PTA), a procedure exploiting the inflation of low-profile balloon to enforce the stenosis enlargement. The sole PTA provided an immediate gain of the lumen patency but a significant part of the patients experienced restenosis within a year and need further treatment. For this reason, the placement of a stent immediately after PTA was included in the percutaneous procedure leading to a significant decrease of the acute re-occlusion; this innovative device transformed the practice of interventional cardiology, selling one mln units in less than two years and creating a \$700 mln annual market nearly overnight. It is worth noting that the mechanisms underlining the Palmaz-Schatz stent and its offspring is based on the local plastic deformation occurring during the balloon inflation at the hinge points of the design; in this manner, the stent remains in an open configuration also after the balloon deflation, counteracting the arterial elastic recoil. As soon as the use of stenting started to extend to peripheral vessels, characterized by long lesion, tortuous anatomies and complex kinematics, such plastic deformations showed undesired drawbacks and the Nitinol features appeared as a key factor to build a new type of devices, the so called self-expanding stents. The idea of using Nitinol to make self-expanding cardiovascular device is not certainly recent; in fact, in the 80s, Charles Dotter used Nitinol coils as scaffolds for arteries, showing the promising functional qualities of Nitinol for endovascular treatments. Unfortunately, at that time, the manufacturing procedures were not advanced enough and mechanical qualities of Nitinol had not been completely understood yet, so it took many years before the first Nitinol stents began to be marketed, [206]. This is the reason why at the beginning of the 90ies Nitinol was just available in wire form, so Nitinol stents were not very successful. In the mid-90ies, laser cutting began to be performed on Nitinol tubes. The availability of Nitinol tubing made this material the first choice for self-expanding stents and stent-grafts, [297]. Bard released the Memotherm in 1997, and Cordis released the SMART stent in 1998. The SMART stent became the dominant design in the endovascular marketplace, and remains the leader today. The success of the SMART stent design was largely due to its very fine mesh structure that offered exceptional contouring, flexibility, and apposition characteristics. It is estimated that Nitinol stents now comprise 60% of the endovascular stent market. Nitinol stents also dominate non-vascular markets including urologic, upper and lower gastrointestinal, and trachea-bronchial applications, [55]. Currently, there is a number of self-expandign Nitinol stents which have been marketed or are under development, [51]. Generally, stents for endovascular applications are

made of V-shaped struts forming circumferential rows, linked together by bridges. This ring configuration offers indeed a good compromise between flexibility, strength, and capability of the design to get small diameter to accomplish the accommodation within the low-profile catheter. There are various designs showing different link types between struts. The two main configurations of ring type stents are the open-cell and the closed-cell ones. Struts can be connected through peak-to-peak, peak-to-valley or mid-strut connections. Virtually every combination of peak, valley, and mid-strut connections has been designed, and even hybrid connections have been provided. The overall mechanical features of the stents are influenced both by geometrical design details, such as the type of ring "bridges", strut width, length, thickness, shape, and by the material processing, as well explained by Stoeckel et al. and Bonsignore on 2003, [317, 55]. In this context, it is worth mentioning the appealing initiative of an open-source design tool for self-expanding stent recently proposed by Bonsignore and colleagues, [241], who has resumed their experience of stent designers in a practical guide and resource for design and analysis of a generic Nitinol stent. The majority of self-expanding Nitinol stents is cut from tubing, but there are some exceptions, including wire-based and sheet-based manufacture. For example, NexStent (Boston Scientific), for use in patients with carotid artery disease, is made from a laser cut Nitinol sheet. The sheet is tightly rolled up for delivery into the catheter and can be deployed to adjust to a variety of diameters. Another exception is the IntraCoil (Sulzer IntraTherapeutics Inc.), a wire coil stent for the treatment of superficial femoral artery and popliteal artery lesions, based on the same principle of first Dotter's experiments, [206]. Some stents made of wire coil are also available, but they never met with great success in vascular applications because they usually present a larger diameter in the constrained state than ring type designs. Instead, wire coil stents are generally used in non-vascular applications (e.g., prostrate and urethral stenting) because they are usually fully retrievable after weeks or months since implantation, [55]. The main manufacturing method for Nitinol tubes is laser micromachining, but also photochemical etching has been demonstrated to be a viable procedure. It is worth mentioning nano-manufacturing, a method implying high vacuum sputtering in order to build metallic implants in an additive fashion, [55]. To appreciate the importance of the stent-related market and the corresponding economical and social impact, we report in the following some data about that. Coronary artery disease is a major cause of death around the world, so coronary stenting is a widely used technique. The global market for coronary stent devices reached \$7.1 bln in 2011. By 2016, it is expected

that total market value will reach \$10.6 bln. The Americas region dominated coronary stent device revenues for 2011 with a 40% share. This segment was worth \$2.8 bln in 2011 and is projected to reach \$4.3 bln by 2016. Europe is the second largest shareholder with 37% of the market for coronary stent devices. Its market size is expected to increase from \$2.6 bln in 2011 to \$3.4 bln in 2016, [114]. The peripheral angioplasty procedures are expected to reach 3.3 mln procedures by 2016, while coronary angioplasty procedures are estimated to reach 4.5 mln procedures by 2016. The major driving factor for these markets would be the increasing demand for minimally invasive percutaneous endovascular treatment. The stents used in interventional procedures represent the largest segment of the market. Also the market of stent-graft appears to be promising. In fact, a research made by Medtech Ventures reports that approximately 700,000 new cases of aortic aneurysms are estimated to be diagnosed every year in the developed world. Given this data, the global market for aortic stent-grafts was estimated at \$1.8 bln in 2012, a growth of 12% over its 2011 level of \$1.6 bln. The market has been growing at an average annual growth rate of 15% over the previous five years, [4].

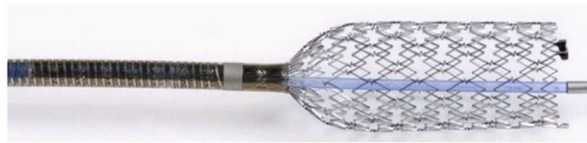


Figure 2.24: Example of Nitinol self-expanding stent for cardiovascular applications, [315]. The device is partially deployed during a free-expansion deployment: while the distal part has gained the original expanded configuration, the proximal part is still compressed within the delivery system.

## **Others**

### **Percutaneous valves**

Another frontier of cardiovascular surgery is the minimally-invasive replacement of the heart valves and in particular of the aortic valve. Also in this context, Nitinol and its capability to recover the initial shape after a severe deformation is playing a key role. In fact, in 2002 Cribier performed the first clinical implant of a percutaneous balloon-expandable aortic valve at the level of the native valve while, in 2004, Grube implanted for the first time a self-expandable transcatheter valve. In the last decade, different devices have been designed and submitted to clinical evaluation (Figure 2.25) confirming that, on

one hand, such an innovative technique represents a promising solution for aortic stenosis even though, on the other hand, at present, it is still an immature procedure due to limited follow-up data and durability evaluation. Two types of transcatheter devices are currently available: cobalt chromium balloon-expandable (Edwards Sapien XT) or nitinol self-expandable stent (Medtronic Corevalve). In the case of balloon-expandable devices, a balloon inflation leads to the valved stent expansion which excludes and compresses the native diseased leaflets. In the case of self-expandable valve placement procedure is very similar to the previous one except for the fact that self-expandable prostheses automatically open through a step-wise deployment when gradually extracted from the delivery catheter, [17].



Figure 2.25: Transcatheter aortic valve prostheses currently used in clinical practice: the Medtronic CoreValve (left) and the Edwards SAPIEN XT (right). For more details please refer to [17].

## Coils

Coils are often used to treat cerebral aneurysms, i.e., localized dilations of the intracranial arteries; they are wires which are positioned into the aneurysm in a ball-shaped fashion, with the aim to induce clotting reaction, eliminating the risk of rupture. Traditionally, coils are made of platinum, but recently a coil made with a mixture of platinum and NiTi has been produced (ev3 Neurovascular, Irvine, CA), resulting in less stretching and better resistance to compaction with respect to other types of coils, [259].

## Clips for cardiac surgery

Nitinol U-Clip (Coalescent Surgical, Inc, Sunnyvale, Calif) is a device which can be used for vascular sutures, exploiting the superelasticity of Nitinol which provides an auto-

matic closure of the clips. Studies on animal models have been performed and it has been demonstrated that Nitinol clips have the same effectiveness of conventional sutures when used for anastomosis, with the advantage that the procedure is faster because there is no necessity to tie knots, [85, 130]. Another type of SMA clip used in cardiovascular surgery is represented by the thermoreactive Nitinol clips, used for sternal closure after cardiac operations. Since healing complications after cardiac surgery, such as dehiscence, osteomyelitis, mediastinitis and superficial wound infection, often occur and produce a significant mortality, it is apparent that the technique of sternal closure is an important factor to analyze. Thermoreactive Nitinol clips offer an improved method for sternal closure, which results in less post-operational complications and improves osteosynthesis thanks to the lighter forces produced on the sternum with respect to conventional closures, [234, 228, 63].

### **Occlusion devices**

In order to treat Patent Ductus Arteriosus, or Atrial and Ventricular Septal Defects, anomalies which can reduce life expectancy, self-expanding occlusion devices made of Nitinol have been developed (e.g., AGA Medical Corp., LEPU medical), which present single or multiple lobes made of a fine Nitinol mesh and which can be introduced in vessels through a catheter by a minimally invasive procedure. The SMA occlusion device, made of SMA wires and a waterproof film of polyurethane, represents an alternative to open surgery, which is an extremely invasive treatment. The device is initially inserted through the hole in the septum, by means of a catheter, and is partially deployed, so that it covers the opening in the septum. Then it is pulled against the opening and is further deployed from the catheter, creating a second cover on the other side of the opening, [89].

### **Heart surgery instruments**

Another cardiovascular application of Nitinol is an open-heart stabilizer, used to prevent regional heart movement while performing surgery. Superelasticity and constant force plateau presented by SMAs are exploited also in the tissue spreader, used to spread fatty tissue on the heart, [344].

### **Clamps**

The clamp technique, used to arrest bleeding and to control blood flow from the arteries, is essential in any surgical operation. SMA features allow a constant stress response over a large range of strains allowing thus innovative concept of clamping, able to guarantee a better control on occlusive pressure on the vessel wall, [364].

### **Annuloplasty band**

Mitral valve regurgitation is often due to structural defects of the valve, treatable with surgical intervention. Mitral valve repair, when possible, is preferred to mitral valve replacement, because it is more effective and durable, and it doesn't require anticoagulant drug therapy. Main mitral valve repair techniques involve securing a full ring or partial band around the mitral annulus. Also this type of intervention can be performed through minimally invasive approaches as recently reported by Purser and colleagues, [273], who developed a prototype ring composed of a NiTi SMA, a silicone sheath, and a polyester sewing cuff, which meets the requirement of being flexible enough to be deployed through an 8-mm trocar, but stiff enough to provide benefits to the damaged mitral valve. The trade-off between flexibility and stiffness is fulfilled by the NiTi core of the prototype, which is flexible if maintained at lower temperatures (in the martensitic phase), allowing for simpler deployment, placement, and suturing, while it is semi-rigid over 37°C, i.e., at normal human body temperature, providing the desired support to the mitral valve. Ex vivo trials performed by Purser and colleagues clearly demonstrated that the device could be easily implanted through robot-assisted surgery and showed a good durability and a positive reduction effect on mitral valve regurgitation, [272, 273].

### **Prosthetic pump**

An early patent, [271], reports the design of a prosthetic pump, intended for application as an artificial heart, able to reproduce the natural movement of contracting and relaxing muscles and whose contractile elements are formed of NiTi.

### **Nitinol blades for resecting calcified aortic heart valves**

Calcified aortic heart valves are often replaced by equine or porcine pericardial valves on a metal stent structure. However, the calcified layer may be non-circular, causing leakage, regurgitation and even distortion of the installed artificial valve, resulting in reduction of effectiveness and durability of the implant. A device showing foldable Nitinol blades is presented by Hauck and colleagues, [129], with the aim of resecting the degenerated aortic valve, in order to leave a proper circular geometry ideal for installation of the artificial valve. The objective is not only the creation of better conditions for the artificial valve to operate, but also a reduction of the surgery intervention time and complications.

### **Snare**

Conceptually simple SMA devices, called snares, have already been cited in the previous



chapter: indeed, they are used in various surgical fields, among which the cardiovascular one, to remove foreign bodies in a minimally invasive fashion. Nitinol snares, thanks to flexibility and radiopacity of the material, have been demonstrated to offer good torque control and grasping capacity, being able to remove various foreign bodies of different size. Such a device allows to eliminate in a quick and safe manner undesired obstructions from vascular conduits, [62].

### 2.2.2 Examples of computer-based design

Finite element analysis (FEA) was developed over 70 years ago to solve complex elasticity and structural analysis problems in civil and aeronautical engineering, [366]. Thanks to the significant advances of computational facilities, the use of FEA in biomechanics is nowadays diffused and the application of various modeling and simulation tools in medicine and clinical translational research has been proposed by a diverse group of investigators, posing the problem of the homogenization of methods and result reporting, [98]. In this scenario, the FEA-based simulation of SMA-based cardiovascular implants to assess the structural performance of various types of devices is steadily increasing. In particular, the simulations, in addition to traditional in-vitro techniques, are used to improve the design and testing of medical devices, such as cardiovascular stents. In fact, to date, these devices are mostly developed using a trial and error approach: a first prototype is manufactured and physical tests are performed to check whether the design criteria are fulfilled. If this is not the case, the design is adapted and a new prototype is manufactured and tested. Unfortunately, this approach is time-consuming, expensive and often not able to fully address the product's performance and (bio)mechanical requirements. Moreover, performing physical tests on these generally small devices is challenging. A promising strategy to design medical devices is virtual product development, which enables the development and optimization of novel designs and, consequently, reduces the costs and the time to market, [78]. Starting from such considerations, the goal of the present chapter is to provide a comprehensive overview of the use of structural FEA to analyze and optimize SMA-based cardiovascular devices. We have organized the chapter categorizing the literature review with respect to the vascular region treated by the analyzed devices. Nevertheless, a preliminary section is instead dedicated to the collection of studies addressing the mechanical response of a given SMA-base device in a general environment. In conclusion, we discuss

the research perspective suggested by the review.

### **General purpose studies**

Most of the studies, addressing the use of FEA to predict or optimize SMA-based cardiovascular devices, are focused on self-expanding stents. It is easy to understand that the steady increase of the minimally-invasive approaches has led to an important commercial interest in this sector, calling for engineering tools supporting the design of new and competing devices. One of the pioneering works about Nitinol stent simulation is the study of Witcher, [351], who, in 1997, proposed the use of FEA to estimate the structural behavior of Boston Scientific's Symphony stent, under in-vivo loading conditions. The study presents a lot of simplificative assumptions, e.g., a von Mises-yield criterion elasto-plastic model is adopted for the constitutive modeling of Nitinol, while the in-vivo loading conditions are replicated through the application of a pressure load on a stent portion, neglecting thus the inclusion of the arterial model. Few years later, in 2000, Rebelo and Perry, [279], discussed the use of FEA to simulate the expansion of Nitinol stent implementing, for the pseudo-elasticity, the constitutive model originally proposed by Auricchio and Taylor, [8, 9], and based on the concept of generalized plasticity, [188]. In 2002, the study has been extended to evaluate the fatigue resistance of the stent by Perry and colleagues, [257]. A further insight on the fatigue of self-expanding stent components was provided in 2003 by Pelton and colleagues, [253], who quantified the cyclic deformation behavior of superelastic Nitinol in order to calculate design safety factors for medical devices. In particular, the study combines experiments and numerical analysis: the authors performed displacement-controlled fatigue testing on laser-cut stent-like devices, while the fatigue strains were calculated from displacements with non-linear FEA methods. Surprisingly, the results demonstrate that the oscillating strain amplitude is the main contributor to fatigue behavior. A more fundamental work regarding the constitutive modeling of SMA was done in 2004 by Jung et al., [145], and by Auricchio and Petrini, [11], who developed constitutive models suitable for numerical analysis, such as FEA, with a particular attention to the robustness of the algorithms in order to facilitate the analysis of real industrial application like the design of medical stents, [258]. A significant attempt to tailor the design of a novel self-expandable stent by the use of FEA has been proposed in 2006 by Theriault and colleagues, [326], who discussed the development of a Nitinol stent with a progressive expansion device made of polyethylene, allowing smooth and gradual contact between the stent and the artery's wall

by creep effect. The Nitinol is modeled with a superelastic law and the study presents two simulations: 1) the first simulation determines the final geometry of the stent laser cut from a small tube; 2) the second simulation examines the behavior of the prosthesis during surgery and over the 4 weeks following the operation. In 2008, Kim et al., [155], discussed the mechanical modeling of self-expandable stents fabricated using braiding technology. For this purpose, they proposed a finite element model by coupling a preprocessing program for the three-dimensional geometrical modeling of the braiding structure of the stent. The Nitinol wires of the stent were assumed to be superelastic and their mechanical behavior was incorporated into the finite element software through a user material subroutine employing a one-dimensional super elastic model. In 2010, given the growing interest toward an exhaustive modeling of SMA macroscopic behavior due to their extensive use in a number of applications in many fields of engineering, and in particular in biomedical engineering, Auricchio et al., [12], reviewed the properties of a robust three-dimensional model able to reproduce both pseudo-elastic and shape-memory effect. In particular, the model parameters are calibrated with respect to experimental data and, finally, the model is used to perform the finite element analysis of pseudo-elastic Nitinol stent deployment in a simplified atherosclerotic artery model (Figure 2.26). In 2011, Rebelo and colleagues, [282], proposed a comparative study which grounds its motivation on the statement that FEA of Nitinol medical devices has become prevalent in the industry. Starting from this idea, the authors presented a study in which some commonly made assumptions in FEA of Nitinol devices were verified. The base model pertains to the simulation of the fabrication of a diamond shape stent specimen, followed by cyclic loading, [367], which is being used by a consortium of several stent manufacturers focused on the assessment of fatigue-life prediction for Nitinol devices. In 2012, Azaouzi et al., [36], proposed a simplified model of a Nitinol stent, in order to perform a FEA of the stent deployment as well as the pulsatile loading inside the artery. The aim is to provide a tool to forecast the fatigue life of Nitinol stents and to optimize the design phase. Similarly, in the same year, Garcia and colleagues, [109], studied the influence of the main geometrical parameters on the radial force of a self-expanding stent. Using FEA, they performed a parametric analysis of a commercial stent model (Acculink, Abbot Vascular), developed to estimate the influence of geometrical variables on the stent radial expansion force. The study proposed as result of the optimization a new stent design with variable radial stiffness, which was virtually implanted on both healthy and atheromatous vessels to evaluate its effectiveness. Other

three recent studies target the stent design optimization using FEA. Khalil-Abad and colleagues, [197], proposed a planar lattice free of stress concentrators for the synthesis of a stent with smooth cell shapes. The authors discussed a design optimization to minimize the curvature and reduce the bending strain of the elements defining the lattice cells, resulting in a novel cell geometry with improved fatigue life and radial supportive force suitable for Nitinol self-expandable stent-grafts. One year later, in 2013, Hsiao and Yin, [135], proposed the key-idea to shift the highly concentrated stresses/strains away from the stent crown and re-distribute them along the stress-free bar arm by tapering its strut width. The authors used FEA to evaluate the mechanical integrity and pulsatile fatigue resistance of the stent to various loading conditions proving an increase of the fatigue safety factor when compared to the standard stent with constant strut width. In the same year, Azaouzi, [37], and colleagues targeted the objective to optimize the stent design by reducing the strain amplitude and mean strain over the stent, which are generated by the cyclic pulsating load, proposing an optimization based simulation methodology, in order to improve the fatigue endurance of the stent. The design optimization approach is based on the Response Surface Method, which is used in conjunction with Kriging interpolation and Sequential Quadratic Programming algorithm. A more simplified analysis has been proposed by Nematzadeh and Sadrnezhaad, [229], who used FEA to investigate the effect of crimping and Af of Nitinol on mechanical performance of Z-shaped open-cell. Their study shows that low Af Nitinol has better mechanical and clinical performance due to small chronic outward force, large radial resistive force, and appropriate superelastic behavior.

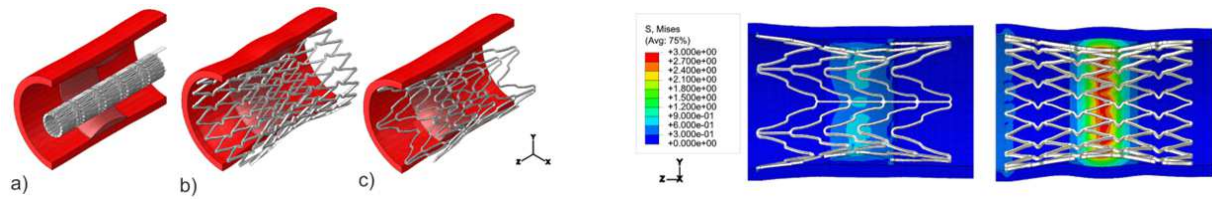


Figure 2.26: Simulation of self-expanding Nitinol stent expansion. Two difference stent designs are virtually deployed by means of FEA in the same idealized stenotic artery (on the right), inducing different vessel wall solicitation (on the left), represented by contour-plot of computed von Mises stress for the arterial model. For more details please refer to [12].

### 2.2.3 Carotid artery

The use of self-expanding Nitinol stents for the minimally-invasive treatment of carotid stenosis represents an important share of the market of SMA-based medical devices. In fact, the world market for carotid stent systems, which was valued at \$150 mln in 2010, is expected to double by 2015. Abbott Vascular, Cordis, Boston Scientific, Medtronic and Covidien have transformed the competitive landscape of the market by bundling their carotid stents with their embolic protection devices as complete Carotid Stent Systems, [60]. Despite such a significant industrial interest in this specific sector, few studies are addressing the use of FEA to design or optimize the carotid stent design. In fact, the first study in this direction was done in 2007 by Wu et al., [354], who evaluated biomechanical properties of Nitinol carotid stents and their interactions with carotid arteries through FEA. Wu and colleagues adopted a geometrical idealization of the carotid bifurcation simulating the implant of a segmented-design Nitinol stent, accounting also for the delivery sheath. Few years later, in 2011, Auricchio and colleagues, [14], further extended the study by Wu et al. to a patient-specific case. The authors used FEA to evaluate the performance of three different self-expanding stent designs in the same carotid artery model, based on computed angiography tomography images. In particular, adopting the simulation strategy presented in Reference [72], the authors defined six stent models considering the three designs in different sizes and configurations (i.e., straight and tapered), evaluating the stress induced in the vessel wall, the lumen gain and the vessel straightening. The study represents a first step towards a quantitative assessment of the relation between a given carotid stent design and a given patient-specific carotid artery anatomy. The same computational framework was subsequently experimentally validated, [73], and used to assess the impact of the carotid stent design on its capability to scaffold the artery, [16], with a particular attention to a realistic modeling of the artery (Figure 2.27), [19].

### 2.2.4 Aorta

The rapid evolution of self-expandable stent-grafts in the last decade motivates the use of FEA also in this emerging sector. One of the first investigations in this area was presented in 2008 by Kleinstreuer et al., [159], who discussed a finite element analysis of tubular, diamond-shaped stent grafts under representative cyclic loading conditions for abdominal aortic aneurysm (AAA) repair. In particular, the authors studied the mechanical behavior

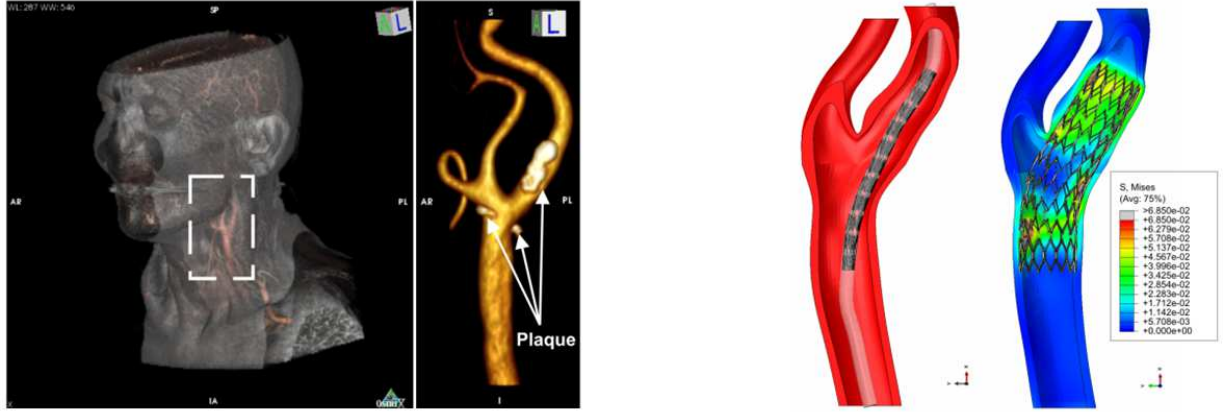


Figure 2.27: Elaboration of Computed Tomography Angiography images resulting into the 3D reconstruction of both lumen of left carotid bifurcation and plaque (on left). Results of simulation of carotid artery stenting; the stent crimped within the catheter is virtually deployed by means of FEA in a patient-specific carotid artery model. Adapted from [18].

and fatigue performance of different materials found in commercially available stent-graft systems, evaluating and comparing the effects of crimping, deployment, and cyclic pressure loading on stent-graft fatigue life, radial force, and wall compliance through the numerical simulations. More recently, De Bock and colleagues, [79], experimentally validated the use of FEA to virtually deploy a bifurcated stent graft (Medtronic Talent) in a patient-specific model of an abdominal aortic segment. The authors modeled the entire deployment procedure, with the stent graft being crimped and bent according to the vessel geometry, and subsequently released. The validation of numerical procedure was performed comparing the simulation outcomes with the in-vitro data regarding the placement of the device in a silicone mock aneurysm, imaged by high resolution CT (computed tomography). In the same year, Demanget et al., [82], simulated numerically the bending of two manufactured stent-grafts (Aorfix by Lombard Medical and Zenith by Cook Medical Europe) using finite element analysis (FEA). The authors studied the global behavior of the stent-grafts by assessing stent spacing variation and cross-section deformation. The study is motivated by the potential relationship between the clinical complications and the insufficient stent-graft flexibility, especially when devices are deployed in tortuous arteries. The same authors validated the numerical procedure in a subsequent study, [83], where the two commercially available stent-grafts were subjected to severe bending tests and their 3D geometries in undeformed and bent configurations were imaged from X-ray microtomography. The im-

ages were elaborated to set up stent-graft numerical models, subjected to the boundary conditions measured experimentally. The computational framework was further used to numerically assess the flexibility and mechanical stresses undergone by stents and fabric of currently marketed stent-graft limbs (Aorfix, Anaconda, Endurant, Excluder, Talent, Zenith Flex, Zenith LP, and Zenith Spiral-Z), [84]. In 2013, Auricchio and colleagues, [19], described the use of a custom-made stent-graft to perform a fully endovascular repair of an asymptomatic ascending aortic pseudoaneurysm in a patient, who was a poor candidate for open surgery (Figure 2.28). The authors also discussed the possible contribution of a dedicated medical images analysis and patient-specific simulation as support to procedural planning. In particular, the authors have compared the simulation prediction based on pre-operative images with post-operative outcomes. The agreement between the computer-based analysis and reality demonstrated by this study further encourages the use of FEA-based simulations not only as a tool for device designers but also as a procedural planning tool for the physicians.

### 2.2.5 Intracranial artery

As in the case of other vascular districts, the endovascular treatment of cerebral aneurysms using stents has advanced markedly in the last decade. Intracranial stents must be very flexible longitudinally and have low radial stiffness: although there are a number of designs of intracranial stents, there are really few studies examining the stress distribution and deformation of cerebrovascular stents using FEA and/or experiments. One of the pioneering works in this field is the study by Shobayashi et al., [305], who investigated the relationship between stent mesh patterns and the mechanical properties of different variants of design units of the stent, the so-called cells, evaluating several mesh patterns through FEA. It is worth noting that the superelastic behavior of Nitinol was approximated by a homogeneous, isotropic and elastic-plastic material using the Von Mises plasticity model. Moreover, the adopted loading conditions were idealized, neglecting the actual conformation of the cerebral vascular anatomy. More recently, De Bock and colleagues, [80], overcame such a limitation using finite element analysis to perform nine virtual stenting procedures, i.e., the virtual deployment of three different Nitinol stent designs in three patient-specific cerebral aneurysmatic vessels. The authors evaluated the performance of the devices assessing the percentage of strut area covering the aneurysm neck, the straightening induced on the

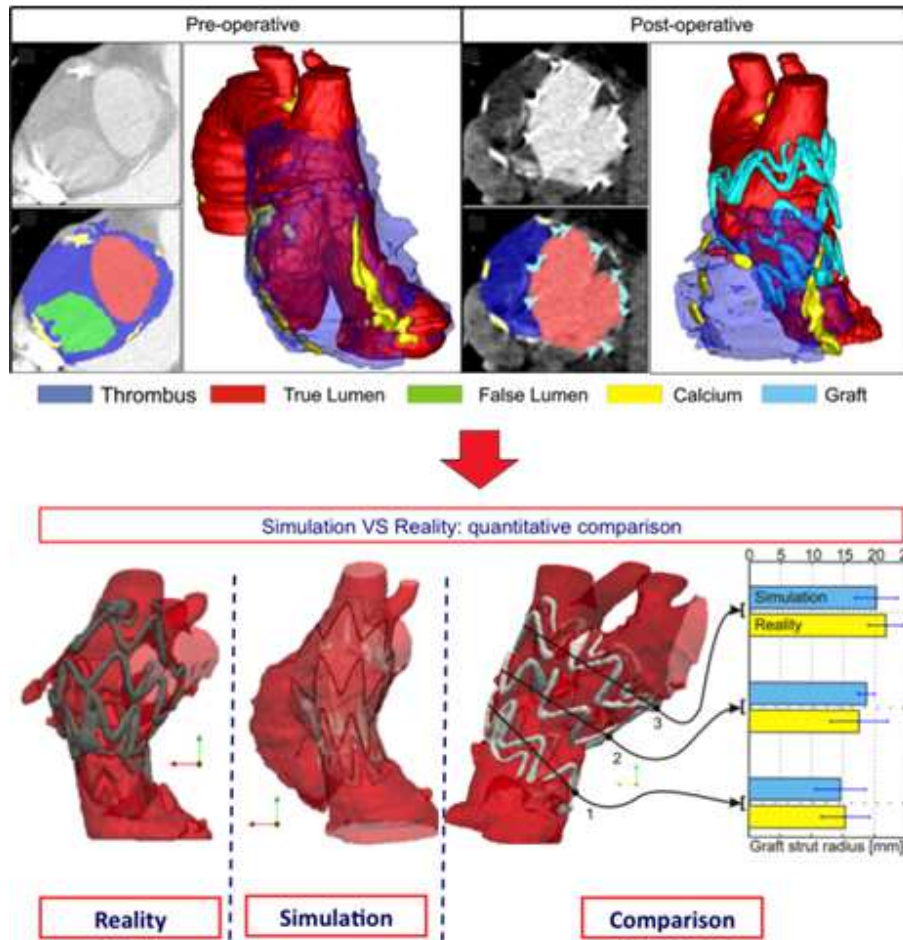


Figure 2.28: Segmentation of pre- and post-operative images regarding the implant of self-expanding endograft in the ascending aorta. The pre-operative images are used as input for the simulation of the implant, which resemble the reality for both the qualitative and quantitative point of view. For more details please refer to [19].



cerebrovasculature by the stent placement (i.e. the reduction of vessel tortuosity), and stent apposition to the wall, quantified as the percentage of struts within 0.2 mm of the vessel.

### **2.2.6 Superficial femoral artery (SFA) and renal artery**

The SFA runs from the hip to the knee, through muscle and joints, being the main blood supplier for the leg, so it undergoes severe changes in geometry associated with leg movement, [348]. As other vascular districts, also SFA and its branches, such as the popliteal artery, located below the knee, can suffer atherosclerosis or develop aneurysm. Thanks to the successful use of self-expanding Nitinol stents in other anatomical conduits, also SFA has been targeted as a candidate for revascularization through stenting. In fact, several clinical reports and trials evaluated the effect of stents in the superficial femoral artery (SFA), proving that for long lesions the use of stents is beneficial compared to balloon angioplasty alone. This result has opened the door to a widespread employ of stents in the SFA but, unfortunately, there are still concerns about the long-term results of the implants because of their non-negligible fracture rate (1.8% to 18%, see [226] and references therein). In order to identify the potential fracture risks of currently available or new SFA stent designs, a number of theoretical, numerical and experimental studies have been performed (Figure 2.29). In the following, we just mention the most recent literature with a particular focus on the use of structural FEA as an investigation method. In 2009 Rebelo and colleagues, [281], performed simulations of peripheral stenting, obtaining realistic artery geometry from magnetic resonance imaging scans of a patient in the fetal and supine positions, and comparing deformation of the stent deployed into the two different artery configurations. Despite the study accounts for the main issues of stenting modeling, the authors consider a small portion of the superficial femoral artery far from the popliteal artery and consequently the configuration change of the artery appears to be fairly limited. In 2011 Harvey, [128], evaluated through FEA the fatigue performance of two stent geometries. Two vessel models were used: i) a constant diameter straight tube; ii) a segment of the superficial femoral artery obtained from CTA (computed tomography angiography) dataset. The author imposed two types of loading to the stent model through the vessel model. Although the study proves the utility of combining advanced nonlinear finite element simulations and fatigue predictions for the design of peripheral

Nitinol stents, the imposed loading conditions are rather idealized. In 2012, Petrini and colleagues, [260], presented an integrated numerical and experimental approach to foresee Nitinol stent fatigue fracture, reproducing also a wide range of in-vivo conditions. This study was further integrated by Meoli and colleagues, [207], who used FEA coupled to fatigue analysis to investigate two in vitro set-ups proposed in the literature, [233, 226] and to increase the understanding of fatigue behavior of commercial Nitinol stents. Their results indicate that the two investigated testing conditions produce quite a different fatigue behavior both in terms of constant-life diagram and strain distribution in the stents but, also in these studies, the imposed loading conditions are rather idealized, leaving space for further developments embedding patient-specific loading conditions derived by medical image.

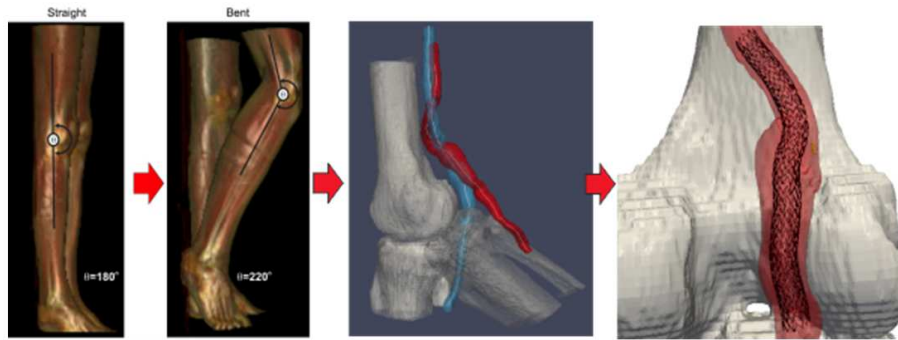


Figure 2.29: Elaboration of Computed Tomography Angiography of the lower limbs; in particular two scans are performed: one with the right leg in straight and the other in bent position. Such an imaging and the related corresponding image elaboration and analysis allows at reconstructing the configuration change of the limb arteries, such as the popliteal artery. This data can be used to simulate the stent implant and calculate the device solicitation due to knee bending. For more details please refer to [74].

### 2.2.7 Heart valves

As discussed in the section 3, the recent developments in percutaneous implantation, to replace heart-valves in a minimally-invasive fashion through stent-mounted prosthetic valves, have opened another wide field of application for the unique features of Nitinol. Clearly, also in this specific sector, structural FEA has been used to assess and optimize new SMA-based devices, as briefly discussed in the following. In 2004, DeHerrera and colleagues, [81], numerically investigated the mechanical adequacy of a new valve design, presenting

a flat-sheet based stent, which would be rolled up to about a 20 French (6.66mm outside diameter, or OD) size and delivered percutaneously. The same research group proposed a similar approach to analyze a new percutaneously-delivered device, at that time under development at Edwards Lifesciences, which induces mitral valve reshaping. The device is intended to be placed in the coronary sinus and is basically a spring with anchoring stents at each end. In particular, the FEA study examined the mechanical behavior of one of the anchoring stents, from its forming from a small diameter tube to its deployment into the coronary sinus. Some years later, in 2013, Tzamtzis et al., [335], presented a numerical study on the different mechanisms responsible for the radial force exerted on the aortic annulus by self-expanding and balloon-expandable prostheses; in particular, the authors simulated and compared the mechanical behavior of the Medtronic CoreValve (self-expanding) and the Edwards SAPIEN (balloon expandable) devices. The results indicate that in the case of the self-expanding valve the radial force is essentially dependent on the diameter of the left ventricular outflow tract, which is the heart region where the valve is anchored. In the same year, Kumar et al., [270], published a study using computational modeling and simulation to design a new Nitinol-based mitral valve stent and to evaluate its crimpability and fatigue behavior. A self-expandable stent with new features, addressing issues of valve migration and paravalvular leaks, was proposed, and its expansion, crimpability, deployment patterns, and fatigue behavior was simulated and analyzed. Moreover, the proposed simulations embed also cyclic cardiac muscle loading, cyclic blood pressure loading, as well as cyclic valve leaflet forces in the fatigue life assessment for mitral valves.

## 2.3 Conclusions

As it can be deduced from the wide overview which has been provided about the numerous applications of SMAs in the biomedical field, SMA technology has been deeply explored during the last decades. Nevertheless, success of SMA in medicine is not ending: the ever-increasing exploitation of SMAs in medical devices is indeed proved by the strong ascending trend of publications and patents produced on the subject during the last decades, as it is easy to verify through statistic data concerning publication and patent evolution.



# Chapter 3

## Constitutive modeling of SMAs

### 3.1 Introduction

Several efforts have been made since the 1980ies to propose reliable constitutive models for SMA, which can be generally categorized as microscopic, macroscopic, or micro-macro. Microscopic models consider a detailed description of the fundamental phenomena occurring at the crystallographic level, such as phase nucleation and interface motion. Micro-macro models (e.g., [50, 248]) are based on the micro-modeling of a single grain and averaging the results on a representative volume element (RVE) to describe the behavior of a polycrystalline material. Both micro and micro-macro models do not find widespread use in industrial application development due to a significant computational cost and a high number of input parameters. On the other hand, macroscopic models (e.g., [181, 247, 25, 299, 319, 5, 174, 22, 56, 93, 250, 362]) are based on the principles of continuum thermodynamics and provide the phenomenological description of the material; their numerical implementation is usually simple and entails a lower computational effort.

Given a simple and reliable mathematical SMA constitutive model, the development of efficient and robust integration schemes plays a crucial role in embedding such models within a FEA framework.

In the present Chapter, a three-dimensional phenomenological model for polycrystalline SMAs, called the Souza-Auricchio model, will be described. Such model has been widely used in numerical studies, e.g. in engineering and medical fields [31, 32], and implemented in commercially available FEA software [1].

## 3.2 Souza-Auricchio model

At first, a three-dimensional small strain phenomenological model for polycrystalline shape-memory alloys has been introduced by Souza in [312], based on the framework of Generalized Standard Materials. The model has been then combined with finite elements in [24, 25, 26], originating the Souza-Auricchio model, and analyzed in [23]. The case of a given, non-constant temperature has been discussed in [217, 214] whereas the full thermo-mechanical coupling is investigated in [167, 166] in one space dimension. The reader is referred to the recent survey [121] for details on the extension of the model to finite strains [100, 102, 106], residual plasticization [27, 28, 96, 120], asymmetric behaviors [29], magnetic effects [21, 20, 47, 48, 290], as well as for space discretization [215, 216] and control [95, 97, 314].

The present section briefly reviews the time-continuous framework for the three-dimensional Souza-Auricchio model. The reader is referred to [312, 25] for further details about the model formulation. In the following, we use the notation  $|\cdot|$  to denote the Euclidean norm and  $\langle \cdot \rangle$  to indicate the positive part function; notations  $(\cdot : \cdot)$  and  $(\cdot \otimes \cdot)$  denote the scalar and tensor product, respectively [119].

Let  $\mathbf{u} : \Omega \rightarrow \mathbb{R}^3$  be the displacement from the reference configuration  $\Omega \subset \mathbb{R}^3$  of the body. In the small-deformation regime, the linearized strain can be expressed as

$$\boldsymbol{\varepsilon} = \boldsymbol{\varepsilon}(\mathbf{u}) = \frac{\nabla \mathbf{u} + \nabla \mathbf{u}^\top}{2}.$$

Let us introduce the following decomposition of the linearized strain:

$$\boldsymbol{\varepsilon} = \boldsymbol{\varepsilon}^{\text{el}} + \mathbf{e}^{\text{tr}}.$$

Here,  $\boldsymbol{\varepsilon}^{\text{el}} = \mathbb{C}^{-1} \boldsymbol{\sigma} \in \mathbb{R}_{\text{sym}}^{3 \times 3}$  corresponds to the elastic part of the strain,  $\mathbb{C}$  is the isotropic elasticity tensor, and  $\boldsymbol{\sigma}$  is the stress. The tensor  $\mathbf{e}^{\text{tr}} \in \mathbb{R}_{\text{dev}}^{3 \times 3}$  is the inelastic strain originating from the martensitic transformation and reorientation. In particular,  $\mathbf{e}^{\text{tr}}$  is assumed to be trace-free, as experiments suggest that martensitic transformations are approximately isochoric [347]. The quantity  $|\mathbf{e}^{\text{tr}}|$  serves as a measure of the martensitic content of the specimen and fulfills  $|\mathbf{e}^{\text{tr}}| \leq \epsilon_L$  where  $\epsilon_L$  is the maximal strain which is obtainable by martensitic reorientation. On the other hand,  $\mathbf{e}^{\text{tr}}/|\mathbf{e}^{\text{tr}}|$  is an indicator of the local orienta-

tion of martensites.

The assumed control variables are therefore the total strain  $\boldsymbol{\varepsilon}$  and the absolute temperature  $\theta$ , while the transformation strain  $\mathbf{e}^{\text{tr}}$  is taken as internal variable. Following experimental evidences,  $\mathbf{e}^{\text{tr}}$  is assumed to be traceless, since the austenite-martensite phase change is a diffusionless nearly isochoric solid-solid transformation [347]. The transformation strain satisfies the constraint:

$$|\mathbf{e}^{\text{tr}}| \leq \epsilon_L, \quad (3.1)$$

where  $\epsilon_L$  is a material parameter corresponding to the maximum transformation strain reached at the end of the phase transformation during an uniaxial test.

The equilibrium of the medium is described by the *free-energy* density

$$\psi(\boldsymbol{\varepsilon}, \mathbf{e}^{\text{tr}}, \theta) := c\theta(1 - \log \theta) + \frac{1}{2}(\boldsymbol{\varepsilon} - \mathbf{e}^{\text{tr}}) : \mathbb{C}(\boldsymbol{\varepsilon} - \mathbf{e}^{\text{tr}}) + \frac{H}{2}|\mathbf{e}^{\text{tr}}|^2 + f(\theta)|\mathbf{e}^{\text{tr}}| + I(\mathbf{e}^{\text{tr}}).$$

The parameter  $c > 0$  stands for specific heat capacity. The second and third terms in  $\psi$  correspond to the free-energy of linearized elastoplasticity with linear kinematic hardening. In particular,  $H$  is a hardening parameter. A simplifying assumption is made that austenite and martensite present the same elastic response. The last two terms in  $\psi$  are instead specific of the SMA model. The value  $f(\theta)$  corresponds to the martensite-to-austenite equilibrium stress at temperature  $\theta$ . Thermal expansion is here neglected as it appears often to be small in applications. Finally,  $I$  is the indicator function enforcing the constraint  $|\mathbf{e}^{\text{tr}}| \leq \epsilon_L$  and reads

$$I_{\epsilon_L}(\mathbf{e}^{\text{tr}}) = \begin{cases} 0 & \text{if } |\mathbf{e}^{\text{tr}}| \leq \epsilon_L \\ +\infty & \text{otherwise} \end{cases}, \quad (3.2)$$

As the transformation strain  $\mathbf{e}^{\text{tr}}$  is deviatoric, it is convenient to express the free energy in terms of the decomposition  $\boldsymbol{\varepsilon} = (v/3)\mathbf{1}_2 + \mathbf{e}$  where  $v = \text{tr } \boldsymbol{\varepsilon}$  is the volumetric strain and  $\mathbf{e} = \text{dev } \boldsymbol{\varepsilon}$  is the deviatoric strain, respectively. In particular, we have

$$\begin{aligned} \psi &= \psi(v, \mathbf{e}, \mathbf{e}^{\text{tr}}, \theta) = c\theta(1 - \log \theta) + \frac{K}{2}v^2 + G|\mathbf{e} - \mathbf{e}^{\text{tr}}|^2 \\ &\quad + \frac{H}{2}|\mathbf{e}^{\text{tr}}|^2 + f(\theta)|\mathbf{e}^{\text{tr}}| + I(\mathbf{e}^{\text{tr}}) \end{aligned}$$

where  $K, G > 0$  are here the bulk and the shear modulus, respectively.

Following standard arguments [119], the constitutive equations are derived.

We classically obtain the constitutive relations from the variations of the free energy with respect to its variables. In particular, we have that the pressure  $p$ , the deviatoric stress  $\mathbf{s}$  (so that, in particular, we can compute the Cauchy stress as:  $\boldsymbol{\sigma} = p\mathbf{1}_2 + \mathbf{s}$ ), the entropy density  $s$ , and the thermodynamic variable  $\mathbf{X}$  associated to the internal variable  $\mathbf{e}^{\text{tr}}$  read

$$p = \partial_\theta \psi = Kv, \quad (3.3)$$

$$\mathbf{s} = \partial_{\mathbf{e}} \psi = 2G(\mathbf{e} - \mathbf{e}^{\text{tr}}), \quad (3.4)$$

$$s = -\partial_\theta \psi = -f'(\theta)|\mathbf{e}^{\text{tr}}| + c \log \theta - c, \quad (3.5)$$

$$\mathbf{X} = -\partial_{\mathbf{e}^{\text{tr}}} \psi = \mathbf{s} - H\mathbf{e}^{\text{tr}} - f(\theta)\partial|\mathbf{e}^{\text{tr}}| - \partial I(\mathbf{e}^{\text{tr}}). \quad (3.6)$$

The symbol  $\partial$  indicate the classical partial differentiation. In particular:

$$\partial I(\mathbf{e}^{\text{tr}}) = \begin{cases} \mathbf{0} & \text{if } |\mathbf{e}^{\text{tr}}| < \epsilon_L, \\ \ell \frac{\mathbf{e}^{\text{tr}}}{|\mathbf{e}^{\text{tr}}|}, \quad \ell \geq 0 & \text{if } |\mathbf{e}^{\text{tr}}| = \epsilon_L, \\ \emptyset & \text{if } |\mathbf{e}^{\text{tr}}| > \epsilon_L \end{cases}$$

The internal energy density  $u$  can be classically computed as

$$\begin{aligned} u &= u(\boldsymbol{\varepsilon}, \mathbf{e}^{\text{tr}}, \theta) = \psi + \theta s \\ &= c\theta + \frac{K}{2}v^2 + G|\mathbf{e} - \mathbf{e}^{\text{tr}}|^2 + (f(\theta) - \theta f'(\theta))|\mathbf{e}^{\text{tr}}| + \frac{H}{2}|\mathbf{e}^{\text{tr}}|^2 + I(\mathbf{e}^{\text{tr}}). \end{aligned} \quad (3.7)$$

To describe phase transformation and inelasticity evolution, a classical Mises-type limit function  $F = F(\mathbf{X})$  is introduced in the following form:

$$F = |\mathbf{X}| - R_Y, \quad (3.8)$$

where  $R_Y$  is a positive material parameter corresponding to the radius of the elastic domain in the deviatoric stress space.

The evolution equation for the internal variable takes the form:

$$\dot{\mathbf{e}}^{\text{tr}} = \xi \frac{\partial F}{\partial \mathbf{X}} = \xi \frac{\mathbf{X}}{|\mathbf{X}|}, \quad (3.9)$$



where  $\xi$  is the non-negative consistency parameter. The model is then completed by the classical Kuhn-Tucker conditions:

$$\xi \geq 0, \quad F \leq 0, \quad \xi F = 0 . \quad (3.10)$$



## Chapter 4

# Explicit formulation of Souza-Auricchio model

The study presented in this chapter is included in a paper which is in preparation [295].

### 4.1 Introduction

In the last three decades the utilization of SMAs has rapidly evolved from academic and niche applications to the mass production of a wide variety of industrial components. The great commercial success of SMA is due to two unique mechanical properties: pseudoelasticity and shape-memory effect. These features have enabled a wide range of commercial applications [142], such as biomedical components (e.g., self-expandable stents [55], flexible surgical instruments [76], prostheses [139, 39]), civil engineering devices (e.g., energy dissipation systems [6]), as well as mechanical systems (e.g., actuators [210], fasteners [318]).

The continuing demand for SMA materials in engineering and technical applications motivates a constant investigation of constitutive models able to accurately reproduce material response under diverse conditions. Additionally, the importance of incorporating modern computer design and analysis tools, such as computer-aided design (CAD) and finite element analysis (FEA), into the production and development of innovative SMA applications further motivates the formulation of improved constitutive and numerical frameworks in terms of both efficiency and accuracy [142].

Several efforts have been made during the past years to propose reliable constitutive models for SMA, which can be generally categorized as microscopic, macroscopic, or micro-

macro (see, e.g., [151] for a review). On one hand, both microscopic and micro-macro models, which consider a detailed description of the fundamental phenomena occurring at the crystallographic level, accurately reproduce the unique SMA mechanical behavior. However, such models do not find widespread use in industrial application development due to a significant computational cost, high number of input parameters, scale transition challenges. On the other hand, macroscopic models [247, 25, 299, 319, 5, 174, 22], many based on the principles of continuum thermodynamics, are widely employed because of their simple numerical implementation and reduced cost of calculation. Given a simple and reliable mathematical SMA constitutive model, the development of efficient and robust integration schemes plays a crucial role in embedding such models within a FEA framework.

Most of the phenomenological models available in the literature are implemented in an implicit time integration framework (see, e.g., [93, 319, 250, 22, 5, 362]), with only few recent contributions utilizing an explicit alternative [245, 325, 141, 313, 294]<sup>1</sup>. Particularly, Pan et al. [245] presented a finite-deformation model and its explicit algorithm for the simulation of the one-way shape-memory effect, also validated on experimental data related to rods and to a stent strut. Thamburaja and Nikabdullah [325] proposed a three-dimensional thermo-mechanical SMA model and coded a corresponding explicit algorithm; the model was validated through a comparison between experimental data and simulations on cuboidal and sheet specimens. Jähne [141] developed an explicit integration algorithm for the model proposed by Souza [312] and then investigated by Auricchio and Petrini [25], to simulate the pseudoelastic behavior of sheets for solid-state hinges, observed in experimental tests. Recently, Stebner and Brinson [313] proposed the explicit implementations of an improved SMA model [247]; the presented algorithms were compared in uniaxial and biaxial tests on a three-dimensional brick element, and in tension tests on a two-dimensional bar with a hole. Scalet et al. [294] developed and implemented an explicit algorithm for the model by Lagoudas et al. [174]. The performance of the implicit and explicit methods in terms of analysis time and parallelization efficiency were also investigated.

The employment of explicit methods becomes truly enabling in cases where complexity makes implicit algorithms impractical, such as in high-speed dynamic analyses, highly

---

<sup>1</sup>For the sake of clarity, the expression *implicit integration scheme* refers to a numerical time integration algorithm where unknowns at the current time instant are calculated through an iterative solution procedure, while *explicit integration scheme* refers to a numerical time integration algorithm where unknowns at the current time instant can be derived using closed-form formulas, only containing previous time instant values and given quantities .

non-linear quasi-static and dynamic problems (e.g., those involving widespread buckling or contact), and fully coupled thermo-mechanical dynamic analyses, which characterize several SMA applications (e.g., energy dissipating devices or vibration dampers undergoing wave propagation phenomena due to impact [175], biomedical devices interacting with bodily fluids [279, 14, 18], or self-assembling technologies [256]). In fact, even if unconditionally stable, an implicit implementation can encounter difficulties when a complicated three-dimensional problem is considered. Indeed, if several non-linearities are present in the material formulation and/or in large geometric change and/or from contact considerations, local and global instabilities can prevent from convergence of an implicit algorithm outright. Even if convergence is possible, the analysis may require many iterations and progressively smaller time steps, and the computational cost for the repeated calculation of the global tangent stiffness matrix impractically increases. Explicit techniques are thus introduced to overcome the disadvantages of the implicit method, since iterations are not involved and the global stiffness matrix does not need to be computed [1]. The drawback of explicit procedures are the need to heed the stability conditions that govern attainable accuracy; these require decreasing time increments. Additionally, convergence to the correct solution is not guaranteed, so results must be carefully interpreted.

It is interesting to observe that in the general-purpose commercial FEA solver Abaqus [1] (Dassault Systèmes), simulations of SMA applications both using implicit (Abaqus/Standard) and explicit (Abaqus/Explicit) solvers are most often performed using the user material subroutine implementation of the model by Auricchio, Taylor, and Lubliner [8], available as a built-in material model [237, 280]. However, although this model is able to provide a robust and accurate description of the pseudoelastic behavior, it is not able to reproduce the zero-stress shape-memory effect (see [8] for details), despite its importance in several industrial applications [90, 58, 127, 124].

The present paper aims to improve the current state-of-the-art regarding explicit implementation of SMA models by proposing an explicit integration scheme for the three-dimensional phenomenological model presented in [312, 25], and defined in the following as the *Souza-Auricchio model*. In particular, the Souza-Auricchio model has been chosen because it provides a good overall description of pseudoelastic and shape-memory behaviors, requires a reduced number of material parameters, and has been successfully employed in several academic and industrial studies (see, e.g., [32, 31, 15]). An improvement over the previously cited Auricchio-Taylor-Lubliner model is that the Souza-Auricchio model

reproduces the important zero-stress shape-memory effect.

The present study provides a detailed description of the explicit integration scheme for the Souza-Auricchio model and an in-depth investigation of the corresponding algorithm. An elastic predictor-inelastic corrector scheme is here used to solve the time-discrete non-linear constitutive equations in the explicit framework. The main advantage of the presented explicit algorithm is its extremely simple solution scheme and its ability to effectively reproduce both pseudoelasticity and shape-memory effect. The constitutive and algorithmic framework is tested via the simulation of six full three-dimensional boundary-value problems involving both pseudoelasticity and shape-memory effect, demonstrating the potential of the proposed computational framework to provide a virtual engineering tool for design, simulation, and optimization of SMA devices. To this end, both the implicit [25] and explicit integration schemes are implemented within Abaqus/Standard and Abaqus/Explicit user-material subroutines [1], respectively. We first focus on simple uniaxial and biaxial quasi-static tests to emphasize specific model features; then, we extend the discussion to more complex situations by performing several quasi-static simulations accounting for realistic SMA devices and applications (i.e., a stent strut, a helical spring, a micro-gripper); finally, we present a superelastic SMA cable segment subjected to tensile and bending load, where widespread frictional contact is considered between the twisted SMA wires. The simulations differ in terms of degrees of freedom (DOFs), applied loading, and boundary conditions. The paper is organized as follows: Section 3 provides an overview of the Souza-Auricchio model equations in the time-continuous framework; Section 4.2 focuses on the model time-discrete framework by first reviewing the implicit integration scheme and subsequently by presenting the novel explicit algorithm; Section 5.6 presents the results of several numerical simulations; at last, conclusions are outlined in Section 4.4.

## 4.2 Souza-Auricchio model: time-discrete framework

We now focus on the algorithmic treatment of the continuum model equations. For the sake of notation simplicity, we omit the subscript  $n + 1$  for all the variables computed at the current time  $t_{n+1}$  and adopt subscript  $n$  for the variables computed at the previous time  $t_n$ . We assume as given the state  $(\mathbf{e}_n^{\text{tr}}, \lambda_n, \gamma_n)$  at the previous time  $t_n$  and, focusing on the traditional displacement-driven non linear FEA implementation, admit global guess

values of the total strain  $\boldsymbol{\varepsilon}$  and temperature  $T$  at time  $t_{n+1}$ . A procedure based on the elastic predictor/inelastic corrector scheme [308] is adopted to derive the stress and the other variables at the current time  $t_{n+1}$ .

The time-discrete evolution equation for the transformation strain is here expressed in the general form [274]:

$$\mathbf{e}^{\text{tr}} = \mathbf{e}_n^{\text{tr}} + \xi \left( \alpha \frac{\mathbf{X}}{|\mathbf{X}|} + (1 - \alpha) \frac{\mathbf{X}_n}{|\mathbf{X}_n|} \right), \quad (4.1)$$

where  $\xi$  is the consistency parameter and  $\alpha$  is a parameter varying between 0 and 1. Assuming  $\alpha > 0$ , an implicit scheme is obtained; assuming  $\alpha = 0$ , the explicit forward Euler scheme is recovered.

In the following, we first review the implicit backward Euler algorithm ( $\alpha = 1$ ), as proposed in [11], then present the novel explicit forward Euler algorithm ( $\alpha = 0$ ).

#### 4.2.1 Implicit backward Euler algorithm

According to the implicit backward Euler scheme ( $\alpha = 1$ ), the evolution equation (4.1) reads:

$$\mathbf{e}^{\text{tr}} = \mathbf{e}_n^{\text{tr}} + \xi \frac{\mathbf{X}}{|\mathbf{X}|}. \quad (4.2)$$

We approach the solution with an elastic-predictor inelastic-corrector procedure (see Table 4.1). First, the elastic trial state (denoted with subscript  $TR$ ) is evaluated, for which the internal variables read:

$$\begin{cases} \xi_{TR} = 0 \\ \mathbf{e}_{TR}^{\text{tr}} = \mathbf{e}_n^{\text{tr}} \\ \ell_{TR} = 0 \end{cases}, \quad (4.3)$$

giving:

$$\begin{cases} \mathbf{s}_{TR} = 2G(\mathbf{e} - \mathbf{e}_{TR}^{\text{tr}}) \\ \mathbf{X}_{TR} = \mathbf{s}_{TR} - f(\theta) \frac{\mathbf{e}_{TR}^{\text{tr}}}{|\mathbf{e}_{TR}^{\text{tr}}|} - h\mathbf{e}_{TR}^{\text{tr}} \end{cases}. \quad (4.4)$$

Then, the limit function (3.8) is computed to verify the admissibility of the trial state. If

the trial state is admissible, the loading increment is deemed elastic, the trial solution is admitted as the true solution, and the algorithm exits to the global update of the tangent matrix. Otherwise, the increment is deemed inelastic and the transformation strain must be updated through the time-discrete evolution equation (4.2). We perform the inelastic step (referred to as the *first phase transformation* or *PT1 step* in Table 4.1) by solving the following non-linear system with a Newton-Raphson scheme (see Table 4.2):

$$\begin{cases} \mathbf{e}^{tr} - \mathbf{e}_n^{tr} - \xi \frac{\mathbf{X}}{|\mathbf{X}|} = \mathbf{0} \\ |\mathbf{X}| - R_Y = 0 \end{cases} . \quad (4.5)$$

If the above solution is not admissible (i.e., constraint (3.1) is not verified), a second inelastic step (referred to as the *second phase transformation* or *PT2 step* in Table 4.1) is performed to satisfy constraint (3.1) and the following non-linear system is solved with a Newton-Raphson method (see Table 4.3):

$$\begin{cases} \mathbf{e}^{tr} - \mathbf{e}_n^{tr} - \xi \frac{\mathbf{X}}{|\mathbf{X}|} = \mathbf{0} \\ |\mathbf{X}| - R_Y = 0 \\ \overline{|\mathbf{e}^{tr}|} - \epsilon_L = 0 \end{cases} . \quad (4.6)$$

It should be noticed that, from the computational point of view, the ratio  $\mathbf{e}^{tr}/|\mathbf{e}^{tr}|$  is undefined when  $\mathbf{e}^{tr}$  is null (i.e., in a pure austenitic state). Therefore, the norm  $|\mathbf{e}^{tr}|$  is replaced with the following expression:

$$\overline{|\mathbf{e}^{tr}|} = \sqrt{|\mathbf{e}^{tr}|^2 + \delta} , \quad (4.7)$$

where  $\delta$  is a positive regularization parameter ( $\sim 10^{-8}$ ).

Table 4.1 reports the implicit algorithmic scheme implemented as user material subroutine (UMAT) in Abaqus/Standard. Note that the implicit implementation requires also the formulation of the consistent tangent matrix (see [11] for the corresponding expression).



Table 4.1: Implicit backward Euler algorithm applied to the Souza-Auricchio model [312, 11].

*Given quantities:*  $\boldsymbol{\varepsilon}, T, \mathbf{e}_n^{\text{tr}}, \ell_n$

Compute trial state:

$$\begin{aligned}\xi_{TR} &= 0; \\ \mathbf{e}_{TR}^{\text{tr}} &= \mathbf{e}_n^{\text{tr}} \\ \ell_{TR} &= 0 \\ \mathbf{s}_{TR} &= 2G(\mathbf{e} - \mathbf{e}_{TR}^{\text{tr}}) \\ \mathbf{X}_{TR} &= \mathbf{s}_{TR} - f(\theta) \frac{\mathbf{e}_{TR}^{\text{tr}}}{|\mathbf{e}_{TR}^{\text{tr}}|} - h\mathbf{e}_{TR}^{\text{tr}} \\ F_{TR} &= |\mathbf{X}_{TR}| - R_Y\end{aligned}$$

IF  $F_{TR} \leq \text{tol}$  THEN

Elastic step:

$$\xi = \xi_{TR}; \mathbf{e}^{\text{tr}} = \mathbf{e}_{TR}^{\text{tr}}; \ell = \ell_{TR}; \mathbf{s} = \mathbf{s}_{TR}; \mathbf{X} = \mathbf{X}_{TR}$$

ELSE

Inelastic PT1 step: see Table 4.2

$$\begin{aligned}\text{IF } |\mathbf{e}_{PT1}^{\text{tr}}| &\leq \epsilon_L \text{ THEN} \\ \xi &= \xi_{PT1} \\ \mathbf{e}^{\text{tr}} &= \mathbf{e}_{PT1}^{\text{tr}} \\ \ell &= \ell_{TR} \\ \mathbf{s} &= 2G(\mathbf{e} - \mathbf{e}^{\text{tr}}) \\ \mathbf{X} &= \mathbf{s} - f(\theta) \frac{\mathbf{e}^{\text{tr}}}{|\mathbf{e}^{\text{tr}}|} - h\mathbf{e}^{\text{tr}}\end{aligned}$$

ELSE

Inelastic PT2 step: see Table 4.3

$$\begin{aligned}\xi &= \xi_{PT2} \\ \mathbf{e}^{\text{tr}} &= \mathbf{e}_{PT2}^{\text{tr}} \\ \ell &= \ell_{PT2} \\ \mathbf{s} &= 2G(\mathbf{e} - \mathbf{e}^{\text{tr}}) \\ \mathbf{X} &= \mathbf{s} - (f(\theta) + \ell) \frac{\mathbf{e}^{\text{tr}}}{|\mathbf{e}^{\text{tr}}|} - h\mathbf{e}^{\text{tr}}\end{aligned}$$

END IF

END IF

Table 4.2: Implicit backward Euler algorithm PT1 step (see Table 4.1).

Initialize:

$$k = 0$$

$$\mathbf{h}^{(0)} = \{\mathbf{e}^{tr(0)}, \xi^{(0)}\} = \{\mathbf{e}_{TR}^{tr}, \xi_{TR}\}$$

REPEAT

$$\mathbf{s}^{(k)} = 2G(\mathbf{e} - \mathbf{e}^{tr(k)})$$

$$\mathbf{X}^{(k)} = \mathbf{s}^{(k)} - f(\theta) \frac{\mathbf{e}^{tr(k)}}{|\mathbf{e}^{tr(k)}|} - h\mathbf{e}^{tr(k)}$$

$$\text{Solve system } \mathbf{Q}^{(k)} = \begin{pmatrix} \mathbf{e}^{tr(k)} - \mathbf{e}_n^{tr} - \xi^{(k)} \frac{\mathbf{X}^{(k)}}{|\mathbf{X}^{(k)}|} \\ |\mathbf{X}^{(k)}| - R_Y \end{pmatrix} = \mathbf{0}$$

via Newton-Raphson procedure to find:

$$\mathbf{h}^{(k+1)} = \{\mathbf{e}^{tr(k+1)}, \xi^{(k+1)}\} = \mathbf{h}^{(k)} + \Delta \mathbf{h}^{(k)} = \mathbf{h}^{(k)} - \left[ \nabla_{\mathbf{h}} \mathbf{Q}^{(k)} \right]^{-1} \mathbf{Q}^{(k)}$$

$$k = k + 1$$

UNTIL  $|\Delta \mathbf{h}^{(k-1)}| < tol_{NR}$

*Resulting quantities:*

$$\mathbf{e}_{PT1}^{tr} = \mathbf{e}^{tr(k)}$$

$$\xi_{PT1} = \xi^{(k)}$$

Table 4.3: Implicit backward Euler algorithm PT2 step (see Table 4.1).

Initialize:

$$k = 0$$

$$\mathbf{h}^{(0)} = \{\mathbf{e}^{tr(0)}, \xi^{(0)}, \ell^{(0)}\} = \{\mathbf{e}_{TR}^{tr}, \xi_{TR}, \ell_{TR}\}$$

REPEAT

$$\mathbf{s}^{(k)} = 2G(\mathbf{e} - \mathbf{e}^{tr(k)})$$

$$\mathbf{X}^{(k)} = \mathbf{s}^{(k)} - (f(\theta) + \ell^{(k)}) \frac{\mathbf{e}^{tr(k)}}{|\mathbf{e}^{tr(k)}|} - h\mathbf{e}^{tr(k)}$$

$$\text{Solve system } \mathbf{Q}^{(k)} = \begin{pmatrix} \mathbf{e}^{tr(k)} - \mathbf{e}_n^{tr} - \xi^{(k)} \frac{\mathbf{X}^{(k)}}{|\mathbf{X}^{(k)}|} \\ \frac{|\mathbf{X}^{(k)}|}{|\mathbf{e}^{tr(k)}|} - R_Y \\ \frac{|\mathbf{X}^{(k)}|}{|\mathbf{e}^{tr(k)}|} - \epsilon_L \end{pmatrix} = \mathbf{0}$$

via Newton-Raphson procedure to find:

$$\mathbf{h}^{(k+1)} = \{\mathbf{e}^{tr(k+1)}, \xi^{(k+1)}, \ell^{(k+1)}\} = \mathbf{h}^{(k)} + \Delta \mathbf{h}^{(k)} = \mathbf{h}^{(k)} - \left[ \nabla_{\mathbf{h}} \mathbf{Q}^{(k)} \right]^{-1} \mathbf{Q}^{(k)}$$

$$k = k + 1$$

UNTIL  $|\Delta \mathbf{h}^{(k-1)}| < tol_{NR}$

*Resulting quantities:*

$$\mathbf{e}_{PT2}^{tr} = \mathbf{e}^{tr(k)}$$

$$\xi_{PT2} = \xi^{(k)}$$

$$\ell_{PT2} = \ell^{(k)}$$

### 4.2.2 Explicit forward Euler algorithm

According to the explicit forward Euler scheme ( $\alpha = 0$ ), the evolution equation (4.1) reads:

$$\mathbf{e}^{\text{tr}} = \mathbf{e}_n^{\text{tr}} + \xi \frac{\mathbf{X}_n}{|\mathbf{X}_n|}. \quad (4.8)$$

Again, we approach the solution with an elastic-predictor inelastic-corrector procedure (see Table 4.4). The algorithm begins with the evaluation of an elastic trial state for which the internal variables read:

$$\begin{cases} \xi_{TR} = 0 \\ \mathbf{e}_{TR}^{\text{tr}} = \mathbf{e}_n^{\text{tr}} \\ \ell_{TR} = 0 \end{cases}, \quad (4.9)$$

from which we calculate:

$$\begin{cases} \mathbf{s}_{TR} = 2G(\mathbf{e} - \mathbf{e}_{TR}^{\text{tr}}) \\ \mathbf{X}_{TR} = \mathbf{s}_{TR} - f(\theta) \frac{\mathbf{e}_{TR}^{\text{tr}}}{|\mathbf{e}_{TR}^{\text{tr}}|} - h\mathbf{e}_{TR}^{\text{tr}} \end{cases}. \quad (4.10)$$

Then, the limit function (3.8) is computed to verify the admissibility of the trial state. If the trial state is admissible, the step is elastic; otherwise, the step is inelastic and the transformation strain must be updated through the time-discrete evolution equation (4.8). We perform the inelastic step (referred to as the *first phase transformation* or *PT1 step* in Table 4.4) to evaluate the consistency parameter  $\xi$ . We derive the needed relation for  $\xi$  by enforcing the consistency condition  $F(\xi) = 0$ . The consistency parameter  $\xi = \xi_{PT1}$  is explicitly derived by applying a single iteration of the Newton-Raphson scheme to the consistency condition, as follows:

$$\xi_{PT1} = \xi^{(0)} + \delta\xi^{(0)} = \xi^{(0)} - \left( \frac{dF}{d\xi} \Big|^{(0)} \right)^{-1} F^{(0)}, \quad (4.11)$$

where we consider:

$$\begin{cases} \xi^{(0)} = \xi_{TR} = 0 \\ F^{(0)} = F_{TR} \\ \frac{dF}{d\xi} \Big|^{(0)} = \frac{dF}{d\xi} \Big|_{TR} \end{cases}. \quad (4.12)$$

The derivative  $dF/d\xi$  is therefore computed as:

$$\left. \frac{dF}{d\xi} \right|_{TR} = \frac{\mathbf{X}_{TR}}{|\mathbf{X}_{TR}|} : \left\{ -(2G + h)\mathbb{I} - \frac{f(\theta)}{|\mathbf{e}_{TR}^{\text{tr}}|} \left[ \mathbb{I} - \frac{\mathbf{e}_{TR}^{\text{tr}} \otimes \mathbf{e}_{TR}^{\text{tr}}}{|\mathbf{e}_{TR}^{\text{tr}}|} \right] \right\} : \frac{\mathbf{X}_{TR}}{|\mathbf{X}_{TR}|}, \quad (4.13)$$

where  $\mathbb{I}$  is the fourth order identity tensor. Thus, we can write the explicit forward Euler integration of the transformation strain evolution equation, as follows:

$$\mathbf{e}_{PT1}^{\text{tr}} = \mathbf{e}_n^{\text{tr}} + \xi_{PT1} \frac{\mathbf{X}_{TR}}{|\mathbf{X}_{TR}|}. \quad (4.14)$$

After the inelastic step is performed, a check is made on the transformation strain constraint (3.1). If the constraint is not satisfied, a further inelastic step (referred to as *PT2 step* in Table 4.4) is performed, where the transformation strain  $\mathbf{e}^{\text{tr}} = \mathbf{e}_{PT2}^{\text{tr}}$  is calculated starting from the PT1 step solution, by the following expression:

$$\mathbf{e}_{PT2}^{\text{tr}} = \epsilon_L \frac{\mathbf{e}_{PT1}^{\text{tr}}}{|\mathbf{e}_{PT1}^{\text{tr}}|}. \quad (4.15)$$

Such an approximation allows for a simplified calculation and reduced number of functional evaluations for each time increment, but small increments are required to avoid accumulation of error and to achieve solution accuracy. The following expression can be obtained from Eqs (3.8) and (3.9):

$$\mathbf{X} = R_Y \frac{\mathbf{e}^{\text{tr}} - \mathbf{e}_n^{\text{tr}}}{|\mathbf{e}^{\text{tr}} - \mathbf{e}_n^{\text{tr}}|}. \quad (4.16)$$

Such expression is equivalent to Eq. (37) in [312]. Combining Eqs (4.15), (4.16) and (3.4), it is possible to obtain the following relation:

$$R_Y \frac{\mathbf{e}_{PT2}^{\text{tr}} - \mathbf{e}_n^{\text{tr}}}{|\mathbf{e}_{PT2}^{\text{tr}} - \mathbf{e}_n^{\text{tr}}|} - 2G (\mathbf{e} - \mathbf{e}_{PT2}^{\text{tr}}) + f(\theta) \frac{\mathbf{e}_{PT2}^{\text{tr}}}{|\mathbf{e}_{PT2}^{\text{tr}}|} + h \mathbf{e}_{PT2}^{\text{tr}} + \ell_{PT2} \frac{\mathbf{e}_{PT2}^{\text{tr}}}{|\mathbf{e}_{PT2}^{\text{tr}}|} = 0, \quad (4.17)$$

from which we derive the saturation coefficient  $\ell = \ell_{PT2}$ :

$$\ell_{PT2} = \left( -R_Y \frac{\mathbf{e}_{PT2}^{\text{tr}} - \mathbf{e}_n^{\text{tr}}}{|\mathbf{e}_{PT2}^{\text{tr}} - \mathbf{e}_n^{\text{tr}}|} + 2G (\mathbf{e} - \mathbf{e}_{PT2}^{\text{tr}}) - f(\theta) - h\mathbf{e}_{PT2}^{\text{tr}} \right) : \frac{\mathbf{e}_{PT2}^{\text{tr}}}{|\mathbf{e}_{PT2}^{\text{tr}}|}. \quad (4.18)$$

The considerations on the regularization parameter  $\delta$ , introduced in Eq. (4.7), remain valid for the present scheme. Additionally, we have to consider the regularized expression introduced in Eq. (4.18) for the norm  $|\mathbf{e}^{\text{tr}} - \mathbf{e}_n^{\text{tr}}|$ .

Table 4.4 summarizes the explicit scheme implemented as a VUMAT user material subroutine in Abaqus/Explicit. The proposed algorithm is simple to implement. Compared to the work by Jähne [141], our procedure does not include a convergence criterion to determine  $\xi_{PT1}$  (see Eq. (4.11)), thus making it truly explicit and allowing a low computational cost per increment. Obviously, this requires small time steps to maintain an acceptable solution accuracy and avoid instability. Similarly, the computation of  $\ell_{PT2}$  (see Eq. (4.18)) is straightforward, contrary to the method of [141], which proposed a linearization and then an iterative procedure for the PT2 step. Finally, unlike the implicit scheme, the explicit algorithm does not require the often expensive computation of a tangent matrix, consistent or otherwise.

### 4.3 Numerical simulations

In this section we compare the implicit and explicit algorithms employed toward numerical simulations involving quasi-static pseudoelastic and shape-memory response of SMA bodies. The complexity of the simulations increases as the section progresses; we start with simple uniaxial and biaxial tests, and subsequently consider complex three-dimensional FEA of SMA-based devices related to engineering applications (i.e., stent strut, helical spring, micro-gripper, cable segment).

The explicit integration scheme is implemented within Abaqus/Explicit through a VUMAT user subroutine, while the implicit algorithm is implemented within Abaqus/Standard through a UMAT user subroutine [1]. In particular, we use the package AceGen [163] of the symbolic software Mathematica [209] to generate the numerical subroutines for Abaqus. This package combines the symbolic and algebraic capabilities of Mathematica, automatic differentiation technique, automatic code generation, and simultaneous

Table 4.4: Explicit forward Euler algorithm.

Given quantities:  $\boldsymbol{\varepsilon}, T, \mathbf{e}_n^{\text{tr}}, \xi_n, \ell_n$

Compute trial state:

$$\begin{aligned}\xi_{TR} &= 0 \\ \mathbf{e}_{TR}^{\text{tr}} &= \mathbf{e}_n^{\text{tr}} \\ \ell_{TR} &= 0 \\ \mathbf{s}_{TR} &= 2G(\mathbf{e} - \mathbf{e}_{TR}^{\text{tr}}) \\ \mathbf{X}_{TR} &= \mathbf{s}_{TR} - f(\theta) \frac{\mathbf{e}_{TR}^{\text{tr}}}{|\mathbf{e}_{TR}^{\text{tr}}|} - h\mathbf{e}_{TR}^{\text{tr}} \\ F_{TR} &= |\mathbf{X}_{TR}| - R_Y\end{aligned}$$

IF  $F_{TR} \leq \text{tol}$  THEN

Elastic step:

$$\xi = \xi_{TR}; \mathbf{e}^{\text{tr}} = \mathbf{e}_{TR}^{\text{tr}}; \ell = \ell_{TR}; \mathbf{s} = \mathbf{s}_{TR}; \mathbf{X} = \mathbf{X}_{TR}$$

ELSE

Inelastic step:

Compute  $\xi_{PT1}$  via Eq. (4.11)

$$\mathbf{e}_{PT1}^{\text{tr}} = \mathbf{e}_n^{\text{tr}} + \xi_{PT1} \frac{\mathbf{X}_{TR}}{|\mathbf{X}_{TR}|}$$

IF  $|\mathbf{e}_{PT1}^{\text{tr}}| \leq \epsilon_L$  THEN

$$\begin{aligned}\xi &= \xi_{PT1} \\ \mathbf{e}^{\text{tr}} &= \mathbf{e}_{PT1}^{\text{tr}} \\ \ell &= \ell_{TR} \\ \mathbf{s} &= 2G(\mathbf{e} - \mathbf{e}^{\text{tr}}) \\ \mathbf{X} &= \mathbf{s} - f(\theta) \frac{\mathbf{e}^{\text{tr}}}{|\mathbf{e}^{\text{tr}}|} - h\mathbf{e}^{\text{tr}}\end{aligned}$$

ELSE

Saturation step:

$$\begin{aligned}\mathbf{e}^{\text{tr}} &= \mathbf{e}_{PT2}^{\text{tr}} = \epsilon_L \frac{\mathbf{e}_{PT1}^{\text{tr}}}{|\mathbf{e}_{PT1}^{\text{tr}}|} \\ \text{Compute } \ell &= \ell_{PT2} \text{ via Eq. (4.18)} \\ \mathbf{s} &= 2G(\mathbf{e} - \mathbf{e}^{\text{tr}}) \\ \mathbf{X} &= \mathbf{s} - (f(\theta) + \ell) \frac{\mathbf{e}^{\text{tr}}}{|\mathbf{e}^{\text{tr}}|} - h\mathbf{e}^{\text{tr}}\end{aligned}$$

END IF

END IF

optimization of expressions for the derivation of codes to be used in numerical procedures [163].

For both the implicit and explicit methods, all bodies considered are discretized into first-order hexahedral elements with full and reduced integration, respectively (Abaqus designation **C3D8** and **C3D8R**).

During the implicit analysis, the time increment is set to  $10^{-2}$  s.

Moreover, since the explicit method is here used to solve quasi-static problems, we employ the method of mass scaling to artificially reduce the simulation runtime for the problems involving the largest number of DOFs<sup>2</sup>. To avoid inflation of the mass and oscillations during the quasi-static solution due to an artificially inflated kinetic energy, we check carefully for both oscillations and unrealistic kinetic energy. In particular, the kinetic energy (Abaqus designation **ALLKE**) is not allowed to exceed 5-10% of the internal energy (Abaqus designation **ALLIE**) over the majority of the analysis [1].

In all numerical studies we adopt the material parameters of NiTi wire reported in Table 4.5, calibrated as described in [30], by referring to [266]. Figure 4.1 shows the phase diagram in terms of limit transformation stress  $\sigma$  (i.e. the scalar stress value which identifies the forward transformation) and temperature generated with the reported model parameters. In all the pseudoelastic tests, we consider a constant temperature of 310 K, except for the SMA cable test where temperature is set equal to 300 K.

Table 4.5: Material parameters for the Souza-Auricchio model adopted in all the simulations after [30].

Description	Symbol	Value	Unit
Young's modulus	$E$	53,000	MPa
Poisson's ratio	$\nu$	0.33	-
Stress-strain slope during transformation	$h$	1,000	MPa
Maximum axial transformation strain	$\varepsilon_L$	0.056	-
Reference temperature	$T^*$	243	K
Term related to the following $\tau_M$ definition: $\tau_M = \beta(T - T^*)^+$	$\beta$	6.1	MPa/K
Elastic domain radius in the deviatoric stress space	$R_Y$	100	MPa

<sup>2</sup>All mesh elements are scaled by a single factor so that the minimum stable increment becomes fixed. The mass scaling options are labeled by the keywords **\*Mass Scaling: Semi-Automatic, Whole Model, Fixed Mass Scaling, dt=, type=uniform**. Then, the analysis is conducted by fixing the time increment, labeled by the keyword **\*Dynamic, Explicit, direct user control**.



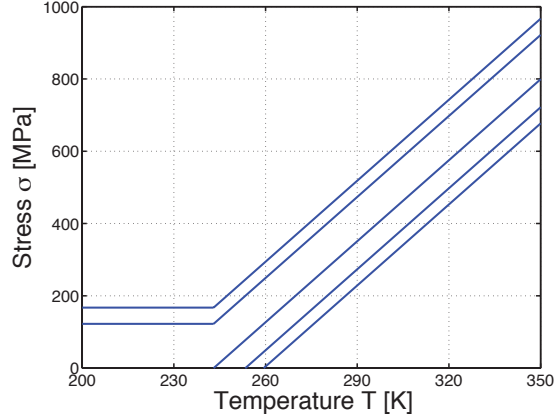


Figure 4.1: One-dimensional phase diagram generated with material parameters of Table 4.5.

### 4.3.1 Preliminary tests

First of all, two preliminary tests are performed on the strain-driven material constitutive drivers coded in the software *Mathematica* [209], for both explicit and implicit algorithms, in order to compare them in terms of computational time.

The first one is a uniaxial test where the imposed strain reads

$$\boldsymbol{\varepsilon}(t) = \begin{bmatrix} \varepsilon_{11}(t) & 0 & 0 \\ 0 & -\frac{1}{2}\varepsilon_{11}(t) & 0 \\ 0 & 0 & -\frac{1}{2}\varepsilon_{11}(t) \end{bmatrix}$$

where the trend of  $\varepsilon_{11}(t)$  is displayed in Figure 4.2(a). The number of time steps is 200.

The second one is a hourglass biaxial test where the imposed strain reads

$$\boldsymbol{\varepsilon}(t) = \begin{bmatrix} \varepsilon_{11}(t) & 0 & 0 \\ 0 & \varepsilon_{22}(t) & 0 \\ 0 & 0 & 0 \end{bmatrix}$$

where the trend of  $\varepsilon_{11}(t)$  and  $\varepsilon_{22}(t)$  is displayed in Figure 4.2(b) and 4.2(c). The test consists of 800 time steps.

The computational times of explicit and implicit algorithms are reported in Table 4.6. It can be noted that the explicit driver is considerably faster than the implicit one.

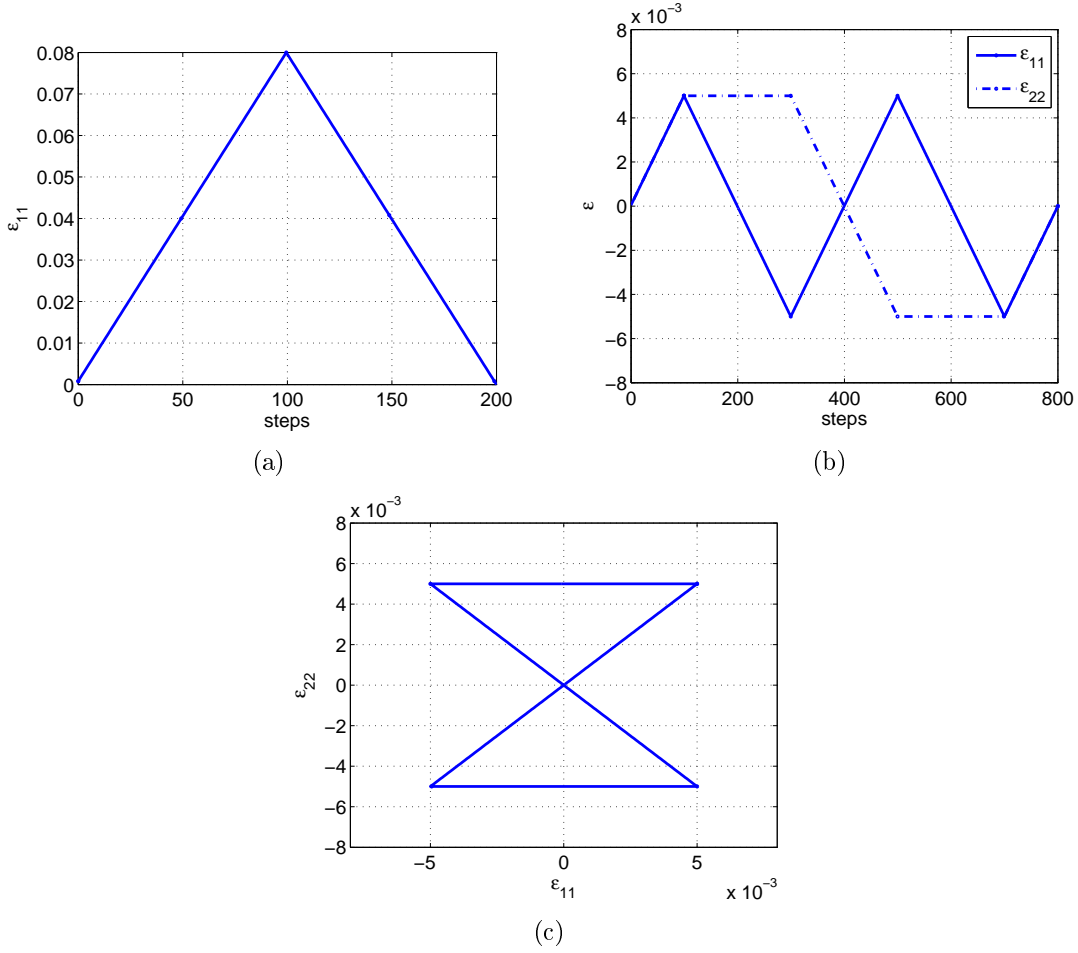


Figure 4.2: Trend of the input variables for the preliminary uniaxial test (a) and for the preliminary biaxial test (b)-(c).

### 4.3.2 Uniaxial tests

To provide a baseline comparison, we first consider a uniaxial tensile test on a single-element cube at constant temperature. We consider an applied tensile displacement of 0.1 mm to one surface of the cube, constraining out-of-plane displacement on the opposite face and on two consecutive lateral faces. Figure 4.3(a) presents the stress-strain curves obtained via both the implicit and explicit algorithms. As it can be observed, the pseudoelastic curves perfectly match.

We then consider a thermal cycling test at constant tensile stress, simulated by applying a tensile traction of 300 MPa to two opposing faces and a homogeneous but time-varying temperature field. Figure 4.3(b) reports the strain-temperature diagram. Again, both

Table 4.6: Computational times, in seconds, of explicit and implicit material constitutive drivers.

	Implicit	Explicit
uniaxial test	0.5650	0.1040
biaxial test	1.1161	0.2720

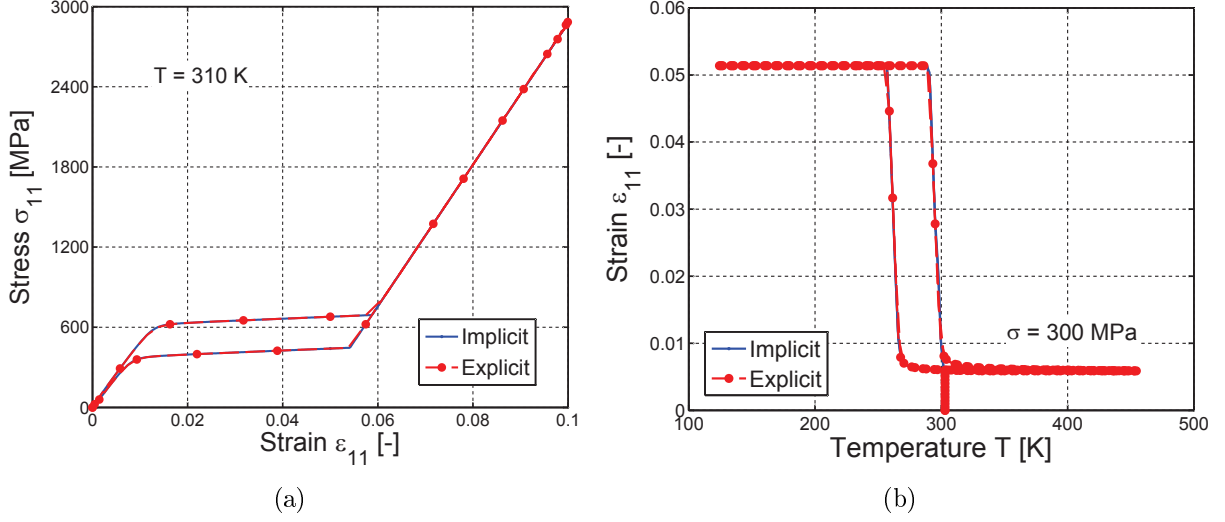


Figure 4.3: Model response for superelastic and thermal-cycling uniaxial tests. (a) Stress-strain diagram related to a pseudoelastic tensile test, and (b) strain-temperature diagram related to a thermal-cycling test at constant tensile stress.

curves match well.

Finally, we consider a zero-stress shape recovery test. Initially, the temperature is set at 200 K. The cube is uniaxially loaded by applying a displacement of 0.1 mm to one surface of the cube. Then the cube is unloaded until reaching a zero-stress condition. Finally, the temperature is raised to 400 K, allowing shape recovery to take place. Figure 4.4 reports the stress-strain and strain-temperature plots, where the shape recovery upon heating can be noticed. Again, the implicit and explicit results perfectly overlap.

### 4.3.3 Biaxial test

To verify the two implementations against each other under more complex loading, we also consider biaxial non-proportional stress-strain loading obtained by assuming control of two strain components,  $\{\varepsilon_{22}, \varepsilon_{33}\}$ . We consider the hourglass-shaped strain history input shown in Figure 4.5(a). Figure 4.5(b) represents the resulting non-zero stress components.

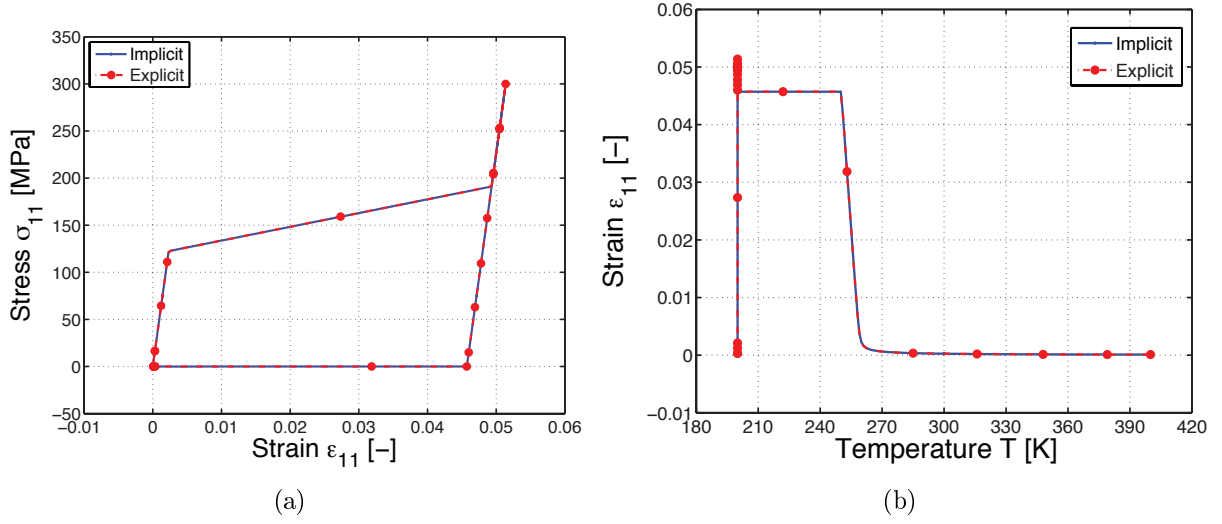


Figure 4.4: Model response for shape-memory uniaxial tests. (a) Stress-strain diagram, and (b) strain-temperature diagram.

Implicit and explicit methods give matching curves.

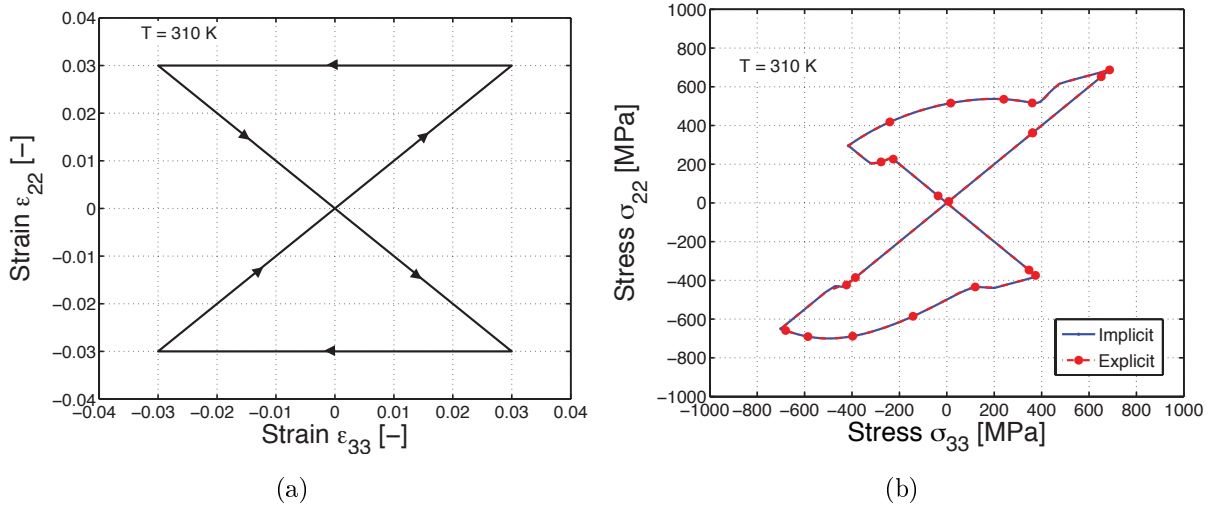


Figure 4.5: Model response for biaxial test. (a) Butterfly-shaped strain control history input; (b) non-zero stress component outputs of both algorithms.

#### 4.3.4 Pseudoelastic cardiovascular stent strut

The use of SMA materials to manufacture cardiovascular stents, where by pseudoelasticity enables the essential self-deployment behaviors, is increasing. We investigate the behavior

of such a pseudoelastic stent strut, providing an example study for bending response.

The stent strut is obtained from the planar CAD representation of a stent geometrically resembling a Bard ViVEXX carotid stent (C.R. Bard Angiomed GmbH&Co., Germany). Figure 4.6 shows the Bard ViVEXX carotid stent geometry and the adopted mesh of the stent strut, consisting of 62,304 elements and 75,933 nodes (corresponding to 227,799 DOFs).

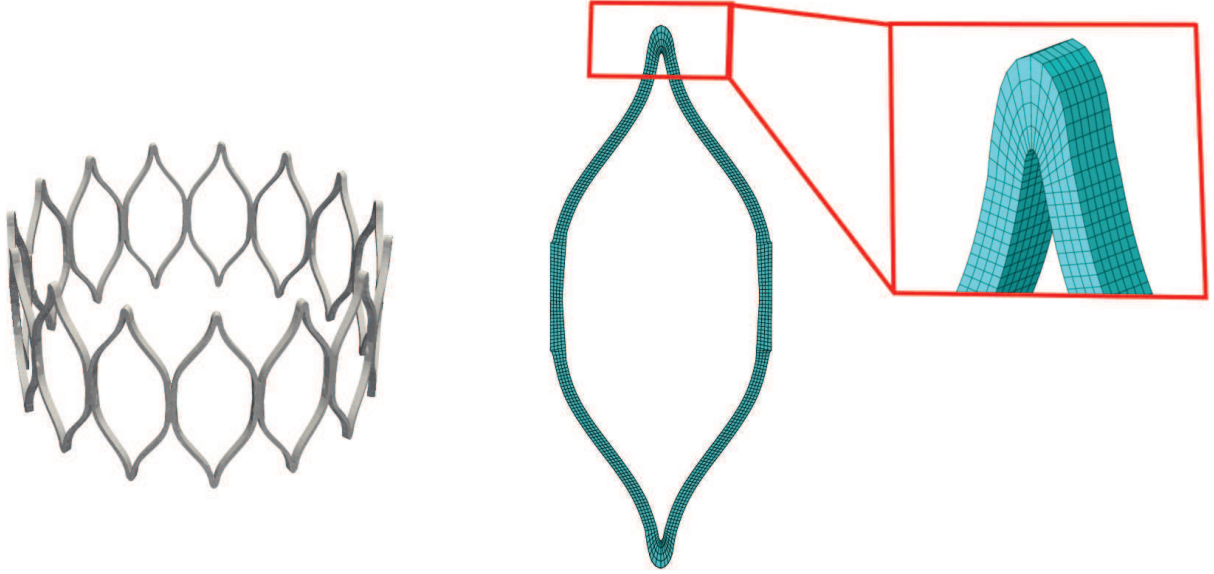


Figure 4.6: SMA cardiovascular stent strut: geometry of the Bard ViVEXX carotid stent; mesh and initial geometry of the strut set modeled herein.

We apply a tensile displacement  $u$  of 1 mm to one side of the strut while the other side is fully constrained (see Figure 4.7). All other surfaces are traction free. We increase the displacement  $u$  from zero to its maximum value then unload the structure fully. Figure 4.7 shows the deformed shape at maximum displacement, compared to the initial geometry of the strut. Figure 4.8 shows applied displacement  $u$  and total reaction force of the fixed side and Figure 4.9 compares the transformation strain distribution with implicit and explicit integration. The curves and the contour plots match well.

In the explicit analysis, the stable time increment for the investigated solid model, evaluated by Abaqus at the beginning of the analysis, is  $1.04 \cdot 10^{-9}$  s. Mass scaling is here applied; in particular, the minimum stable time increment and the time increment are both set to  $10^{-7}$  s. Figure 4.10 provides the plot of the internal and kinetic energies versus the total analysis time and it is observed that the mass scaling does not threaten

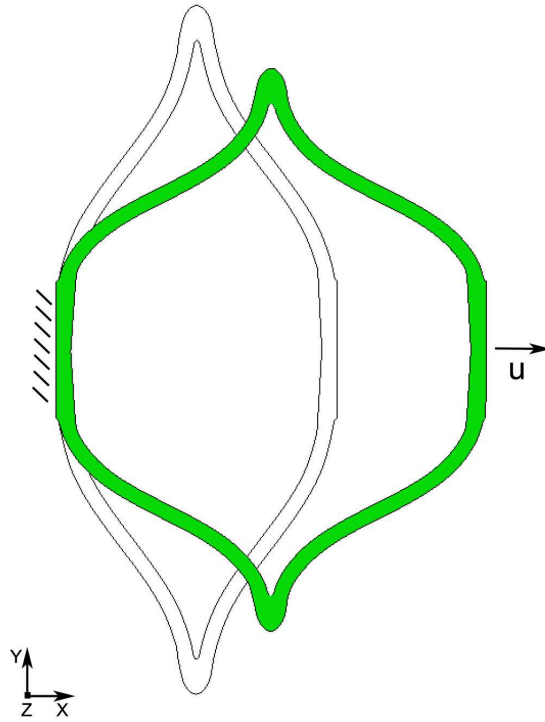


Figure 4.7: SMA cardiovascular stent strut: initial geometry, boundary conditions, and deformed shape under the maximum displacement.

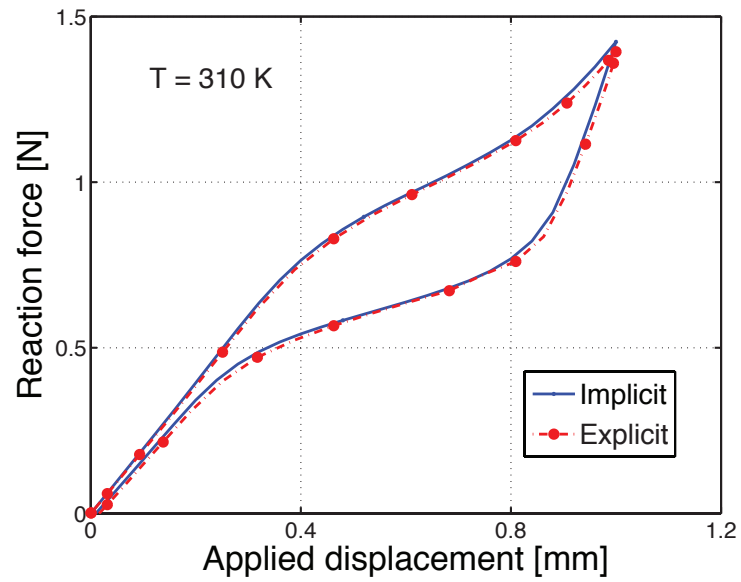


Figure 4.8: SMA cardiovascular stent strut: applied displacement vs. reaction force of the fixed side diagram.

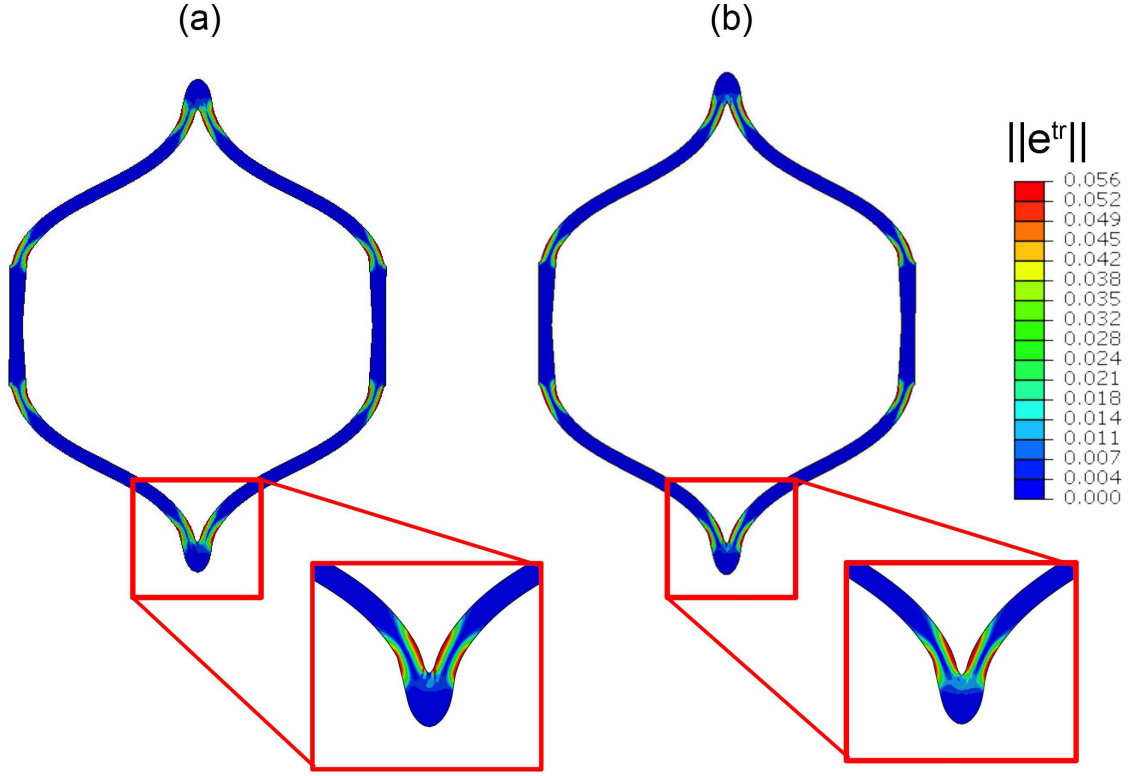


Figure 4.9: SMA cardiovascular stent strut: implicit (a) and explicit (b) transformation strain norm contour plots.

the quasi-static condition of the simulation.

#### 4.3.5 Pseudoelastic helical spring

We now consider a pseudoelastic SMA helical spring. SMA springs can be used in vibration isolation and dampening applications. Vibration isolation results from the relatively soft response of the transformation plateau. Dampening is a consequence of the hysteretic nature of phase transformation. One example is the application in structures under earthquake loads [219]. Despite the apparent simplicity, the behavior of such a component is rather complex and includes local combined torsional and axial deformations.

The analyzed helical spring consists of 2 full free coils having a pitch of 2.5 mm (i.e., initial total length of 5.0 mm) and an external diameter of 6.0 mm, constructed from a wire with a diameter of 1.0 mm. Figure 4.11(a) reports the adopted mesh, consisting of 3,712 elements and 4,485 nodes (corresponding to 14,455 DOFs), and the initial geometry.

We apply a displacement  $w$  of 15 mm at one end of the helical spring along the spring

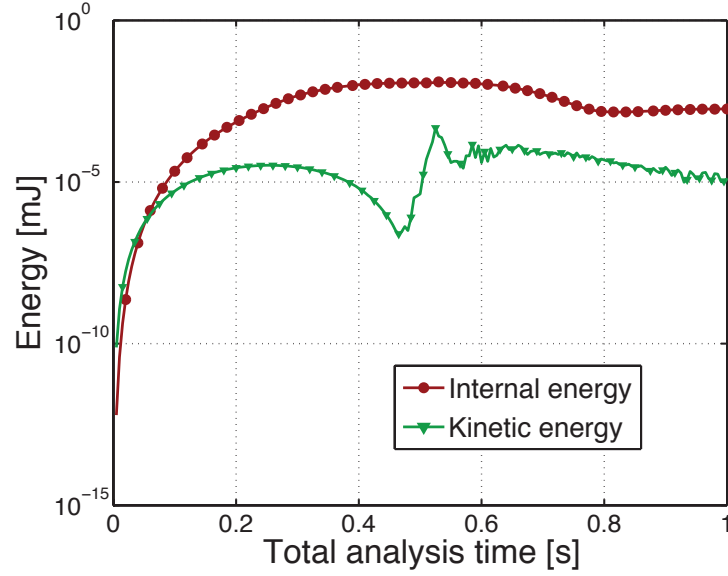


Figure 4.10: SMA cardiovascular stent strut: plot of the internal and kinetic energies vs. total analysis time related to the explicit analysis. A total of 1 time unit is used for loading and unloading.

axis, while the entire cross-sectional surface at the other end is completely fixed in all directions, thus preventing rotation at this end as well (see Figure 4.11(b)). We increase the displacement from zero to its maximum value and then unload the structure bringing the displacement back to 0. Figure 4.11(b) shows the deformed shape at fully maximum applied displacement, compared to the initial geometry of the spring. Figure 4.12 shows the response in terms of reaction force versus applied displacement  $w$  of the free end, while Figures 4.13 and 4.14 compare the transformation strain and Von Mises stress distributions using implicit and explicit integration, respectively. The curves and the transformation strain contour plots generally match well. For both implicit and explicit schemes, after unloading, the spring recovers its original shape as expected in the pseudoelastic regime.

In the explicit analysis, the stable time increment for the investigated solid model, evaluated by Abaqus at the beginning of the analysis, is  $5.07 \cdot 10^{-9}$  s. To reduce the computational time, a mass scaling is applied such that the new minimum stable time increment becomes  $10^{-8}$  s; the analysis time increment is therefore set to  $10^{-8}$  s. Figure 4.15 provides the plot of the internal and kinetic energies versus the total analysis time. It is observed that the kinetic energy remains negligible with respect to the internal energy, thus we can conclude that the mass scaling did not impair the quasi-static condition.



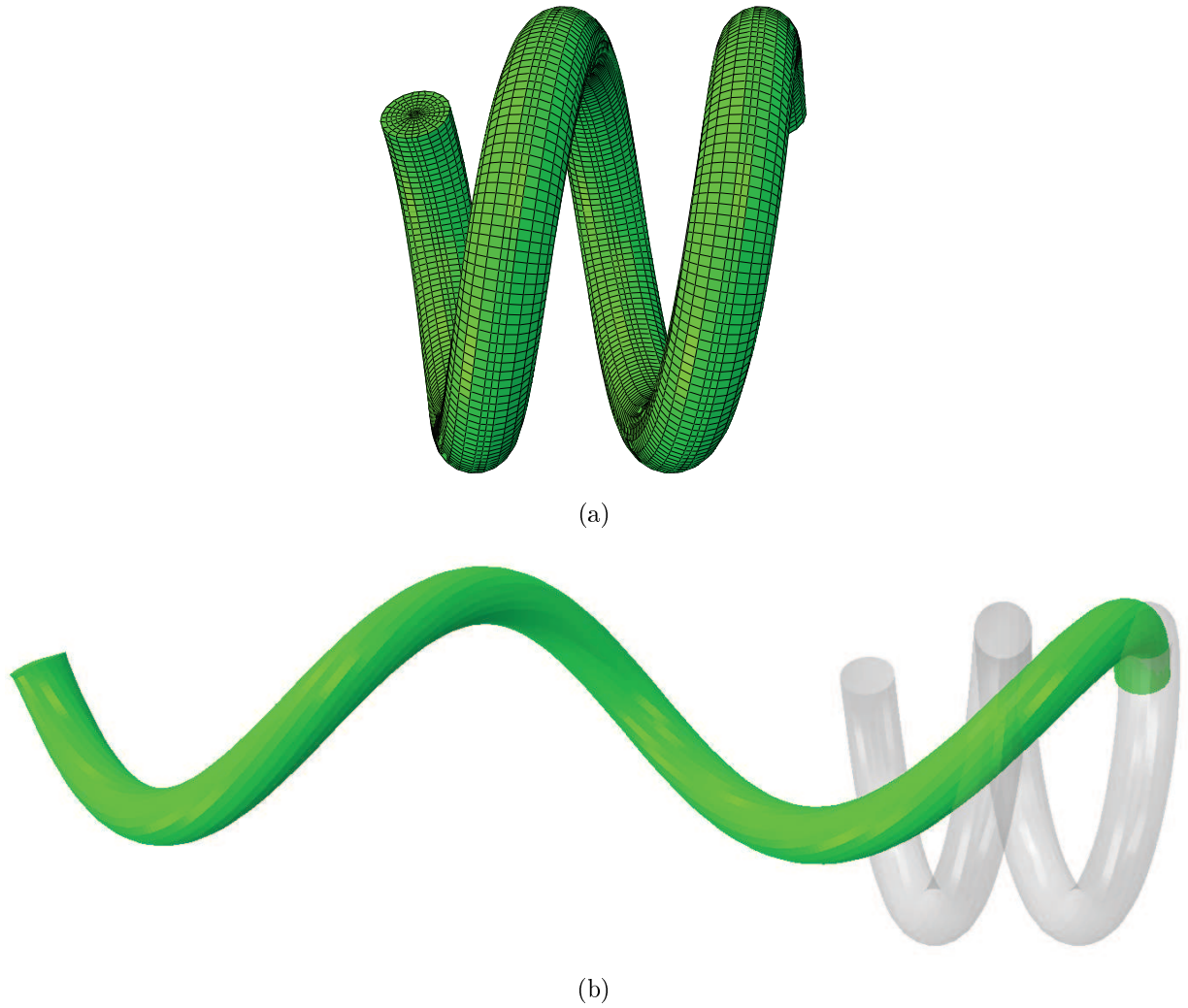


Figure 4.11: SMA helical spring: (a) adopted mesh; (b) initial geometry, boundary conditions, and deformed shape under the maximum displacement.

#### 4.3.6 Actuation of a micro-gripper

Whereas the previous two SMA components of complex shape were analyzed under pseudoelastic loading, we now consider thermally induced actuation. Specifically, a SMA micro-gripper for micro-parts manipulation is assessed [49]. The adopted geometry is similar to the one reported by Kohl [162]. Figure 4.16 reports the adopted reference mesh, consisting of 14,376 elements and 24,417 nodes (corresponding to 73,251 DOFs).

The micro-gripper operates via a quite complex antagonistic actuation cycle, as shown in Figure 4.17. In other words, two regions of the device actuate in opposition to one

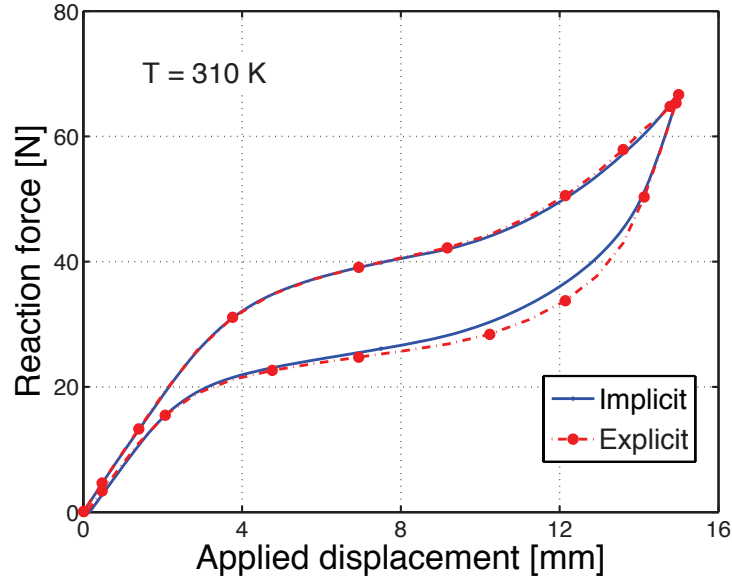


Figure 4.12: SMA helical spring: applied vertical displacement vs. reaction force of the fixed end diagram.

another. The gripper is in fact divided in two actuation units: an upper part, actually devoted to gripping, and referred to as the *rotational stage*, and a lower part, which stretches and contracts, referred to as the *linear stage*. Four small quadrilateral features can be noted in Figure 4.17, which are referred to as *tabs*. During the full working cycle, the tabs of the linear stage are fully constrained (see steps A-C of Figure 4.17). At the beginning of the actuation cycle, the gripper is at low temperature. In step A, a displacement  $v$  of 2.5 mm is applied to the region connecting the two stages, and the linear stage is stretched. During step B, the tabs of the rotational stage are fully constrained and the linear stage is heated; the heat allows activation of the linear stage, which tends to recover its original configuration and contracts (the direction is indicated by the black arrow in step B). The contraction of the linear stage combined with the full constraint on the four tabs produces the gripping action (clockwise rotation of the rotational part in step B). Finally, during step C, the linear stage is cooled down, and the rotational stage is heated; the rotational stage activates and recovers its initial shape, reaching the open position (anti-clockwise rotation in step C). As the rotational stage moves, it forces the linear stage to stretch (the direction is indicated by the grey arrow in step C).

Figure 4.19 shows the deformed state of the micro-gripper and corresponding contour plots of the transformation strain norm at states B and C of Figure 4.18) for both implicit

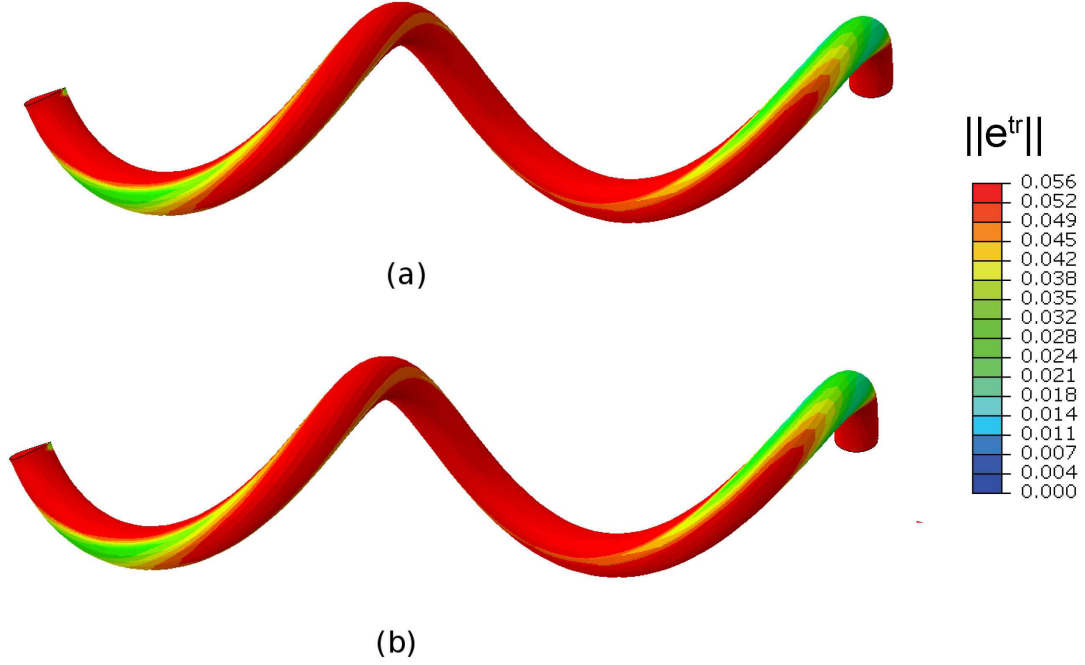


Figure 4.13: SMA helical spring: implicit (a) and explicit (b) transformation strain norm distributions.

and explicit analyses. Since a different element integration type has been used in the implicit and explicit analyses, it can be noted that some difference exists between the two deformed shapes at state B; moreover, some very small concentrations of transformation strain are observable in the highly curved regions of the micro-gripper in the case of the implicit analysis results.

In the explicit analysis, the stable time increment evaluated by Abaqus at the beginning of the analysis is  $9.64 \cdot 10^{-9}$  s. Mass scaling is here applied, in such a way that the minimum stable time increment (and the used time increment) can be set to  $10^{-8}$  s. Figure 4.20 provides the plot of the internal and kinetic energies versus the total analysis time. As it can be observed, the kinetic energy presents a peak that is about 35% of the internal energy at about 1.1 s, attributable to the application of the boundary conditions to the two tabs of the rotational actuator. Despite this small response feature, the mass scaling does not impair the quasi-static condition during the gripper actuation.

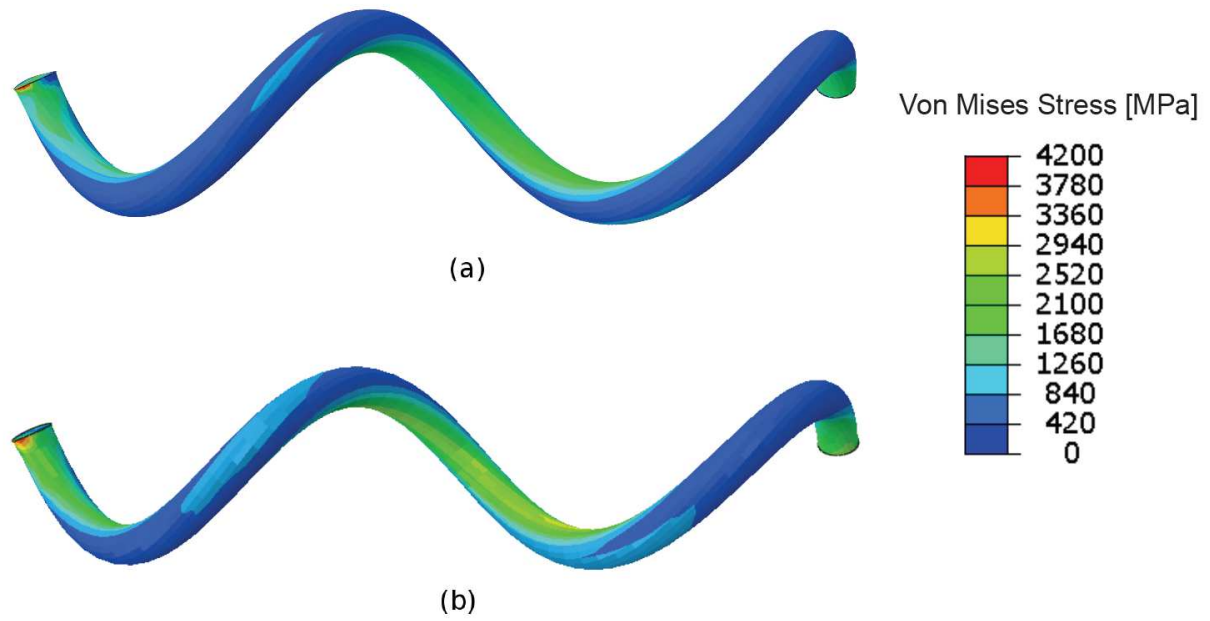


Figure 4.14: SMA helical spring: implicit (a) and explicit (b) Von Mises stress distributions.

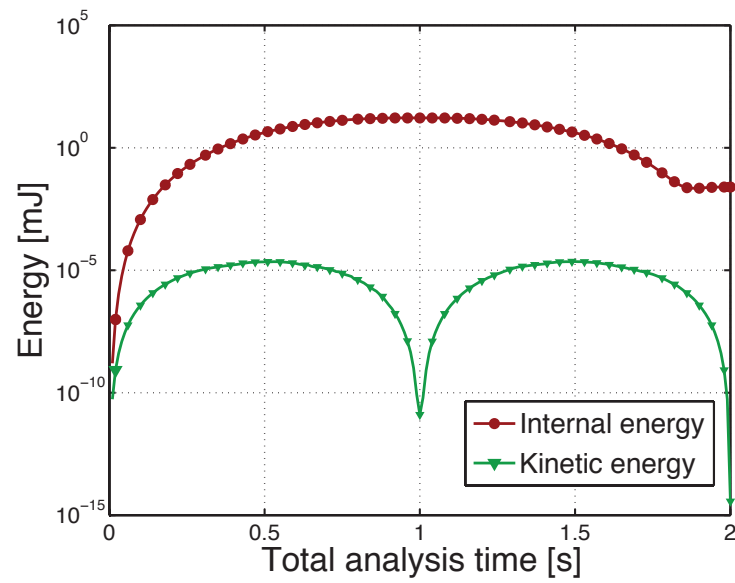


Figure 4.15: SMA helical spring: plot of the internal and kinetic energies vs. total analysis time related to the explicit analysis. A total of 2 time units are used for loading and unloading.

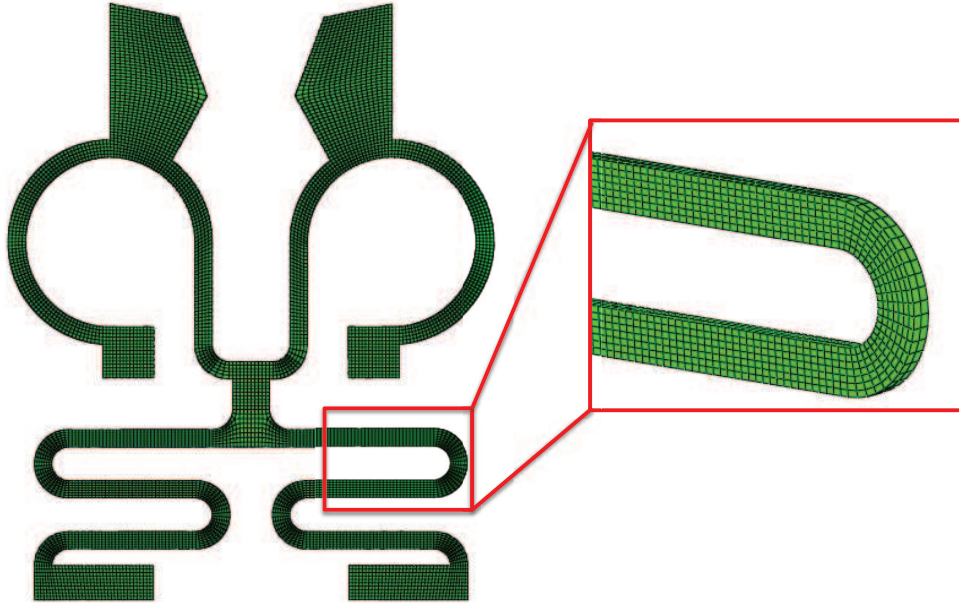


Figure 4.16: SMA micro-gripper: mesh and initial geometry.

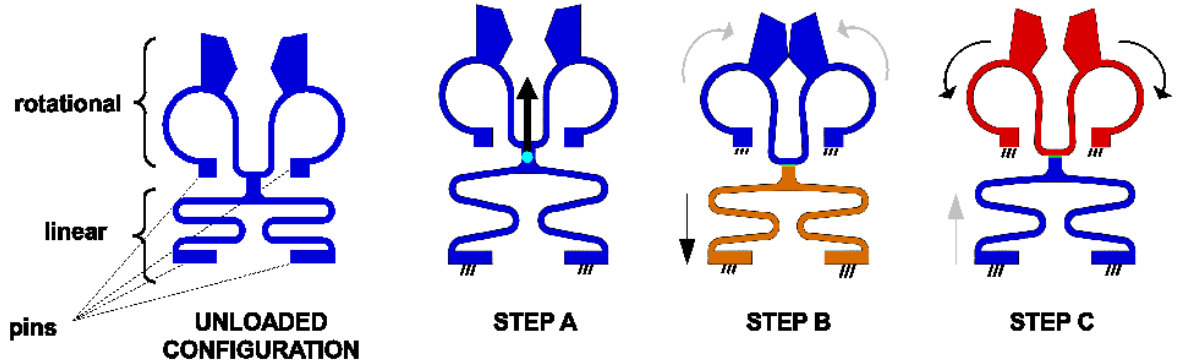


Figure 4.17: Working principle of the micro-gripper.

#### 4.3.7 Analysis of a pseudoelastic SMA strand

We conclude the investigation by analyzing a structural strand model consisting of SMA wire assemblies, as used in the development of a vibration absorber. In fact, besides the well known axial load-bearing capabilities of these elements, also the frictional dissipation occurring during bending deformation can be exploited for applications in civil and seismic engineering [328, 61, 283]. In this aspect, the interaction of different part geometries,

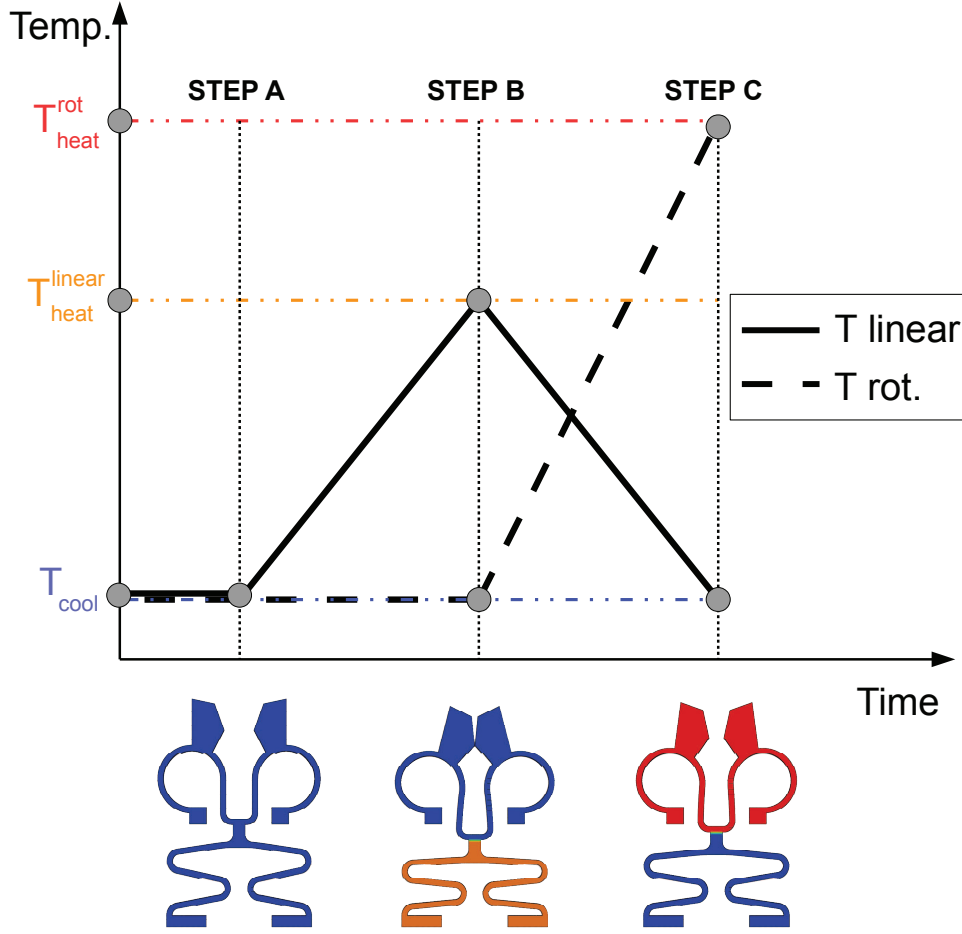


Figure 4.18: SMA micro-gripper: temperature trends.  $T_{linear}$  is the temperature history for the linear stage, while  $T_{rotational}$  is the temperature history for the rotational stage.

contact modeling, and non linear material behavior calls for the development of reliable computational models to fully understand the capabilities of SMA strands [94, 149].

The model considers a three layers straight strand having a total diameter of 30 mm. The strand is composed by a central straight wire (core) and two layers helically wrapped around the core (see Figure 4.21(a)). In particular, The first layer is composed by 6 wires wrapped in right-hand way with a pitch length of 15.7 mm and helix angle  $\alpha_1$  of 76.2 degree, while the second layer presents 12 wires wrapped in left-hand way with a pitch length of 25.7 mm and helix angle  $\alpha_2$  of 73.6 degree (see Figure 4.21(b)). The adopted discretization is reported in Figure 4.22, consisting of 323,158 solid brick elements and 416,357 nodes.

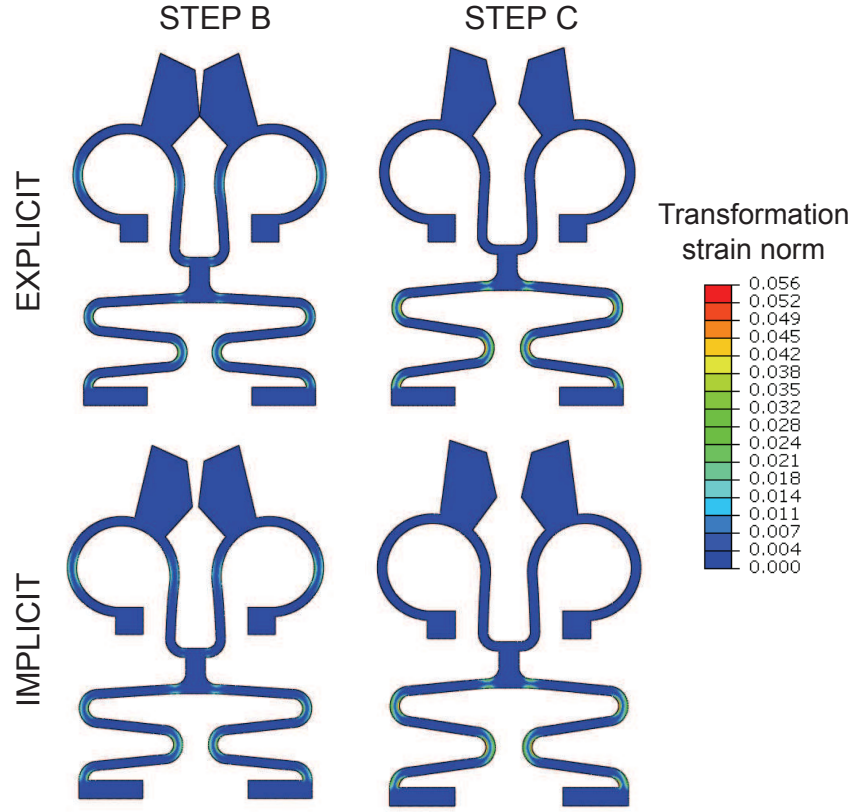


Figure 4.19: Deformed shape of the gripper for implicit and explicit analyses at states A and B of Figure 4.18. The contour plot of the transformation strain norm is displayed.

Following the experimental setup proposed by Carboni et al. [59], the goal of the analysis is to describe a hysteretic load-displacement cycle in the transverse direction  $Y$  preceded by a pretension phase along the longitudinal direction  $Z$  (Figure 4.23). During the first step, one end of the strand is fixed, while the other is subjected to a longitudinal displacement; in the second step, a sinusoidal transverse displacement with respect to the strand axis is applied to the free end while maintaining the longitudinal displacement (see Figure 4.23(a)). The longitudinal displacement  $w$  along  $Z$ -axis is 0.8 mm, while the transverse displacement  $v$  along  $Y$ -axis is 10 mm. The displacement history is summarized in Figure 4.23(b).

Contacts between wires exist and must be taken into account. To do so, a penalty formulation with Coulomb model is employed using a friction coefficient equal to 0.5.

The implicit solver is unable to complete the simulation. As mentioned, widespread

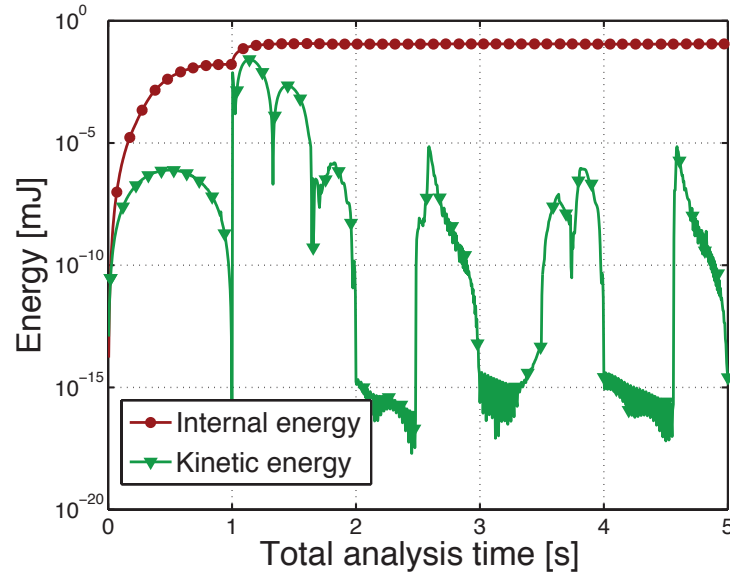


Figure 4.20: SMA micro-gripper: plot of the internal and kinetic energies vs. total analysis time related to the explicit analysis.

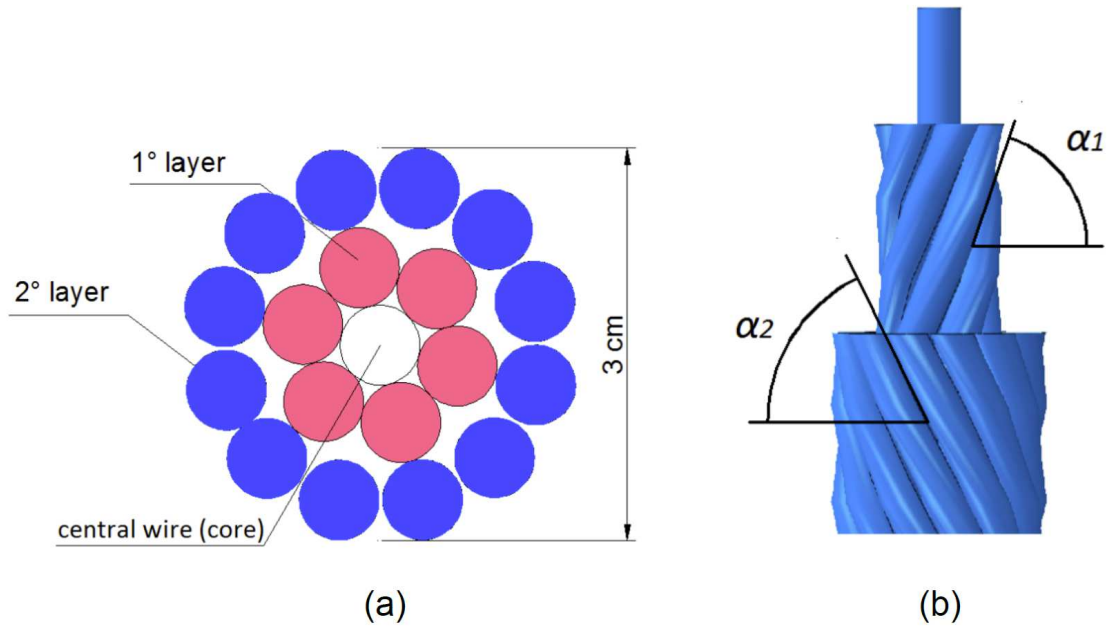


Figure 4.21: SMA cable: (a) three layers straight cable cross section; (b) angles of outer helical wires rotation.

contact, highly non-linear problems, or the presence of buckling can prevent implicit implementations converging upon a solution. When the implicit iterative solver encounters a highly non-linear response, as in the present case, very small time increments have to be



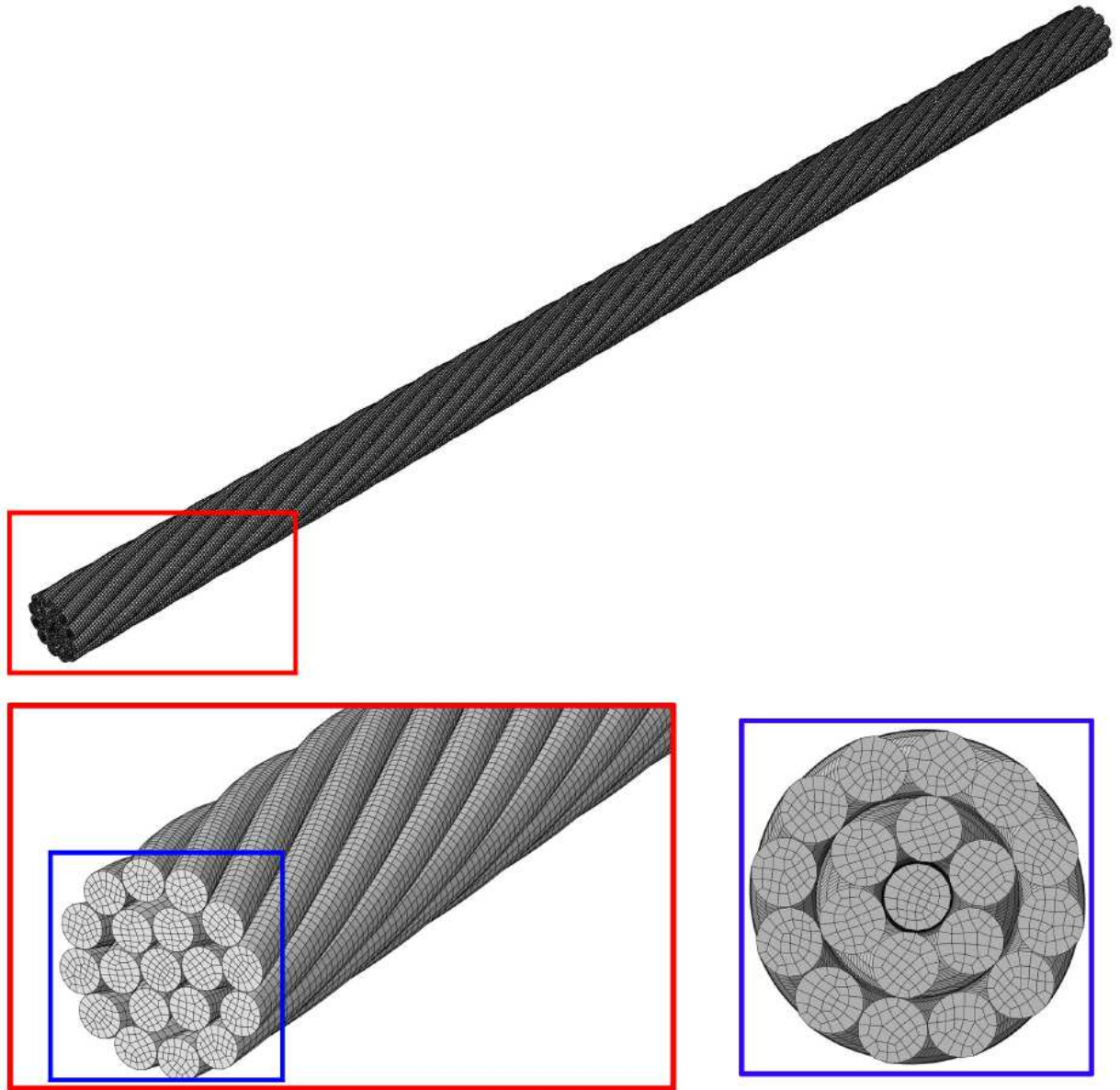


Figure 4.22: SMA cable: adopted mesh.

employed to solve the equilibrium equations. In this case, the solver attempts increasingly small time increments without achieving equilibrium. Specifically, prior to termination of the job, time increments in the order of  $10^{-8}$  are attempted without success.

Therefore, natural alternative to solve such problems is an explicit approach. The stable time increment for the investigated solid model, evaluated by Abaqus at the beginning of the analysis, is  $1.12 \cdot 10^{-8}$  s. Due to the large number of DoFs in the model, mass scaling

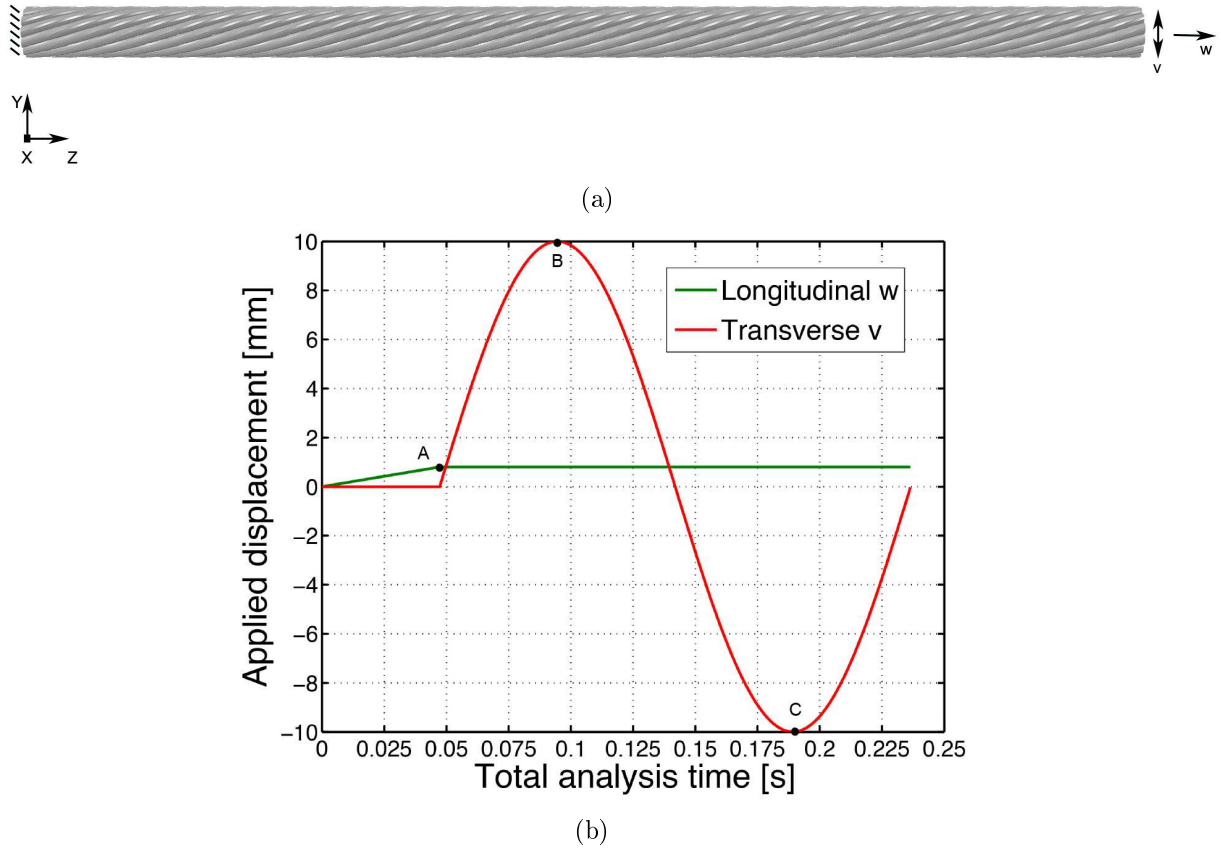
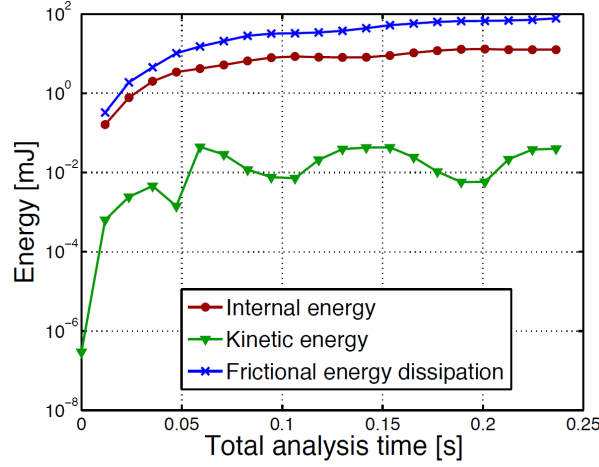


Figure 4.23: SMA strand: (a) applied boundary conditions and (b) loading history in terms of displacements. A total of 0.2364336 time units are used.

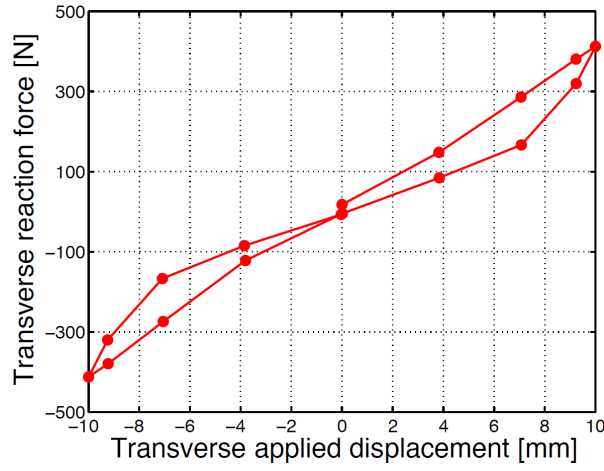
is applied considering, a fixed time increment of  $10^{-7}$  s.

Figure 4.24(a) presents the trend of the frictional energy dissipation (Abaqus designation ALLFD) with respect to internal and kinetic energies. Particularly, the frictional energy dissipation is associated to forces exchanged between wires. Despite some oscillations in the kinetic energy can be observed, the kinetic energy remains negligible with respect to the internal energy for the fixed time increment of  $10^{-7}$ , validating the initial hypothesis of quasi-static condition.

Moreover, Figure 4.24(b) presents the hysteretic load displacement diagram evaluated at the free end of the strand. Figure 4.25 shows the contour plot of the Von Mises stress evaluated at the mid section of the strand during pretension (a), maximum displacement (b), and minimum displacement (c) phases.



(a)



(b)

Figure 4.24: SMA strand: plot of (a) internal, kinetic, and frictional dissipation energies related to the explicit analysis (b) Hysteric force-displacement diagram.

## 4.4 Conclusions

The present chapter is focused on a novel implementation of the three-dimensional phenomenological Souza-Auricchio model, which is able to reproduce both pseudoelasticity and shape-memory effect. In particular, the work has investigated the robust and effective numerical implementation of the model using an explicit framework. A novel explicit integration scheme for the considered constitutive laws has been presented and tested on several full three-dimensional boundary-value problems of increasing complexity. A comparison of output results with the implicit integration scheme has also been made where

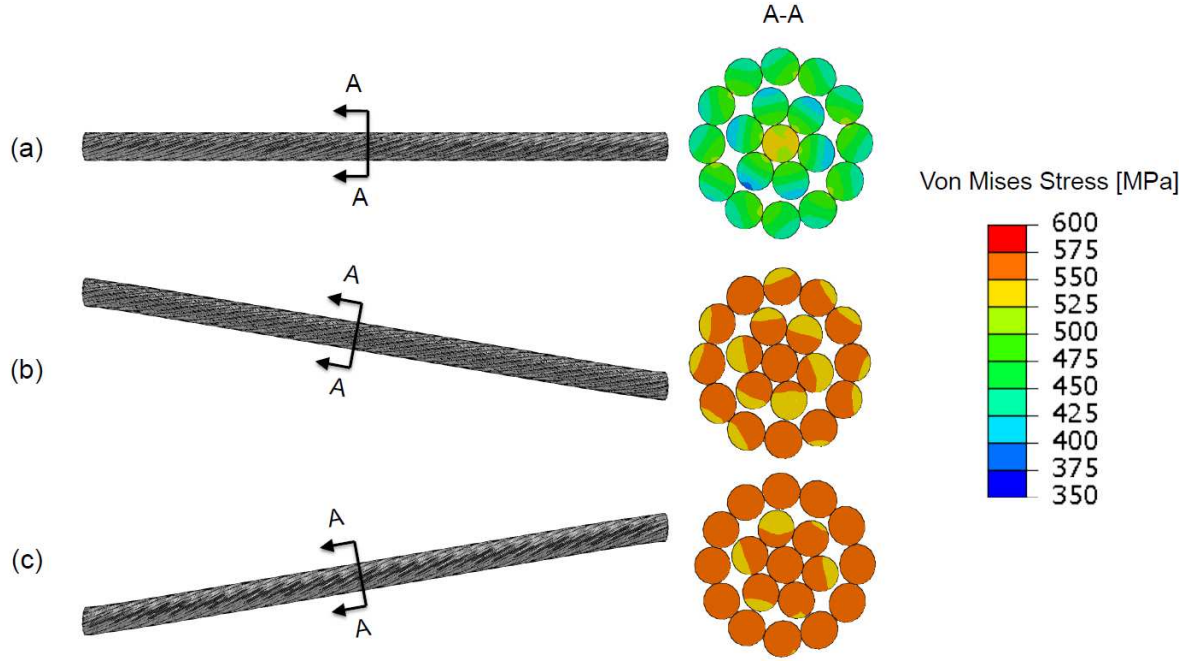


Figure 4.25: SMA strand: contour plot of the Von Mises stress for points (a) A (b) B, and (c) C of Figure 4.23(b).

possible. The results have shown the capability of the explicit implementation to successfully predict the quasi-static response of the considered devices and the possibility to exploit explicit FEA for structural simulations. Particularly, the analysis of SMA cables has demonstrated the effectiveness of the explicit algorithm to solve complex problems involving contact. However, since new advancements in SMA modeling continue, understanding the nature, advantages, and disadvantages of both implicit and explicit methods is very helpful to choose the right algorithm for the problem under investigation. Future developments will use the proposed explicit algorithm for high-speed dynamic simulations which are widely exploited in SMA-based seismic or impact applications.

## Chapter 5

# Gradient structures for the thermomechanics of shape-memory materials

The present study is included in a paper which has been submitted to *Computer Methods in Applied Mechanics and Engineering* [35].

### 5.1 Introduction

Shape-memory alloys (SMA) are *active* materials: considerably large deformations (up to 10 %) can be activated either by mechanical or thermal means. Such amazing material properties, combined with the typical resistance and workability of metals, make SMAs attractive for innovative engineering applications in various industrial fields including, e.g., automotive, robotics, civil, seismic, and biomedical [142]. The interest for this class of materials is currently triggering intense research efforts toward the implementation of appropriate constitutive models capable of efficiently and robustly reproduce the SMA behavior. The SMA response is a genuinely coupled thermomechanical effect. As such, the accurate and efficient treatment of nonisothermal situations bears a crucial importance.

The present Chapter investigates the variational structure of the three-dimensional thermo-mechanical constitutive model, firstly presented in [312], and then reformulated in [25] and [26], see the recent survey [121]. Our aim is to present a variational reformulation of the full nonisothermal evolution of the system as a *generalized gradient flow* of the *total*

entropy  $\mathbf{y} \mapsto \mathcal{S}(\mathbf{y})$  as a function of the state vector  $\mathbf{y}$ , including temperature as well as mechanical and internal variables. In particular, we shall be considering the following differential system

$$\partial_{\dot{\mathbf{y}}} \mathcal{K}(t, \mathbf{y}; \dot{\mathbf{y}}) - \partial \mathcal{S}(\mathbf{y}) \ni \mathbf{0}, \quad (5.1)$$

where  $\mathcal{K}(t, \mathbf{y}; \cdot)$  corresponds to the *entropy-production potential*. Here, the dot represent here differentiation with respect to time whereas  $\partial$  stands for some suitable notion of gradient, to be detailed below. The symbol  $\ni$  refers to the fact that, in absence of smoothness, the left hand side terms in (5.1) can be sets. As  $\mathcal{K}$  depends not only on the rate  $\dot{\mathbf{y}}$  but also on the state  $\mathbf{y}$ , we refer to (5.1) as a *generalized* gradient flow.

The interest in this perspective relies on the possibility of exploiting this variational structure both for the theoretical and the numerical discussion of the model. Different choices for  $\mathcal{K}$  will be presented, all satisfying the following fundamental structural property

$$\begin{aligned} &\text{for all } (t, \mathbf{y}) \text{ the map } \dot{\mathbf{y}} \mapsto \mathcal{K}(t, \mathbf{y}; \dot{\mathbf{y}}) \\ &\text{is convex, nonnegative, and } \mathcal{K}(t, \mathbf{y}; \mathbf{0}) = 0. \end{aligned} \quad (5.2)$$

This structural property immediately entails the *dissipativity* of the evolution. By assuming sufficient smoothness, one can multiply both sides of (5.1) by  $\dot{\mathbf{y}}$  and obtain

$$\frac{d}{dt} \mathcal{S}(\mathbf{y}) = \partial \mathcal{S}(\mathbf{y}) \cdot \dot{\mathbf{y}} = \partial_{\dot{\mathbf{y}}} \mathcal{K}(t, \mathbf{y}; \dot{\mathbf{y}}) \cdot \dot{\mathbf{y}} \geq \mathcal{K}(t, \mathbf{y}; \dot{\mathbf{y}}) \geq 0 \quad (5.3)$$

where we have used the convexity of  $\dot{\mathbf{y}} \mapsto \mathcal{K}(t, \mathbf{y}; \dot{\mathbf{y}})$  as well as the fact that  $\mathcal{K}(t, \mathbf{y}; \mathbf{0}) = 0 = \min \mathcal{K}(t, \mathbf{y}; \cdot)$ . In particular, the entropy increases along all sufficiently smooth evolutions.

The phrasing of the full thermomechanical problem as (5.1) is inspired to the theory of General Equations for Non-Equilibrium Reversible-Irreversible Coupling (GENERIC). Introduced by Grmela & Öttinger [122, 242] and recently reinterpreted by Mielke in a series of contributions [211, 213], GENERIC provides a far-reaching variational paradigm for reformulating in a thermodynamically consistent way a variety of physical systems. In particular, GENERIC is tailored to the unified treatment of reversible and irreversible (or even hysteretic) dynamics. GENERIC has recently attracted increasing attention and has been applied to a number of situations ranging from complex fluids, to dissipative quantum mechanics [213], to thermomechanics [211], and to the Vlasov-Fokker-Planck equation [251].

The novelty of this work is threefold. At the modeling level, we present a new variational formulation of the thermomechanically coupled system. As already commented, this formulation directly entails the dissipativity of the flow. In addition, we are able to include external actions in the picture. Let us mention that, up to now, the GENERIC framework is restricted to the description of *isolated* systems [212]. At first, we systematically eliminate the mechanical part from the problem by solving the quasistatic equilibrium system. This procedure allows us to consider body and traction forces, see Subsection 5.3.1. Secondly, by specifically reducing to the space-homogeneous case, we allow equilibration with a given external temperature, see Subsection 5.3.4.

A second novelty of the work consists in presenting an unconditionally stable and convergent time-discrete scheme for the fully coupled thermomechanical system. Although restricted to the space-homogeneous setting, such a result is unprecedented in the frame of this class of models in three dimensions [121]. By discretizing the system at the functional level, we directly obtain a numerical scheme reproducing the basic properties and, in particular, the dissipativity of the model. As a by-product of the convergence proof, we also establish the existence of a strong solution to the system in the continuous-time setting.

We shall refer to Peigney & Seguin [249, 250] for an alternative analysis towards a variational formulation of nonisothermal evolution problems in generalized standard materials. In particular, in [249, 250] the Authors focus on the time incremental step and augment the time-discrete relations by means of additional terms in order to let the corresponding nonlinear system be symmetric, hence the gradient of some potential energy. These additional terms turn out to be consistent in case of continuous temperature evolution. The incremental step is then solved by minimization. Our approach is completely different as we propose a variational frame making sense at both the continuous and the discrete level simultaneously.

## 5.2 Preliminaries

For a description of Souza-Auricchio model please see Chapter 3. Here below, only the choices and the relations relative to the full thermomechanically coupled version of the model proposed in the present Chapter will be reported.

### 5.2.1 Choice of $f$

As mentioned in Chapter 3, the value  $f(\theta)$  indicates the martensite-austenite transformation stress at temperature  $\theta$ . In particular,  $f = 0$  for low temperatures and  $f' = \beta > 0$  for large temperatures. The transition between these two regimes takes place in a neighborhood of the martensite-to-austenite transition temperature at zero stress  $\theta_{\text{tr}}$ . For the sake of definiteness, in the following we specifically choose the function

$$f(\theta) = \begin{cases} 0 & \text{for } \theta < \theta_{\text{tr}} - \rho \\ \frac{\beta}{4\rho}(\theta - (\theta_{\text{tr}} - \rho))^2 & \text{for } |\theta - \theta_{\text{tr}}| \leq \rho \\ \beta(\theta - \theta_{\text{tr}}) & \text{for } \theta > \theta_{\text{tr}} + \rho \end{cases} \quad (5.4)$$

being however intended that other choices would be possible.

Note that  $f$  is bounded, together with its first two derivatives. In particular, the upper bound of the second derivative is strictly needed for the thermodynamic consistency of the model. This forces the parameter  $\rho > 0$  to be not too small, see below. Indeed, for  $\rho \rightarrow 0$  one has that  $f(\theta) \rightarrow \beta(\theta - \theta_{\text{tr}})^+$  uniformly, which is not differentiable. Following the discussion in [166], we shall tacitly assume in all of the following the consistency condition

$$c - \theta f''(\theta)|e^{\text{tr}}| > 0. \quad (5.5)$$

This condition amounts to ensure that  $\partial_{\theta}s = -f''(\theta)|e^{\text{tr}}| + c/\theta > 0$  so that the effective heat capacity of the medium is positive.

Let us anticipate that, along the analysis, the introduction of a smooth truncation of  $f$  will be needed and additional constraints on the material parameters will be introduced, namely (5.31), (5.35), and (5.45). These constraints are aimed at ensuring the dissipativity of the system and are to be compared with analogous conditions from [166, 167]. Let us explicitly stress that these requirements are compatible with the experimentally observed material parameters, see Table 5.8.



### 5.2.2 Dissipation and flow rule

In order to describe the evolution of the medium we shall prescribe a (pseudo-)potential of *dissipation*  $D : \mathbb{R}_+ \times \mathbb{R}_{\text{dev}}^{3 \times 3} \rightarrow [0, \infty)$  of Von-Mises type, namely

$$D(\theta; \dot{\mathbf{e}}^{\text{tr}}) := \frac{R}{\theta} |\dot{\mathbf{e}}^{\text{tr}}|$$

where  $R > 0$  is an activation radius, measured in MPaK. The flow rule consists in the classical normality principle

$$\partial_{\dot{\mathbf{e}}^{\text{tr}}} D(\theta; \dot{\mathbf{e}}^{\text{tr}}) \ni \frac{\mathbf{X}}{\theta}. \quad (5.6)$$

Note that relation (5.6) can be equivalently expressed in the complementary form

$$F(\theta; \mathbf{X}) \leq 0, \quad \dot{\xi} \geq 0, \quad F(\theta; \mathbf{X}) \dot{\xi} = 0, \quad \dot{\mathbf{e}}^{\text{tr}} = \dot{\xi} \frac{\partial_{\mathbf{X}} F(\theta; \mathbf{X})}{|\partial_{\mathbf{X}} F(\theta; \mathbf{X})|}$$

where the yield function  $F$  is defined as

$$F(\theta; \mathbf{X}) := |\mathbf{X}| - \frac{R}{\theta}.$$

In particular,  $F$  is related to  $D$  via the duality formula

$$D(\theta; \dot{\mathbf{e}}^{\text{tr}}) = \sup\{\mathbf{X} : \dot{\mathbf{e}}^{\text{tr}} \mid F(\theta; \mathbf{X}) \leq 0\}.$$

By combining (3.6) with (5.6) we obtain the constitutive material relation equation

$$\partial_{\dot{\mathbf{e}}^{\text{tr}}} D(\theta; \dot{\mathbf{e}}^{\text{tr}}) + \partial_{\mathbf{e}^{\text{tr}}} \psi(\boldsymbol{\varepsilon}, \mathbf{e}^{\text{tr}}, \theta) \ni 0. \quad (5.7)$$

### 5.2.3 Momentum balance and energy conservation

Assume that the reference configuration of the body  $\Omega \subset \mathbb{R}^3$  is nonempty, open, connected, and has a Lipschitz continuous boundary  $\Gamma$ . We decompose the latter as  $\Gamma = \Gamma^{\text{D}} \cup \Gamma^{\text{N}} \cup \partial\Gamma$  where  $\Gamma^{\text{D}}$  and  $\Gamma^{\text{N}}$  are disjoint and relatively open in  $\Gamma$ ,  $\partial\Gamma$  is the boundary of both  $\Gamma^{\text{D}}$  and  $\Gamma^{\text{N}}$ , and  $\Gamma^{\text{D}}$  has positive surface measure. Given some final reference time  $T > 0$ , we shall be considering the quasistatic momentum balance

$$\nabla \cdot \boldsymbol{\sigma} + \mathbf{f} = \mathbf{0} \quad \text{in } \Omega \times (0, T) \quad (5.8)$$

to be combined with the boundary conditions

$$\boldsymbol{\sigma}\mathbf{n} = \mathbf{g} \quad \text{on } \Gamma^N \times (0, T), \quad \mathbf{u} = \mathbf{h} \quad \text{on } \Gamma^D \times (0, T). \quad (5.9)$$

Here,  $\mathbf{n}$  denotes the outward unit normal to  $\Gamma^N$  and  $\mathbf{f} : \Omega \times (0, T) \rightarrow \mathbb{R}^3$  and  $\mathbf{g} : \Gamma^N \times (0, T) \rightarrow \mathbb{R}^3$  are a body force and a surface traction, respectively, while  $\mathbf{h} : \Gamma^D \times (0, T) \rightarrow \mathbb{R}^3$  is a prescribed displacement.

The conservation of energy reads

$$\dot{u} + \nabla \cdot \mathbf{q} = \boldsymbol{\sigma} : \dot{\boldsymbol{\varepsilon}} \quad \text{in } \Omega \times (0, T) \quad (5.10)$$

where  $\mathbf{q}$  represents the heat flux. We shall complement the latter with the homogeneous Neumann boundary conditions

$$\mathbf{q} \cdot \mathbf{n} = 0 \quad \text{on } \Gamma \times (0, T).$$

Let us however anticipate that different boundary conditions of Robin type will be allowed in the space-homogeneous situation of Subsection 5.3.4.

#### 5.2.4 Full system

The thermomechanical evolution of the medium is described by the system of quasistatic equilibrium (5.8), energy conservation (5.10), and the constitutive material relation (5.7). Along with the current choices for the free energy  $\psi$  and the dissipation  $D$ , the form of the resulting differential system in terms of the variables  $(\mathbf{u}, \theta, \mathbf{e}^{\text{tr}})$  reads

$$\nabla \cdot \mathbb{C}(\boldsymbol{\varepsilon}(\mathbf{u}) - \mathbf{e}^{\text{tr}}) + \mathbf{f} = \mathbf{0}, \quad (5.11)$$

$$(c - \theta f''(\theta) |\mathbf{e}^{\text{tr}}|) \dot{\theta} + \nabla \cdot \mathbf{q} = R |\dot{\mathbf{e}}^{\text{tr}}| + \theta f'(\theta) |\mathbf{e}^{\text{tr}}|, \quad (5.12)$$

$$R \partial |\dot{\mathbf{e}}^{\text{tr}}| + H \mathbf{e}^{\text{tr}} + f(\theta) \partial |\mathbf{e}^{\text{tr}}| + \partial I(\mathbf{e}^{\text{tr}}) \ni 2G(\mathbf{e}(\mathbf{u}) - \mathbf{e}^{\text{tr}}), \quad (5.13)$$

where we recall that  $\mathbf{e}(\mathbf{u}) := \text{dev } \boldsymbol{\varepsilon}(\mathbf{u})$ . The thermomechanical coupling depends on the total martensitic content  $|\mathbf{e}^{\text{tr}}|$ . This reflects that the transformation from austenite to martensite is a second-order phase transition whereas the reorientation of martensitic variants is not associated with latent heat production.

### 5.2.5 Dissipativity

Let us explicitly comment on the thermodynamic consistency of the model by evaluating the entropy-release-rate density

$$r := \dot{s} + \nabla \cdot \mathbf{Q}$$

where  $\mathbf{Q} := \mathbf{q}/\theta$  is the entropy flux. Note preliminarily that energy conservation (5.10) can be equivalently rewritten as

$$\theta \dot{s} + \nabla \cdot \mathbf{q} = \mathbf{X} : \dot{\mathbf{e}}^{\text{tr}}. \quad (5.14)$$

Then, we use (5.14) and (5.6) in order to compute

$$\begin{aligned} r &\stackrel{(5.14)}{=} \frac{1}{\theta} \mathbf{X} : \dot{\mathbf{e}}^{\text{tr}} + \nabla \cdot \left( \frac{\mathbf{q}}{\theta} \right) - \frac{1}{\theta} \nabla \cdot \mathbf{q} = \frac{1}{\theta} \mathbf{X} : \dot{\mathbf{e}}^{\text{tr}} + \mathbf{q} \cdot \nabla \left( \frac{1}{\theta} \right) \\ &\stackrel{(5.6)}{=} \partial_{\dot{\mathbf{e}}^{\text{tr}}} D(\theta; \dot{\mathbf{e}}^{\text{tr}}) : \dot{\mathbf{e}}^{\text{tr}} + \mathbf{q} \cdot \nabla \left( \frac{1}{\theta} \right) = D(\theta; \dot{\mathbf{e}}^{\text{tr}}) + \mathbf{q} \cdot \nabla \left( \frac{1}{\theta} \right) \geq 0 \end{aligned}$$

where the inequality follows from the fact that  $D > 0$  whenever  $\mathbf{q} = \boldsymbol{\alpha}(1/\nabla\theta)$  with  $\boldsymbol{\alpha}$  monotone and  $\boldsymbol{\alpha}(\mathbf{0}) = \mathbf{0}$ . For the sake of definiteness we shall let  $\mathbf{q} = \kappa \nabla(1/\theta)$  for some conductivity  $\kappa \geq 0$ , this choice being particularly adapted to the present nonisothermal situation, see below. It is however intended that our discussion can be reproduced in greater generality. In particular, the classical Fourier law  $\mathbf{q} = -\kappa \nabla\theta$  (which actually corresponds to a linearization of  $\mathbf{q} = \kappa \nabla(1/\theta)$  around some reference temperature) can also be accommodated.

## 5.3 Gradient structures

We are now in the position of introducing the generalized-gradient-flow reformulation of the full thermomechanical evolution system presented in the previous section. This corresponds to relation (5.1) along with the choice  $\mathbf{y} = (\mathbf{e}^{\text{tr}}, \theta)$  and the definition of the total entropy

$$\mathcal{S}(\mathbf{y}) = \int_{\Omega} s(\mathbf{y}) dx = \int_{\Omega} (-f'(\theta)|\mathbf{e}^{\text{tr}}| + c \log \theta - c) dx$$

so that one has

$$\partial\mathcal{S}(\mathbf{y}) = \begin{pmatrix} -f'(\theta)\partial|\mathbf{e}^{\text{tr}}| \\ (c-\theta f''(\theta)|\mathbf{e}^{\text{tr}}|)/\theta \end{pmatrix}.$$

To obtain this variational formulation, we start by eliminating the mechanical variable  $\mathbf{u}$  by solving the equilibrium, for given transformation strain  $\mathbf{e}^{\text{tr}}$  and time  $t$ , see Subsection 5.3.1. This preliminary step is unavoidable as mechanical equilibrium follows from energy stationarity rather than from entropic effects. The gradient reformulation of resulting thermo-mechanical problem (5.11)+(5.13) then follows from the choice of the entropy-dissipation potential  $\mathcal{K}(t, \mathbf{y}; \cdot)$  fulfilling the structural assumption (5.2). By dualizing  $\mathcal{K}(t, \mathbf{y}; \cdot)$  with respect to the rates, one can equivalently express relation (5.1) as

$$\dot{\mathbf{y}} \in \partial_{\boldsymbol{\xi}} \mathcal{K}^*(t, \mathbf{y}; \partial\mathcal{S}(\mathbf{y})) \quad (5.15)$$

where the *dual-entropy-dissipation potential*  $\mathcal{K}^*(t, \mathbf{y}; \cdot)$  is a function of the thermodynamic force  $\boldsymbol{\xi} = \partial\mathcal{S}(\mathbf{y})$ .

We start by presenting a reformulation for the isothermal problem in Subsection 5.3.2. Then, we consider the general nonisothermal situation in Subsection 5.3.3. Finally, in Subsection 5.3.4 we tackle the special case of space-homogeneous fields as this is both often close to real applications and a clear benchmark for implementation.

### 5.3.1 Resolution of the quasistatic equilibrium

The first step in the direction of a variational reformulation of the system (5.11)-(5.13) consists in expressing  $\mathbf{u}$  in terms of  $\mathbf{e}^{\text{tr}}$  and external actions by solving the quasistatic mechanical equilibrium system. Indeed, for all  $\mathbf{e}^{\text{tr}} \in L^2(\Omega; \mathbb{R}_{\text{dev}}^{3 \times 3})$ ,  $\mathbf{f}(t) \in L^2(\Omega; \mathbb{R}^3)$ , and  $\mathbf{g}(t) \in L^2(\Gamma^{\text{tr}}; \mathbb{R}^3)$  one can find a unique  $\mathbf{u} \in \mathcal{U} := H^1(\Omega; \mathbb{R}^3)$  solving (5.8)-(5.9). We shall indicate such  $\mathbf{u}$  as  $\hat{\mathbf{u}}(t, \mathbf{e}^{\text{tr}})$ . Given  $(\mathbf{f}, \mathbf{g}) \in C([0, T], L^2(\Omega; \mathbb{R}^3) \times L^2(\Gamma^{\text{tr}}; \mathbb{R}^3))$ , the solution operator  $\hat{\mathbf{u}} : [0, T] \times L^2(\Omega; \mathbb{R}_{\text{sym}}^{3 \times 3}) \rightarrow \mathcal{U}$  is hence well-defined, linear in  $\mathbf{e}^{\text{tr}}$ , and continuous in  $(t, \mathbf{e}^{\text{tr}})$ , although nonlocal in space. The latter solution operator  $\hat{\mathbf{u}}$  will be systematically employed in the remainder of the chapter.

Note that by assuming  $\hat{\mathbf{u}}$  to be independent of time (that is,  $\mathbf{f}$ ,  $\mathbf{g}$ , and  $\mathbf{h}$  to be independent of time) we deduce that  $\boldsymbol{\varepsilon}(\hat{\mathbf{u}}(\mathbf{e}^{\text{tr}}))$  coincides with  $\mathbf{e}^{\text{tr}}$  up to a linear shift. In this case (which, strictly speaking, is the only one covered by the original GENERIC theory, which presently does not allow external actions) the evolution of the material is driven solely by

temperature relaxation.

### 5.3.2 Gradient structure of the isothermal problem

Let us firstly concentrate on the *isothermal* problem (5.11)+(5.13). This can be written in the general form (5.1) by defining  $\mathbf{y} = \mathbf{e}^{\text{tr}}$  and

$$\mathcal{K}^*(t, \mathbf{y}; \boldsymbol{\xi}) := \int_{\Omega} I_{R_Y/\theta}(\boldsymbol{\xi} - \mathbf{b}(t, \mathbf{y})) dx$$

where  $I_{R_Y/\theta}$  is the indicator function of the convex set  $\{\mathbf{a} \in \mathbb{R}_{\text{dev}}^{3 \times 3} : |\mathbf{a}| \leq R_Y/\theta\}$  and we used the short-hand notation

$$\mathbf{b}(t, \mathbf{y}) \in \frac{1}{\theta} (-2G(\mathbf{e}(\widehat{\mathbf{u}}(t, \mathbf{e}^{\text{tr}})) - \mathbf{e}^{\text{tr}}) + H\mathbf{e}^{\text{tr}} + (f(\theta) - \theta f'(\theta))\partial|\mathbf{e}^{\text{tr}}| + \partial I(\mathbf{e}^{\text{tr}}))$$

for the purely state-dependent nonlinear operator  $\mathbf{b}$ , which is continuous in time. The above-defined dual-entropy production potential  $\boldsymbol{\xi} \mapsto \mathcal{K}^*(t, \mathbf{y}; \boldsymbol{\xi})$  is clearly convex. By computing its dual we get

$$\mathcal{K}(t, \mathbf{y}; \dot{\mathbf{y}}) = \int_{\Omega} \frac{R_Y}{\theta} |\dot{\mathbf{e}}^{\text{tr}}| dx + \int_{\Omega} \mathbf{b}(t, \mathbf{y}) : \dot{\mathbf{e}}^{\text{tr}} dx$$

which obviously fulfills the convexity assumption (5.2).

The above choices for  $\mathcal{S}$  and  $\mathcal{K}$  entail a reformulation of the isothermal evolution in terms of (5.1). Note nonetheless that the isothermal case can be also classically formulated as the gradient flow in the variables  $(\mathbf{u}, \mathbf{e}^{\text{tr}})$  of the complementary energy

$$\begin{aligned} \Psi(t; \mathbf{u}, \mathbf{e}^{\text{tr}}) := & \int_{\Omega} \left( \frac{1}{2} (\boldsymbol{\varepsilon}(\mathbf{u}) - \mathbf{e}^{\text{tr}}) : \mathbb{C}(\boldsymbol{\varepsilon}(\mathbf{u}) - \mathbf{e}^{\text{tr}}) + \frac{H}{2} |\mathbf{e}^{\text{tr}}|^2 + f(\theta) |\mathbf{e}^{\text{tr}}| + I(\mathbf{e}^{\text{tr}}) \right) dx \\ & - \int_{\Omega} \mathbf{f}(t) \cdot \mathbf{u} dx - \int_{\Gamma^{\text{tr}}} \mathbf{g}(t) \cdot \mathbf{u} d\Gamma \end{aligned}$$

subject to the Von Mises dissipative potential

$$\mathcal{D}(\dot{\mathbf{u}}, \dot{\mathbf{e}}^{\text{tr}}) := R_Y |\dot{\mathbf{e}}^{\text{tr}}|.$$

Indeed, the system (5.11)+(5.13) (along with boundary conditions) corresponds to the

relation

$$\partial\mathcal{D}(\dot{\mathbf{u}}, \dot{\mathbf{e}}^{\text{tr}}) + \partial\Psi(t; \mathbf{u}, \mathbf{e}^{\text{tr}}) \ni 0$$

which is indeed formally close to (5.1). By solving for  $\mathbf{u} = \widehat{\mathbf{u}}(t, \mathbf{e}^{\text{tr}})$  one can additionally reformulate the latter in the sole variable  $\mathbf{e}^{\text{tr}}$  (and time) as

$$\partial R_Y |\dot{\mathbf{e}}^{\text{tr}}| + \partial_{\mathbf{e}^{\text{tr}}} \Psi(t; \widehat{\mathbf{u}}(t, \mathbf{e}^{\text{tr}}), \mathbf{e}^{\text{tr}}) \ni 0.$$

Note that the latter equation, although local in space and time, features the nonlocal-in-space operator  $\widehat{\mathbf{u}}$ .

### 5.3.3 Gradient structure in the general case

In the general nonisothermal case we can follow [212, Sec. 3.4] and recast the evolution problem in the form of (5.15) by letting the dual entropy-production potential be defined by

$$\mathcal{K}^*(t, \mathbf{y}; \boldsymbol{\xi}) = \int_{\Omega} I_{R_Y/\theta}(\boldsymbol{\xi}_1 - \mathbf{a}(t, \mathbf{y})\xi_2) dx + \int_{\Omega} \frac{\kappa}{2} \left| \frac{\nabla \xi_2}{\gamma(\mathbf{y})} \right|^2 dx \quad (5.16)$$

for  $\boldsymbol{\xi} = (\boldsymbol{\xi}_1, \xi_2) \in L^2(\Omega; \mathbb{R}_{\text{sym}}^{3 \times 3}) \times L^2(\Omega)$  where we have denoted by

$$\begin{aligned} \gamma(\mathbf{y}) &:= c - \theta f''(\theta) |\mathbf{e}^{\text{tr}}| \\ \mathbf{a}(t, \mathbf{y}) &\in \frac{1}{\gamma(\mathbf{y})} (-2G(\mathbf{e}(\widehat{\mathbf{u}}(t, \mathbf{e}^{\text{tr}})) - \mathbf{e}^{\text{tr}}) + H\mathbf{e}^{\text{tr}} + (f(\theta) - \theta f'(\theta)) \partial |\mathbf{e}^{\text{tr}}| + \partial I(\mathbf{e}^{\text{tr}})) \end{aligned}$$

In this case, we can compute

$$\partial_{\boldsymbol{\xi}} \mathcal{K}^*(t, \mathbf{y}; \boldsymbol{\xi}) \supset \begin{pmatrix} \partial I_{R_Y/\theta}(\boldsymbol{\xi}_1 - \mathbf{a}(t, \mathbf{y})\xi_2) \\ -\partial I_{R_Y/\theta}(\boldsymbol{\xi}_1 - \mathbf{a}(t, \mathbf{y})\xi_2) : \mathbf{a}(t, \mathbf{y}) - \frac{\kappa}{(\gamma(\mathbf{y}))^2} \Delta \xi_2 \end{pmatrix}$$

so that, by substituting

$$\boldsymbol{\xi} \in \partial \mathcal{S}(\mathbf{y}) = \begin{pmatrix} -f'(\theta) \partial |\mathbf{e}^{\text{tr}}| \\ \frac{\gamma(\mathbf{y})}{\theta} \end{pmatrix}$$

one gets

$$\partial_{\xi} \mathcal{K}^*(t, \mathbf{y}; \partial \mathcal{S}(\mathbf{y})) \supset \left( \begin{array}{c} \partial I_{R_Y/\theta} \left( -f'(\theta) \partial |\mathbf{e}^{\text{tr}}| - \mathbf{a}(t, \mathbf{y}) \frac{\gamma(\mathbf{y})}{\theta} \right) \\ -\partial I_{R_Y/\theta} \left( -f'(\theta) \partial |\mathbf{e}^{\text{tr}}| - \mathbf{a}(t, \mathbf{y}) \frac{\gamma(\mathbf{y})}{\theta} \right) : \mathbf{a}(t, \mathbf{y}) - \frac{\kappa}{\gamma(\mathbf{y})} \Delta \left( \frac{1}{\theta} \right) \end{array} \right).$$

By using the above-introduced expressions for  $\mathbf{a}$  and  $\gamma$  one obtains that the argument of the subdifferential  $\partial I_{R_Y/\theta}$  is nothing but  $-\mathbf{X}/\theta$  so that (5.15) reads

$$\begin{pmatrix} \dot{\mathbf{e}}^{\text{tr}} \\ \dot{\theta} \end{pmatrix} \in \left( \begin{array}{c} \partial I_{R_Y/\theta} (\mathbf{X}/\theta) \\ -\partial I_{R_Y/\theta} (\mathbf{X}/\theta) : \mathbf{a}(t, \mathbf{y}) - \frac{\kappa}{\gamma(\mathbf{y})} \Delta \left( \frac{1}{\theta} \right) \end{array} \right)$$

corresponding indeed to relations (5.12)-(5.13).

By computing the dual of  $\mathcal{K}^*(t, \mathbf{y}; \cdot)$  one obtains the entropy-production potential

$$\mathcal{K}(t, \mathbf{y}; \dot{\mathbf{y}}) = \int_{\Omega} \frac{R_Y}{\theta} |\dot{\mathbf{e}}^{\text{tr}}| dx + \frac{1}{2\kappa} \|\gamma(\mathbf{y})(\dot{\theta} + \mathbf{a}(t, \mathbf{y}) : \dot{\mathbf{e}}^{\text{tr}})\|_{H_{\text{av}}^{-1}}^2 \quad (5.17)$$

featuring the norm

$$\|v\|_{H_{\text{av}}^{-1}}^2 := \int_{\Omega} |\nabla(-\Delta^{-1}v)|^2 dx = \int_{\Omega} |\nabla w|^2 dx.$$

Here,  $w$  is the unique solution in

$$H_{\text{av}}^1 := \left\{ w \in H^1(\Omega) : \int_{\Omega} w dx = 0 \right\}$$

of  $-\Delta w = v$  for

$$v \in H_{\text{av}}^{-1} := \{v \in H^{-1}(\Omega) : \langle v, 1 \rangle = 0\}$$

where  $\langle \cdot, \cdot \rangle$  stands for the duality pairing between  $H^{-1}(\Omega)$  and  $H^1(\Omega)$ . Note that  $\mathcal{K}(t, \mathbf{y}, \cdot)$  fulfills the general structural assumption (5.2).

We hence compute

$$\partial_{\dot{\mathbf{y}}} \mathcal{K}(t, \mathbf{y}; \dot{\mathbf{y}}) \supset \left( \begin{array}{c} \frac{R_Y}{\theta} \partial |\dot{\mathbf{e}}^{\text{tr}}| + \frac{\gamma(\mathbf{y})}{\kappa} (-\Delta^{-1})(\gamma(\mathbf{y})(\dot{\theta} + \mathbf{a}(t, \mathbf{y}) : \dot{\mathbf{e}}^{\text{tr}})) \mathbf{a}(t, \mathbf{y}) \\ \frac{\gamma(\mathbf{y})}{\kappa} (-\Delta^{-1})(\gamma(\mathbf{y})(\dot{\theta} + \mathbf{a}(t, \mathbf{y}) : \dot{\mathbf{e}}^{\text{tr}})) \end{array} \right).$$

By substituting  $\partial\mathcal{S}(\mathbf{y})$  into (5.1) we obtain

$$\left( \begin{array}{c} \frac{R_Y}{\theta} \partial|\dot{\mathbf{e}}^{\text{tr}}| + \frac{\gamma(\mathbf{y})}{\kappa} (-\Delta^{-1})(\gamma(\mathbf{y})(\dot{\theta} + \mathbf{a}(t, \mathbf{y}) : \dot{\mathbf{e}}^{\text{tr}})) \mathbf{a}(t, \mathbf{y}) \\ \frac{\gamma(\mathbf{y})}{\kappa} (-\Delta^{-1})(\gamma(\mathbf{y})(\dot{\theta} + \mathbf{a}(t, \mathbf{y}) : \dot{\mathbf{e}}^{\text{tr}})) \end{array} \right) - \left( \begin{array}{c} -f'(\theta) \partial|\mathbf{e}^{\text{tr}}| \\ \frac{\gamma(\mathbf{y})}{\theta} \end{array} \right) \ni \begin{pmatrix} \mathbf{0} \\ 0 \end{pmatrix}$$

and relations (5.12)-(5.13) follow from the actual choices of  $\mathbf{a}$  and  $\gamma$ . Note that the argument of the  $H^{-1}$ -norm above is required to have zero mean. Given the equation for  $\theta$ , this amounts to say that  $\mathbf{q} = \kappa \nabla(1/\theta)$  has no flux through the boundary  $\Gamma$ . Namely, the body is assumed to be thermally insulated from the exterior.

### 5.3.4 Gradient structures for space-homogeneous fields

We shall be here concerned with some specific degenerate case in which the energy conservation equation (5.12) can be actually reduced to an ordinary differential relation. In particular, we assume that the temperature is constant in space. This can be regarded as a sensible approximation in many applicative instances, especially in connection with relatively thin structures activated at low frequencies. The advantage of this approximation is that the energy conservation equation (5.12) is pointwise in space and time. In particular, by dropping the differential term in (5.12) one gets

$$(c - \theta f''(\theta) |\mathbf{e}^{\text{tr}}|) \dot{\theta} = R_Y |\dot{\mathbf{e}}^{\text{tr}}| + \theta f'(\theta) |\mathbf{e}^{\text{tr}}|. \quad (5.18)$$

which can be seen as the entropy gradient flow driven by the entropy-production potential

$$\mathcal{K}(t, \mathbf{y}; \dot{\mathbf{y}}) = \begin{cases} \int_{\Omega} \frac{R_Y}{\theta} |\dot{\mathbf{e}}^{\text{tr}}| dx & \text{if } \gamma(\mathbf{y})(\dot{\theta} + \mathbf{a}(t, \mathbf{y}) : \dot{\mathbf{e}}^{\text{tr}}) = 0, \\ \infty & \text{otherwise.} \end{cases}$$

Note that this choice of  $\mathcal{K}$  formally corresponds to the limit as  $\kappa \rightarrow 0$  in (5.17). In particular, it translates at the variational level the situation where the term  $\kappa \Delta(1/\theta)$  in (5.12) is dropped by letting  $\kappa \rightarrow 0$ . The reduced energy-conservation relation (5.12) reads in this case

$$\gamma(\mathbf{y})(\dot{\theta} + \mathbf{a}(t, \mathbf{y}) : \dot{\mathbf{e}}^{\text{tr}}) = 0$$

and is directly enforced as a constraint in the definition of  $\mathcal{K}$ .



One can extend the above discussion by including a relaxation dynamics for the temperature. Indeed, by replacing  $\kappa\Delta(1/\theta)$  by  $-\lambda/\theta$  in (5.12) one gets

$$(c - \theta f''(\theta) |\mathbf{e}^{\text{tr}}|) \dot{\theta} - \frac{\lambda}{\theta} = R_Y |\dot{\mathbf{e}}^{\text{tr}}| + \theta f'(\theta) |\mathbf{e}^{\text{tr}}|. \quad (5.19)$$

corresponding indeed to a viscous flow. Note that this approximation can be made rigorous by assuming all fields to be space-homogeneous and integrating (5.12) in space with the aid of the Robin-type boundary condition

$$\mathbf{q} \cdot \mathbf{n} = -\frac{\widehat{\lambda}}{\theta}$$

where  $\widehat{\lambda} = \lambda|\Omega|/|\Gamma|$ , being  $|\Gamma|$  and  $|\Omega|$  the measures of  $\Gamma$  and  $\Omega$ , respectively. This case corresponds to the gradient flow of the entropy driven by the dual-entropy-production potential (compare with (5.16))

$$\mathcal{K}^*(t, \mathbf{y}; \boldsymbol{\xi}) = \int_{\Omega} I_{R_Y/\theta}(\boldsymbol{\xi}_1 - \mathbf{a}(t, \mathbf{y})\boldsymbol{\xi}_2) dx + \int_{\Omega} \frac{\lambda}{2} \left| \frac{\boldsymbol{\xi}_2}{\gamma(\mathbf{y})} \right|^2 dx \quad (5.20)$$

and, correspondingly, the entropy-production potential

$$\mathcal{K}(t, \mathbf{y}; \dot{\mathbf{y}}) = \int_{\Omega} \frac{R_Y}{\theta} |\dot{\mathbf{e}}^{\text{tr}}| dx + \int_{\Omega} \frac{1}{2\lambda} |\gamma(\mathbf{y})(\dot{\theta} + \mathbf{a}(t, \mathbf{y}) : \dot{\mathbf{e}}^{\text{tr}})|^2 dx. \quad (5.21)$$

Note that the above entropy potential features no differentiation terms with respect to space and fulfills the structural assumption (5.2).

We are in the position of generalizing the choice of the boundary condition even further and let the system adapt to some given external temperature. In particular, this amounts in asking for

$$\mathbf{q} \cdot \mathbf{n} = \widehat{\lambda} \left( \frac{1}{\theta^e(t)} - \frac{1}{\theta} \right)$$

for some possibly time-dependent external temperature  $t \mapsto \theta^e(t) > 0$ . By assuming space-homogeneity, one replaces (5.12) with the ordinary differential equation

$$(c - \theta f''(\theta) |\mathbf{e}^{\text{tr}}|) \dot{\theta} + \lambda \left( \frac{1}{\theta^e(t)} - \frac{1}{\theta} \right) = R_Y |\dot{\mathbf{e}}^{\text{tr}}| + \theta f'(\theta) |\mathbf{e}^{\text{tr}}|. \quad (5.22)$$

Then, the system (5.13)+(5.22) corresponds to the choice

$$\mathcal{K}^*(t, \mathbf{y}; \boldsymbol{\xi}) = I_{R_Y/\theta}(\xi_1 - \mathbf{a}\xi_2) + \frac{\widehat{\lambda}}{2} \left| \frac{\xi_2}{\gamma(\mathbf{y})} - \frac{1}{\theta_e(t)} \right|^2 + \frac{1}{\theta_e(t)} \left( \frac{\xi_2}{\gamma(\mathbf{y})} - \frac{1}{\theta_e(t)} \right).$$

By duality we obtain the time-dependent entropy-production potential

$$\mathcal{K}(t, \mathbf{y}, \dot{\mathbf{y}}) = \frac{R_Y}{\theta} |\dot{\mathbf{e}}^{\text{tr}}| + \frac{1}{2\widehat{\lambda}} |\gamma(\mathbf{y})(\dot{\theta} + \mathbf{a}(t, \mathbf{y}) : \dot{\mathbf{e}}^{\text{tr}})|^2 + \frac{\gamma(\mathbf{y})}{\theta_e(t)} (\dot{\theta} + \mathbf{a}(t, \mathbf{y}) : \dot{\mathbf{e}}^{\text{tr}})$$

which again fulfills the basic assumption (5.2). By computing (5.1) in this case one obtains in particular (5.22). One has to mention that the corresponding system cannot be regarded to be closed, as the external temperature  $\theta^e$  provides an entropic source.

## 5.4 Time discretization

As observed in the Introduction, the generalized gradient system (5.1) is dissipative, as the corresponding entropy increases along trajectories. By designing a numerical method for nonisothermal evolution one is interested in reproducing dissipativity at the discrete level. This can be done by addressing discrete schemes which are adapted to the variational structure of (5.1). The aim of this section is to present some ideas as well as a concrete example of a time-discrete scheme within this class. We shall detail here the analysis of the scheme and postpone algorithmical considerations and numerical tests to the forthcoming Section 5.6.

Let a time-partition  $\{0 = t_0 < t_1 < \dots < t_N = T_{\text{final}}\}$  be given and define  $\tau_i = t_i - t_{i-1}$ . Starting from some given initial value  $\mathbf{y}^0$ , by replacing the time derivative  $\dot{\mathbf{y}}$  by the differential quotient  $(\mathbf{y}_i - \mathbf{y}_{i-1})/\tau_i$  in (5.1) (equivalently in (5.15)) one is left with the subsequent solution of the systems

$$\partial_{\dot{\mathbf{y}}} \mathcal{K} \left( t_i, \mathbf{y}_\star; \frac{\mathbf{y}_i - \mathbf{y}_{i-1}}{\tau_i} \right) - \partial \mathcal{S}(\mathbf{y}_i) \ni \mathbf{0} \quad \text{for } i = 1, \dots, N. \quad (5.23)$$

The symbol  $\mathbf{y}_\star$  in the above relation is a place-holder for either  $\mathbf{y}_\star = \mathbf{y}_i$  (implicit) or  $\mathbf{y}_\star = \mathbf{y}_{i-1}$  (explicit). More generally, the choice whether the state-dependence is implicit or explicit can be made independently in *each* occurrence of  $\mathbf{y}_\star$  in  $\mathcal{K}$ . An example of this situation is in Subsection 5.5 below.

The dissipative character of the scheme can be readily checked in case  $\mathcal{S}$  is concave. Indeed, one tests on  $\mathbf{y}_i - \mathbf{y}_{i-1}$  and exploits the concavity of  $\mathcal{S}$  in order to get that

$$\begin{aligned} \mathcal{S}(\mathbf{y}_i) - \mathcal{S}(\mathbf{y}_{i-1}) &\geq (\partial \mathcal{S}(\mathbf{y}_i), \mathbf{y}_i - \mathbf{y}_{i-1}) = \left( \partial_{\mathbf{y}} \mathcal{K} \left( t_i, \mathbf{y}_\star; \frac{\mathbf{y}_i - \mathbf{y}_{i-1}}{\tau_i} \right), \mathbf{y}_i - \mathbf{y}_{i-1} \right) \\ &\geq \tau_i \mathcal{K} \left( t_i, \mathbf{y}_\star; \frac{\mathbf{y}_i - \mathbf{y}_{i-1}}{\tau_i} \right) - \tau_i \mathcal{K} (t_i, \mathbf{y}_\star; \mathbf{0}) \stackrel{(5.2)}{=} \tau_i \mathcal{K} \left( t_i, \mathbf{y}_\star; \frac{\mathbf{y}_i - \mathbf{y}_{i-1}}{\tau_i} \right). \end{aligned} \quad (5.24)$$

In particular, by taking the sum in the latter for  $i = 1, \dots, m \leq N$  we have that

$$\mathcal{S}(\mathbf{y}_m) \geq \sum_{i=1}^m \tau_i \mathcal{K} \left( t_i, \mathbf{y}_\star; \frac{\mathbf{y}_i - \mathbf{y}_{i-1}}{\tau_i} \right) + \mathcal{S}(\mathbf{y}_0)$$

where we have not only checked the monotonicity of the entropy but also provided a lower bound to the entropy production by means of the above sum.

In case the dependence of the entropy-production potential  $\mathcal{K}$  on  $\mathbf{y}_\star$  is explicit, one can coordinate to (5.23) a system of incremental minimization problems, namely

$$\mathbf{y}_i \in \text{Arg min}_{\mathbf{y}} \left( \tau_i \mathcal{K} \left( t_i, \mathbf{y}_{i-1}; \frac{\mathbf{y} - \mathbf{y}_{i-1}}{\tau_i} \right) - \mathcal{S}(\mathbf{y}) \right) \quad \text{for } i = 1, \dots, N.$$

In this case, relation (5.24) is a direct consequence of minimality

$$\begin{aligned} &\tau_i \mathcal{K} \left( t_i, \mathbf{y}_{i-1}; \frac{\mathbf{y}_i - \mathbf{y}_{i-1}}{\tau_i} \right) - \mathcal{S}(\mathbf{y}_i) \\ &\leq \tau_i \mathcal{K} \left( t_i, \mathbf{y}_{i-1}; \frac{\mathbf{y}_{i-1} - \mathbf{y}_{i-1}}{\tau_i} \right) - \mathcal{S}(\mathbf{y}_{i-1}) \stackrel{(5.2)}{\leq} -\mathcal{S}(\mathbf{y}_{i-1}) \end{aligned} \quad (5.25)$$

and no concavity of  $\mathcal{S}$  is required.

## 5.5 Semi-implicit scheme for the space-homogeneous case

The gradient flow structure of the model may be used to derive and analyze some dissipative numerical scheme. We shall detail this possibility by focusing here on the space-

homogeneous case of relations (5.22)+(5.13), which equivalently read

$$\gamma(\mathbf{y}) \left( \dot{\theta} + \mathbf{a}(t, \mathbf{y}) : \dot{\mathbf{e}}^{\text{tr}} \right) + \lambda \left( \frac{1}{\theta_{\text{ext}}(t)} - \frac{1}{\theta} \right) = 0, \quad (5.26)$$

$$\frac{R_Y}{\theta} \partial |\dot{\mathbf{e}}^{\text{tr}}| + \frac{\gamma(\mathbf{y})}{\theta} \mathbf{a}(t, \mathbf{y}) + f'(\theta) \partial |\mathbf{e}^{\text{tr}}| \ni 0 \quad (5.27)$$

where we recall that

$$\begin{aligned} \gamma(\mathbf{y}) &= c - \theta f''(\theta) |\mathbf{e}^{\text{tr}}| \\ \mathbf{a}(t, \mathbf{y}) &\in \frac{1}{\gamma(\mathbf{y})} \left( -2G(\mathbf{e}(\widehat{\mathbf{u}}(t, \mathbf{e}^{\text{tr}})) - \mathbf{e}^{\text{tr}}) + H\mathbf{e}^{\text{tr}} + (f(\theta) - \theta f'(\theta)) \partial |\mathbf{e}^{\text{tr}}| + \partial I(\mathbf{e}^{\text{tr}}) \right). \end{aligned}$$

This approximation of the original system, indeed justified for space-homogeneous fields, bears a particular interest as it is space-localized and even rate-independent, for  $\lambda = 0$ . We hence believe this to be a relevant test case. PDE couplings will be investigated in a forthcoming paper.

We are interested in a semi-implicit time-discretization scheme. Let a time-partition  $\{0 = t_0 < t_1 < \dots < t_N = T\}$  be given and define the possibly variable time step  $\tau_i = t_i - t_{i-1}$ . We focus here on the strain- and external-temperature-driven setting. In particular, we assume to be given  $t \in [0, T] \mapsto \mathbf{e}(t) := \text{dev } \boldsymbol{\varepsilon}(\mathbf{u}(t)) \in \mathbb{R}_{\text{dev}}^{3 \times 3}$  and  $t \in [0, T] \mapsto \theta^e(t) > 0$  and a suitable initial conditions on  $\mathbf{e}_0^{\text{tr}} \in \mathbb{R}_{\text{dev}}^{3 \times 3}$  and  $\theta_0 > 0$ , and we are interested in the time-discrete scheme

$$\gamma_\eta(\mathbf{y}_{i-1}) \left( \frac{\theta_i - \theta_{i-1}}{\tau_i} + \mathbf{a}_\eta(t_i, \mathbf{y}_i) : \frac{\mathbf{e}_i^{\text{tr}} - \mathbf{e}_{i-1}^{\text{tr}}}{\tau_i} \right) + \tau_i \lambda \left( \frac{1}{\theta^e(t_i)} - \frac{1}{\theta_i} \right) = 0, \quad (5.28)$$

$$\frac{R_Y}{\theta_i} \partial |\mathbf{e}_i^{\text{tr}} - \mathbf{e}_{i-1}^{\text{tr}}| + \frac{\gamma_\eta(\mathbf{y}_{i-1})}{\theta_i} \mathbf{a}_\eta(t_i, \mathbf{y}_i) + f'_*(\theta_i) \partial |\mathbf{e}_i^{\text{tr}}|_\eta \ni 0, \quad (5.29)$$

where the state dependence is explicit in  $\gamma$  and implicit everywhere else. The variational structure of (5.26)-(5.27) is indeed reflected in this choice, as all occurrences of  $\gamma$  are likewise discretized. Additionally, for the purpose of presenting a complete theoretical analysis of the scheme, we are forced to perform a regularization of the thermomechanical coupling term  $f(\theta) |\mathbf{e}^{\text{tr}}|$  by  $f_*(\theta) |\mathbf{e}^{\text{tr}}|_\eta$ . Here,

$$|\mathbf{e}^{\text{tr}}|_\eta := \min \left\{ \frac{|\mathbf{e}^{\text{tr}}|^2}{2\eta} + \frac{\eta}{2}, |\mathbf{e}^{\text{tr}}| \right\}$$

where  $\eta > 0$  is a small user-defined parameter (the modification  $f^*$  of  $f$  is described below). By reflecting the variational structure of the problem, this regularization entails modifications on the terms  $\gamma$  and  $\mathbf{a}$  as follows

$$\begin{aligned}\gamma_\eta(\mathbf{y}) &:= c - \theta f_*''(\theta) |\mathbf{e}^{\text{tr}}|_\eta \\ \mathbf{a}_\eta(t, \mathbf{y}) &\in \frac{1}{\gamma(\mathbf{y})} (-2G(\mathbf{e}(t) - \mathbf{e}^{\text{tr}}) + H\mathbf{e}^{\text{tr}} + (f_*(\theta) - \theta f_*'(\theta)) \partial |\mathbf{e}^{\text{tr}}|_\eta + \partial I(\mathbf{e}^{\text{tr}})).\end{aligned}$$

The purpose of the regularization is to ensure that

$$\partial |\mathbf{e}^{\text{tr}}|_\eta = (\eta \mathbf{1}_2 + \partial I)^{-1}(\mathbf{e}^{\text{tr}}) \quad (5.30)$$

is Lipschitz continuous of constant  $1/\eta$ , which turns out crucial for proving the convergence of the numerical scheme. Note that  $|\partial |\mathbf{e}^{\text{tr}}|_\eta| \leq 1$  for all  $\mathbf{e}^{\text{tr}} \in \mathbb{R}_{\text{dev}}^{3 \times 3}$ . On the other hand, let us mention that the modification is performed *at the functional level*, namely without perturbing the variational structure of the problem. We shall also mention that analogous regularizations have been already considered for this problem [23, 217, 214] and proved to be consistent with their limit  $\eta \rightarrow 0$  and that the numerical scheme performs well in the case  $\eta = 0$ , despite the absence of a complete analysis. We collect some comment in this direction in Section 5.6 below.

As for the modified function  $f_*$  we simply prescribe a monotone smooth truncation so that  $f_* \equiv f$  for  $\theta \leq \theta_* - 2\rho$ ,  $f_*' = 0$  for  $\theta \geq \theta_*$ , and  $\|f_*'\|_{L^\infty} := \sup_{\theta > 0} |f_*'(\theta)| \leq \beta$ , and  $\|f_*''\|_{L^\infty} \leq \beta/(2\rho)$  so that (5.31) holds. In particular,  $\theta_* > 0$  is some prescribed maximal temperature. This modification with respect to the original  $f$  is essentially immaterial with respect to applications, for it suffices to choose  $\theta_*$  larger than the experimentally observed and computationally simulated temperatures. The temperature upper bound, combined with a compatibility assumption on the parameter, see (5.45) below, ensures that the overall behavior of the system remains dissipative under cyclic testing. In the context of the Souza-Auricchio model a similar although weaker assumption has been advanced in [166]. The situation was there simpler as the constitutive relation of the material was taken to be scalar and an order method could be used.

We shall prove that the system (5.28)-(5.29) admits a solution for all  $i$ . This will be done in Subsection 5.5.3 by means of a fixed point argument based on the iterative solution of (5.28) and (5.29). In order to prepare for this, we discuss separately the mechanical and

the thermal subproblems in Subsections 5.5.1 and 5.5.2, respectively. As mentioned in the Introduction, some first requirement for this to hold is that the effective heat capacity of the system is positive. This amounts to ask for

$$0 < \gamma_0 := \inf_{\theta > 0} (c - \theta f''_*(\theta)) \quad (5.31)$$

which indeed follows with our actual choice of parameters, see Table 5.8.

### 5.5.1 Mechanical subproblem

Relation (5.29) can be rewritten as

$$R_Y \partial |e_i^{\text{tr}} - e_{i-1}^{\text{tr}}| + (H+2G)e_i^{\text{tr}} + f_*(\theta_i) \partial |e_i^{\text{tr}}|_\eta + \partial I(e_i^{\text{tr}}) \ni 2Ge_i. \quad (5.32)$$

For all given  $e_{i-1}^{\text{tr}} \in \mathbb{R}_{\text{dev}}^{3 \times 3}$ ,  $\theta_i > 0$ , and  $e_i := e(t_i)$ , relation (5.32) admits a unique solution  $e_i^{\text{tr}} \in \mathbb{R}_{\text{dev}}^{3 \times 3}$ . Indeed,  $e_i^{\text{tr}}$  is the unique minimizer of the uniformly convex functional

$$e^{\text{tr}} \mapsto R_Y |e^{\text{tr}} - e_{i-1}^{\text{tr}}| + \frac{1}{2}(H+2G)|e^{\text{tr}}|^2 + f_*(\theta_i)|e^{\text{tr}}|_\eta + I(e^{\text{tr}}) - 2Ge_i : e^{\text{tr}}.$$

Take now two different pairs of data  $(e_i^1, \theta_1)$  and  $(e_i^2, \theta_2)$  and let  $e_i^{\text{tr},1}$  and  $e_i^{\text{tr},2}$  be the corresponding solutions to (5.32). By taking the difference of the respective equations, testing on  $e_i^{\text{tr},1} - e_i^{\text{tr},2}$ , and exploiting monotonicity we obtain that

$$\begin{aligned} (H+2G)|e_i^{\text{tr},1} - e_i^{\text{tr},2}|^2 &\leq 2G(e_i^1 - e_i^2) : (e_i^{\text{tr},1} - e_i^{\text{tr},2}) + (f_*(\theta_1) - f_*(\theta_2)) \partial |e_i^{\text{tr},2}|_\eta : (e_i^{\text{tr},1} - e_i^{\text{tr},2}) \\ &\leq (2G|e_i^1 - e_i^2| + \beta|\theta_1 - \theta_2|) |e_i^{\text{tr},1} - e_i^{\text{tr},2}|. \end{aligned}$$

Hence, we have checked the Lipschitz continuity

$$|e_i^{\text{tr},1} - e_i^{\text{tr},2}| \leq \frac{2G}{H+2G} |e_i^1 - e_i^2| + \frac{\beta}{H+2G} |\theta_1 - \theta_2|. \quad (5.33)$$

Note that the well-posedness of (5.32) is indeed independent of the regularization  $\eta$  as well as of the truncation  $f_*$  and would hold also in absence of such modifications.

### 5.5.2 Thermal subproblem

Assume now to be given  $\theta_{i-1} > 0$ ,  $\theta_i^e := \theta^e(t_i) > 0$ , and  $\mathbf{e}_i^{\text{tr}} \in \mathbb{R}_{\text{dev}}^{3 \times 3}$ . Equation (5.28) can be equivalently rewritten as

$$\begin{aligned} \gamma_\eta(\mathbf{y}_{i-1})\theta_i - \frac{\tau_i \lambda}{\theta_i} &= -\frac{\tau_i \lambda}{\theta_i^e} + \gamma_\eta(\mathbf{y}_{i-1})\theta_{i-1} \\ &+ R_Y |\mathbf{e}_i^{\text{tr}} - \mathbf{e}_{i-1}^{\text{tr}}| + \theta_i f'_*(\theta_i) \partial |\mathbf{e}_i^{\text{tr}}|_\eta (\mathbf{e}_i^{\text{tr}} - \mathbf{e}_{i-1}^{\text{tr}}). \end{aligned} \quad (5.34)$$

As the map  $\theta \in \mathbb{R}_+ \mapsto \gamma_\eta(\mathbf{y}_{i-1})\theta - \lambda/\theta$  is injective and onto  $\mathbb{R}$ , for all  $\tilde{\theta}$  we can find a unique solution  $\theta_i > 0$  to the above equation where the term  $\theta_i f'_*(\theta_i)$  in the right-hand side is replaced by  $\tilde{\theta} f'_*(\tilde{\theta})$ . This defines a map  $\tilde{\theta} \mapsto \theta_i$  which can be proved to be a contraction under the condition

$$\phi_0 := \sup_\theta |f'_*(\theta) - \theta f''_*(\theta)| < \frac{\gamma_0}{2\epsilon_L}. \quad (5.35)$$

Indeed, assume to be given  $\tilde{\theta}^1$  and  $\tilde{\theta}^2$  and the corresponding solutions  $\theta_i^1$  and  $\theta_i^2$ . Take the difference between equation (5.34) written for  $\theta_i^1$  and the same equation for  $\theta_i^2$  and test it on  $\theta_i^1 - \theta_i^2$  in order to get that

$$\begin{aligned} \gamma_\eta(\mathbf{y}_{i-1})|\theta_i^1 - \theta_i^2|^2 &\leq |\tilde{\theta}^1 f'_*(\tilde{\theta}^1) - \tilde{\theta}^2 f'_*(\tilde{\theta}^2)| |\mathbf{e}_i^{\text{tr}} - \mathbf{e}_{i-1}^{\text{tr}}| |\theta_i^1 - \theta_i^2| \\ &\leq 2\epsilon_L \sup_\theta (f'_*(\theta) - \theta f''_*(\theta)) |\tilde{\theta}^1 - \tilde{\theta}^2| |\theta_i^1 - \theta_i^2|. \end{aligned}$$

Also by using (5.31), we deduce the Lipschitz continuity bound

$$|\theta_i^1 - \theta_i^2| \leq \frac{2\epsilon_L \phi_0}{\gamma_0} |\tilde{\theta}^1 - \tilde{\theta}^2| \quad (5.36)$$

for the map  $\tilde{\theta} \mapsto \theta$ . Under condition (5.35), this map is hence a contraction and relation (5.34) has a unique solution.

We can directly check that indeed the solution  $\theta_i$  is bounded from below, depending on data. To this aim, choose

$$\theta_{\min} = \min\{\theta_{i-1}, \theta_i^e, \theta_{\text{tr}} - 2\rho\} > 0$$

and multiply (5.34) by  $-(\theta_i - \theta_{\min})^- = \min\{\theta_i - \theta_{\min}, 0\} < 0$  getting

$$\begin{aligned} \gamma_\eta(\mathbf{y}_{i-1})|(\theta_i - \theta_{\min})^-|^2 &= \gamma_\eta(\mathbf{y}_{i-1})(\theta_{\min} - \theta_{i-1})(\theta_i - \theta_{\min})^- - \lambda\tau_i \left( \frac{1}{\theta_i} - \frac{1}{\theta_i^e} \right) (\theta_i - \theta_{\min})^- \\ &\quad - R_Y |\mathbf{e}_i^{\text{tr}} - \mathbf{e}_{i-1}^{\text{tr}}| (\theta_i - \theta_{\min})^- - \theta_i f'_*(\theta_i) \partial |\mathbf{e}_i^{\text{tr}}|_\eta : (\mathbf{e}_i^{\text{tr}} - \mathbf{e}_{i-1}^{\text{tr}}) (\theta_i - \theta_{\min})^-. \end{aligned} \quad (5.37)$$

The four terms in the above right-hand side are nonpositive. Indeed, the term  $\gamma_\eta(\mathbf{y}_{i-1})(\theta_{\min} - \theta_{i-1})(\theta_i - \theta_{\min})^-$  is nonpositive by (5.31) as  $\theta_{\min} \leq \theta_{i-1}$ . Moreover, we have that

$$-\lambda\tau_i \left( \frac{1}{\theta_i} - \frac{1}{\theta_i^e} \right) (\theta_i - \theta_{\min})^- = -\lambda\tau_i \frac{\theta_i^e - \theta_i}{\theta_i \theta_i^e} (\theta_i - \theta_{\min})^- \leq 0$$

as  $0 < \theta_i \leq \theta_{\min} \leq \theta_i^e$  whenever  $(\theta_i - \theta_{\min})^- \neq 0$ . The nonpositivity of the term  $-R_Y |\mathbf{e}_i^{\text{tr}} - \mathbf{e}_{i-1}^{\text{tr}}| (\theta_i - \theta_{\min})^-$  is clear. As  $f_*(\theta)$  vanishes for  $\theta < \theta_{\text{tr}} - 2\rho$  we finally have that

$$(\theta_i - \theta_{\min})^- \neq 0 \Rightarrow \theta_i f'_*(\theta_i) \partial |\mathbf{e}_i^{\text{tr}}|_\eta : (\mathbf{e}_i^{\text{tr}} - \mathbf{e}_{i-1}^{\text{tr}}) = 0.$$

Owing to the nonpositivity of the right-hand side of (5.37) and to (5.31) we have proved that  $(\theta_i - \theta_{\min})^- = 0$  hence

$$\theta \geq \theta_{\min} > 0. \quad (5.38)$$

Let us now consider  $\theta_i^1$  and  $\theta_i^2$  to be the unique solutions of (5.34) with  $\mathbf{e}_i^{\text{tr}} = \mathbf{e}_i^{\text{tr},1}$  and  $\mathbf{e}_i^{\text{tr}} = \mathbf{e}_i^{\text{tr},2}$ , respectively. By arguing as above we readily obtain that

$$\begin{aligned} \gamma_0 |\theta_i^1 - \theta_i^2|^2 &\leq R_Y |\mathbf{e}_i^{\text{tr},1} - \mathbf{e}_i^{\text{tr},2}| |\theta_i^1 - \theta_i^2| \\ &\quad + (\theta^1 f'_*(\theta^1) \partial |\mathbf{e}^{\text{tr},1}|_\eta : (\mathbf{e}^{\text{tr},1} - \mathbf{e}_{i-1}^{\text{tr}}) - \theta^2 f'_*(\theta^2) \partial |\mathbf{e}^{\text{tr},2}|_\eta : (\mathbf{e}^{\text{tr},2} - \mathbf{e}_{i-1}^{\text{tr}})) (\theta_i^1 - \theta_i^2). \end{aligned} \quad (5.39)$$

In the following, we will consider the case of temperature bounded from above by  $\theta^* > 0$ . By exploiting the Lipschitz continuity of  $\partial |\cdot|_\eta$  and assuming  $\theta_i^1, \theta_i^2 \leq \theta^*$  one deduces that

$$\begin{aligned} \gamma_0 |\theta_i^1 - \theta_i^2| &\leq R_Y |\mathbf{e}_i^{\text{tr},1} - \mathbf{e}_i^{\text{tr},2}| + 2\epsilon_L \phi_0 |\theta_i^1 - \theta_i^2| \\ &\quad + \frac{2\epsilon_L \beta \theta_*}{\eta} |\mathbf{e}^{\text{tr},1} - \mathbf{e}^{\text{tr},2}| + \beta \theta_* |\mathbf{e}^{\text{tr},1} - \mathbf{e}^{\text{tr},2}|. \end{aligned} \quad (5.40)$$



### 5.5.3 Existence for the discrete problem

Let us now check that the discrete system (5.28)-(5.29) can be solved for all given  $\theta_{i-1} > 0$ ,  $\mathbf{e}_{i-1}^{\text{tr}} \in \mathbb{R}_{\text{dev}}^{3 \times 3}$ ,  $\theta_i^e > 0$ , and  $\mathbf{e}_i \in \mathbb{R}_{\text{dev}}^{3 \times 3}$ . The strategy here is to consider an iterative procedure, solving indeed the mechanical and the thermal problems sequentially.

For some trial

$$\tilde{\mathbf{e}}_i^{\text{tr}} \in B := \{\mathbf{e}^{\text{tr}} \in \mathbb{R}_{\text{dev}}^{3 \times 3} : |\mathbf{e}^{\text{tr}}| \leq \epsilon_L\},$$

we find the unique solution  $\tilde{\theta} = S^1(\tilde{\mathbf{e}}_i^{\text{tr}})$  of (5.34) with  $\mathbf{e}_i^{\text{tr}} = \tilde{\mathbf{e}}_i^{\text{tr}}$ . Note that the map  $S^1$  is Lipschitz continuous by (5.40). Then, we uniquely solve (5.32) with  $\theta_i = \tilde{\theta}$  for  $\mathbf{e}_i^{\text{tr}} = S^2(\tilde{\theta})$ . Recall from (5.33) that the solution operator  $S^2$  is Lipschitz continuous as well. In conclusion, we have defined a Lipschitz continuous map  $S = S^2 \circ S^1$  from the ball  $B$  to itself. Hence,  $S$  has a fixed point  $\mathbf{e}^{\text{tr}}$  by the classical Browder Theorem, and the pair  $(\theta, \mathbf{e}^{\text{tr}}) = (S^1(\mathbf{e}^{\text{tr}}), \mathbf{e}^{\text{tr}})$  solves (5.32)+(5.34).

Before closing this section let us remark that the above existence proof is nonconstructive. In particular, we are not in the position of proving that the iterative procedure actually converges, but rather that *some subsequence* of such iterations converges. Our numerical evidence shows however that this issue is not jeopardizing the performance of the algorithm. Namely, the numerical procedure always detects a fixed point.

### 5.5.4 Unconditional stability

In order to possibly check the unconditional stability of the scheme, as well as its convergence, let us introduce some assumptions on the data. In what follows we shall ask for

$$\begin{aligned} \theta^e &\in W^{1,1}(0, T), \theta^e \geq \theta_{\min}^e > 0, \mathbf{e} \in W^{1,\infty}(0, T; \mathbb{R}_{\text{dev}}^{3 \times 3}), \\ \theta_0 &> 0, \mathbf{e}_0^{\text{tr}} \in B, \exists \mathbf{e}_{-1}^{\text{tr}} \in \mathbb{R}_{\text{dev}}^{3 \times 3} \text{ such that} \\ R_Y \partial |\mathbf{e}_0^{\text{tr}} - \mathbf{e}_{-1}^{\text{tr}}| &+ (H + 2G)\mathbf{e}_0^{\text{tr}} + f(\theta_0)|\mathbf{e}_0^{\text{tr}}|_{\eta} \ni 2G\mathbf{e}(0). \end{aligned} \quad (5.41)$$

Moreover, let us introduce the short-hand notation for incremental quotients

$$\delta\theta_i = \frac{\theta_i - \theta_{i-1}}{\tau_i}, \quad \delta\mathbf{e}_i^{\text{tr}} = \frac{\mathbf{e}_i^{\text{tr}} - \mathbf{e}_{i-1}^{\text{tr}}}{\tau_i},$$

and so on. In the following, the symbol  $C$  stands for any constant depending on data but not on the partition, and possibly varying from line to line.

By induction on  $i$ , the lower bound (5.38) entails the following uniform lower bound

$$\theta_i \geq \min\{\theta_0, \theta_{\min}^e, \theta_{\text{tr}} - 2\rho\} =: \theta_{\min} > 0. \quad (5.42)$$

For the sake of later purposes, let us assume to have chosen  $\theta_0$ ,  $\theta^e$ , and  $\theta_{\text{tr}}$  in such a way that  $\theta_{\min} > 250 \text{ K}$ .

We start by testing the temperature equation (5.34) by  $\tau_i \delta \theta_i$  getting

$$\begin{aligned} & \gamma_0 \tau_i |\delta \theta_i|^2 - \lambda (\log \theta_i - \log \theta_{i-1}) \\ & \leq \frac{\lambda \tau_i}{\theta_i^e} \delta \theta_i + \tau_i R_Y |\delta \mathbf{e}_i^{\text{tr}}| \delta \theta_i + \theta_i f'_*(\theta_i) \partial |\mathbf{e}_i^{\text{tr}}|_{\eta} : \delta \mathbf{e}_i^{\text{tr}} \delta \theta_i. \end{aligned} \quad (5.43)$$

Let us now take the difference between (5.32) written at level  $i$  and the same relation at level  $i = 1$ . By making use of  $\mathbf{e}_{-1}^{\text{tr}}$  from (5.41) this can be accomplished for all  $i = 1, \dots, m \leq N$ . We test this difference by  $\delta \mathbf{e}_i^{\text{tr}}$  and exploit the fact that  $\xi_i \in \partial R_Y |\mathbf{e}_i^{\text{tr}} - \mathbf{e}_{i-1}^{\text{tr}}|$  iff  $\mathbf{e}_i^{\text{tr}} - \mathbf{e}_{i-1}^{\text{tr}} \in \partial I_{R_Y}(\xi_i)$  in order to deduce that

$$\tau_i (H + 2G) |\delta \mathbf{e}_i^{\text{tr}}|^2 \leq \tau_i 2G \delta \mathbf{e}_i : \delta \mathbf{e}_i^{\text{tr}} - \tau_i \delta f(\theta_i) \partial |\mathbf{e}_i^{\text{tr}}|_{\eta} : \delta \mathbf{e}_i^{\text{tr}}.$$

Let us now multiply the latter by  $\theta_i > 0$  and add it to (5.43) getting

$$\begin{aligned} & \gamma_0 \tau_i |\delta \theta_i|^2 - \lambda (\log \theta_i - \log \theta_{i-1}) + \tau_i \theta_i (H + 2G) |\delta \mathbf{e}_i^{\text{tr}}|^2 \\ & \leq \frac{\lambda \tau_i}{\theta_i^e} \delta \theta_i + \tau_i R_Y |\delta \mathbf{e}_i^{\text{tr}}| \delta \theta_i + \tau_i \theta_i (f'_*(\theta_i) \delta \theta_i - \delta f(\theta_i)) \partial |\mathbf{e}_i^{\text{tr}}|_{\eta} : \delta \mathbf{e}_i^{\text{tr}} + \tau_i 2G \theta_i \delta \mathbf{e}_i : \delta \mathbf{e}_i^{\text{tr}} \\ & = \frac{\lambda \tau_i}{\theta_i^e} \delta \theta_i + \tau_i R_Y |\delta \mathbf{e}_i^{\text{tr}}| \delta \theta_i + \tau_i^2 \theta_i \frac{f''(\tilde{\theta})}{2} |\partial \theta_i|^2 \partial |\mathbf{e}_i^{\text{tr}}|_{\eta} : \delta \mathbf{e}_i^{\text{tr}} + \tau_i 2G \theta_i \delta \mathbf{e}_i : \delta \mathbf{e}_i^{\text{tr}} \\ & \leq \tau_i C |\delta \theta_i| + \tau_i R_Y |\delta \mathbf{e}_i^{\text{tr}}| |\delta \theta_i| + \tau_i \frac{\epsilon_L \beta \tilde{\theta}_*}{2\rho} |\delta \theta_i|^2 + \tau_i C |\theta_i| |\delta \mathbf{e}_i^{\text{tr}}| \end{aligned}$$

where  $\tilde{\theta}$  is an intermediate value between  $\theta_i$  and  $\theta_{i-1}$ . By taking the sum of the latter

inequality for  $i = 1, \dots, m \leq N$  we deduce

$$\begin{aligned} & \left( \gamma_0 - \frac{\epsilon_L \beta \theta_*}{2\rho} \right) \sum_{i=1}^m \tau_i |\delta \theta_i|^2 - \lambda \log \theta_m + \sum \tau_i \theta_i (H+2G) |\delta \mathbf{e}_i^{\text{tr}}|^2 \\ & \leq C + C \sum_{i=1}^m \tau_i |\delta \theta_i| + R_Y \sum_{i=1}^m \tau_i |\delta \mathbf{e}_i^{\text{tr}}| |\delta \theta_i| + C \sum_{i=1}^m \tau_i |\theta_i| |\delta \mathbf{e}_i^{\text{tr}}|. \end{aligned} \quad (5.44)$$

Under the compatibility conditions

$$\gamma_0 - \frac{\epsilon_L \beta \theta_*}{2\rho} > 0 \quad \text{and} \quad R_Y^2 < \theta_{\min} \gamma_0 (H+2G), \quad (5.45)$$

which are satisfied by our data set (see Table 5.8) by letting, for instance,  $\theta_* = 450$  K and  $\rho = 30$  K and recalling that  $\theta_{\min} > 250$  K, one has that

$$\sum_{i=1}^N \tau_i (|\delta \theta_i|^2 + |\delta \mathbf{e}_i^{\text{tr}}|^2) \leq C. \quad (5.46)$$

### 5.5.5 Convergence

Let us consider a sequence of partitions  $\{t_i\}$  so that the corresponding maximal time step  $\tau = \max_i (t_i - t_{i-1})$  converges to 0. We shall index these partitions by their diameter  $\tau$ . Letting  $\{u_i\}_{i=0}^N$  be a vector, we denote by  $u_\tau$ ,  $\overline{u}_\tau$ ,  $\underline{u}_\tau$  three functions of the time interval  $[0, T]$  which interpolate the values of the generic vector  $\{u_i\}$  on the partition with size  $\tau$ . In particular, for all  $t \in (t_{i-1}, t_i]$ ,  $i = 1, \dots, N$ ,

$$\begin{aligned} u_\tau(0) &:= u_0, \quad u_\tau(t) := \alpha_i(t) u_i + (1 - \alpha_i(t)) u_{i-1}, \\ \overline{u}_\tau(0) &:= u_0, \quad \overline{u}_\tau(t) := u_i, \\ \underline{u}_\tau(0) &:= u_0, \quad \underline{u}_\tau(t) = u_{i-1} \end{aligned}$$

where

$$\alpha_i(t) := (t - t_{i-1}) / \tau_i.$$

Owing to these notations we can rewrite the discrete system (5.28)-(5.29) in the compact form

$$\gamma_\eta(\underline{\mathbf{y}}_\tau)\dot{\theta}_\tau - \frac{\lambda}{\bar{\theta}_\tau} = -\frac{\lambda}{\bar{\theta}_\tau^e} + R_Y|\dot{\mathbf{e}}_\tau^{\text{tr}}| + \bar{\theta}_\tau f'_*(\bar{\theta}_\tau)\partial|\bar{\mathbf{e}}_\tau^{\text{tr}}|_\eta:\dot{\mathbf{e}}_\tau^{\text{tr}}, \quad (5.47)$$

$$\bar{\boldsymbol{\eta}}_\tau + (H+2G)\bar{\mathbf{e}}_\tau^{\text{tr}} + f_*(\bar{\theta}_\tau)\partial|\bar{\mathbf{e}}_\tau^{\text{tr}}|_\eta + \bar{\boldsymbol{\xi}}_\tau = 2G\bar{\mathbf{e}}_\tau, \quad (5.48)$$

$$\bar{\boldsymbol{\eta}}_\tau \in R_Y\partial|\dot{\mathbf{e}}_\tau^{\text{tr}}|, \quad \bar{\boldsymbol{\xi}}_\tau \in \partial I(\bar{\mathbf{e}}_\tau^{\text{tr}}) \quad (5.49)$$

for almost all  $t \in (0, T)$ . In particular, by the boundedness of  $\partial|\cdot|$  and  $\partial|\cdot|_\eta$  one obtains from the bound (5.46) and by comparison in (5.48) that the norms

$$\|\theta_\tau\|_{H^1}, \|\mathbf{e}_\tau^{\text{tr}}\|_{H^1}, \|\bar{\boldsymbol{\eta}}_\tau\|_{L^\infty}, \|\bar{\boldsymbol{\xi}}_\tau\|_{L^\infty} \text{ are bounded, independently of } \tau.$$

Hence, we can extract not relabeled subsequences such that

$$\theta_\tau \rightarrow \theta \text{ strongly in } C[0, T] \text{ and weakly in } H^1(0, T), \quad (5.50)$$

$$\bar{\theta}_\tau, \underline{\theta}_\tau \rightarrow \theta \text{ strongly in } L^\infty(0, T), \quad (5.51)$$

$$\mathbf{e}_\tau^{\text{tr}} \rightarrow \mathbf{e}^{\text{tr}} \text{ strongly in } C([0, T]; \mathbb{R}_{\text{dev}}^{3 \times 3}) \text{ and weakly in } H^1(0, T; \mathbb{R}_{\text{dev}}^{3 \times 3}), \quad (5.52)$$

$$\bar{\mathbf{e}}_\tau^{\text{tr}}, \underline{\mathbf{e}}_\tau^{\text{tr}} \rightarrow \mathbf{e}^{\text{tr}} \text{ strongly in } L^\infty(0, T; \mathbb{R}_{\text{dev}}^{3 \times 3}). \quad (5.53)$$

$$\bar{\boldsymbol{\eta}}_\tau \rightarrow \boldsymbol{\eta} \text{ weakly star in } L^\infty(0, T; \mathbb{R}_{\text{dev}}^{3 \times 3}). \quad (5.54)$$

$$\bar{\boldsymbol{\xi}}_\tau \rightarrow \boldsymbol{\xi} \text{ weakly star in } L^\infty(0, T; \mathbb{R}_{\text{dev}}^{3 \times 3}). \quad (5.55)$$

We shall now pass to the limit in relations (5.47)-(5.49). By using also the uniform positivity of  $\underline{\theta}_\tau$  from (5.42) we have that  $\gamma_\eta(\underline{\mathbf{y}}_\tau) \rightarrow \gamma_\eta(\mathbf{y})$  strongly in  $L^\infty(0, T)$  so that convergence (5.50) entails that  $\gamma_\eta(\underline{\mathbf{y}}_\tau)\dot{\theta}_\tau \rightarrow \gamma_\eta(\mathbf{y})\dot{\theta}$  weakly in  $L^2(0, T)$ . The convergence of the terms  $-\lambda/\bar{\theta}_\tau \rightarrow -\lambda/\theta$  and  $-\lambda/\bar{\theta}_\tau^e \rightarrow -\lambda/\theta^e$  in  $L^\infty(0, T)$  follow by the strict bound (5.42), convergence (5.51), and the fact that  $\bar{\theta}_\tau^e \rightarrow \theta^e$  in  $C[0, T]$ . Moreover, we readily check that

$$\bar{\theta}_\tau f'_*(\bar{\theta}_\tau)\partial|\bar{\mathbf{e}}_\tau^{\text{tr}}|_\eta:\dot{\mathbf{e}}_\tau^{\text{tr}} \rightarrow \theta f'_*(\theta)\partial|\mathbf{e}^{\text{tr}}|_\eta:\dot{\mathbf{e}}^{\text{tr}} \text{ weakly in } L^2(0, T; \mathbb{R}_{\text{dev}}^{3 \times 3})$$

where we have in particular used the Lipschitz continuity of  $\partial|\cdot|_\eta$ . We can pass to the limit in each term in (5.48) getting

$$\boldsymbol{\eta} + (H+2G)\mathbf{e}^{\text{tr}} + f_*(\theta)\partial|\mathbf{e}^{\text{tr}}|_\eta + \boldsymbol{\xi} = 2G\mathbf{e}. \quad (5.56)$$

In addition, by the classical strong-weak closure of subdifferentials we get that  $\boldsymbol{\xi} \in \partial I(\mathbf{e}^{\text{tr}})$  almost everywhere in time. In order to identify  $\boldsymbol{\eta}$  we proceed by lower semicontinuity by computing

$$\begin{aligned}
& \limsup_{\tau \rightarrow 0} \left( \int_0^T \bar{\boldsymbol{\eta}}_\tau : \dot{\mathbf{e}}_\tau^{\text{tr}} \, dt \right) \\
& \leq \limsup_{\tau \rightarrow 0} \left( -\frac{H+2G}{2} (|\mathbf{e}_\tau^{\text{tr}}(T)|^2 - |\mathbf{e}_0^{\text{tr}}|^2) - I(\mathbf{e}_\tau^{\text{tr}}(T)) + I(\mathbf{e}_0^{\text{tr}}) \right. \\
& \quad \left. - \int_0^T f_*(\bar{\theta}_\tau) \partial |\bar{\mathbf{e}}_\tau^{\text{tr}}|_\eta : \dot{\mathbf{e}}_\tau^{\text{tr}} \, dt + \int_0^T 2G \bar{\mathbf{e}}_\tau : \dot{\mathbf{e}}_\tau^{\text{tr}} \, dt \right) \\
& \leq -\frac{H+2G}{2} (|\mathbf{e}^{\text{tr}}(T)|^2 - |\mathbf{e}_0^{\text{tr}}|^2) - I(\mathbf{e}^{\text{tr}}(T)) + I(\mathbf{e}_0^{\text{tr}}) - \int_0^T f_*(\theta) \partial |\mathbf{e}^{\text{tr}}|_\eta : \dot{\mathbf{e}}^{\text{tr}} \, dt \\
& \quad - \int_0^T 2G \mathbf{e} : \dot{\mathbf{e}}^{\text{tr}} \, dt = \int_0^T \boldsymbol{\eta} : \dot{\mathbf{e}}^{\text{tr}} \, dt.
\end{aligned}$$

In particular, by the classical result [57, Prop. 2.5, p. 27] we obtain that  $\boldsymbol{\eta} \in R_Y \partial |\dot{\mathbf{e}}^{\text{tr}}|$  almost everywhere and

$$\int_0^T R_Y |\dot{\mathbf{e}}_\tau^{\text{tr}}| \, dt = \int_0^T \bar{\boldsymbol{\eta}}_\tau : \dot{\mathbf{e}}_\tau^{\text{tr}} \, dt \rightarrow \int_0^T \boldsymbol{\eta} : \dot{\mathbf{e}}^{\text{tr}} \, dt = \int_0^T R_Y |\dot{\mathbf{e}}^{\text{tr}}| \, dt.$$

The above estimate can be also localized to subsets  $[s, t] \subset [0, T]$  so that it indeed entails the convergence  $R_Y |\dot{\mathbf{e}}_\tau^{\text{tr}}| \rightarrow R_Y |\dot{\mathbf{e}}^{\text{tr}}|$  in  $L^1(0, T)$ . This concludes the convergence proof.

## 5.6 Numerical results

The aim of this section is to illustrate the performance of the proposed semi-implicit scheme. We shall implement the discretization procedure described in Subsection 5.5.3. Given a time partition  $\{t_i\}$ , initial data  $(\theta_0, \mathbf{e}_0^{\text{tr}})$ , and possibly time-dependent external data  $i \mapsto (\theta_i^e, \mathbf{e}_i)$ , we solve the system (5.28)-(5.29) for  $i = 1, \dots, N$  by iterating, at each time step, the solution of the mechanical and thermal subproblems until convergence. As the computationally observed temperatures do not exceed the threshold  $\theta_* - 2\rho$ , no actual truncation of  $f$  is needed in the algorithm. We shall hence keep the notation  $f$  in the remainder of the section.

From the algorithmical viewpoint, the solution of the iteration in the (scalar) ther-

mal subproblem is straightforward. On the other hand, the discussion of the mechanical subproblem, namely relation (5.32), is more delicate so that we shall concentrate on the latter. Indeed, the interplay of the three nonlinear terms of relation (5.32) is at the same time a distinctive feature of the model and a criticality, in term of the use of generalized Newton methods. The introduced regularization  $|\cdot|_\eta$  of a norm in (5.32) is clearly beneficial from the algorithmical viewpoint. This approximation is widely used in this context [24, 214, 217, 290] and has been proved to converge to the nonregularized situation for  $\eta \rightarrow 0$  in a number of relevant cases [23]. Still, this regularization is to a large extent not needed here, as we comment in the following subsection.

### 5.6.1 Nonregularized case in (5.32)

We shall collect here some discussion on the possibility of considering directly the nonregularized case  $\eta = 0$  in relation (5.32). Although not accessible to a complete theoretical analysis, the nonregularized case corresponds to the original formulation of the material relation. As such, we believe it to be of interest from both the modeling and numerical viewpoint.

Given data  $\theta_i > 0$  and  $\mathbf{e}_{i-1}^{\text{tr}}, \mathbf{e}_i \in \mathbb{R}_{\text{dev}}^{3 \times 3}$ , the idea is to perform some *a priori* tests in order to check if the solution  $\mathbf{e}_i^{\text{tr}}$  of relation (5.32) is

$$\text{neither } \{\mathbf{e}_{i-1}^{\text{tr}}\} \text{ nor } \{\mathbf{0}\},$$

which exactly correspond to the singular sets of the nonlinearities  $\partial|\mathbf{e}^{\text{tr}} - \mathbf{e}_{i-1}^{\text{tr}}|$  and  $\partial|\mathbf{e}^{\text{tr}}|$  (that is  $\partial|\mathbf{e}^{\text{tr}}|_\eta$  for  $\eta = 0$ ) in (5.32), respectively (the treatment of the constraint  $\partial I(\mathbf{e}_i^{\text{tr}})$  follows *ex post*, see below). We shall proceed by distinguishing mutual cases.

**Case (1):**  $\mathbf{e}_i^{\text{tr}} = \mathbf{e}_{i-1}^{\text{tr}} = \mathbf{0}$ . In this case relation (5.32) corresponds to

$$(R_Y + f(\theta_i))B \ni 2G\mathbf{e}_i$$

where  $B = \{|\mathbf{e}^{\text{tr}}| \leq 1\}$  is the unit ball. This can be achieved iff

$$2G|\mathbf{e}_i| \leq R_Y + f(\theta_i). \tag{5.57}$$

**Case (2):**  $\mathbf{e}_{i-1}^{\text{tr}} \neq \mathbf{e}_i^{\text{tr}} = \mathbf{0}$ . Here, relation (5.32) reads

$$R_Y \frac{\mathbf{e}_{i-1}^{\text{tr}}}{|\mathbf{e}_{i-1}^{\text{tr}}|} + f(\theta_i)B \ni 2G\mathbf{e}_i$$

which can be fulfilled iff

$$\left| 2G\mathbf{e}_i - R_Y \frac{\mathbf{e}_{i-1}^{\text{tr}}}{|\mathbf{e}_{i-1}^{\text{tr}}|} \right| \leq f(\theta_i). \quad (5.58)$$

**Case (3):**  $\mathbf{e}_i^{\text{tr}} = \mathbf{e}_{i-1}^{\text{tr}} \neq \mathbf{0}$  and  $|\mathbf{e}_i^{\text{tr}}| < \epsilon_L$ . We can rewrite relation (5.32) as

$$RB + (H+2G) \frac{\mathbf{e}_{i-1}^{\text{tr}}}{|\mathbf{e}_{i-1}^{\text{tr}}|} + f(\theta_i) \frac{\mathbf{e}_{i-1}^{\text{tr}}}{|\mathbf{e}_{i-1}^{\text{tr}}|} \ni 2G\mathbf{e}_i$$

which holds iff

$$\left| 2G\mathbf{e}_i - (H+2G)\mathbf{e}_{i-1}^{\text{tr}} - f(\theta_i) \frac{\mathbf{e}_{i-1}^{\text{tr}}}{|\mathbf{e}_{i-1}^{\text{tr}}|} \right| \leq R_Y. \quad (5.59)$$

**Case (4):**  $\mathbf{e}_i^{\text{tr}} = \mathbf{e}_{i-1}^{\text{tr}}$  and  $|\mathbf{e}_i^{\text{tr}}| = \epsilon_L$ . In this situation relation (5.32) reads

$$RB + (H+2G) \frac{\mathbf{e}_{i-1}^{\text{tr}}}{|\mathbf{e}_{i-1}^{\text{tr}}|} + f(\theta_i) \frac{\mathbf{e}_{i-1}^{\text{tr}}}{|\mathbf{e}_{i-1}^{\text{tr}}|} + \ell \frac{\mathbf{e}_{i-1}^{\text{tr}}}{|\mathbf{e}_{i-1}^{\text{tr}}|} \ni 2G\mathbf{e}_i$$

where  $\ell \geq 0$  is the (norm of the) Lagrange multiplier corresponding to the constraint  $|\mathbf{e}_i^{\text{tr}}| \leq \epsilon_L$ . The inclusion holds iff, by letting

$$\mathbf{d} := \frac{\mathbf{e}_{i-1}^{\text{tr}}}{|\mathbf{e}_{i-1}^{\text{tr}}|}, \quad \mathbf{w} := 2G\mathbf{e}_i - (H+2G)\mathbf{e}_{i-1}^{\text{tr}} - f(\theta_i) \frac{\mathbf{e}_{i-1}^{\text{tr}}}{|\mathbf{e}_{i-1}^{\text{tr}}|},$$

one has that

$$\mathbf{w} \in [0, \infty)\mathbf{d} + RB.$$

This is equivalent to ask for  $\ell \geq 0$  and  $|\mathbf{x}| \leq R_Y$  such that  $\mathbf{w} = \ell\mathbf{d} + \mathbf{x}$ . Given  $\mathbf{w}$  and  $\mathbf{d}$ , this condition can be readily checked to hold iff

$$(\mathbf{w}:\mathbf{d} \leq 0 \text{ and } |\mathbf{w}| \leq R_Y) \quad \text{or} \quad (\mathbf{w}:\mathbf{d} > 0 \text{ and } |\mathbf{w} - (\mathbf{w}:\mathbf{d})\mathbf{d}| \leq R_Y). \quad (5.60)$$

By performing the checks (5.57)-(5.60) we can identify the singular situations  $\mathbf{e}_i^{\text{tr}} = \mathbf{e}_{i-1}^{\text{tr}}$  or  $\mathbf{e}_i^{\text{tr}} = \mathbf{0}$  completely. In case  $\mathbf{e}_i^{\text{tr}} \neq \mathbf{e}_{i-1}^{\text{tr}}$  and  $\mathbf{e}_i^{\text{tr}} \neq \mathbf{0}$ , we may proceed in solving relation

$$R_Y \partial |\mathbf{e}_i^{\text{tr}} - \mathbf{e}_{i-1}^{\text{tr}}| + (H+2G)\mathbf{e}_i^{\text{tr}} + f(\theta_i) \partial |\mathbf{e}_i^{\text{tr}}| \ni 2G\mathbf{e}_i, \quad (5.61)$$

which is nothing but (5.32) where the constraint  $\partial I(\mathbf{e}_i^{\text{tr}})$  has been removed. Relation (5.61) also admits a unique solution  $\tilde{\mathbf{e}}_i^{\text{tr}}$ , which we have already checked to be different from  $\mathbf{e}_{i-1}^{\text{tr}}$  and  $\mathbf{0}$ . In particular, we can avoid regularizing the norms in (5.61) as long as we remain in a neighborhood of the solution  $\tilde{\mathbf{e}}_i^{\text{tr}}$ .

Eventually, if  $|\tilde{\mathbf{e}}_i^{\text{tr}}| \leq \epsilon_L$  then  $\mathbf{e}_i^{\text{tr}} = \tilde{\mathbf{e}}_i^{\text{tr}}$  is the unique solution of (5.32). On the contrary, one has to treat directly (5.32), where now  $\eta = 0$  is allowed. On the other hand, the constraining term  $\partial I(\mathbf{e}_i^{\text{tr}})$  could be regularized by penalization as

$$\partial I_\zeta(\mathbf{e}_i^{\text{tr}}) = \frac{1}{\zeta} ( (|\mathbf{e}_i^{\text{tr}}| - \epsilon_L)^+ )^2 \frac{\mathbf{e}_i^{\text{tr}}}{|\mathbf{e}_i^{\text{tr}}|}$$

where  $\zeta > 0$  is a user-defined parameter. For all positive  $\zeta$  the regularized term is Lipschitz continuous and it can be checked that the  $\zeta$ -regularized solution to (5.32) converges as  $\zeta \rightarrow 0$  to the solution of the nonregularized equation [23].

## 5.6.2 Implementation

The strain- and external-temperature-driven constitutive-model driver has been implemented in the *Mathematica* (*Wolfram*) environment and has been tested under different conditions.

The algorithm solves the time-discrete scheme from Section 5.5, along with the provisions of Subsection 5.6.1. At each time  $t_i$ , the values  $\mathbf{e}_i \in \mathbb{R}_{\text{dev}}^{3 \times 3}$ ,  $\theta_i^e > 0$  are given as well as the previous states  $\theta_{i-1} > 0$  and  $\mathbf{e}_{i-1}^{\text{tr}} \in \mathbb{R}_{\text{dev}}^{3 \times 3}$ . The algorithm computes the actual values  $\theta_i > 0$  and  $\mathbf{e}_i^{\text{tr}} \in \mathbb{R}_{\text{dev}}^{3 \times 3}$ . The procedure is iterative and it is summarized in Table 5.1 and in the related sub-cycles.

In particular, the thermal subproblem is also solved iteratively. At each step one solves a scalar nonlinear equation. This iteration is actually a contraction, so that geometric convergence can be guaranteed.

On the contrary, the mechanical subproblem is solved directly. Firstly, one analyzes the four cases presented in Subsection 5.6.1. If all the corresponding checks fail, the solution of the mechanical subproblem is obtained by directly solving the nonlinear system. The (failure of the) preliminary checks ensure that the equation is smooth at the solution. In particular, a Newton-Raphson solution procedure, possibly in combination with a



Table 5.1: Implementation algorithm for the strain- and external-temperature-driven driver.

### Main algorithm

Starting data:  $\{\mathbf{e}_i, \theta_i^e\} \in \mathbb{R}_{\text{dev}}^{3 \times 3} \times \mathbb{R}_+$  and  $\{\mathbf{e}_{i-1}^{\text{tr}}, \theta_{i-1}\} \in \mathbb{R}_{\text{dev}}^{3 \times 3} \times \mathbb{R}_+$

Define  $\mathbf{e}_{i,0}^{\text{tr}} = \mathbf{e}_{i-1}^{\text{tr}}$ .

**while**  $k \geq 1$ ,  $|\theta_{i,k} - \theta_{i,k-1}|/\theta_{i,k} \geq \text{tol}$ , and  $|\mathbf{e}_{i,k}^{\text{tr}} - \mathbf{e}_{i,k-1}^{\text{tr}}|/|\mathbf{e}_{i,k}^{\text{tr}}| \geq \text{tol}$  **do**

Solve the **thermal subproblem** from Subsection 5.5.2:

given  $\{\theta_i^e, \theta_{i-1}, \mathbf{e}_{i-1}^{\text{tr}}\} \in \mathbb{R}_+ \times \mathbb{R}_+ \times \mathbb{R}_{\text{dev}}^{3 \times 3}$  and  $\mathbf{e}_{i,k-1}^{\text{tr}} \in \mathbb{R}_{\text{dev}}^{3 \times 3}$

find  $\theta_{i,k} > 0$  solving (5.34)

(see Table 5.3).

Solve the **mechanical subproblem** from Subsection 5.5.1:

given  $\{\mathbf{e}_i, \theta_{i,k}\} \in \mathbb{R}_{\text{dev}}^{3 \times 3} \times \mathbb{R}_+$  and  $\mathbf{e}_{i-1}^{\text{tr}} \in \mathbb{R}_{\text{dev}}^{3 \times 3}$

find  $\mathbf{e}_{i,k}^{\text{tr}} \in \mathbb{R}_{\text{dev}}^{3 \times 3}$  solving (5.61)

(see Table 5.2).

**end**

constraint, can be used.

### 5.6.3 Material parameters

The parameters used in the simulations are taken from [32] and are listed in Table 5.8. It can be verified that the adopted parameters satisfy conditions (5.31) and (5.45).

### 5.6.4 Proportional tests

In the following, numerical results corresponding to different proportional tests are displayed. The imposed proportional strain is of the form

$$t \mapsto \boldsymbol{\varepsilon}(t) = \mathbf{e}(t) = \varepsilon_V(t) \begin{bmatrix} \sqrt{\frac{2}{3}} & 0 & 0 \\ 0 & -\frac{1}{\sqrt{6}} & 0 \\ 0 & 0 & -\frac{1}{\sqrt{6}} \end{bmatrix}$$

Table 5.2: Algorithm for the thermal subproblem.

<p><b>Thermal subproblem</b></p> <p>Starting data: <math>\{\mathbf{e}_i, \theta_i^e\} \in \mathbb{R}_{\text{dev}}^{3 \times 3} \times \mathbb{R}_+</math>, <math>\mathbf{e}_{i-1}^{\text{tr}}</math>, <math>\mathbf{e}_i^{\text{tr}} \in \mathbb{R}_{\text{dev}}^{3 \times 3}</math>, <math>\theta_{i-1} &gt; 0</math></p> <p>Define <math>\theta_{i,0} = \theta_{i-1}</math>.</p> <p><b>while</b> <math>k \geq 1</math> <i>and</i> <math> \theta_{i,k} - \theta_{i,k-1} /\theta_{i,k} \geq \text{tol}</math> <b>do</b></p> <div style="margin-left: 40px;"> <p>Find <math>\theta_{i,k} &gt; 0</math> solving</p> <math display="block">\gamma_\eta(\mathbf{y}_{i-1})\theta_i - \frac{\tau_i \lambda}{\theta_i} = -\frac{\tau_i \lambda}{\theta_i^e} + \gamma_\eta(\mathbf{y}_{i-1})\theta_{i-1} + R_Y  \mathbf{e}_i^{\text{tr}} - \mathbf{e}_{i-1}^{\text{tr}}  + \theta_{i,k-1} f'_*(\theta_{i,k-1}) \partial  \mathbf{e}_i^{\text{tr}} _\eta : (\mathbf{e}_i^{\text{tr}} - \mathbf{e}_{i-1}^{\text{tr}}).</math> </div> <p><b>end</b></p>
--

Table 5.3: Algorithm for the mechanical subproblem.

<p><b>Mechanical subproblem</b></p> <p>Starting data: <math>\{\mathbf{e}_i, \theta_i\} \in \mathbb{R}_{\text{dev}}^{3 \times 3} \times \mathbb{R}_+</math>, and <math>\mathbf{e}_{i-1}^{\text{tr}} \in \mathbb{R}_{\text{dev}}^{3 \times 3}</math>.</p> <p>Check Cases (1) to (4), see Tables 5.4-5.7.</p> <p><b>if</b> Checks (1) to (4) fail <b>then</b></p> <div style="margin-left: 40px;"> <p>find <math>\tilde{\mathbf{e}}_i^{\text{tr}} \in \mathbb{R}_{\text{dev}}^{3 \times 3}</math> solving</p> <math display="block">R_Y \partial  \tilde{\mathbf{e}}_i^{\text{tr}} - \mathbf{e}_{i-1}^{\text{tr}}  + (H + 2G) \tilde{\mathbf{e}}_i^{\text{tr}} + f(\theta_i) \partial  \tilde{\mathbf{e}}_i^{\text{tr}}  \ni 2G \mathbf{e}_i</math> <p>by Newton-Raphson.</p> </div> <p><b>end</b></p> <p><b>if</b> <math> \tilde{\mathbf{e}}_i^{\text{tr}}  \leq \varepsilon_L</math> <b>then</b></p> <div style="margin-left: 40px;"> <p>define <math>\mathbf{e}_i^{\text{tr}} = \tilde{\mathbf{e}}_i^{\text{tr}}</math>.</p> </div> <p><b>end</b></p> <p><b>if</b> <math> \tilde{\mathbf{e}}_i^{\text{tr}}  &gt; \varepsilon_L</math> <b>then</b></p> <div style="margin-left: 40px;"> <p>define <math>\mathbf{e}_i^{\text{tr}}</math> by solving the system</p> <math display="block">R_Y \partial  \mathbf{e}_i^{\text{tr}} - \mathbf{e}_{i-1}^{\text{tr}}  + (H + 2G) \mathbf{e}_i^{\text{tr}} + f(\theta_i) \partial  \mathbf{e}_i^{\text{tr}}  \ni 2G \mathbf{e}_i \quad \text{and} \quad  \mathbf{e}_i^{\text{tr}}  = \varepsilon_L</math> <p>by Newton-Raphson.</p> </div> <p><b>end</b></p>
---

Table 5.4: Test for Case (1).

<p><b>Check Case (1)</b></p> <p><b>if</b> <math>2G e_i  \leq R_Y + f(\theta_i)</math> <b>then</b></p> <p>    <math>e_i^{\text{tr}} = e_{i-1}^{\text{tr}}</math></p> <p><b>end</b></p>
---

Table 5.5: Test for Case (2).

<p><b>Check Case (2)</b></p> <p><b>if</b> <math>\left  2Ge_i + R_Y \frac{e_{i-1}^{\text{tr}}}{ e_{i-1}^{\text{tr}} } \right  \leq f(\theta_i)</math> <b>then</b></p> <p>    <math>e_i^{\text{tr}} = 0</math></p> <p><b>end</b></p>
--

Table 5.6: Test for Case (3).

<p><b>Check Case (3)</b></p> <p><b>if</b> <math>\left  2Ge_i - (H + 2G)e_{i-1}^{\text{tr}} - f(\theta_i) \frac{e_{i-1}^{\text{tr}}}{ e_{i-1}^{\text{tr}} } \right  \leq R_Y</math> <b>then</b></p> <p>    <math>e_i^{\text{tr}} = e_{i-1}^{\text{tr}}</math></p> <p><b>end</b></p>
--

Table 5.7: Test for Case (4).

<p><b>Check Case (4)</b></p> <p>Define <math>d := e_{i-1}^{\text{tr}}/ e_{i-1}^{\text{tr}} </math>, <math>w := 2Ge_i - (H+2G)e_{i-1}^{\text{tr}} - f(\theta_i)e_{i-1}^{\text{tr}}/ e_{i-1}^{\text{tr}} </math>.</p> <p><b>if</b> <math>w:d \leq 0</math> and <math> w  \leq R_Y</math> <b>then</b></p> <p>    <math>e_i^{\text{tr}} = e_{i-1}^{\text{tr}}</math></p> <p><b>end</b></p> <p><b>if</b> <math>w:d &gt; 0</math> and <math> w - (w:d)d  \leq R_Y</math> <b>then</b></p> <p>    <math>e_i^{\text{tr}} = e_{i-1}^{\text{tr}}</math></p> <p><b>end</b></p>
--

Table 5.8: Material and numerical parameters for the implicit algorithm.

Symbol	Value	Unit	Description
$E$	45000	MPa	Young's modulus
$\nu$	0.3	-	Poisson's coefficient
$K$	37500	MPa	bulk modulus
$G$	17308	MPa	shear modulus
$R_Y$	110	MPa	critical stress
$\beta$	4.49	MPa/K	coefficient of function $f$
$H$	1000	MPa	hardening constant
$\theta_{tr}$	343	K	martensite finish temperature
$\epsilon_L$	0.049	-	saturation strain limit
$\theta_0$	300	K	initial temperature
$\theta^e$	390	K	external temperature
$c$	3.22	MPa/K	specific heat
$\lambda$	$2 \times 10^3$	(MPa K)/s	heat exchange coefficient
$\rho$	31	K	parameter in the definition of $f$
$tol$	$10^{-6}$	-	tolerance

where the time-dependent function  $t \mapsto \varepsilon_V(t) \in \mathbb{R}$  is given.

A first choice for  $\varepsilon_V$  is illustrated in Figure 5.1. A single tension-compression cycle is performed. In order to clarify the material mechanisms, the first simulation is performed in pure martensitic conditions, with  $\theta^e = \theta^0 = 300K$ , and the second one is performed in purely superelastic conditions, with  $\theta^e = \theta^0 = 380K$ .

The response of the first test is reported in Figure 5.2. Under the temperature transformation region, the only possible transformations regard the martensite reorientation: such mechanism provides a heat release, as it is clearly visible in the right plot of Figure 5.2. Indeed, the temperature of the material increases during the martensite detwinning, despite the heat absorption by the external environment. In the elastic regions, the temperature change is only due to the exchange with the external environment.

The response of the second test is reported in Figure 5.3. As before, we have heat release during the forward austenite-to-martensite transformation. In this case, since the material is in the superelastic region, heat absorption occurs during reverse martensite-to-austenite transformation. Again, in the elastic region the temperature only depends on the heat exchange with the external environment.

The third proportional test is performed using the parameters in Table 5.8. The corresponding mechanical and thermal response curves are displayed in Figure 5.4. It can

be clearly noted that the forward transformation produces a temperature increase, which in turn pulls the strain-stress curve towards higher-stress-level zones. Until time 70, the material stays under the transformation temperature. Therefore, the temperature can only increase, because of both the forward phase transformation, and the heat exchange with the external environment (indeed, the external temperature is here fixed to be  $\theta^e = 390\text{ K}$ ). Below the transformation temperature, only martensitic reorientation takes places and releases heat.

At time 70, the material enters the transition zone, individuated by  $[\theta - \rho; \theta + \rho]$ , so that during the forward transformation the heat release is even higher than the heat amount released at lower temperatures. At time 81, the reverse transformation takes place, absorbing heat. From time 123, a new forward transformation generated by compression occurs, so that we have heat release again. At time 125, the transformation temperature (i.e. the center of the transformation range) is reached. After entering the superelastic region, it is clearly visible that the temperature increases with the increase of the transformation strain during forward phase transformations, and afterwards the temperature decreases (despite the always present environmental heat exchange) during the transformation strain recovery. During the elastic ranges, the temperature changes are only driven by the exchange with the external environment.

In Figure 5.5 we compare the above-described response with the case of no heat exchange with the external environment ( $\lambda = 0$ ). In the adiabatic case, the material does not reach the transformation temperature, so there is no temperature decrease due to recovery. The absence of heat exchange is particularly visible during the elastic steps, when the temperature curve in the adiabatic case is flat, while in the former case it relaxes towards the external temperature.

A second comparison is made between the situation of Figure 5.4 and a case where the strain-load  $\varepsilon_V$  is modified in rate as  $t \mapsto \varepsilon_V(t/5)$ . In Figure 5.6 the response of the two cases is compared. The influence of the change in rate is clearly visible. Indeed, the exchange of heat with the environment makes the model rate-dependent. In order to clarify this concept, a further simulation has been performed to compare different loading rates, in both heat exchange and adiabatic cases. An initial temperature equal to 325 K has been chosen in this case. The results of such a comparison are highlighted in Figure 5.7, where it is easy to see that in the adiabatic case the variation of the loading rate does not affect the response, i.e., the adiabatic case is rate-independent: indeed, the curves related to the

adiabatic situations exactly overlap.

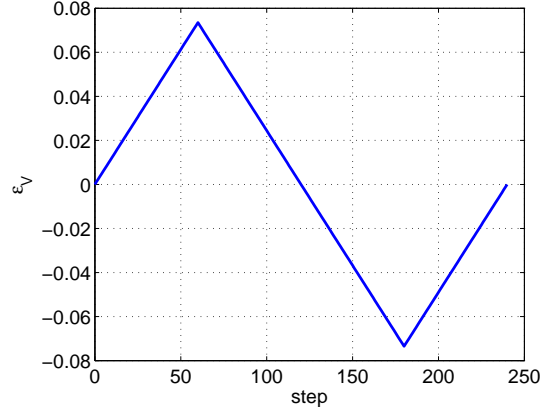


Figure 5.1: First strain history: trend of the variable  $\varepsilon_V$ .

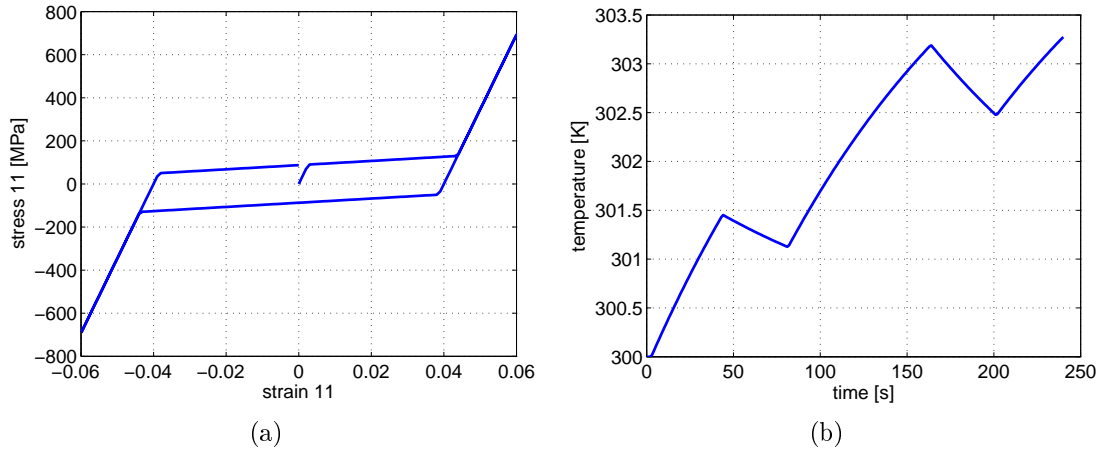


Figure 5.2: First strain history, martensitic conditions case: strain 11 versus stress 11 plot (a) and temperature plot (b).

A second choice for  $t \mapsto \varepsilon_V(t)$  is a multi-cycle test, displayed in Figure 5.8(a). Each cycle is highlighted with a different color, for better readability. The corresponding material response is reported in Figure 5.8(b-c). Also here, it is apparent that during the forward transformation the temperature increases with the increasing transformation strain, while on the contrary, during the reverse transformation the temperature decreases with the decreasing transformation strain, a behavior proved by several experimental evidences [262, 263] and correctly reproduced by the present model.

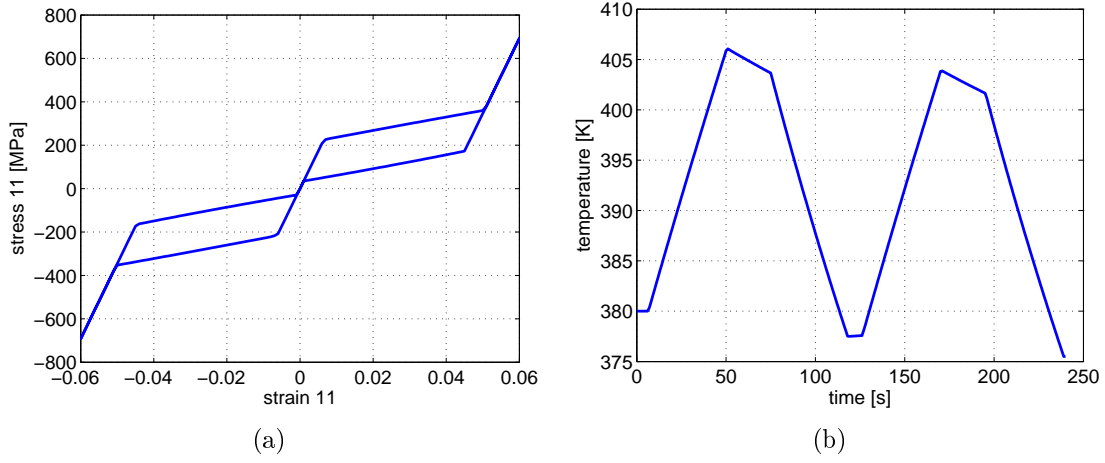


Figure 5.3: First strain history, superelastic conditions case: strain 11 versus stress 11 plot (a) and temperature plot (b).

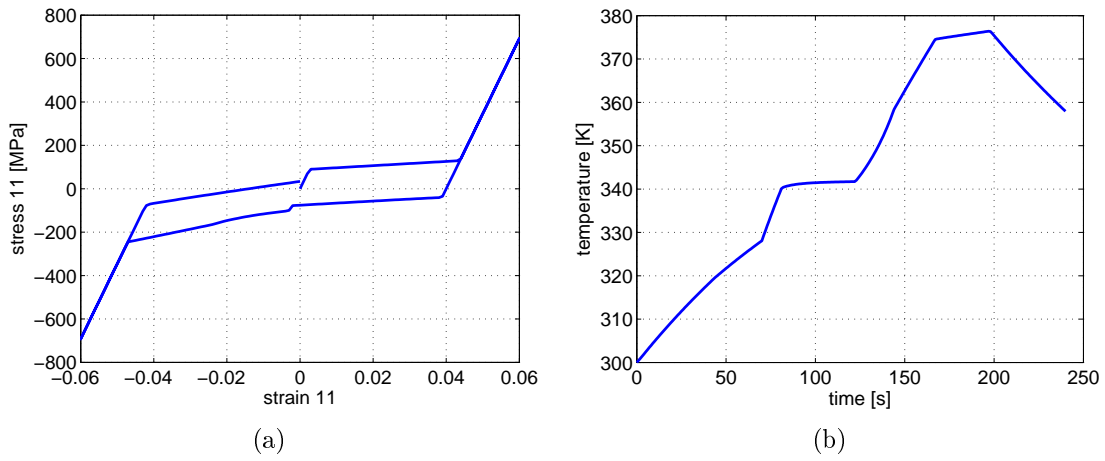


Figure 5.4: First strain history: strain 11 versus stress 11 plot (a) and temperature plot (b).

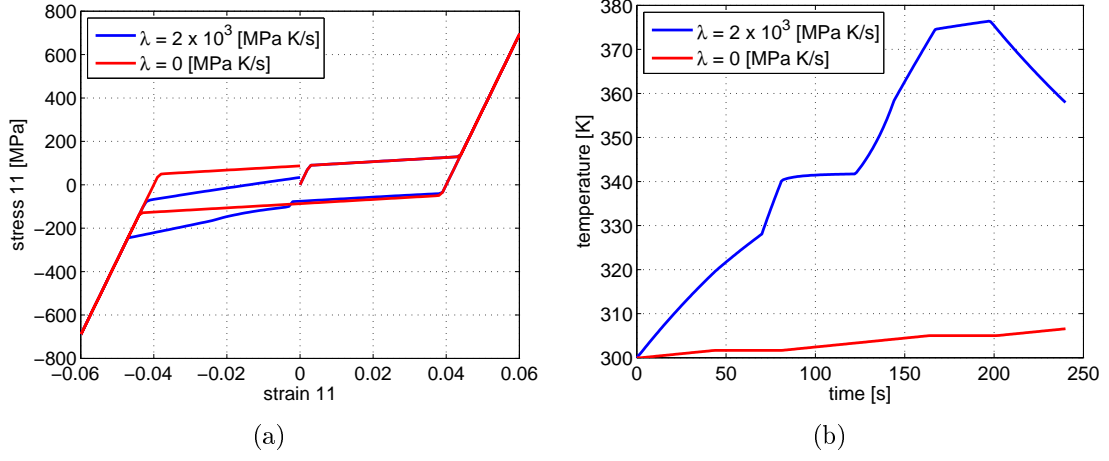


Figure 5.5: First strain history: comparison of the strain 11 versus stress 11 plots (a) and of the temperature trends (b) in the two cases heat exchange (blue) vs adiabatic (red).

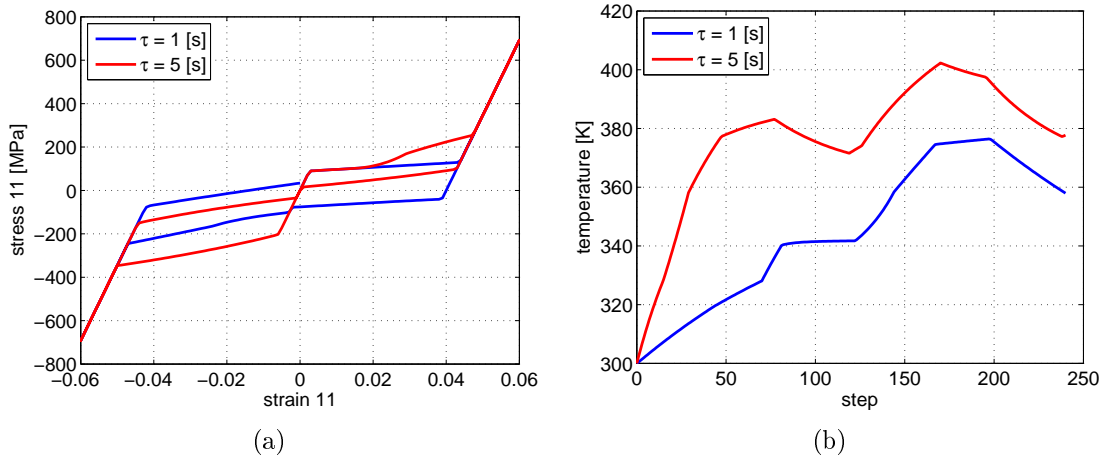


Figure 5.6: First strain history: comparison of the strain 11 versus stress 11 plots (a) and of the temperature trends (b) in the two cases  $\tau = 1$  s (blue) vs  $\tau = 5$  s (red).



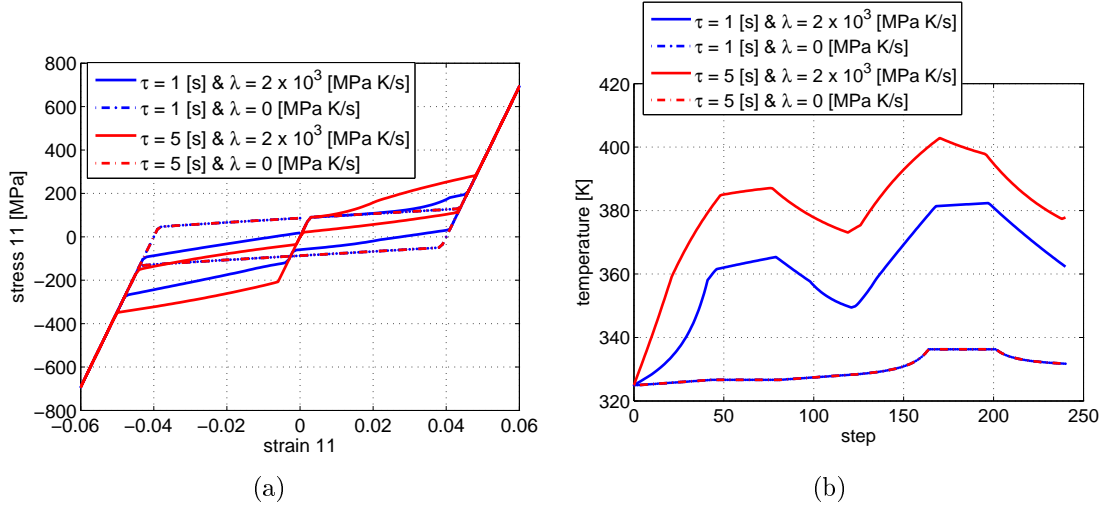


Figure 5.7: First strain history: comparison of the strain 11 versus stress 11 plots (a) and of the temperature trends (b) for changing rate and heat exchange coefficient.

### 5.6.5 Non-proportional tests

We present here also the material response for non-proportional biaxial tests. We perform two hourglass tests as well as a square test. The first hourglass test and the square test present the following strain tensor form

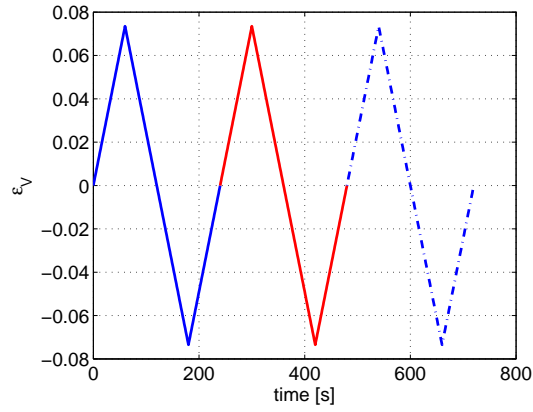
$$t \mapsto \boldsymbol{\varepsilon}(t) = \begin{bmatrix} \varepsilon_{11}(t) & 0 & 0 \\ 0 & \varepsilon_{22}(t) & 0 \\ 0 & 0 & 0 \end{bmatrix}$$

where the two components  $t \mapsto \varepsilon_{11}(t)$  and  $t \mapsto \varepsilon_{22}(t)$  are given. The strain tensor of the second hourglass test is instead

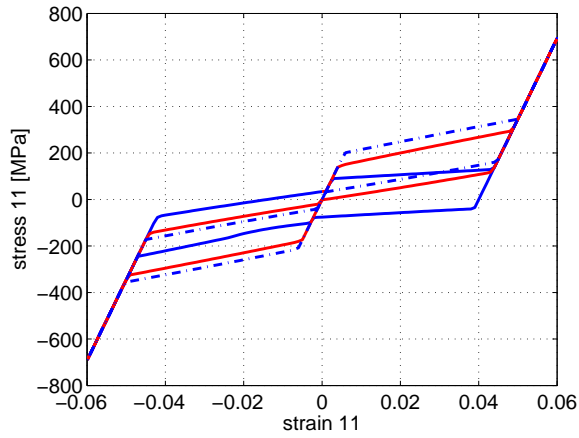
$$t \mapsto \boldsymbol{\varepsilon}(t) = \begin{bmatrix} \varepsilon_{11}(t) & \varepsilon_{12}(t) & 0 \\ \varepsilon_{12}(t) & 0 & 0 \\ 0 & 0 & 0 \end{bmatrix}$$

with  $t \mapsto \varepsilon_{11}(t)$  and  $t \mapsto \varepsilon_{12}(t)$  given.

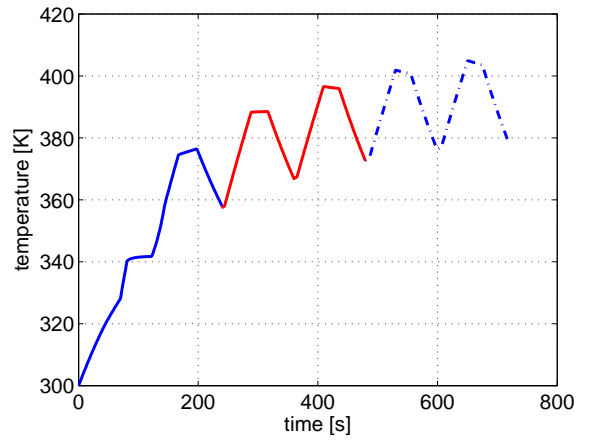
In Figures 5.9, 5.10, and 5.11 the imposed strain and the response in terms of stress/strain and temperature plots are presented. The results show that the model is capable of de-



(a)



(b)



(c)

Figure 5.8: Second strain history: trend of the variable  $\varepsilon_V$  (a), strain 11 versus stress 11 plot (b) and temperature trend plot (c). Each traction-compression cycle is highlighted with a different colour.

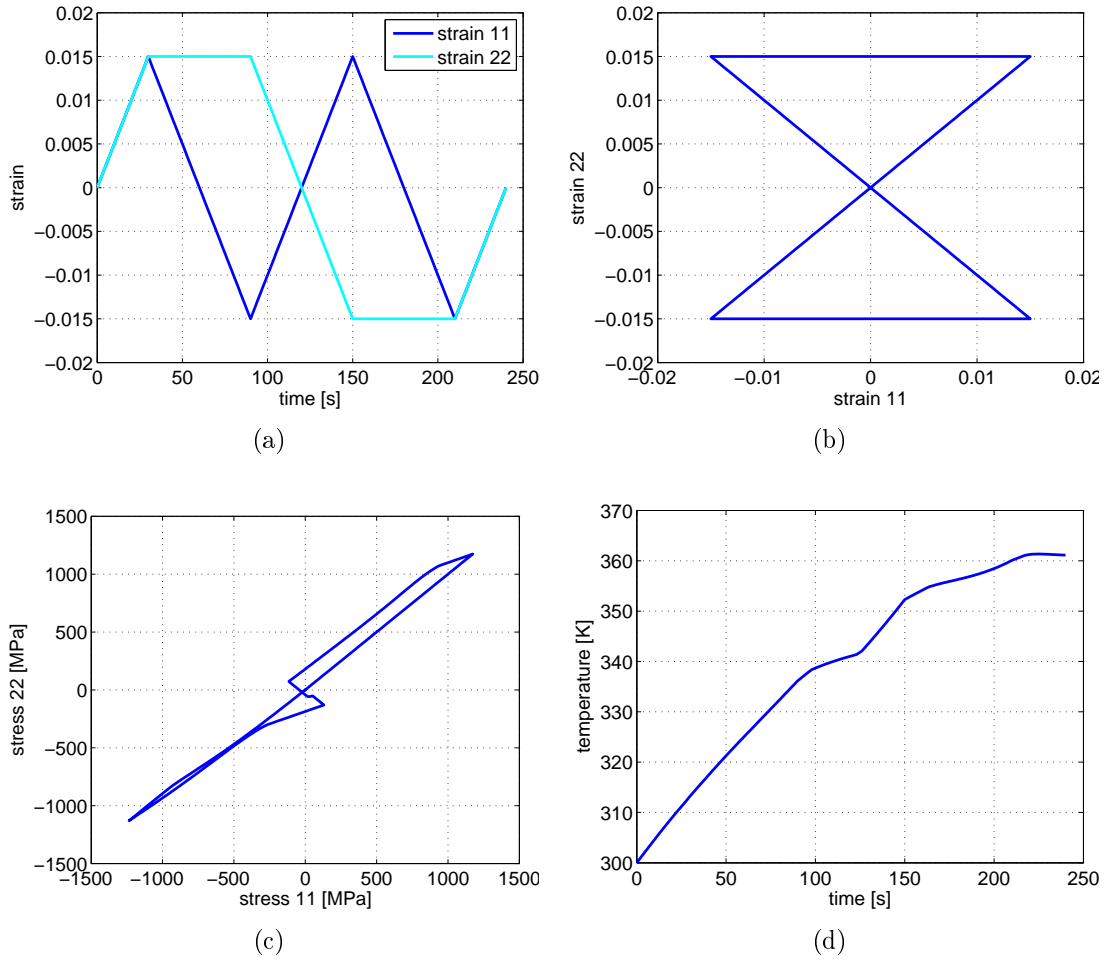


Figure 5.9: First hourglass strain history: trend of the strain 11 and strain 22 components (a), strain 11 versus strain 22 plot (b), stress 11 versus stress 22 plot (c) and temperature trend plot (d).

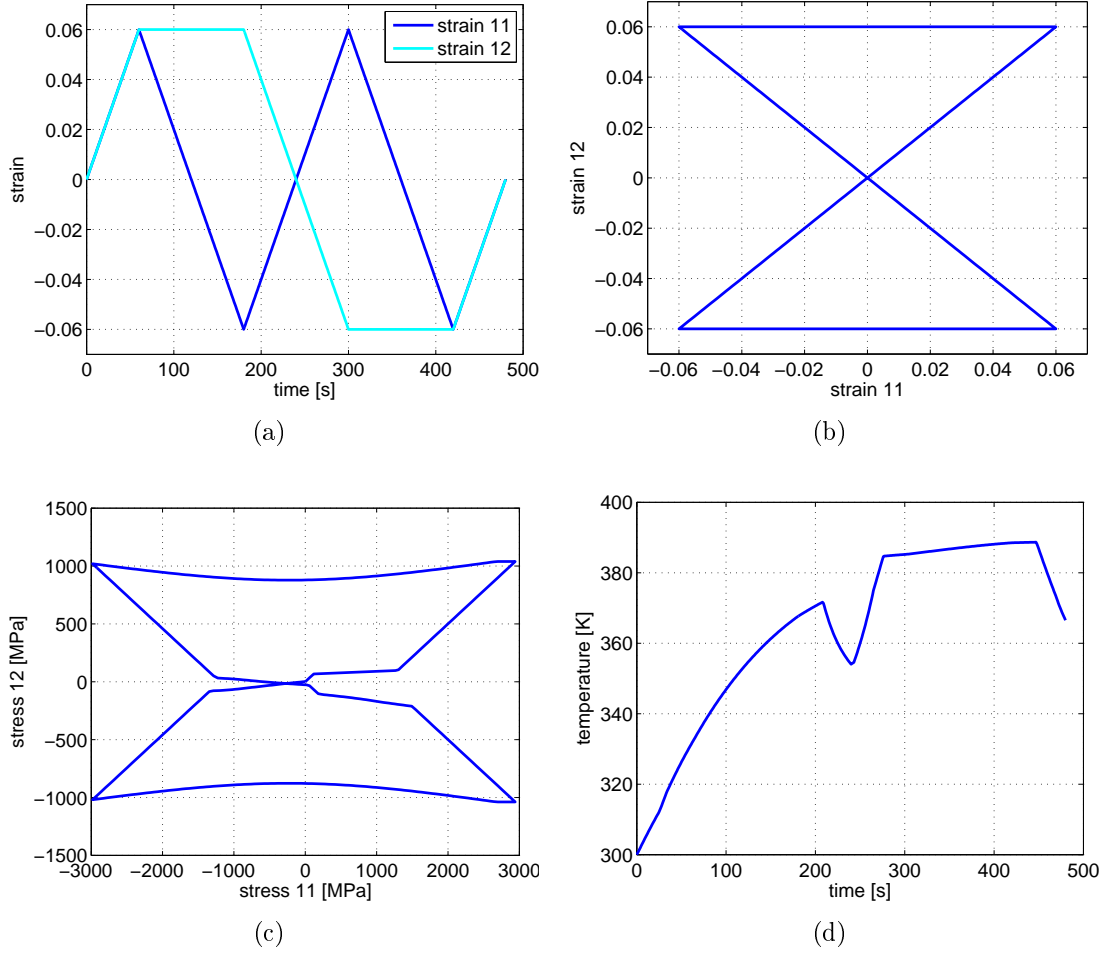


Figure 5.10: Second hourglass strain history: trend of the strain 11 and strain 12 components (a), strain 11 versus strain 12 plot (b), stress 11 versus stress 12 plot (c) and temperature trend plot (d).

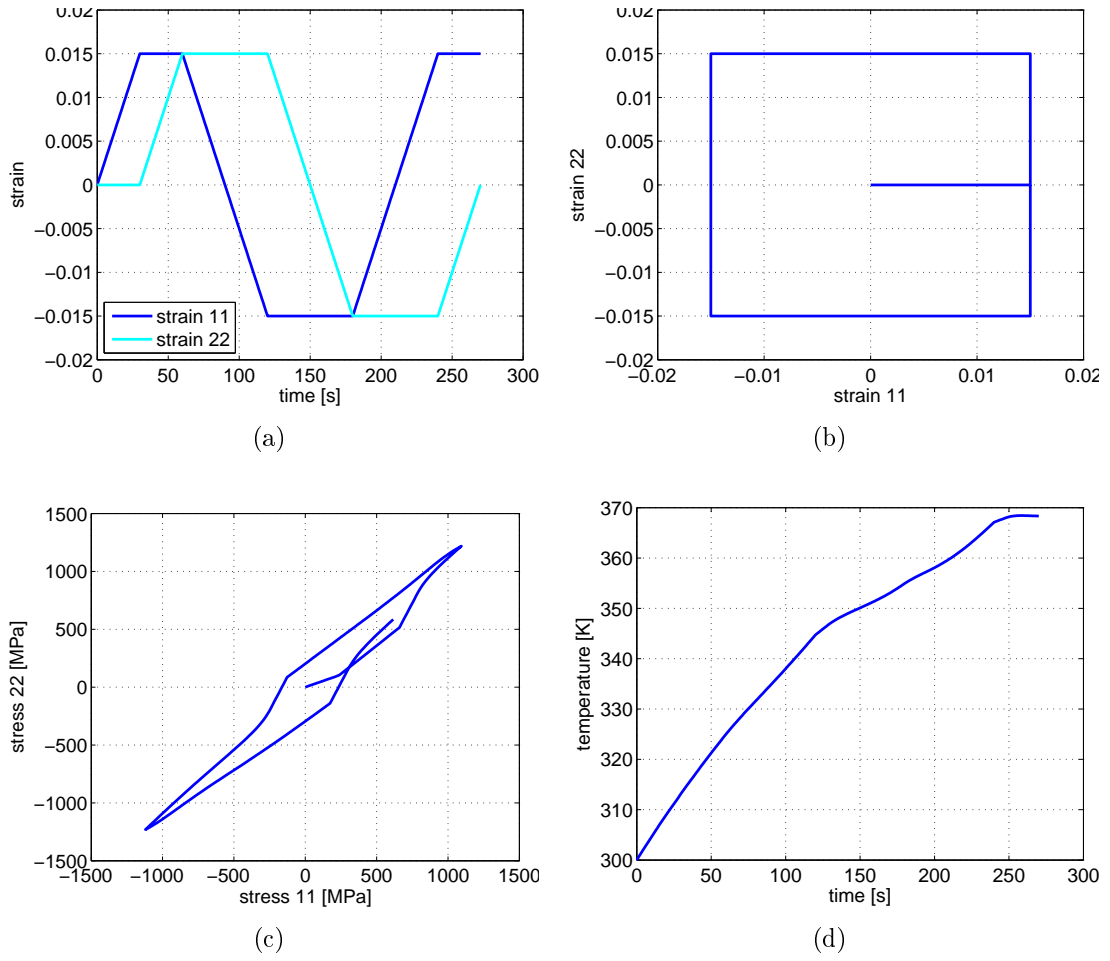


Figure 5.11: Square strain history: trend of the strain 11 and strain 22 components (a), strain 11 versus strain 22 plot (b), stress 11 versus stress 22 plot (c) and temperature trend plot (d).

scribing the coupled thermomechanical effects also in non-proportional tests.

### 5.6.6 Thermal tests

A set of thermal tests are presented, where a constant strain, with the same tensor form of the proportional tests and  $\varepsilon_V = 0.044$ , is imposed and the external temperature is cycled between 300 and 500 K. Different heating/cooling rates have been imposed in order to compare the time-dependent results. The curves are displayed in Figure 5.12: the model can properly reproduce a shape-memory actuator response.

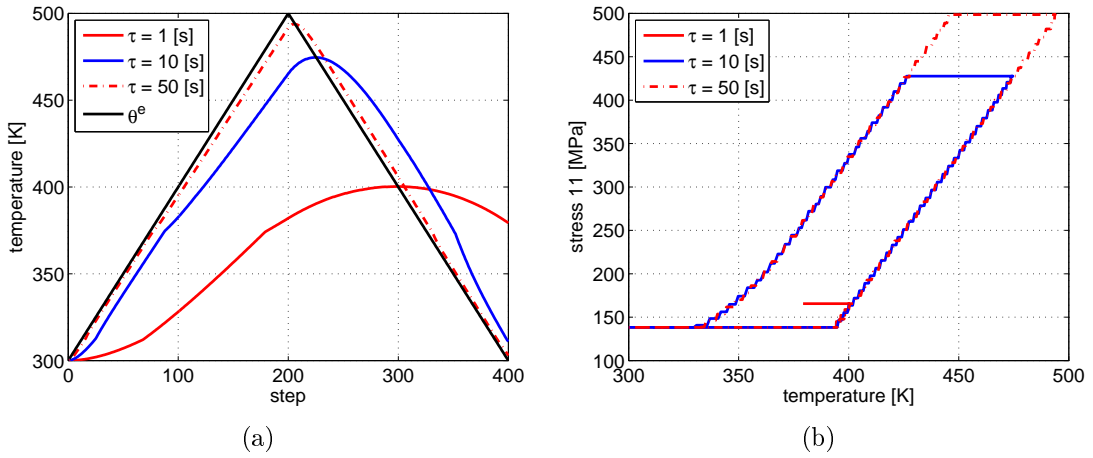


Figure 5.12: Thermal tests: comparison of the temperature plots (a) and of the temperature vs stress 11 plots (b) for changing heating/cooling rate.

## 5.7 Conclusions

Inspired by the GENERIC variational framework, we have presented a reformulation of a thermomechanically coupled model for SMA in terms of a generalized gradient flow of thermal and mechanical variables. This reformulation has been then specialized to the case of space-homogeneous fields, where it is coordinated with heat exchange with the external environment, here responsible for the rate-dependence in the model.

Based on this reformulation, a semi-implicit time-discrete scheme for the thermomechanically coupled system in the space-homogeneous setting has been presented. The scheme is proved to be unconditionally stable and convergent. In particular, the corresponding continuous counterpart admits a solution.

The performance of the time discretization has been assessed through a number uniaxial and biaxial numerical tests. At the algorithmical level, the nonlinear character of the constitutive model is resolved by a dedicated testing procedure, combined with the solution of a smooth differential system. The computational results prove that the model properly and robustly reproduces the thermomechanical behavior of the material with respect to different loading and environmental regimes.





## Chapter 6

# A three-dimensional finite-strain phenomenological model for shape-memory polymers

The present study is included in a paper which is currently in preparation.

### 6.1 Introduction

The increasing interest and employment of SMPs in the design of innovative devices motivates a deep investigation of the material behavior as well as the introduction of effective constitutive models. Several works available from the literature present experimental campaigns, e.g. [40, 330, 186, 337, 246, 320]. Noticeable progress has been made over the last decades in terms of constitutive modeling, from earlier simple stress-strain relationships and descriptions of shape-memory processes [244] to recent complex structure analyses at different levels [269, 165]; however, such a research is still an active field, since material behavior varies considerably due to the vast range of polymer types [136].

Several models have been developed for thermo-responsive SMPs; see [136] for a review. In the literature, two main approaches have been used to describe the behavior of thermo-responsive SMPs [88]. The first approach is based on the concept of phase transition: the material is assumed to be softer (lower Young's modulus) at high temperature and harder at low temperature; often, the high-temperature state is referred to as "rubbery" phase and the low-temperature state is called "glassy" state. During the phase transition, a fraction

of the material is in the glassy state while the remainder is in the rubbery state. Internal variables and constraints are used to describe the transition between the two phases, see, e.g., [186, 284, 41, 42, 357, 275, 45, 65, 66, 156, 293, 221]; in particular, a rule of mixture is generally introduced. The second approach is based on the standard linear viscoelastic models commonly used to simulate polymers behavior. The second approach is based on the standard linear viscoelastic models commonly used to simulate polymer behavior; see, e.g. [329, 2, 88, 231, 349, 111, 112, 230].

Therefore, the first-type models reproduce the overall macroscopic behavior of SMPs and may use non-physical parameters, such as the volume fractions of the material phases, while the second-type models describe the underlying mechanisms of the shape-memory effect, e.g. chain mobility and interface motion. The choice of the model to use depends on how many details we need to accurately describe material response, in relation to the investigated application. The first-type models can be the most efficient route in engineering applications, especially considering that they are usually less expensive in terms of computational time compared to the second-type models.

Motivated by the above considerations and following the line of the first-type models discussed above, the present chapter aims to introduce a constitutive model for thermo-responsive SMPs. The following consideration will be taken into account: in order to properly describe the shape-memory behavior of SMPs, a constitutive model should (i) be introduced within a thermodynamically consistent mathematical framework; (ii) be formulated in a three-dimensional setting to allow its application to a broad variety of cases; (iii) be developed in a finite-strain setting, since a fundamental feature of SMPs is their capability to undergo severe deformations; (iv) consider the peculiar thermomechanical features of SMPs, since temperature plays a key role in shape-fixing and shape-recovery.

The proposed model satisfies all the listed requirements and is motivated by the earlier work of Reese and coworkers [284], who introduced a three-dimensional model and an effective algorithm to simulate SMP behavior in various situations. Accordingly, the model is based on a phenomenological description of SMP behavior, considering a rubbery phase stable at temperatures above the transition range, and a glassy phase stable at temperatures below the transition range. A rule of mixture is introduced to describe the free energy distribution of the two phases.

The novelty of the proposed approach is the inclusion in the modeling formulation of several material features that are significant from the application point of view and that have

not been addressed to date. Specifically, the model reproduces both high-temperature and low-temperature shape-fixing, differently from [284] where only high-temperature shape-fixing is considered, and it takes into account the non-ideal behavior of real SMPs (i.e. imperfect shape-fixity and incomplete shape-recovery), which is not considered in [284]. To this purpose, we introduce additional tensorial and scalar quantities to reproduce the cited features. Thanks to the just mentioned novelties with respect to [284], the proposed model becomes very versatile and, therefore, it can be adapted to describe the behavior of a wide range of polymer types and operating conditions.

As further advantages of the proposed model, we recall that it presents a low number of material parameters, which can be derived from intuitive physical considerations. Moreover, the model can reproduce the overall SMP behavior using a relatively simple solution algorithm, thus entailing a low computational effort.

Model performances are assessed through several numerical tests ranging from uniaxial and biaxial tests to more complex simulations of biomedical devices. Model validation is performed through a comparisons with two sets of experimental data taken from the literature [107, 337].

The chapter is organized as follows. Section 6.2 and 6.3 present the proposed constitutive model in a time-continuous and time-discrete setting, respectively. Then, Section 6.4 describes the performed numerical simulations and the comparison with experimental data from the literature. Finally, conclusions are given in Section 6.5.

## 6.2 Time-continuous model formulation

This section addresses a three-dimensional phenomenological model for thermo-responsive SMPs, along the lines of the work by [284].

### 6.2.1 State and internal variables

In the framework of macroscopic modeling and of finite-strain continuum mechanics, we assume the total deformation gradient  $\mathbf{F}$  and temperature  $\theta$  as state variables. The right Cauchy-Green strain tensor and the Green-Lagrange strain tensor are then, respectively, defined as:

$$\mathbf{C} = \mathbf{F}^T \mathbf{F} \tag{6.1}$$

$$\mathbf{E} = \frac{\mathbf{C} - \mathbf{1}}{2} \quad (6.2)$$

where  $\mathbf{1}$  is the second-order identity tensor.

As mentioned in Section 6.1, the model aims to reproduce the shape-fixing and shape-recovery due to reversible state changes between the glassy and rubbery phases as well as to include, as a novelty, the description of both high-temperature and low-temperature shape-fixing and of the non-ideal behavior of realistic SMPs (i.e. imperfect shape-fixity and incomplete shape-recovery). In fact, since realistic SMP materials often display an imperfect shape-fixity and/or a limited shape-recovery, it becomes important to include such a behavior in the material response description. To this purpose, we propose to interpret the thermomechanical behavior of SMPs from a phenomenological viewpoint by exploiting the principles of continuum thermodynamics with internal variables, without explicitly incorporating details on the molecular interactions. We therefore introduce scalar and tensorial variables in the model formulation, as described in the following. We now provide a summary of the adopted variables and of their physical meaning.

As previously mentioned, we distinguish between a *glassy* and a *rubbery* phase: the first one stable at temperatures below the transition temperature, the second one stable at temperatures above the transition temperature. In the following, we adopt superscripts "g" and "r" to indicate the glassy and rubbery phase, respectively.

The volume fractions of the glassy and rubbery phases are represented by the scalar variables  $z^g$  and  $z^r$ , respectively, such that  $z^g, z^r \in [0, 1]$  and  $z^g + z^r = 1$ . Thanks to this last constraint, the model restricts itself to just one independent volume fraction,  $z^g$ , letting  $z^r = 1 - z^g$ .

We assume that the total deformation gradient  $\mathbf{F}$  is the same for both rubbery and glassy phase, such that:

$$\mathbf{F} = \mathbf{F}^{tg} = \mathbf{F}^{tr} \quad (6.3)$$

where  $\mathbf{F}^{tg}$  is the total deformation gradient of the glassy phase and  $\mathbf{F}^{tr}$  is the total deformation gradient of the rubbery phase.

To simulate the high-temperature shape-fixing, we introduce the *frozen* deformation gradient  $\mathbf{F}^f$ , i.e. the amount of temporary deformation which is stored during the high-temperature shape-fixing. This choice is motivated by the fact that the deformation induced by the high-temperature loading can be stored temporarily (i.e. "frozen") at low

temperatures by emerging molecular interactions; it can be released only when such interactions disappear upon subsequent heating over the transition temperature [186]. To model the storage of  $\mathbf{F}^f$ , we propose a local multiplicative decomposition of the total deformation gradient  $\mathbf{F}^{tg}$  into an *active* glassy phase contribution and a frozen contribution, respectively  $\mathbf{F}^g$  and  $\mathbf{F}^f$ . Therefore, we obtain:

$$\mathbf{F}^{tg} = \mathbf{F} = \mathbf{F}^g \mathbf{F}^f \quad (6.4)$$

It can be observed that the deformation gradient in the glassy phase,  $\mathbf{F}^g$ , can be easily derived once given  $\mathbf{F}$  and  $\mathbf{F}^f$ .

In the following, we adopt an elastoplastic behavior for the active glassy phase. Following a well-established approach [54], we assume a local multiplicative decomposition of the mechanical deformation gradient of the glassy phase,  $\mathbf{F}^g$ , into an elastic part  $\mathbf{F}^{eg}$ , defined with respect to an intermediate configuration, and a plastic part  $\mathbf{F}^{pg}$ , defined with respect to the reference configuration. Accordingly,

$$\mathbf{F}^g = \mathbf{F}^{eg} \mathbf{F}^{pg} \quad (6.5)$$

To reproduce the low-temperature shape-fixing procedure, and the subsequent shape-recovery (see Figure 1.14), we employ the plastic deformation gradient of the glassy phase,  $\mathbf{F}^{pg}$ . In fact, experimental tests, e.g. [293], show typical elastoplastic stress-strain curves for the glassy phase, with a (partially) recoverable plastic deformation accumulated during low-temperature shape-fixing. An appropriate evolution equation will be proposed in Subsection 6.2.5 to reproduce the recovery of such deformation.

To simulate the imperfect shape-fixing, we introduce a positive material parameter  $c$  governing the evolution of the frozen deformation gradient  $\mathbf{F}^f$ . Particularly, in case of perfect shape-fixing all the applied deformation is stored, i.e.  $\mathbf{F}^f = \mathbf{F}$  (and therefore  $\mathbf{F}^g = \mathbf{1}$ ) in Eq. (6.4); further details about the evolution of  $\mathbf{F}^f$  will be provided in Subsection 6.2.5.

Finally, to reproduce the incomplete shape-recovery, we introduce the *permanent* deformation gradient  $\mathbf{F}^p$ , taking into account the amount of applied deformation which is not recovered through heating. A further multiplicative decomposition is considered for the total deformation gradient  $\mathbf{F}^{tr} = \mathbf{F}$ , into an *active* rubbery phase contribution and an

irrecoverable contribution, as follows:

$$\mathbf{F}^{tr} = \mathbf{F} = \mathbf{F}^r \mathbf{F}^p \quad (6.6)$$

It can be observed that the deformation gradient in the rubbery phase,  $\mathbf{F}^r$ , can be easily derived once given  $\mathbf{F}$  and  $\mathbf{F}^p$ .

We assume a hyperelastic behavior for the rubbery phase, i.e. the mechanical deformation gradient in the rubbery phase  $\mathbf{F}^r$  coincides with the elastic part  $\mathbf{F}^{er}$ , as commonly accepted in the literature, e.g. [110].

Thanks to the adopted variables, the model is able to describe the classical shape-memory behavior of SMPs, as also demonstrated by the numerical simulations presented in Section 5.6. While the model by [284] can only reproduce an ideal shape-memory behavior, the proposed model includes the possibility to simulate both imperfect shape-fixity and incomplete shape-recovery and is therefore more realistic. Moreover, the introduction of the plastic deformation gradient in the glassy phase allows to simulate the low-temperature shape-fixing, again extending the model by [284].

## 6.2.2 Helmholtz free-energy function

The Helmholtz specific free energy  $\Psi = \Psi(\mathbf{F}^r, \mathbf{F}^g, z^g)$  is determined by employing the rule of mixtures, considering that the material is a combination of rubbery and glassy phases. In particular, we set:

$$\Psi = z^g \Psi^g + (1 - z^g) \Psi^r \quad (6.7)$$

where  $\Psi^g = \Psi^g(\mathbf{F}^g)$  and  $\Psi^r = \Psi^r(\mathbf{F}^r)$  are the free energies of the glassy and rubbery phases, respectively.

Accordingly to our assumptions on the behavior of the glassy and rubbery phases (see Subsection 6.2.1), we define the free-energy contributions as follows:

$$\Psi^g = \Psi^{eg} + \Psi^{pg} + \Psi_{th}^g + \Psi_{ref}^g \quad (6.8)$$

$$\Psi^r = \Psi^{er} + \Psi_{th}^r + \Psi_{ref}^r \quad (6.9)$$

where  $\Psi^{eg} = \Psi^{eg}(\mathbf{F}^{eg})$  and  $\Psi^{er} = \Psi^{er}(\mathbf{F}^{er})$  are the elastic contributions of the glassy and

rubbery phases, while  $\Psi^{pg} = \Psi^{pg}(\mathbf{F}^{pg})$  is the plastic contribution of the glassy phase;  $\Psi_{th}^i$  ( $i = g, r$ ) is the specific free energy related to thermal expansion;  $\Psi_{ref}^i$  ( $i = g, r$ ) is the specific free energy related to the temperature change with respect to the reference state, in which  $T = T_{ref}$ .

In the following we model the hyperelastic responses of the rubbery and glassy phases through a Saint Venant-Kirchhoff type expression. The Saint Venant-Kirchhoff model for hyperelasticity has been chosen here merely for its simplicity, since we are not considering one particular polymer type and the goal of our study is mainly to present a flexible phenomenological modeling framework for SMPs. Saint Venant-Kirchhoff model could be replaced by other hyperelasticity laws (e.g. Neo-Hookean, Arruda-Boyce, Ogden-Roxburgh), which allow a better description under tension and compression loading, according to the specific polymer under investigation. The free-energy contributions are defined as:

$$\Psi^{eg} = \frac{\lambda^g}{2} [\text{tr}(\mathbf{E}^{eg})]^2 + \mu^g \text{tr}(\mathbf{E}^{eg2}) \quad (6.10)$$

$$\Psi^{pg} = \frac{1}{2} h |\mathbf{E}^{pg}|^2 \quad (6.11)$$

$$\Psi^{er} = \frac{\lambda^r}{2} [\text{tr}(\mathbf{E}^{er})]^2 + \mu^r \text{tr}(\mathbf{E}^{er2}) \quad (6.12)$$

$$\Psi_{th}^g = -3\alpha^g \kappa^g (T - T_{ref}) \text{tr}[\mathbf{E}^g] \quad (6.13)$$

$$\Psi_{th}^r = -3\alpha^r \kappa^r (T - T_{ref}) \text{tr}[\mathbf{E}^r] \quad (6.14)$$

$$\Psi_{ref}^g = c^g \left[ (T - T_{ref}) - T \ln \frac{T}{T_{ref}} \right] + (u_{ref}^g - T s_{ref}^g) \quad (6.15)$$

$$\Psi_{ref}^r = c^r \left[ (T - T_{ref}) - T \ln \frac{T}{T_{ref}} \right] + (u_{ref}^r - T s_{ref}^r) \quad (6.16)$$

Here,  $\lambda^i$  and  $\mu^i$  ( $i = g, r$ ) are the first and second Lamé parameters, respectively;  $h$

is a positive parameter describing the material hardening;  $\alpha^i$  ( $i = g, r$ ) is the thermal expansion coefficient;  $\kappa^i$  ( $i = g, r$ ) is the bulk modulus;  $c^i$  ( $i = g, r$ ) is the specific heat capacity;  $T_{ref}$  is the reference temperature;  $u_{ref}^i$  and  $s_{ref}^i$  ( $i = g, r$ ) are respectively the internal energy and the entropy at the reference temperature. Finally,  $\mathbf{E}^{er}$ ,  $\mathbf{E}^{eg}$ , and  $\mathbf{E}^{pg}$  are the Green-Lagrange strain tensors defined as:

$$\mathbf{E}^{er} = \mathbf{E}^r = \frac{\mathbf{F}^{erT} \mathbf{F}^{er} - \mathbf{1}}{2} \quad (6.17)$$

$$\mathbf{E}^{eg} = \frac{\mathbf{F}^{egT} \mathbf{F}^{eg} - \mathbf{1}}{2} \quad (6.18)$$

$$\mathbf{E}^{pg} = \frac{\mathbf{F}^{pgT} \mathbf{F}^{pg} - \mathbf{1}}{2} \quad (6.19)$$

### 6.2.3 Clausius-Duhem inequality and dissipativity

Here, we present the derivation of the model equations and the evaluation of the dissipation inequality.

At first, the second law of thermodynamics in the form of the Clausius-Duhem inequality is evaluated [102, 86]:

$$-\rho \dot{\Psi} + \mathbf{S}^g : \dot{\mathbf{E}}^g + \mathbf{S}^r : \dot{\mathbf{E}}^r - \rho s \dot{T} - \frac{\mathbf{q} \cdot \nabla T}{T} \geq 0 \quad (6.20)$$

where  $\rho$  is the material density,  $s$  is the entropy and  $\mathbf{q}$  is the heat flux vector; the symbol  $\nabla$  represents the gradient operator.

The computation of  $\dot{\Psi}$  is now reported:

$$\dot{\Psi} = \frac{\partial \Psi}{\partial T} \dot{T} + z^g \frac{\partial \Psi^g}{\partial \mathbf{E}^g} : \dot{\mathbf{E}}^g + z^g \frac{\partial \Psi^g}{\partial \mathbf{E}^{pg}} : \dot{\mathbf{E}}^{pg} + (1 - z^g) \frac{\partial \Psi^r}{\partial \mathbf{E}^r} : \dot{\mathbf{E}}^r \quad (6.21)$$

Introducing Eq. (6.21) into the Clausius-Duhem inequality, we have:



$$\begin{aligned}
& -\rho \left[ \frac{\partial \Psi}{\partial T} \dot{T} + z^g \frac{\partial \Psi^g}{\partial \mathbf{E}^g} : \dot{\mathbf{E}}^g + z^g \frac{\partial \Psi^g}{\partial \mathbf{E}^{pg}} : \dot{\mathbf{E}}^{pg} + (1 - z^g) \frac{\partial \Psi^r}{\partial \mathbf{E}^r} : \dot{\mathbf{E}}^r \right] + \\
& + \mathbf{S}^g : \dot{\mathbf{E}}^g + \mathbf{S}^r : \dot{\mathbf{E}}^r - \rho s \dot{T} - \frac{\mathbf{q} \cdot \nabla T}{T} \geq 0 \quad (6.22)
\end{aligned}$$

$$\begin{aligned}
& -\rho \left( \frac{\partial \Psi}{\partial T} + s \right) \dot{T} + \rho z^g \left( -\frac{\partial \Psi^g}{\partial \mathbf{E}^g} + \mathbf{S}^g \right) : \dot{\mathbf{E}}^g + \rho(1 - z^g) \left( -\frac{\partial \Psi^r}{\partial \mathbf{E}^r} + \mathbf{S}^r \right) : \dot{\mathbf{E}}^r \\
& - \rho z^g \frac{\partial \Psi^g}{\partial \mathbf{E}^{pg}} : \dot{\mathbf{E}}^{pg} - \frac{\mathbf{q} \cdot \nabla T}{T} \geq 0 \quad (6.23)
\end{aligned}$$

The term related to plasticity is traditionally expressed according to the plastic velocity gradient, defined as:

$$\mathbf{L}^{pg} := \dot{\mathbf{F}}^{pg} \mathbf{F}^{pg-1} \quad (6.24)$$

Therefore, we can reformulate expression (6.23) as:

$$\begin{aligned}
& -\rho \left( \frac{\partial \Psi}{\partial T} + s \right) \dot{T} + \rho z^g \left( -\frac{\partial \Psi^g}{\partial \mathbf{E}^g} + \mathbf{S}^g \right) : \dot{\mathbf{E}}^g + \rho(1 - z^g) \left( -\frac{\partial \Psi^r}{\partial \mathbf{E}^r} + \mathbf{S}^r \right) : \dot{\mathbf{E}}^r \\
& - \rho z^g \mathbf{F}^{pg} \frac{\partial \Psi^g}{\partial \mathbf{E}^{pg}} \mathbf{F}^{pgT} : \mathbf{L}^{pg} - \frac{\mathbf{q} \cdot \nabla T}{T} \geq 0 \quad (6.25)
\end{aligned}$$

From the Clausius-Duhem inequality we can define the constitutive equations:

$$\begin{aligned}
\mathbf{S}^g &= \frac{\partial \Psi^g}{\partial \mathbf{E}^g} = \mathbf{F}^{pg-1} \frac{\partial \Psi^{eg}}{\partial \mathbf{E}^{eg}} \mathbf{F}^{pg-T} + \frac{\partial \Psi_{th}^g}{\partial \mathbf{E}^g} = \\
&= \mathbf{F}^{pg-1} (\lambda^g \text{tr}(\mathbf{E}^{eg}) \mathbf{1} + 2\mu^g \mathbf{E}^{eg}) \mathbf{F}^{pg-T} - 3\alpha^g \kappa^g (T - T_{ref}) \mathbf{1} \quad (6.26)
\end{aligned}$$

$$\mathbf{S}^r = \frac{\partial \Psi^r}{\partial \mathbf{E}^r} = \frac{\partial \Psi^{er}}{\partial \mathbf{E}^{er}} + \frac{\partial \Psi_{th}^r}{\partial \mathbf{E}^r} = \lambda^r \text{tr}(\mathbf{E}^{er}) \mathbf{1} + 2\mu^r \mathbf{E}^{er} - 3\alpha^r \kappa^r (T - T_{ref}) \mathbf{1} \quad (6.27)$$

$$s = -\frac{\partial \Psi}{\partial T} = s_{ref} - \frac{\partial z^g}{\partial T} (\Psi^g - \Psi^r) + 3\alpha^r \kappa^r \text{tr}[\mathbf{E}^r] + 3\alpha^g \kappa^g \text{tr}[\mathbf{E}^g] + c \ln \frac{T}{T_{ref}} - \frac{\partial \Psi}{\partial \mathbf{F}^f} : \frac{\partial \mathbf{F}^f}{\partial T} - \frac{\partial \Psi}{\partial \mathbf{F}^p} : \frac{\partial \mathbf{F}^p}{\partial T} \quad (6.28)$$

$$\mathbf{X}^g := -\mathbf{F}^{pg} \frac{\partial \Psi^g}{\partial \mathbf{E}^{pg}} \mathbf{F}^{pgT} = \mathbf{C}^{eg} \frac{\partial \Psi^{eg}}{\partial \mathbf{E}^{eg}} - \mathbf{F}^{pg} \frac{\partial \Psi^{pg}}{\partial \mathbf{E}^{pg}} \mathbf{F}^{pgT} = \mathbf{C}^{eg} (\lambda^g \text{tr}(\mathbf{E}^{eg}) \mathbf{1} + 2\mu^g \mathbf{E}^{eg}) - h \mathbf{F}^{pg} \mathbf{E}^{pg} \mathbf{F}^{pgT} \quad (6.29)$$

with  $\mathbf{X}^g$  the thermodynamic force associated to the plastic velocity gradient, where we identify the Mandel stress  $\mathbf{M}^g := \mathbf{C}^{eg} \frac{\partial \Psi^g}{\partial \mathbf{E}^{eg}}$ .

It is worth highlighting that the quantities  $z^g, \mathbf{F}^f, \mathbf{F}^p$  cannot be considered internal variables, so the Clausius-Duhem inequality does not restrain their evolution laws. Moreover, such variables are only dependent on temperature: therefore, when  $\dot{\Psi}$  is calculated, they are incorporated into  $\frac{\partial \Psi}{\partial T}$ .

In order to satisfy the second law of thermodynamics, we need positive mechanical and thermal dissipation. Since we are in the isotropic case, the plastic velocity gradient can be identified with its symmetric part, i.e.  $\mathbf{L}^{pg} \approx \mathbf{D}^{pg} = \frac{1}{2} \left( \dot{\mathbf{F}}^{pg} \mathbf{F}^{pg-1} + \mathbf{F}^{pg-T} [\dot{\mathbf{F}}^{pg}]^T \right)$ . We can therefore express the mechanical dissipation as:

$$\mathbf{X}^g : \mathbf{D}^{pg} \geq 0 \quad (6.30)$$

To ensure the positiveness of the mechanical dissipation term, we assume a convex limit function:

$$F_Y = |\text{dev}(\mathbf{X}^g)| - R^{pg} \quad (6.31)$$

and we express the flow rule according to the normality property:

$$\mathbf{D}^{pg} = \dot{\gamma} \frac{\partial F_Y}{\partial \mathbf{X}^g} = \dot{\gamma} \frac{\text{dev}(\mathbf{X}^g)}{|\text{dev}(\mathbf{X}^g)|} \quad (6.32)$$

Considering the definition of the plastic velocity gradient, Eq. (6.24), the expression (6.32) can be equivalently written as:

$$\dot{\mathbf{F}}^{pg} = \dot{\gamma} \frac{\partial F_Y}{\partial \mathbf{X}^g} \mathbf{F}^{pg} = \dot{\gamma} \frac{\text{dev}(\mathbf{X}^g)}{|\text{dev}(\mathbf{X}^g)|} \mathbf{F}^{pg} \quad (6.33)$$

Finally, we enforce the Kuhn-Tucker conditions:

$$\dot{\gamma} \geq 0, \quad F_Y \leq 0, \quad \dot{\gamma} F_Y = 0. \quad (6.34)$$

The thermal dissipation is:

$$-\frac{\mathbf{q} \cdot \nabla T}{T} \geq 0 \quad (6.35)$$

To guarantee the positiveness of the thermal dissipation term, we can assume  $\mathbf{q} = -k_{th} \nabla T$  according to the Fourier law for the heat conduction, with  $k_{th}$  the heat conduction coefficient of the material.

## 6.2.4 Constitutive equations

Applying a standard Coleman-Noll procedure on the Helmholtz free energy [71, 102], we derive the constitutive equations. The full derivation is reported in the Appedix.

The expressions of the second Piola-Kirchhoff stress tensors of the glassy and rubbery phases, respectively  $\mathbf{S}^g$  and  $\mathbf{S}^r$ , and of the thermodynamic force  $\mathbf{X}^g$  related to the plastic deformation read:

$$\mathbf{S}^g = \mathbf{F}^{pg-1} (\lambda^g \text{tr}(\mathbf{E}^{eg}) \mathbb{1} + 2\mu^g \mathbf{E}^{eg}) \mathbf{F}^{pg-T} - 3\alpha^g \kappa^g (T - T_{ref}) \mathbb{1} \quad (6.36)$$

$$\mathbf{S}^r = \lambda^r \text{tr}(\mathbf{E}^{er}) \mathbb{1} + 2\mu^r \mathbf{E}^{er} - 3\alpha^r \kappa^r (T - T_{ref}) \mathbb{1} \quad (6.37)$$

$$\mathbf{X}^g = \mathbf{C}^{eg}(\lambda^g \text{tr}(\mathbf{E}^{eg}) \mathbf{1} + 2\mu^g \mathbf{E}^{eg}) - h \mathbf{F}^{pg} \mathbf{E}^{pg} \mathbf{F}^{pgT} \quad (6.38)$$

From the second Piola-Kirchhoff stress tensors, the Cauchy stresses for the glassy and rubbery phases can be derived according to the well-known formulas [54]:

$$\sigma^g = J^{eg-1} \mathbf{F}^{eg} \mathbf{S}^g \mathbf{F}^{egT} \quad (6.39)$$

$$\sigma^r = J^{r-1} \mathbf{F}^r \mathbf{S}^r \mathbf{F}^{rT} \quad (6.40)$$

where  $J^{eg}$  and  $J^r$  are the positive determinants of the glassy and rubbery elastic deformation gradient, respectively. The total Cauchy stress  $\sigma$  can be derived through a rule of mixtures, as:

$$\sigma = z^g \sigma^g + (1 - z^g) \sigma^r \quad (6.41)$$

### 6.2.5 Evolution equations

In this subsection we define the equations governing the evolution of the variables presented in Subsection 6.2.1, i.e.  $z^g$ ,  $\mathbf{F}^{pg}$ ,  $\mathbf{F}^f$ , and  $\mathbf{F}^p$ .

We start by assuming the following evolution for the volume fraction of the glassy phase  $z^g$ , as similarly proposed in [284]:

$$z^g = \begin{cases} 1 & \text{if } \theta \leq \theta_t - \Delta\theta \\ \frac{1}{1 + \exp[2w(\theta - \theta_t)]} & \text{if } \theta_t - \Delta\theta < \theta < \theta_t + \Delta\theta \\ 0 & \text{if } \theta \geq \theta_t + \Delta\theta \end{cases} \quad (6.42)$$

where  $\theta_t$  is the transition temperature and  $\Delta\theta$  represents the half-width of the transition temperature range, i.e.  $\Delta\theta = \theta_{\text{high}} - \theta_t = \theta_t - \theta_{\text{low}}$ , with  $\theta_{\text{high}}$  and  $\theta_{\text{low}}$  respectively the upper and lower limit of the transition range. The material parameter  $w$  is a positive constant related to the smoothness of the curve within the transition temperature range. Further details about a proper choice of  $w$  can be found in [284]. According to Eq. (6.42),  $z^g$  depends only on temperature  $\theta$  and ranges between 0 (i.e. rubbery phase at high temperatures) and 1 (i.e. glassy phase at low temperatures). Both glassy and rubbery phases coexist for temperatures  $\theta_t - \Delta\theta < \theta < \theta_t + \Delta\theta$ .

Then, we assume the following evolution for the plastic deformation gradient of the glassy phase,  $\mathbf{F}^{pg}$ :

$$\mathbf{F}^{pg} = \begin{cases} \begin{array}{ll} \text{if } \theta \leq \theta_t - \Delta\theta & \text{evolves according to assigned flow rule} \\ \text{OR} & \\ \text{if } \{ \theta_t - \Delta\theta < \theta < \theta_t + \Delta\theta \text{ and } \dot{\theta} \leq 0 \} & \end{array} \\ \text{constant} & \text{if } \{ \theta_t - \Delta\theta < \theta < \theta_t + \Delta\theta \text{ and } \dot{\theta} > 0 \} \\ 1 & \text{otherwise} \end{cases} \quad (6.43)$$

i.e.  $\mathbf{F}^{pg}$  can only evolve when the material is deformed at lower temperatures than the transition range, or at decreasing temperatures inside the transition range. The glassy plastic deformation is recovered when temperature increases over the transformation range, so that we simply have  $\mathbf{F}^{pg} = \mathbf{1}$ ; it is worth to recall that in this last case, i.e. for  $\theta \geq \theta_t + \Delta\theta$ , the glassy phase is not present ( $z^g = 0$  in Eq. (6.42)).

Regarding the flow rule for the plastic deformation gradient of the glassy phase,  $\mathbf{F}^{pg}$  (see Eq. (6.43)), we follow standard arguments [353, 86] and adopt the following flow rule:

$$\dot{\mathbf{F}}^{pg} = \dot{\gamma} \frac{\text{dev}(\mathbf{X}^g)}{|\text{dev}(\mathbf{X}^g)|} \mathbf{F}^{pg} \quad (6.44)$$

where  $\dot{\gamma}$  is the positive plastic consistent parameter.

The limit function is assumed as:

$$F_Y = |\text{dev}(\mathbf{X}^g)| - R^{pg} \quad (6.45)$$

where  $R^{pg}$  is the limit yield stress.

Further details regarding the derivation of the flow rule for the glassy phase plasticity are reported in Subsection 6.2.3.

Then, we assume the following evolution law for the frozen deformation gradient  $\mathbf{F}^f$ :

$$\mathbf{F}^f = \begin{cases} c(\mathbf{F} - \mathbf{1}) + \mathbf{1} & \text{if } \theta \geq \theta_t + \Delta\theta \\ \text{constant} & \text{otherwise} \end{cases} \quad (6.46)$$

As already mentioned in Subsection 6.2.1,  $c$  is a material parameter allowing to reproduce the imperfect shape-fixing. It ranges between 0 and 1: the shape-fixing is perfect when  $c = 1$ , so that  $\mathbf{F}^f = \mathbf{F}$  (i.e. all the applied deformation is stored); the shape-fixing is imperfect when  $0 < c < 1$ ; whereas if  $c = 0$  there is no shape-fixing.

Finally, we assume the following evolution for the permanent deformation gradient  $\mathbf{F}^p$ :

$$\mathbf{F}^p = \begin{cases} c^p (\mathbf{F}^f + \mathbf{F}^{pg} - 2 \cdot \mathbf{1}) + \mathbf{1} & \text{if } \{ \theta \leq \theta_t + \Delta\theta \text{ and } \|\mathbf{E}^p\| \geq 0 \} \\ \text{constant} & \text{otherwise} \end{cases} \quad (6.47)$$

A fraction of both deformation gradients  $\mathbf{F}^f$  and  $\mathbf{F}^{pg}$  is thus stored in the permanent deformation gradient  $\mathbf{F}^p$ , as an irreversible accumulated deformation. The parameter  $c_p$ , ranging between 0 and 1, tunes the shape-recovery extent: the shape-recovery is complete when  $c^p = 0$ , i.e. when  $\mathbf{F}^p = \mathbf{1}$ ; it is incomplete when  $0 < c^p < 1$ ; no shape-recovery is present if  $c^p = 1$ . The assumption  $\|\mathbf{E}^p\| \geq 0$  is also stated (where  $\mathbf{E}^p = (\mathbf{F}^{pT} \mathbf{F}^p - \mathbf{1})/2$  and  $\|\cdot\|$  denotes the Euclidean norm), i.e. the norm of the Green-Lagrange strain tensor related to the permanent deformation gradient can never decrease during time.

### 6.2.6 Model parameters

The proposed model presents the following material parameters: (i) four elastic material parameters for the glassy and rubbery phases, i.e. the Young's moduli  $E^g$  and  $E^r$  and the Poisson's coefficients  $\nu^g$  and  $\nu^r$ ; (ii) the stress limit  $R^{pg}$  for plastic yielding of the glassy phase; (iii) the plastic hardening coefficient  $h$ ; (iv) the parameter  $\Delta\theta$ , defining half-width of the temperature range; (v) the transformation temperature  $\theta_t$ ; (vi) the transformation coefficient  $w$ ; (vii) the coefficient  $c$  to tune imperfect shape-fixing; (viii) the coefficient  $c_p$  to tune incomplete shape-recovery.

All the listed parameters have a physical interpretation and can be intuitively derived. The mechanical parameters related to the hyperelastic responses of the rubbery and glassy phases (i.e.,  $E^g, E^r, \nu^g, \nu^r$ ) and to the plastic glassy phase response (i.e.,  $R^{pg}, h$ ) are standard parameters adopted in the constitutive modeling of SMPs and are widely used in the literature. The parameters  $\Delta\theta$  and  $\theta_t$  clearly define the transition temperature range, while  $w$  tunes the smoothness of the rubbery/glassy phase transition (see also [284]). Finally,  $c$  and  $c_p$  are two scalars used to add a simple but effective description of the non-ideal behavior of SMPs to the model formulation.

### 6.3 Time-discrete model formulation

We now elaborate on a possible algorithmic treatment of the model equations presented in Section 6.2. The terms related to the thermal expansion and to the temperature change with respect to the reference configuration have been neglected in the finite element implementation of the model, since their impact is significantly lower than the mechanical contribution. For the sake of notation simplicity, we use subscript  $i - 1$  for all the variables evaluated at previous time  $t_{i-1}$ , while we adopt subscript  $i$  for all the variables computed at current time  $t_i$ .

We assume as given the state variables  $\theta_{i-1}, \mathbf{F}_{i-1}^{pg}, \mathbf{F}_{i-1}^f, \mathbf{F}_{i-1}^p$  at previous time  $t_{i-1}$ , and the total deformation gradient  $\mathbf{F}_i$  and the temperature  $\theta_i$  at the current time  $t_i$ .

In order to derive the current time solution, three cases are distinguished according to the current temperature  $\theta_i$ , as described in the following. For each case,  $z_i^g, \mathbf{F}_i^{pg}, \mathbf{F}_i^f, \mathbf{F}_i^p$  are derived, by integrating the evolution equations presented in the previous section. Regarding the glassy phase plasticity, the plastic deformation gradient is calculated according to a classical return-mapping algorithm [298], reported in Table 6.5. Specifically, we apply the exponential mapping scheme to the evolution equation (6.44) of the glassy plastic deformation gradient  $\mathbf{F}^{pg}$ . Accordingly, we obtain:

$$\mathbf{F}_i^{pg} = \exp \left( \Delta\gamma \frac{\text{dev}(\mathbf{X}_i^g)}{|\text{dev}(\mathbf{X}_i^g)|} \right) \mathbf{F}_{i-1}^{pg} \quad (6.48)$$

where  $\Delta\gamma = \int_{t_{i-1}}^{t_i} \dot{\gamma} dt$ . Since we are in the isotropic case, the quantity on the right-hand side of Eq. (6.48) is symmetric (see the 6.2.3 for further details): 6 equations could therefore be considered instead of 9 when calculating the glassy phase plasticity evolution. However, by considering the full set of 9 equations, the algorithm maintains a more general character, allowing for future extensions of the model to the anisotropic case. All the remaining model equations are directly evaluated at time  $t_i$ . The main structure of the time-discrete algorithm is presented in Table 6.1.

*First case:*  $\theta_i \geq \theta_t + \Delta\theta$

In such case, only the rubbery phase is present, i.e.  $z_i^g = 0$ ; see Eq. (6.42). The frozen deformation gradient  $\mathbf{F}_i^f$  is stored according to Eq. (6.46), the permanent deformation gradient  $\mathbf{F}^p$  remains constant according to Eq. (6.47) and the glassy plastic deformation

gradient  $\mathbf{F}_i^{pg}$  is completely recovered, i.e.  $\mathbf{F}_i^{pg} = \mathbf{1}$  (see Eq. (6.43)). Table 6.2 reports the adopted algorithm.

*Second case:*  $\theta_t - \Delta\theta < \theta_i < \theta_t + \Delta\theta$

In such case, both the rubbery and glassy phases are present, i.e.  $z_i^g \in [0, 1]$ ; see Eq. (6.42). The frozen and the permanent deformation gradients,  $\mathbf{F}_i^f$  and  $\mathbf{F}_i^p$  respectively, remain constant according to Eqs. (6.46) and (6.47). The glassy plastic deformation gradient  $\mathbf{F}_i^{pg}$  is allowed to evolve according to the return-mapping algorithm reported in Table 6.5 only if the current temperature is not increasing, while it remains constant otherwise (see Eq. (6.43)). Table 6.3 reports the adopted algorithm.

*Third case:*  $\theta_i \leq \theta_t - \Delta\theta$

In such case, only the glassy phase is present, i.e.  $z_i^g = 1$ ; see Eq. (6.42). The frozen deformation gradient  $\mathbf{F}_i^f$  remains constant, while the glassy plastic deformation gradient  $\mathbf{F}_i^{pg}$  is allowed to evolve according to the return-mapping algorithm reported in Table 6.5. The permanent deformation gradient  $\mathbf{F}_i^p$  is derived through Eq. (6.47). Table 6.4 reports the adopted algorithm.

Finally, the total Cauchy stress  $\sigma$  is calculated using the mixture rule reported in Eq. (6.41).

The implicit implementation of FEM requires also the formulation of the consistent tangent matrix. To avoid coding of complex equations, while maintaining a good convergence rate and an efficient numerical approximation of the tangent moduli, we adopt a numerical Jacobian fourth-order tensor as proposed by [321].

## 6.4 Numerical tests

The present section is devoted to several numerical simulations to demonstrate the performances of the presented constitutive model as well as to verify the effectiveness of the proposed algorithm. The simulations are quasi-static and include simpler uniaxial and biaxial tests as well as complex analyses of two biomedical SMP devices. A comparison with experimental data available from the literature [337, 107] is also provided to effectively validate the model. Particularly, we perform the following finite element analyses:



Table 6.1: Numerical algorithm for the proposed SMP model.

*Given quantities:*  $\theta_{i-1}, \mathbf{F}_{i-1}^f, \mathbf{F}_{i-1}^p, \mathbf{F}_{i-1}^{pg}, \mathbf{F}_i, \theta_i$

- IF  $\theta_i \geq \theta_t + \Delta\theta$

**CASE 1** (see Table 6.2)

- ELSE IF  $\theta_t - \Delta\theta \leq \theta_i \leq \theta_t + \Delta\theta$

**CASE 2** (see Table 6.3)

- ELSE IF  $\theta_i \leq \theta_t - \Delta\theta$

**CASE 3** (see Table 6.4)

- END IF

*Compute:*

$$\mathbf{F}_i^r = \mathbf{F}_i \mathbf{F}_i^{p-1}$$

$$\mathbf{F}_i^{eg} = \mathbf{F}_i \mathbf{F}_i^{f-1} \mathbf{F}_i^{pg-1}$$

$$\mathbf{F}_i^g = \mathbf{F}_i^{eg} \mathbf{F}_i^{pg}$$

total Cauchy stress  $\sigma$  through Eq.(6.41)

Table 6.2: Numerical algorithm for CASE 1.

*Compute:*

$$z_i^g = 0$$

$$\mathbf{F}_i^f = c(\mathbf{F}_i - \mathbf{1}) + \mathbf{1}$$

$$\mathbf{F}_i^p = \mathbf{F}_{i-1}^p$$

$$\mathbf{F}_i^{pg} = \mathbf{1}$$

Table 6.3: Numerical algorithm for CASE 2.

*Compute:*

$$z_i^g = \frac{1}{1 + \exp [2w (\theta_i - \theta_t)]}$$

$$\mathbf{F}_i^f = \mathbf{F}_{i-1}^f$$

$$\mathbf{F}_i^p = \mathbf{F}_{i-1}^p$$

- **IF**  $\theta_i > \theta_{i-1}$

$$\mathbf{F}_i^{pg} = \mathbf{F}_{i-1}^{pg}$$

- **ELSE**

$\mathbf{F}_i^{pg}$  through return-mapping algorithm (see Table 6.5)

- **END IF**

Table 6.4: Numerical algorithm for CASE 3.

*Compute:*

$$z_i^g = 1$$

$$\mathbf{F}_i^f = \mathbf{F}_{i-1}^f$$

$\mathbf{F}_i^{pg}$  through return-mapping algorithm (see Table 6.5)

$$\mathbf{F}_i^p = c^p \left( \mathbf{F}_i^f + \mathbf{F}_i^{pg} - 2 \cdot \mathbf{1} \right) + \mathbf{1}$$

- **IF**  $|\mathbf{E}_i^p| < |\mathbf{E}_{i-1}^p|$

$$\mathbf{F}_i^p = \mathbf{F}_{i-1}^p$$

- **END IF**

Table 6.5: Return-mapping algorithm for glassy phase plasticity.

$$\mathbf{F}_{i \text{ TRIAL}}^{pg} = \mathbf{F}_{i-1}^{pg}$$

Calculate  $\mathbf{X}_{i \text{ TRIAL}}^g$  according to Eq. (6.38)

- **IF**  $|\text{dev}(\mathbf{X}_{i \text{ TRIAL}}^g)| - R^{pg} \leq \text{tol}_{pg}$

*Elastic step:*

$$\mathbf{F}_i^{pg} = \mathbf{F}_{i \text{ TRIAL}}^{pg}$$

- **ELSE**

*Plastic step:*

- INITIALIZE:

$$k = 0$$

$$\mathbf{F}_i^{pg(k)} = \mathbf{F}_{i-1}^{pg}$$

$$\Delta\gamma_i^{(k)} = 0$$

- REPEAT

Solve

$$\mathbf{Q}^{(k)} = \left\{ \begin{array}{l} \mathbf{F}_i^{pg(k)} - \exp\left(\Delta\gamma^{(k)} \frac{\text{dev}(\mathbf{X}_i^{g(k)})}{|\text{dev}(\mathbf{X}_i^{g(k)})|}\right) \mathbf{F}_{i-1}^{pg} \\ |\text{dev}(\mathbf{X}_i^{g(k)})| - r \end{array} \right\} = \mathbf{0}$$

via Newton-Raphson procedure to find:

$$\mathbf{h}^{(k+1)} = \left\{ \mathbf{F}_i^{pg(k+1)}, \Delta\gamma_i^{(k+1)} \right\} = \mathbf{h}^{(k)} + \Delta\mathbf{h}^{(k)}$$

$$= \mathbf{h}^{(k)} - \left[ \nabla_{\mathbf{h}} \mathbf{Q}^{(k)} \right]^{-1} \mathbf{Q}^{(k)}$$

$$k = k + 1$$

- UNTIL

$$|\Delta\mathbf{h}^{(k)}| < \text{tol}_{NR}$$

- Resulting quantities:  $\mathbf{F}_i^{pg}$  and  $\Delta\gamma_i$

- **END IF**

- uniaxial and biaxial tests on a  $1 \times 1 \times 1 \text{ mm}^3$  single-element cube;
- comparison with uniaxial experiments on polyurethane-based SMPs [337] and epoxy-based SMPs [107];
- simulation of a cardiovascular stent;
- simulation of a contraceptive device.

For all the simulations we use the nonlinear finite element software ABAQUS/Standard [1], implementing the described algorithm within a user-defined material subroutine (UMAT).

In the following, all the plots are defined in terms of components of the total Cauchy stress (or true stress) tensor and of the logarithmic strain (or true strain) tensor, unless differently indicated.

#### 6.4.1 Uniaxial and biaxial tests

We start by presenting the results of the uniaxial and biaxial tests. The model parameters used for these simulations are listed in Table 6.6.

We first perform a standard uniaxial tensile test, with displacement control and a prescribed homogeneous constant temperature field. The cube is subjected to 0.4 mm tensile displacement and subsequent unloading until reaching a zero-stress condition. We repeat the test at different temperatures, in order to highlight the dependence of the material behavior on temperature. For this test, the coefficients  $c$  and  $c_p$  are kept respectively equal to 1 and 0, to consider an ideal behavior of the polymer. The resulting stress-strain curves for seven different temperatures are compared in Figure 6.1(a); the curve representing the trend of the volumetric fraction of the glassy phase,  $z^g$ , versus temperature is also provided in Figure 6.1(b). It can be noted that the material behavior is guided by  $z^g$ ; particularly, the trend is symmetric with respect to the transition temperature  $\theta_t = 350 \text{ K}$ .

We then perform a biaxial test at different temperatures, in order to test the model and to investigate material behavior for more complex non-proportional loading cases. The test consists of a hourglass-shaped input in terms of displacement  $u_1$  and  $u_2$ , as depicted in Figure 6.2(a). Again, the coefficients  $c$  and  $c_p$  are kept respectively equal to 1 and 0, to consider an ideal behavior of the polymer. Figures 6.2(b) and 6.2(c) show the obtained curves for the non-zero stress components at two different temperatures. It can be noted

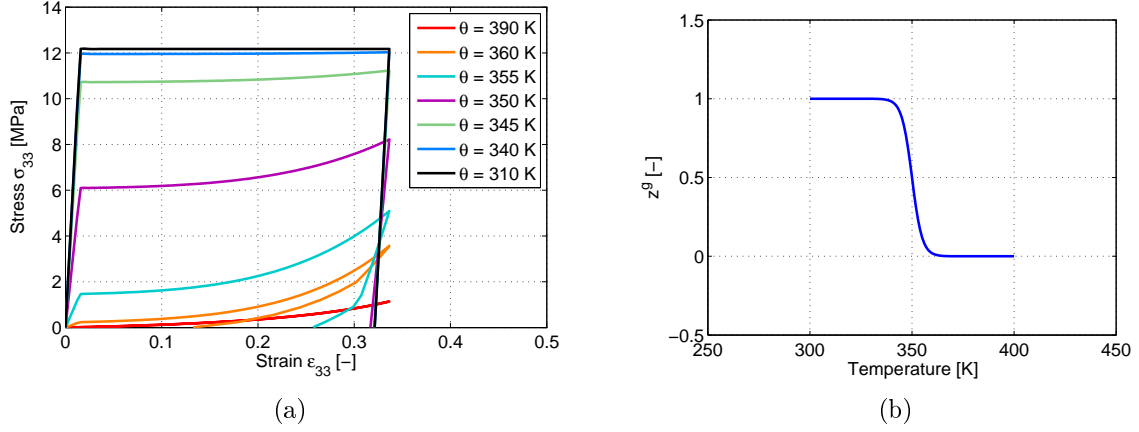
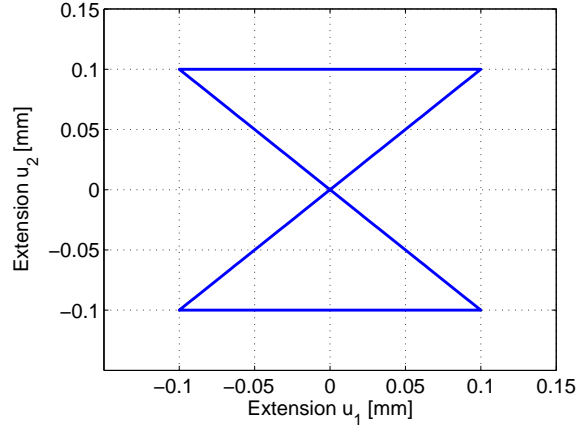


Figure 6.1: Uniaxial test: (a) stress-strain curves at different (constant) temperatures; (b) trend of the volumetric fraction of glassy phase,  $z^g$ , versus temperature.

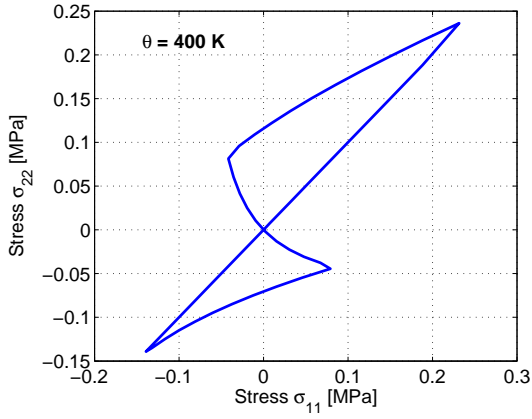
from the plots displayed in Figure 6.2 that the stress components reach different order or magnitudes depending on the test temperature: higher stresses are reached when the temperature is lower than the transition range (i.e.  $\theta < \theta_t$ ), while lower stresses are obtained when the temperature is higher than the transition range (i.e.  $\theta > \theta_t$ ). This is explained by recalling that the glassy phase is stiffer than the rubbery phase. The shape of the two curves is completely different; this depends also on the fact that the behavior of the rubbery phase is hyperelastic, while the behavior of the glassy phase is elastoplastic.

Finally, we perform three uniaxial tests reproducing the shape-memory behavior of SMPs. An ideal ( $c = 0$ ,  $c_p = 0$ ) and a non-ideal ( $c \neq 0$ ,  $c_p \neq 0$ ) case are considered for each of the three tests (see Table 6.6). We refer to the three tests as *Test 1*, *Test 2* and *Test 3*; the loading histories, in terms of the imposed displacement, and the assigned temperature histories for the three analyses are reported in Figure 6.3.

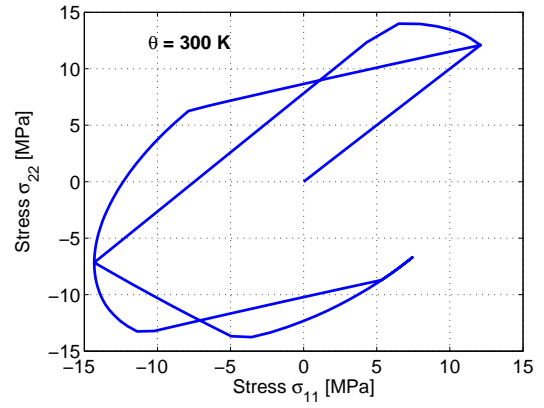
In Test 1, we simulate the high-temperature shape-fixing; the material is indeed deformed at 400 K, then cooled to 200 K while the deformation is maintained constant, then unloaded at 200 K, and finally re-heated up to 400 K to trigger shape-recovery. The results of Test 1 are reported in Figure 6.4, where differences can be noted between the ideal and the non-ideal curves. The imperfect shape-fixing is demonstrated by the small elastic springback shown between 2 and 3 s (as reported in Figures 6.4(a) and 6.4(b)). In fact, in the ideal case all the applied deformation is stored as "frozen", leading to a zero-stress condition at the end of the cooling phase (time instant 2 s). Instead, in the non-ideal case only part of the deformation is accumulated, producing a stress increase during the



(a)



(b)



(c)

Figure 6.2: Biaxial test: (a) hourglass-shaped input in terms of strain components  $u_1$  and  $u_2$ ; (b) curve in terms of the non-zero stress components at  $\theta = 400$  K; (c) curve in terms of the non-zero stress components at  $\theta = 300$  K.

Table 6.6: Model parameters.

Symbol	Value	Unit
$\Delta\theta$	30	K
$w$	0.2	1/K
$E^r$	0.9	MPa
$E^g$	771	MPa
$\nu^r$	0.49	-
$\nu^g$	0.29	-
$\theta_t$	350	K
$c$	0.9 (non-ideal case) - 1 (ideal case)	-
$c_p$	0.2 (non-ideal case) - 0 (ideal case)	-
$r$	10	MPa
$h$	0	MPa

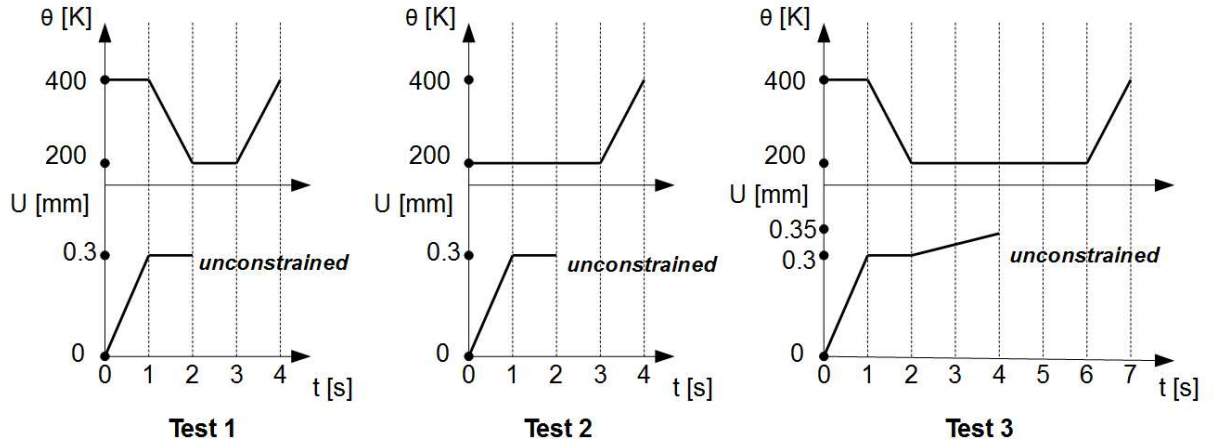


Figure 6.3: Tests 1, 2 and 3. Loading histories, in terms of imposed displacement, and temperature histories for each of the three uniaxial free-recovery traction tests. Test 1: deformation is applied at high temperature (0-1 s); then a constrained cooling is performed (1-2 s); the material is subsequently unloaded at low temperature (2-3 s): from instant 2 s, the displacement is therefore not constrained anymore; finally, the temperature is increased (3-4 s). Test 2: a deformation is applied at low-temperature (0-2 s); then, the material is unloaded (2-3 s); finally, the temperature is increased (3-4 s). In Test 3, both shape-fixing procedures are performed, the high-temperature one during 0-2 s, the low-temperature one during 2-4 s; then, the material is unloaded (4-6 s); finally, the temperature is increased (6-7 s).

cooling phase, due to the higher stiffness of the incoming glassy phase: therefore, during unloading, the deformation decreases until a zero-stress condition is reached, producing an elastic springback. The incomplete shape-recovery can be noted especially in Figures 6.4(a) and 6.4(e), where a residual strain is present at instant 4 s.

In Test 2, we simulate the low-temperature shape-fixing; the material is indeed deformed at 200 K, then unloaded, and finally heated up to 400 K to trigger shape-recovery. The results of Test 2 are reported in Figure 6.5. In this case, no "frozen" deformation is present, because deformation takes place at low temperature. The only accumulated deformation is due to the plastic behavior of the glassy phase. Therefore, in both ideal and non-ideal cases, an elastic springback is present upon unloading (time interval 2-3 s, as shown in Figures 6.5(a), 6.5(b) and 6.5(c)). The difference between the two cases is related to the incomplete shape-recovery of the non-ideal case, which as before can be noted in Figures 6.5(a) and 6.5(e).

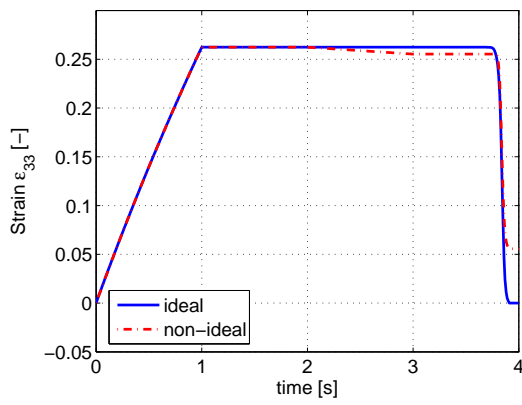
In Test 3 we consider both high-temperature and low-temperature shape-fixing. A first deformation is imposed at 400 K and the material is constrained during cooling to 200 K, in order to operate the high-temperature shape-fixing; then, instead of directly unloading, a further deformation is applied at low temperature; the material is then unloaded and finally re-heated up to 400 K to trigger shape-recovery. The results of Test 3 are reported in Figure 6.6. The recovery of both high-temperature and low-temperature deformations takes place, with full recovery in the ideal case, and incomplete recovery in the non-ideal case.

## 6.4.2 Comparison between numerical and experimental data

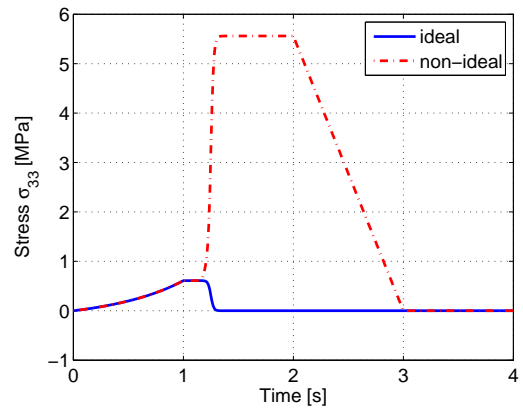
We now perform a validation of the model, by presenting a comparison of the numerical results with experimental data from literature. In order to demonstrate the versatility of the model, we consider two different types of SMPs.

Firstly, a comparison with the experimental results presented by [337] is provided. Free- and constrained-recovery experimental tests are operated on a polyurethane-based SMP. Both the free-recovery and the constrained-recovery test begin with a high-temperature shape-fixing procedure; subsequently, the material is heated to trigger shape-recovery, respectively in unconstrained conditions for the free-recovery test, and with constrained (zero) displacement for the constrained-recovery test. The adopted model parameters are

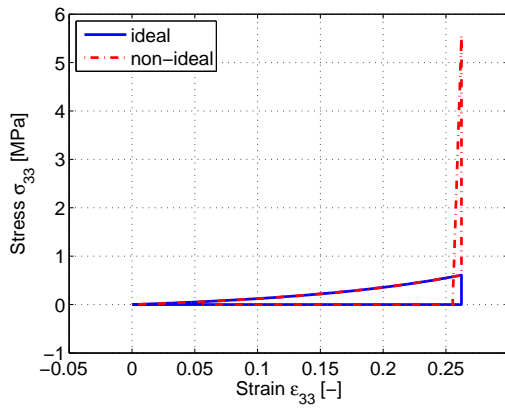




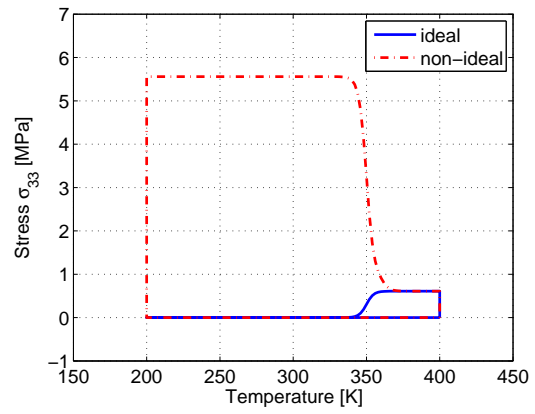
(a)



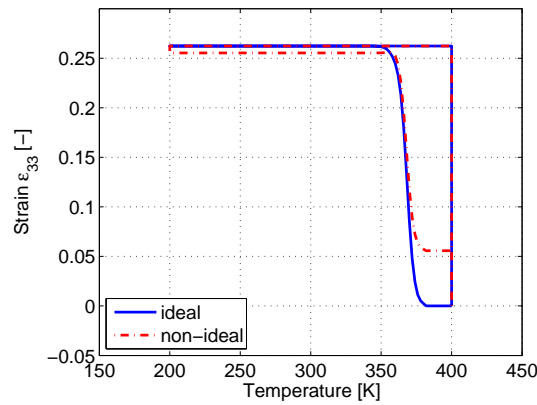
(b)



(c)

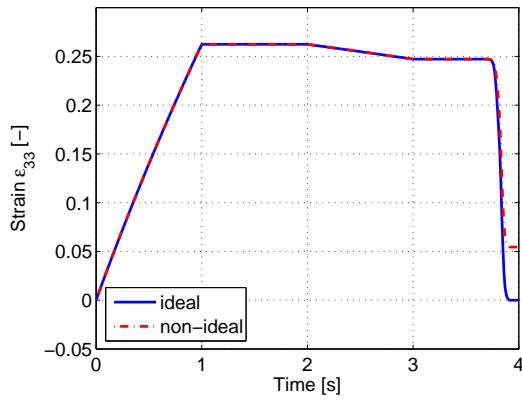


(d)

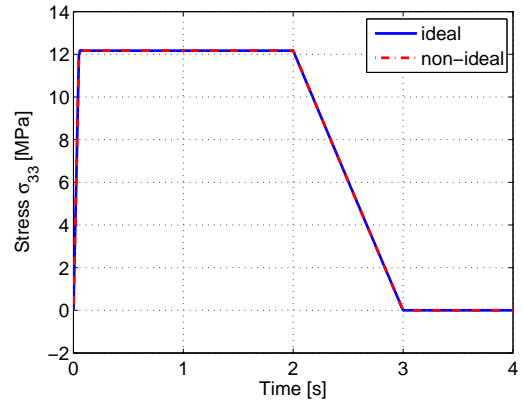


(e)

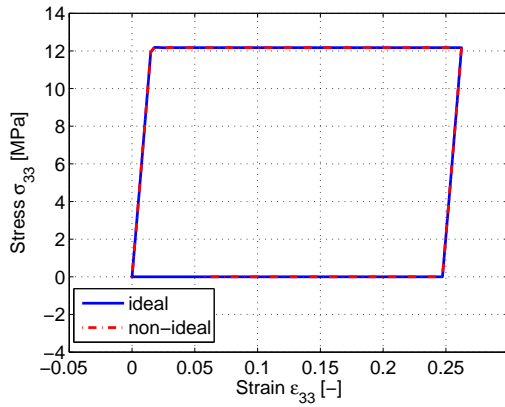
Figure 6.4: Test 1: (a) strain versus time curve; (b) stress versus time curve; (c) stress versus strain curve; (d) stress versus temperature curve; (e) strain versus temperature curve.



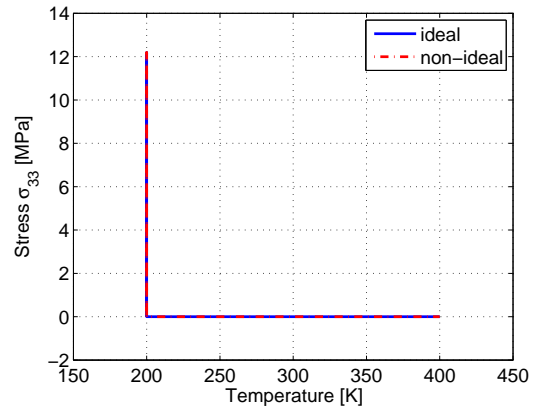
(a)



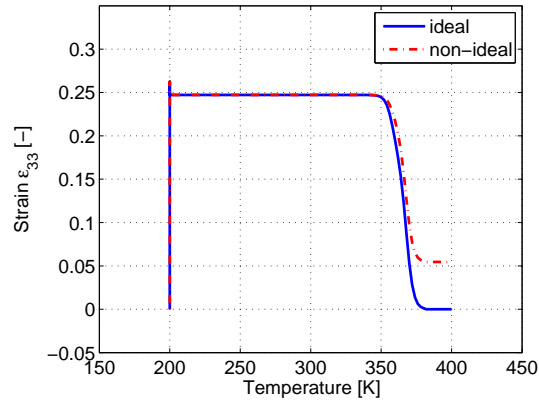
(b)



(c)

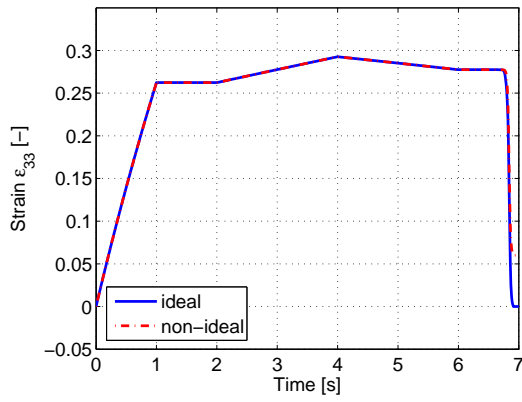


(d)

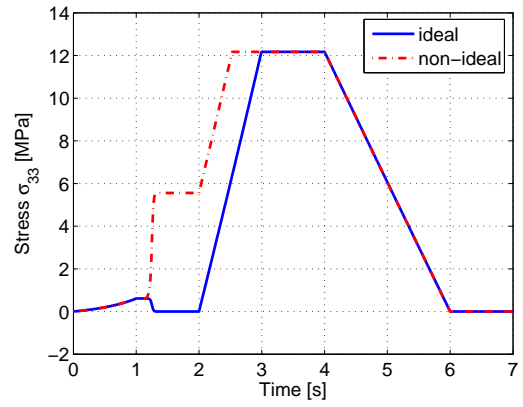


(e)

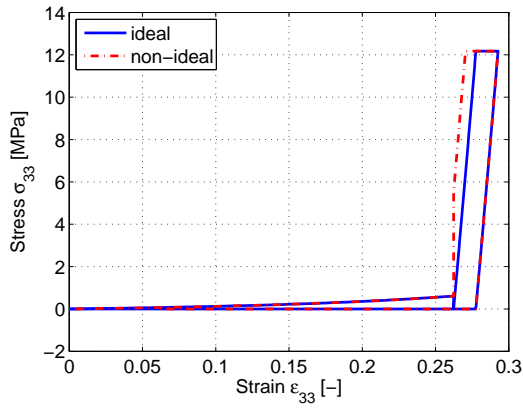
Figure 6.5: Test 2: (a) strain versus time curve; (b) stress versus time curve; (c) stress versus strain curve; (d) stress versus temperature curve; (e) strain versus temperature curve.



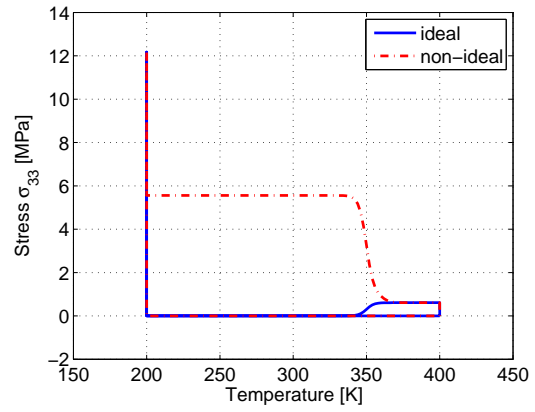
(a)



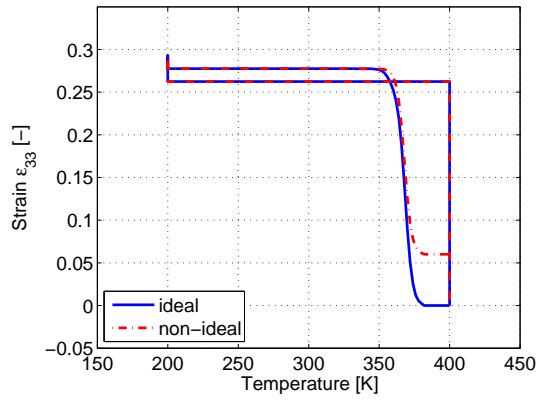
(b)



(c)



(d)



(e)

Figure 6.6: Test 3: (a) strain versus time curve; (b) stress versus time curve; (c) stress versus strain curve; (d) stress versus temperature curve; (e) strain versus temperature curve.

listed in Table 6.7.

Table 6.7: Model parameters adopted for the comparison with experimental data by [337].

Symbol	Value	Unit
$\Delta\theta$	26	K
$w$	0.25	1/K
$E^r$	11	MPa
$E^g$	3200	MPa
$\nu^r$	0.497	-
$\nu^g$	0.3	-
$\theta_t$	336	K
$c$	0.972	-
$c_p$	0	-

The results of the free-recovery and constrained-recovery tests are reported in Figures 6.7 and 6.8, respectively. In this case, the plots are defined in terms of engineering stress. The numerical and experimental curves reported in 6.7(a) and 6.7(c) match well, while the trend of the stress with temperature, in Figure 6.7(b), differ in the upper portion of the curve. This is due to the fact that the path followed by the stress in the experimental data presents differences between heating and cooling. Whereas, in the proposed model formulation, the trend of the stress is linked to the evolution of the glassy phase volume fraction  $z^g$ , which is the same during both heating and cooling. Similar observations can be made for the comparison reported in Figure 6.8.

A further comparison with experimental data obtained on a epoxy-based SMP by [107] is provided. In [107], an epoxy-based SMP reinforced with SiC nanoparticles was subjected to compressive load at 25 °C (low-temperature shape-fixing procedure); then, a constrained recovery has been performed, by heating to 120 °C. The adopted material parameters are listed in Table 6.8.

The experimental and numerical curves are reported in Figure 6.9 and the fitting parameters are listed in Table 6.8. It can be noted from the reported curves that the numerical model results satisfactorily matches with the experimental ones. Even better results may be obtained by using a different model for hyperelasticity, i.e. Neo-Hookean instead of Saint Venant-Kirchhoff, so that the numerical unloading stress-strain curve (see Figure 6.9(a)) could better follow the experimental one.

It is worth to recall that the fitting of the experimental data sets has been performed by

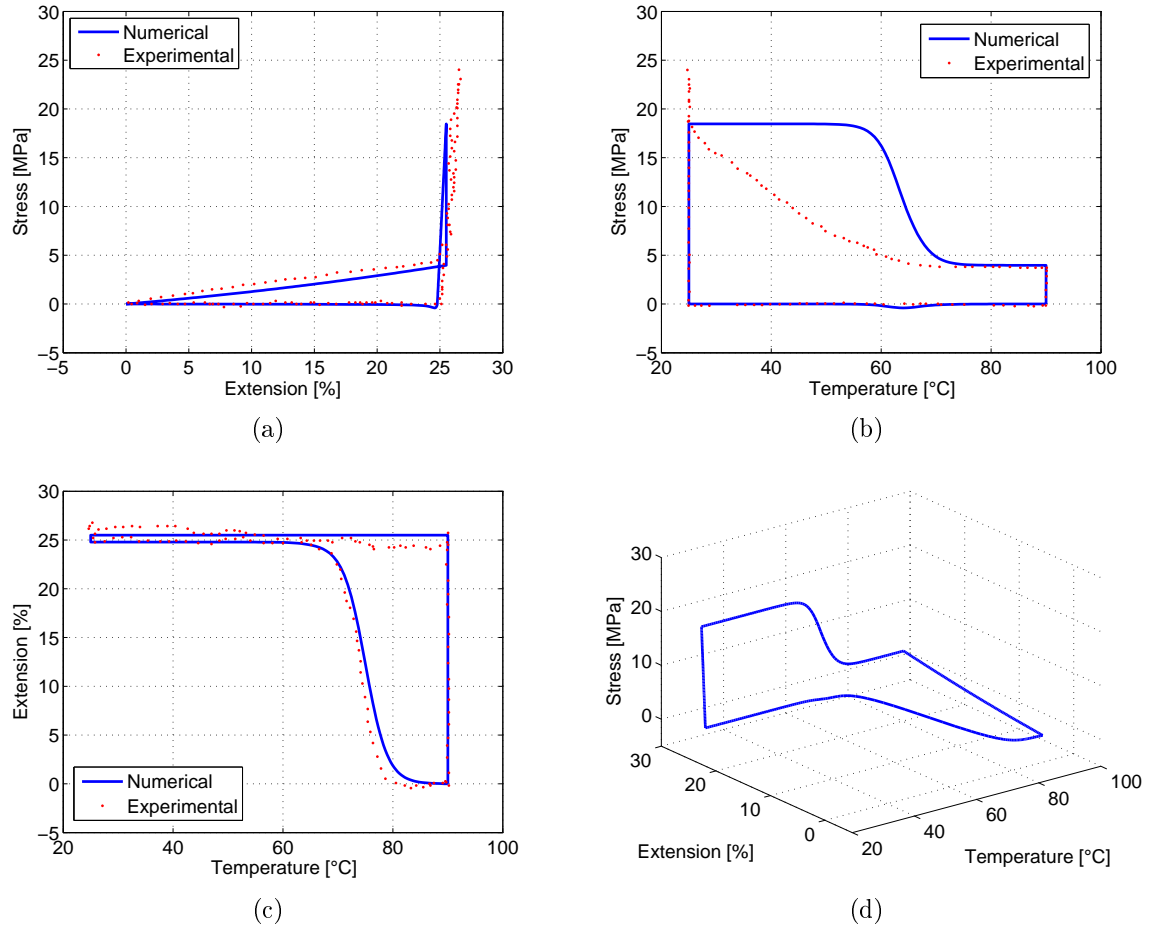
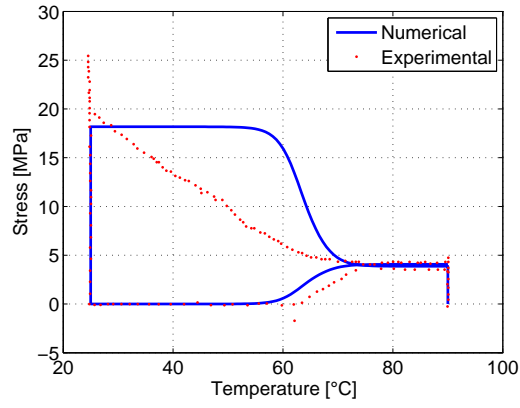
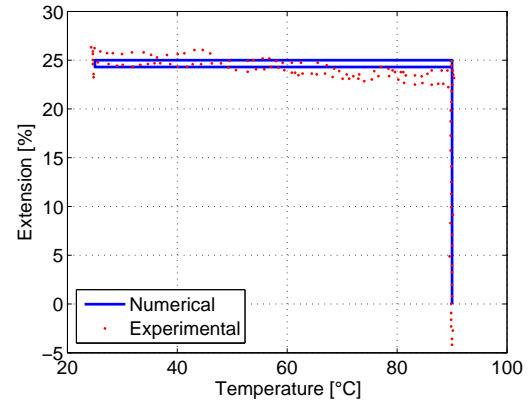


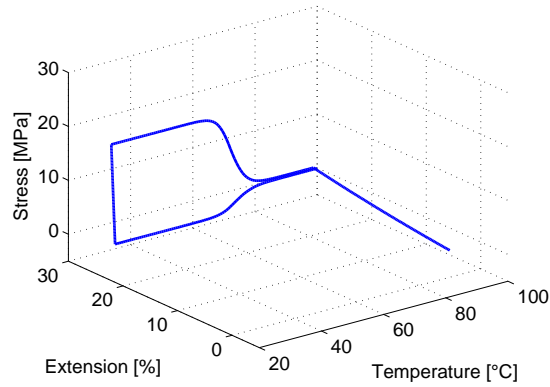
Figure 6.7: Comparison with experimental data by [337]: free-recovery test. (a) Stress versus extension curves; (b) stress versus temperature curves; (c) extension versus temperature curves; (d) stress-extension-temperature curves.



(a)

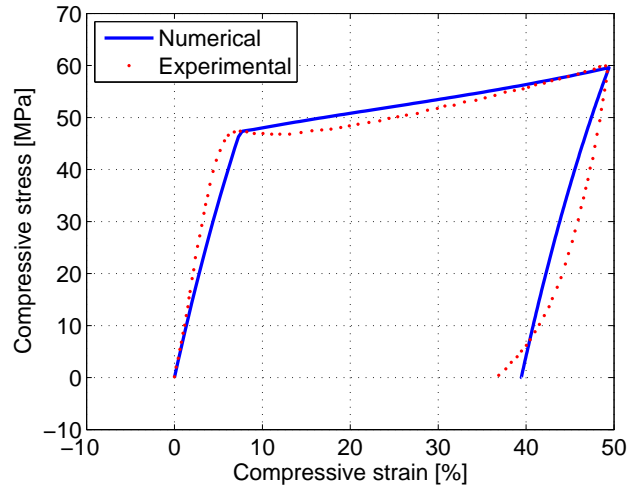


(b)

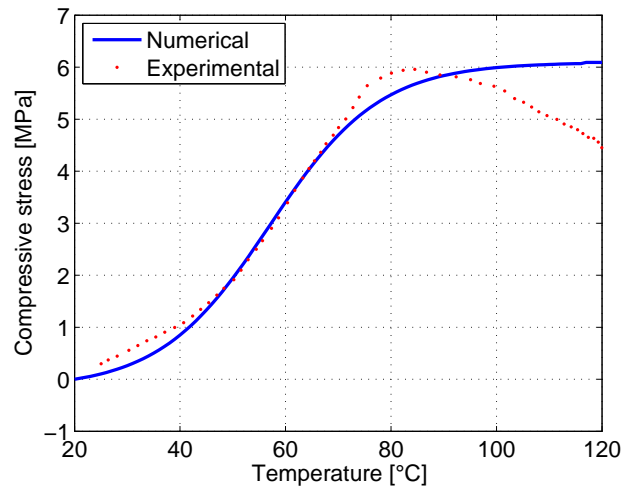


(c)

Figure 6.8: Comparison with experimental data by [337]: constrained-recovery test. (a) Stress versus temperature curves; (b) extension versus temperature curves; (c) stress-extension-temperature curves.



(a)



(b)

Figure 6.9: Comparison with experimental data by [107]: (a) compression stress-strain curves at 25 °C; (b) stress versus temperature curves during constrained-recovery.

Table 6.8: Material parameters adopted for the comparison with experimental data by [107].

Symbol	Value	Unit
$\Delta\theta$	60	K
$w$	0.048	1/K
$E^r$	4.1	MPa
$E^g$	800	MPa
$\nu^r$	0.49	-
$\nu^g$	0.30	-
$\theta_t$	330	K
$c$	1	-
$c_p$	0	-
$r$	39	MPa
$h$	22	MPa

an iterative trial-error procedure. Nonetheless, further developments of the present work may include the investigation of a more efficient procedure to derive the model parameters.

### 6.4.3 Simulation of biomedical devices

We conclude by simulating two biomedical devices. The model parameters used are listed in Table 6.6, considering the ones related to the non-ideal case. Both components are modeled in SolidWorks [311] and are meshed using second-order hexahedral elements with full integration (Abaqus designation C3D10).

The first investigated device is a cardiovascular stent. The geometry is similar to the one reported in [359]. The external diameter is 20 mm, the thickness is 0.5 mm, the length of the stent is 20 mm, and the diameter of the holes is 2 mm. The geometry, the coordinate system, and a scheme of the applied boundary conditions are provided in Figure 6.10: the bottom side of the stent is fixed, while a displacement is imposed on the top side (in  $x$  direction), in order to crush the stent. The histories of imposed temperature and displacement are the same of Test 1 (see Figure 6.3), including a high-temperature shape-fixing procedure and a subsequent shape-recovery. Specifically, the stent is crushed at 400 K, then it is kept in position during cooling to 200 K. Afterwards, it is unloaded, and finally re-heated up to 400 K to induce shape-recovery. Similar loading histories on SMP stents have been previously considered in literature, e.g. in [42, 284].

The results of the stent simulation are reported in Figure 6.11. The displacement is



measured in correspondence of the top side of the stent, while the force is referred to the global reaction force of the bottom fixed side.

Contour plots of the Von Mises stress distribution at the most relevant time instants of the analysis are reported in Figure 6.12. In particular, it can be noted that the stress increases during constrained cooling, since the transformation from rubbery to glassy phase is taking place. After recovery upon heating, a residual deformation remains, since the behavior was chosen to be non-ideal; the original shape is therefore not completely recovered.

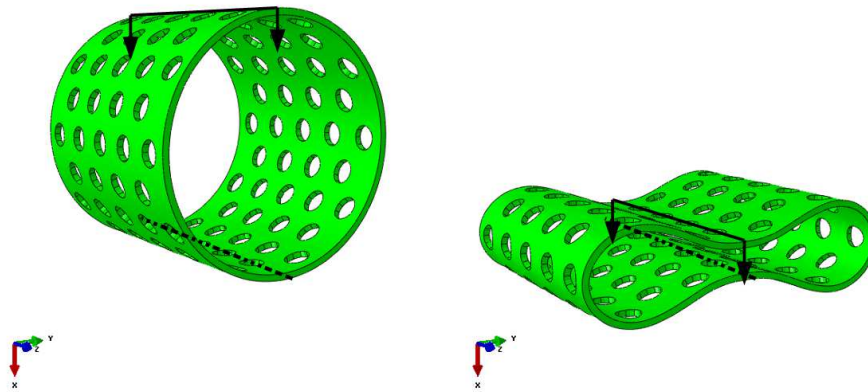
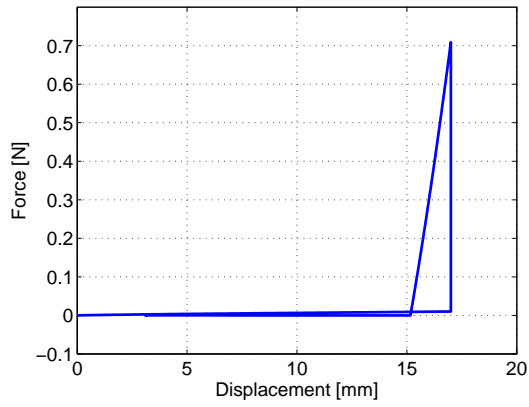


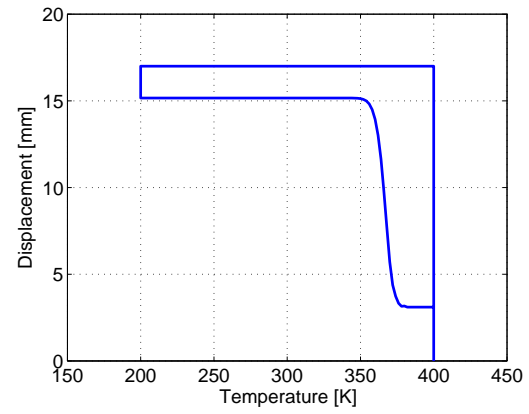
Figure 6.10: Stent simulation: (left) adopted geometry, coordinate system, and scheme of the boundary conditions applied to the stent. The bottom side is fixed, while a displacement is imposed on the top side, in order to crush the stent. (right) Deformed geometry of the stent after crushing at high temperature.

The second investigated device is a contraceptive device similar to the one reported in [323]. Only for this test, the hardening coefficient  $h$  has been set equal to 100 MPa. The device is 58 mm long and its outer diameter measures about 14 mm. The geometry, coordinate system, and a scheme of the boundary conditions are shown in Figure 6.13. One side of the device is fixed; on the other side a displacement is applied in the axial direction. The histories of the temperature and boundary conditions are the same of Test 2 (see Figure 6.3), including a low-temperature shape-fixing procedure and a subsequent shape-recovery. Specifically, the device is first elongated at a temperature of 200 K, it is then unloaded, and finally the temperature re-heated up to 400 K to induce shape-recovery. Such loading history aims to reproduce the experimental procedure performed in [323].

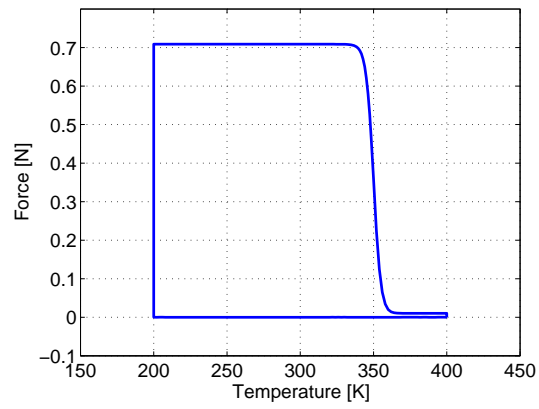
The simulation results of the contraceptive device are reported in Figure 6.14. The displacement is measured in correspondence of the left side, while the force is the reaction force at the constrained (right) side (see Figure 6.13).



(a)



(b)



(c)

Figure 6.11: Stent simulation: (a) force versus displacement curve; (b) displacement versus temperature curve; (c) force versus temperature curve.

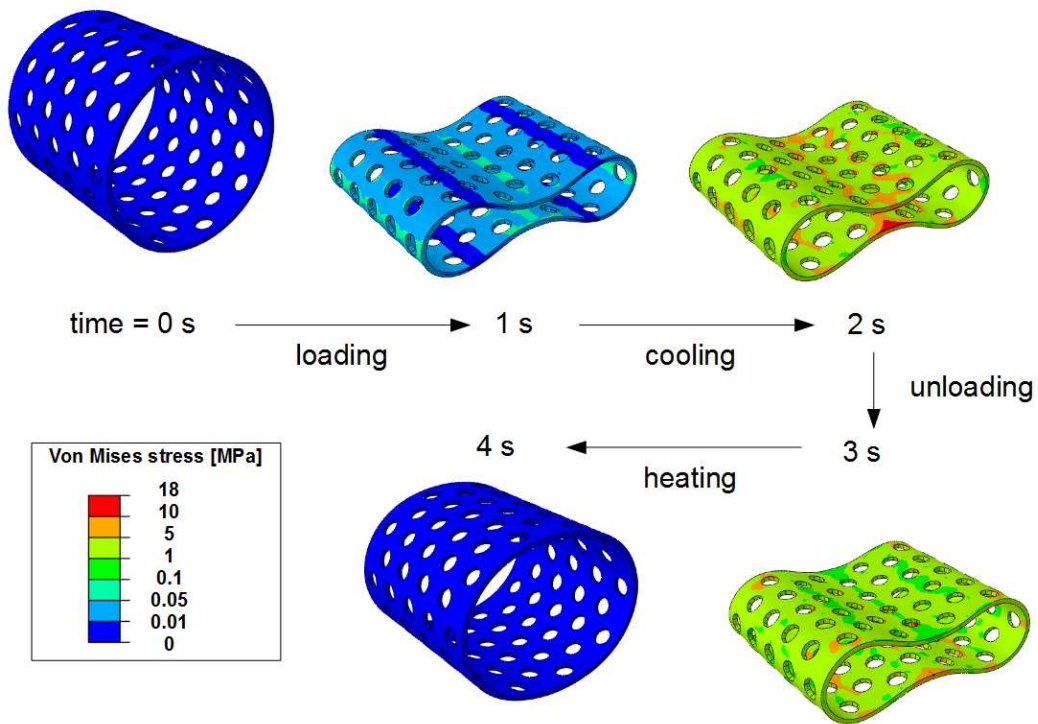


Figure 6.12: Stent simulation: Von Mises stress distribution (in MPa) on the stent at the most relevant time steps of the analysis.

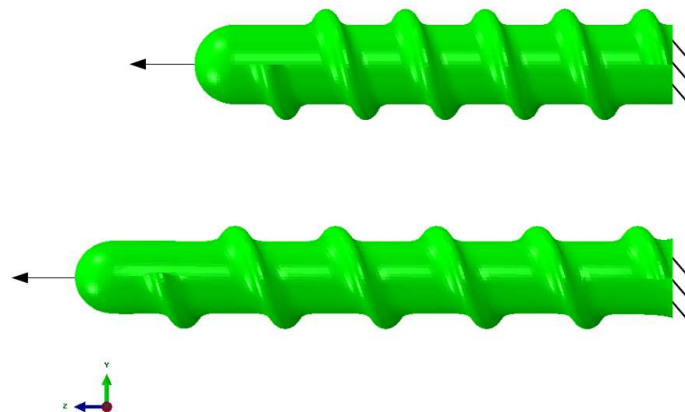


Figure 6.13: Contraceptive device test: scheme of the boundary and loading conditions.

Contour plots related to the Von Mises stress distribution at the most relevant time instants of the analysis are reported in Figure 6.15. As before, the non-ideal character of the material entails an incomplete shape-recovery.

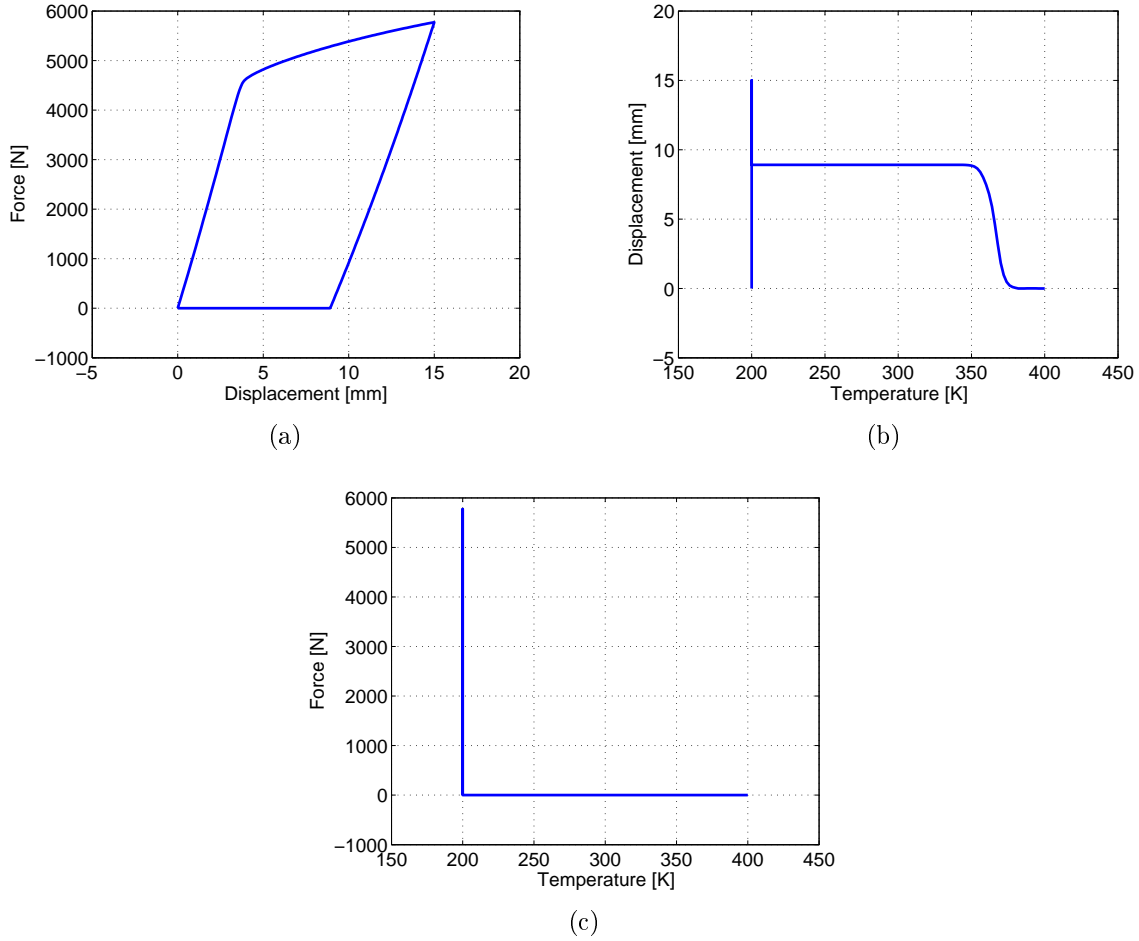


Figure 6.14: Contraceptive device test: (a) force versus displacement curve; (b) displacement versus temperature curve; (c) force versus temperature curve.

## 6.5 Conclusions

The present paper has proposed a constitutive model for SMPs. The presented model is based on a phase-transition approach and therefore cannot describe the underlying thermo-viscoelastic behavior of polymers, but it can be applied to engineering problems where only the macroscopic phenomenology related to SMPs is relevant for the application purposes.

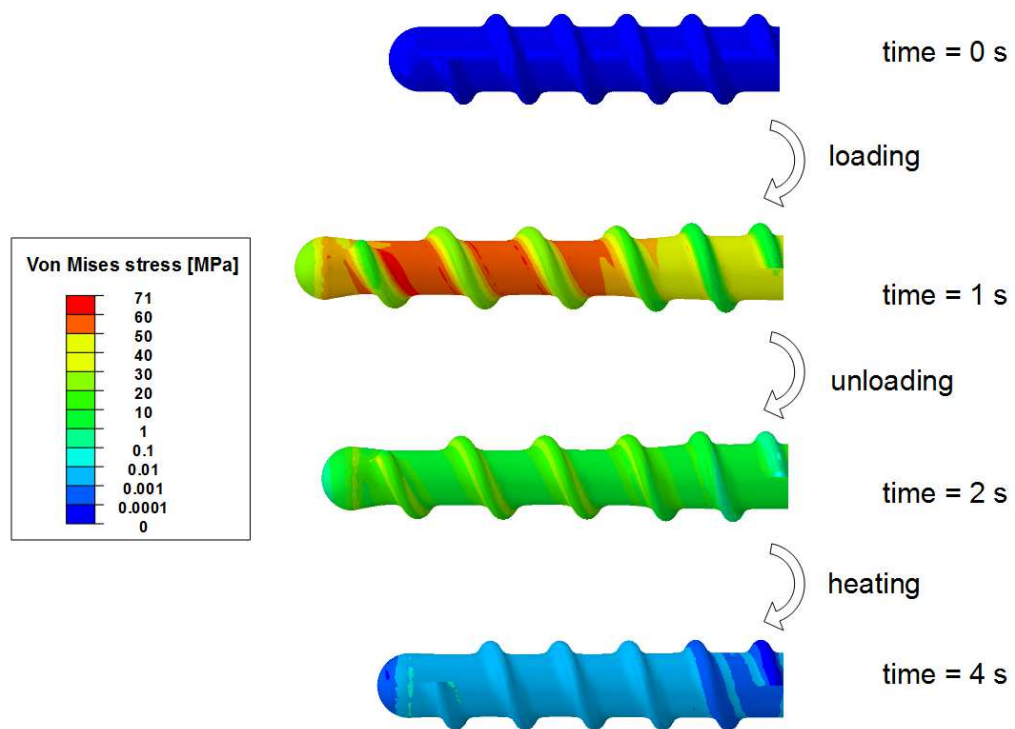


Figure 6.15: Contraceptive device test: Von Mises stress distribution (in MPa) at the most relevant time steps of the analysis.

The time-continuous model equations have been presented, together with the time-discrete algorithm for the numerical implementation. The number of parameters involved in the model formulation is low (11 parameters are required) and they are related to physical quantities, thus promoting the model simplicity. Moreover, the simple algorithmic scheme entails a low computational effort. The model has been assessed through a wide range of uniaxial and biaxial numerical tests; complex simulations of two biomedical devices have been also presented. The model has revealed its ability in reproducing both shape-fixing and shape-recovery of SMPs, also taking into account the imperfection of the real material behavior (i.e. imperfect shape-fixing and incomplete shape-recovery). When compared to experimental results presented in the literature for different polymer types, the numerical curves show a good overall agreement. Model validation on other meaningful applications could be an interesting task for future studies.

The flexibility of the proposed model allows its application over a wide range of polymers. Extensions or modifications can be easily applied to the model to adapt it to the desired category of polymers. As an example, a different evolution for the glassy volume fraction  $z^g$  during cooling and heating could be considered (see Figure 6.7(b)), or a different hyperelastic model can be chosen to describe the elastic behavior of the two phases, e.g. the Ogden-Roxburgh model. However, we should highlight that the viscoelastic behavior during the rubbery-glassy phase transition has been neglected in the present contribution. Such behavior has been observed experimentally, e.g. [265], and can have a significant influence on the shape-memory effect in practical applications. Future improvements of the present model will include the introduction of viscous effects and the consideration of non-quasistatic cases. Also, we have restricted ourselves to the isotropic case, first of all for simplicity, but also due to the lack of experimental data about anisotropic cases. To conclude, the presented model is a valid phenomenological tool to simulate the behavior of SMPs in all sort of applications, e.g. in the biomedical field, in a simple and accurate way.

# Chapter 7

## Semi-automatic UMAT/VUMAT subroutines generation

The work presented in this chapter represents an important and necessary step in achieving the results presented in the paper [104], which I published with other colleagues.

### 7.1 Introduction

The FEA software Abaqus (Dassault Systèmes) [1] provides the user with a wide range of different user subroutines which can be used to adapt the software to customized analysis requirements. Among these subroutine structures, the material user subroutines, called UMAT for Abaqus/Standard solver and VUMAT for Abaqus/Explicit solver, can be used to define any complex mechanical constitutive models which are not present in Abaqus material library. Abaqus user subroutines have to be coded in FORTRAN programming language. The possibility to code non-standard subroutines for user-specific purposes extends the applicability of the software; however, since FORTRAN is not a very high-level language, coding can be complex and time-consuming. Therefore, it would be useful to code in a more intuitive high-level programming language, and then translate the code into FORTRAN statements.

In the present chapter, a method will be presented to derive UMAT/ VUMAT user material subroutines for Abaqus in a semi-automatic way.

## 7.2 From AceGen to FORTRAN

The software involved in semi-automatic UMAT/ VUMAT derivation procedure is AceGen, a package for Mathematica (Wolfram Research) [199] developed by Prof. Korelč (University of Ljubljana). AceGen combines symbolic and algebraic capabilities of Mathematica, automatic differentiation technique, automatic code generation, and simultaneous optimization of expressions for the derivation of codes to be used in numerical procedures [164]. AceGen programming language is very similar to Mathematica language, being therefore intuitive and flexible.

The benefit of using automatic differentiation is that several tedious steps in the traditional computer implementation, such as derivation and coding of the consistent tangent matrix, are automatized. This leads to robust and time-efficient implementation. Also, the resulting computer code is efficient.

The user material subroutines generation procedure is summarized in the following (see Table 7.1). I use AceGen to code the material mechanical behavior. See, e.g., Figure 7.1 where a simple example related to linear elastic mechanical model is reported. The command "SMSInitialize" allows to choose the programming language for subsequent translation (FORTRAN in this case). Then, AceGen language is used to define linear elastic law. Finally, the command "SMSWrite" starts the translation procedure.

Care must be taken in maintaining the same inputs and outputs required by Abaqus UMAT or VUMAT. In general, the inputs are

- the strain tensor components (for small strain conditions), or the deformation gradient tensor components (for large strain conditions)
- an array containing the material parameters,
- an array containing the previous instant state variables,
- the temperature (if needed);

and the outputs are

- the stress tensor components,
- the consistent Jacobian components (only for UMAT),
- an array containing the current instant state variables.



Table 7.1: Semi-automatic UMAT/VUMAT generation procedure.

- |  |
|--|
| <ol style="list-style-type: none"><li>1. Write AceGen code</li><li>2. Perform optimized automatic translation of AceGen code into FORTRAN subroutine</li><li>3. Embed FORTRAN subroutine in UMAT/VUMAT user subroutine</li><li>4. Call UMAT/VUMAT in Abaqus analysis</li></ol> |
|--|

Particular attention has to be kept in exporting the tensors components in the same sequence as required by Abaqus; note that the variable order varies between UMAT and VUMAT.

### 7.3 From FORTRAN to UMAT/VUMAT

After automatic generation of the FORTRAN subroutine, a FORTRAN file with a proper UMAT or VUMAT header is manually created (see Figure 7.2).

The UMAT/VUMAT file can be then directly called from an Abaqus analysis, indicating all the proper parameters in the input file.

I have generated UMAT and VUMAT subroutines for advanced materials constitutive models, in both small and large strains.

I used such UMAT/VUMAT generation technique to code complex constitutive models, such as SMAs and SMPs behavior, throughout my PhD studies. Such procedure allowed me to efficiently perform the Abaqus finite element analyses needed for the research activities described in the present thesis, avoiding the time-consuming task of coding user material subroutines directly in FORTRAN.

### 7.4 Application example

As an example, I wish to report in this chapter the use of a semi-automatically created SMA user subroutine, which has been used for the simulation of SMA self-expandable carotid

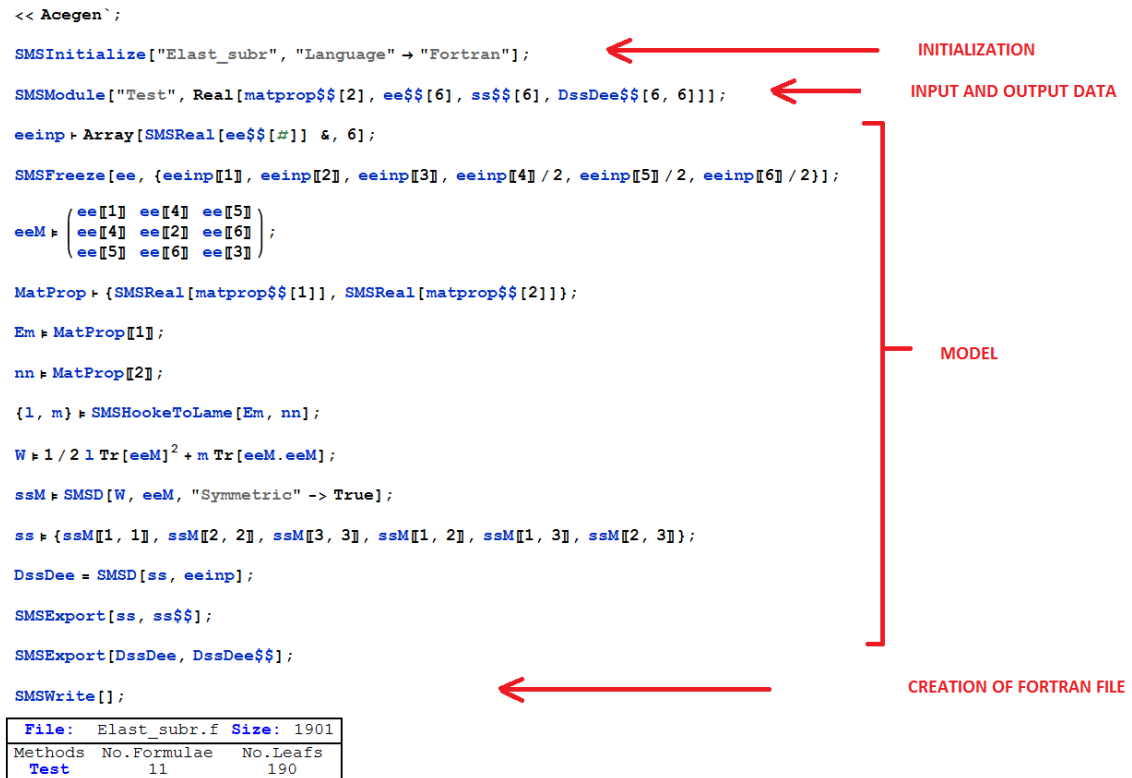


Figure 7.1: Simple example of AceGen code for linear elastic material model. As mentioned, AceGen offers an optimized translation of numerical procedures into other languages, FORTRAN among them.

```

C-----C
C          ***** UMAT USER SUBROUTINE ----> ELASTICITY *****          C
C                                                                              C
C          INPUT: material properties (PROPS), strain (STRAN)                C
C          OUTPUT: stress (STRESS), material tangent matrix (DDSDDE)         C
C                                                                              C
C          PROPS(1) = Young's Modulus                                       C
C          PROPS(2) = Poisson's coefficient                                 C
C                                                                              C
C-----C
C          UMAT PARAMETERS
C
C          SUBROUTINE UMAT(STRESS, STATEV, DDSDDE, SSE, SPC, SCD, RPL, DDSDDT,
C          *              DRPLDE, DRPLDT, STRAN, DSTRAN, TIME, DTIME, TEMP,
C          *              DTEMP, PREDEF, DPRED, CMNAME, NDI, NSHR, NTENS,
C          *              NSTATV, PROPS, NPROPS, COORDS, DROT, PNEWDT,
C          *              CELENT, DFGRD0, DFGRD1, NOEL, NPT, LAYER, KSPT,
C          *              KSTEP, KINC)
C
C          implicit real*8(a-h,o-z)
C          parameter (nprec=2)
C          INCLUDE 'aba_param_dp.inc'
C
C          CHARACTER*80 CMNAME
C
C          DIMENSION STRESS(NTENS), STATEV(NSTATV), DDSDDE(NTENS,NTENS),
C          *          DDSDDT(NTENS), DRPLDE(NTENS), STRAN(NTENS),
C          *          DSTRAN(NTENS), TIME(2), PREDEF(1), DPRED(1),
C          *          PROPS(NPROPS), COORDS(3), DROT(3,3), DFGRD0(3,3),
C          *          DFGRD1(3,3)
C
C-----C
C          SUBROUTINE PARAMETERS
C
C          DIMENSION v(5001)
C
C          CALL OF ELASTICITY SUBROUTINE
C
C          STRAN=STRAN+DSTRAN
C
C          call Test(v,PROPS,STRAN,STRESS,DDSDDE)
C
C-----C
C          END OF UMAT SUBROUTINE
C          return
C          end
C-----C
C          ELASTICITY SUBROUTINE
C          SUBROUTINE Test(v,matprop,ee,ss,DssDee)
C          IMPLICIT NONE
C          INTEGER i01,i02
C          DOUBLE PRECISION v(5001),matprop(2),ee(6),ss(6),DssDee(6,6)
C          v(33)=ee(1)+ee(2)+ee(3)
C          v(32)=1d0/(1d0-2d0*matprop(2))
C          v(31)=1d0/(1d0+matprop(2))
C          v(34)=matprop(1)*v(31)
C          v(15)=matprop(2)*v(32)*v(34)
C          v(23)=v(15)*v(33)
C          v(17)=v(34)/2d0
C          v(27)=v(15)+v(34)
C          ss(1)=v(23)+ee(1)*v(34)
C          ss(2)=2d0*ee(2)*v(17)+v(23)
C          ss(3)=v(23)+ee(3)*v(34)
C          ...

```

**UMAT HEADER**

**PARAMETERS OF THE AUTOMATICALLY GENERATED SUBROUTINE**

**CALL OF AUTOMATICALLY GENERATED SUBROUTINE**

**AUTOMATICALLY GENERATED SUBROUTINE**

Figure 7.2: Generated UMAT for linear elastic material model.

artery stent models. The objective of such study was to develop an efficient computational framework to evaluate the flexibility of self-expandable carotid artery stents. In particular, numerical simulations are performed to compare linear FEA and higher order FEA (or p-FEA). The results suggest that the employment of higher order FEA allows to accurately represent the computational domain and to get a better approximation of the solution with a widely reduced number of degrees of freedom with respect to linear FEA. Moreover, higher order FEA presents superior capability of reproducing the nonlinear local effects related to buckling phenomena.

In Figure 7.3 a comparison between linear FEA and p-FEA is reported. For further details, please refer to the paper that we produced [104].

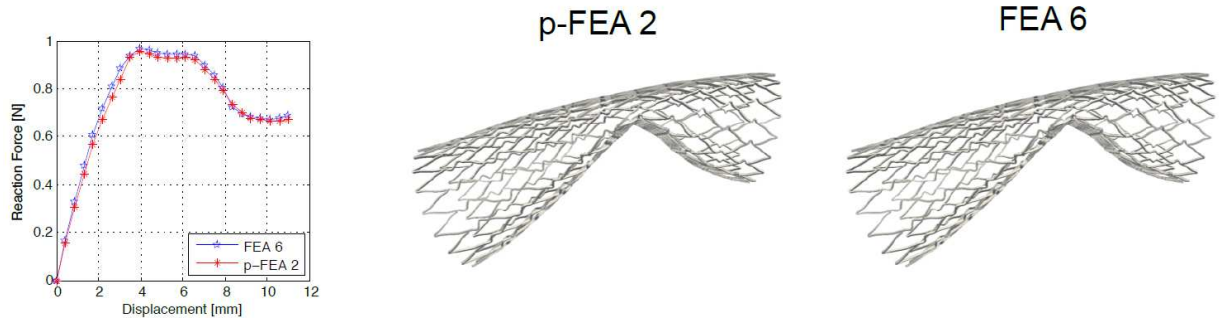


Figure 7.3: Linear FEA and higher order FEA comparison: on the left, force vs displacement curves of the finest mesh used for linear FEA, with roughly  $10^7$  dofs, and an intermediate  $2 \cdot 10^6$  dofs mesh for p-FEA; on the right, comparison of the two analyses deformed configuration.

# Appendix A

## Obtaining tunable phononic crystals from shape-memory polymers

This chapter briefly presents the first results of a study conducted during my stay as a visiting scholar at Harvard University (Cambridge, MA), School of Engineering and Applied Sciences, from November 1st, 2014 to January 31st, 2015.

### A.1 Introduction

SMPs are a category of polymers which present a marked ability in storing a temporary shape and in recovering their permanent shape upon the occurrence of an external stimulus.

The most common SMPs are the thermally activated ones, whose driving force is the micro-Brownian motion, i.e. the variation of the chain mobility with temperature. They present a transformation temperature range which corresponds to a transition between very different material properties.

Thermal SMPs require a shape-fixing procedure to achieve the deformed state and maintain it. Such procedure usually consists of a first heating phase, an imposed deformation at high temperatures, since in those conditions the SMP is softer and pliable, a cooling phase while maintaining the deformation fixed, and a final unloading phase. Upon unloading at low temperature, the temporary deformed shape is maintained. In order to recover the original permanent shape, the SMP should be heated over the transformation temperatures.

Applications of SMPs encompass medical devices, such as cardiovascular stents and wound closure stitches, and innovative industrial applications, such as soft grippers, smart fasteners and packaging solutions.

Phononic crystals are periodically shaped structures which present a phononic wave band gap, i.e. a range of frequencies which are barred. The explanation of the band gap can be found in the multiple interference of the sound waves scattered inside the crystal. Phononic crystals are applied, e.g., for noise canceling, vibration insulation, wave filters, wave guides, acoustic imaging.

Periodic structures may present peculiar buckling patterns, which can be obtained under compression. It has been demonstrated [301] that if buckling is induced by compression of a phononic crystal, variations in its band gap are produced.

The purpose of the present study is to combine the shape-memory properties of SMPs and the peculiar acoustic characteristics of phononic crystals, in order to provide a proof of concept on the possibility to obtain phononic crystals made from SMPs, with a tunable band gap according to external temperature.

## **A.2 Results and discussion**

### **A.2.1 Numerical simulations**

2D simulations have been run in Abaqus, including buckling, post-buckling and wave propagation analyses. The final objective of the numerical simulations was to identify the band gap, given a determined geometrical shape of the phononic crystal.

The structure depicted in Figure A.1 has been considered. It presents a 60% porosity, with a hole diameter of 8.3 mm, and an edge length of 65.5 mm.

The mesh includes 656 elements and 442 nodes (884 degrees of freedom in total). A constitutive model similar to the one presented in the previous chapter (ideal behavior has been considered and no glassy phase plasticity has been taken into account) is used

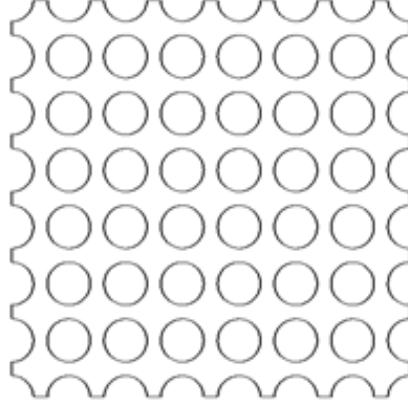


Figure A.1: Geometry considered for the phononic crystal.

to reproduce the SMP behavior. The list of parameters used is reported in Table A.1. Moreover, the material density is set to  $1.17 \cdot 10^{-9}$  tonn/mm<sup>3</sup>. The parameters are referred to the material chosen for the experimental tests and described in the following subsection.

Table A.1: Material parameters used in the simulations.

Value	Unit	Description
40	$K$	half-width of the temperature range $\Delta\theta$
0.09	$1/K$	transformation coefficient $w$
10	$MPa$	Young's modulus of the rubbery phase
3000	$MPa$	Young's modulus of the glassy phase
0.49	-	Poisson's coefficient of the rubbery phase
0.35	-	Poisson's coefficient of the glassy phase
150	$K$	transformation temperature $\theta_t$

At first, a buckling analysis is run to derive the buckling modes of the component under compression. A shape-memory cycle is then simulated on the phononic crystal: the simulation starts with the compression of the component, then the shape-fixing is operated, and finally the temperature is increased to trigger shape recovery. The results of the buckling analysis have been used to add an *imprecision* to the model mesh, in order to obtain buckling during the first phase of the simulation.

Periodic boundary conditions are applied to the opposite edges of the phononic crystal, as described in [243], so that the motion of each node on the component edge is constrained to the motion of the periodically located node on the opposite edge.

In Figure A.2, the results of such simulation are reported. The crystal is initially deformed, while at temperatures higher than the transformation range. It can be noted that the crystal buckles under an imposed compression; the buckled shape is then fixed through constrained cooling, so that the crystal remains deformed after unloading. The original undeformed configuration is that recovered by heating over the transformation temperature.

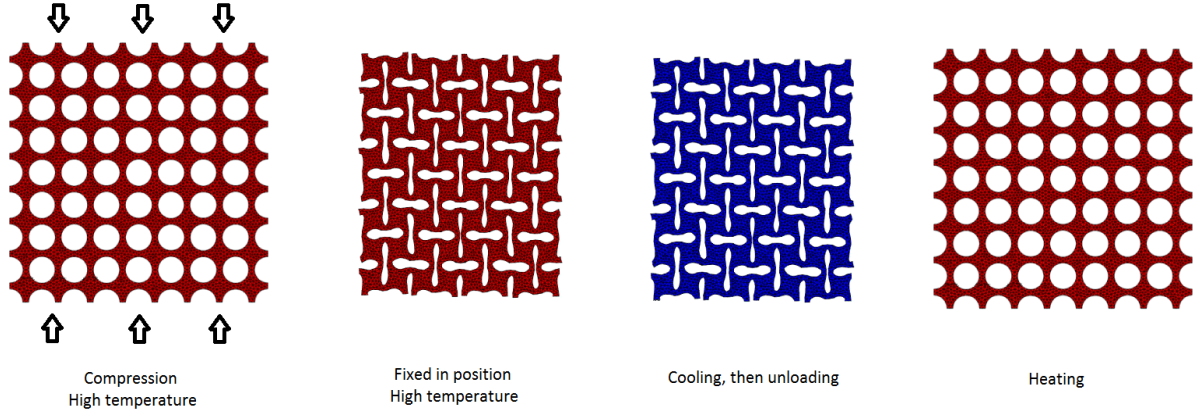


Figure A.2: Shape-memory cycle simulation on the phononic crystal.

Secondly, post-buckling analyses have been performed in order to obtain the deformation pattern of the component under different compression conditions. Wave propagation analyses have been then run on both undeformed and deformed configurations to evaluate the variations in the band gap.

The route which has been taken to perform the wave propagation simulations is the Bloch wave analysis.

Bloch wave analysis considers an infinite periodic structure and is based on a representative volume element (RVE), which is the smallest unit-cell of the structure (Figure A.3(a)).

The reciprocal lattice can be defined as the set of wave vectors  $\mathbf{k}$  that creates plane waves that satisfy the spatial periodicity of the point lattice. The subset of wave vectors  $\mathbf{k}$  that contains all the information about the propagation of plane waves in the structure is called the Brillouin zone. For the geometry considered in this study, the Brillouin zone is identified by the vectors depicted in Figure A.3(b).

The phononic band gaps are identified by checking all eigenfrequencies  $\omega(\mathbf{k})$  for all  $\mathbf{k}$



vectors in the irreducible Brillouin zone: the band gaps are the frequency ranges within which no  $\omega(\mathbf{k})$  exists. These eigenvalues  $\omega(\mathbf{k})$  are continuous functions of the vectors  $\mathbf{k}$  (which individuate the wave direction), but they are discretized when computed through numerical methods such as FEA. Once checked all the eigenvalues in the Brillouin zone, the eigenvalues  $\omega(\mathbf{k})$  can be plotted versus  $\mathbf{k}$ . The  $\omega(\mathbf{k})$  versus  $\mathbf{k}$  plot is called dispersion diagram.

For further information, please consult [196].

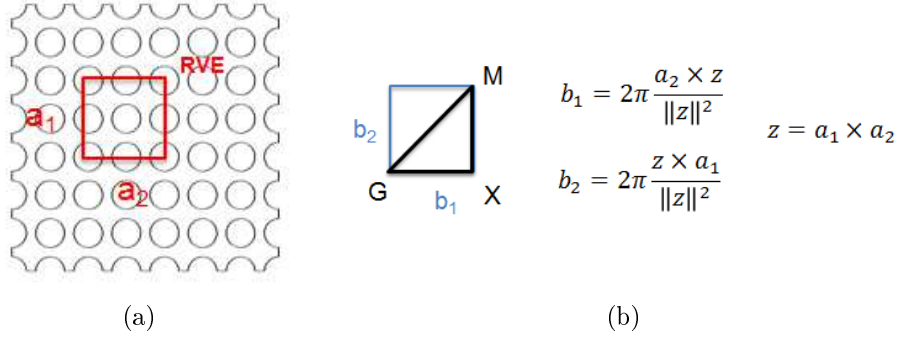


Figure A.3: (a) RVE and (b) Brillouin zone in the reciprocal lattice.

In Figure A.4, the results of the Bloch wave analysis on a RVE of the phononic crystal considered are reported. Dispersion diagrams have been derived for different amounts of compression. It is thus demonstrated that the SMP phononic crystal can be easily deformed while at temperatures higher than the transformation range, and after cooling it can maintain the temporary given shape, resulting in tunable variation of the band gap. Upon re-heating, the original undeformed configuration can be recovered.

A normalized frequency have been used on the vertical axis of the dispersion diagrams, calculated as:

$$f_{norm} = \frac{f a}{c_T} \quad (\text{A.1})$$

where  $a$  is the characteristic dimension of the RVE, and  $c_T$  is the wave propagation speed in the considered material.

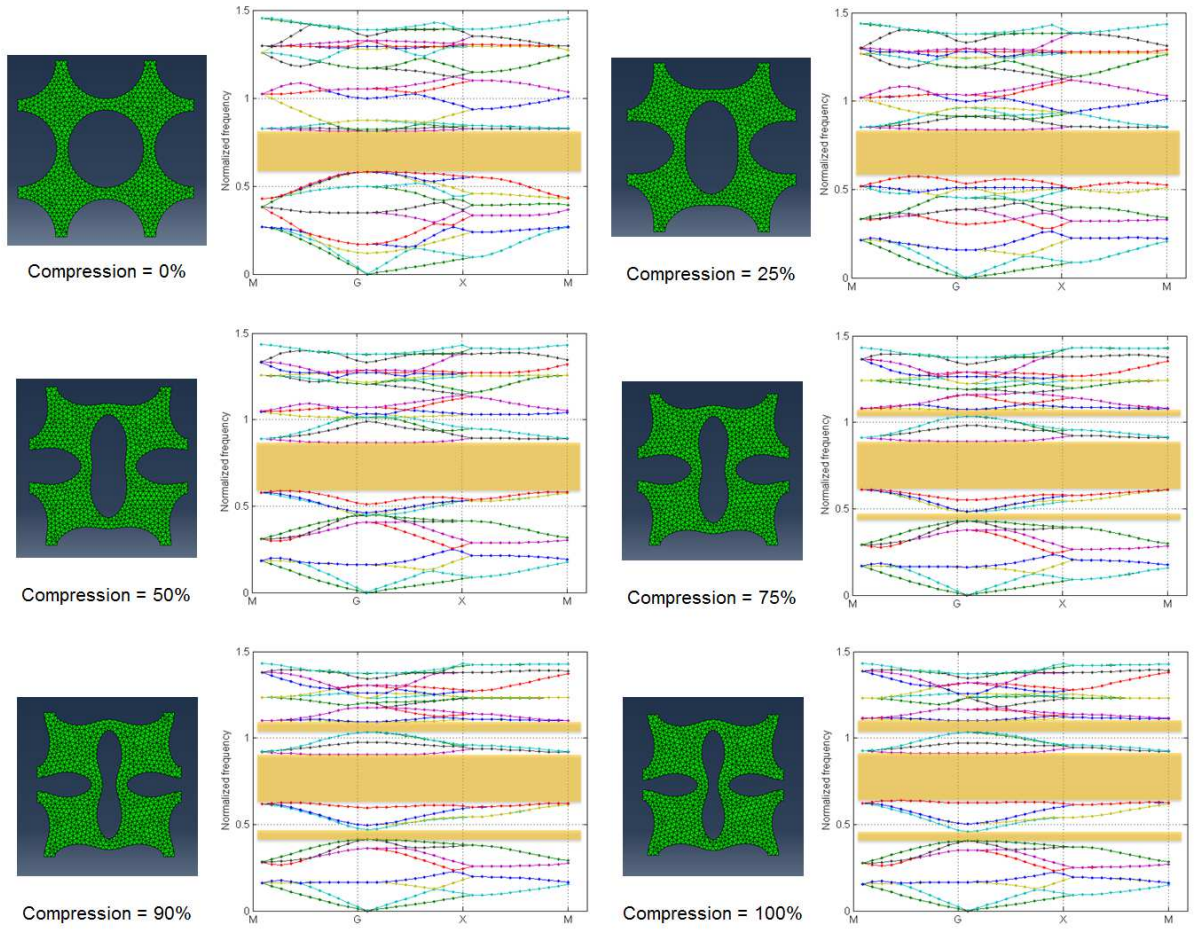


Figure A.4: Dispersion diagrams.

### A.2.2 Experimental testing

The SMP considered in this study was chosen primarily for its readily-availability. It is pre-stretched polystyrene available in thin sheets (Shrink Film, Grafix, Maple Heights, OH). The fundamental characteristic of these sheets is that when they are heated over about 150 °C they shrink and become smaller and thicker, as represented in Figure A.5.



Figure A.5: SMP material used in the experimental testing.

The procedure to obtain a phononic crystal structure like the one represented in Figure A.1 is now described.

A quantity ranging from 3 to 6 SMP sheets has been utilized for each crystal. The sheets were shrunk in an oven at first, and then overlapped and put back in the oven at 150°C to allow sticking of the various layers. A thick block was thus obtained and cooled in air. At this point, the block was engraved using a laser-cutter, to obtain a footprint of the final periodic shape. Since the material was not adapt to be cut through the whole thickness by the laser-cutter, due to melting and burning problems, tool machining was used to manufacture the component in its final shape. A schematic of the production procedure is represented in Figure A.6.

A shape-memory cycle was performed on the final component. While shape-fixing was very good (first step in Figure A.7), the component did not show a satisfactory shape recovery (second step in Figure A.7), so that a stretching operation was necessary to get the material to a nearly undeformed state (third and last step in Figure A.7).



Figure A.6: Manufacturing procedure: the layers are overlapped and heated in order to glue them; the external shape and the holes locations are then obtained through a laser-cutter; finally, the holes are drilled.

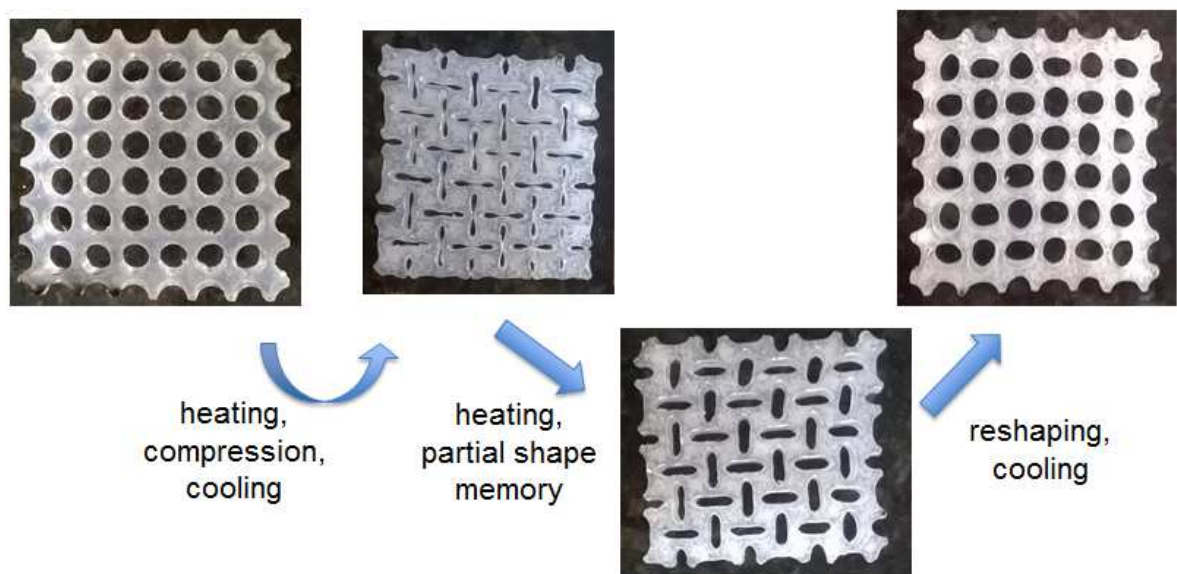


Figure A.7: Shape-memory cycle: shape fixing, partial shape recovering, and final reshaping.

# Appendix B

## Self-sensing ability of SMA actuators

The present chapter briefly summarizes the work done together with a student of Biomedical Engineering (at University of Pavia), whom I supervised during the preparation of his Bachelor thesis.

### B.1 Introduction

Among the numerous applications of SMAs, actuators represent one of the most innovative and promising. For example, SMA-actuated applications can be found in phone-cameras, air-conditioning and hydraulic valves, microelectronic switches, etc.

Many actuators present a closed loop control, therefore a measure of the output is needed to tune the input signal, in order to achieve the desired motion. Conventional actuators often rely on displacement sensors, or sometimes even on predictive models, to provide the controller with some information about the output. In such cases, an indirect method is thus used to measure the output, with consequent issues related to measurement time, precision, eventually increasing complexity and size of the overall device.

SMA actuators do not require the utilization of additional sensors, thanks to an interesting property of the material, namely the *self-sensing* ability. Such characteristic derives from the tight correlation between the phase transformation of the alloy and its electrical resistivity. Since the phase transformation is directly linked to the material shape change, and therefore to the actuation, the measurement of the electrical resistance during the phase transformation provides information on the motion of the SMA actuator, without the need for displacement sensors. This reduces the size and complexity of the device,

along with the manufacturing time and cost. Moreover, the measurement depends directly on the material behavior, resulting in higher reliability and reducing the time for signal transducing.

The self-sensing phenomenon has been investigated in the last years, even though more detailed studies are needed. In fact, while other aspects of SMAs such as the relation between phase transformation, temperature and deformation, have been widely described, the link between phase transformation and resistivity still needs more attention.

The present study has been made in order to assess the self-sensing capabilities of Nitinol wires produced by SAES Getters company (Lainate, MI, Italy), as well as to propose a constitutive model able to describe such phenomenon.

## B.2 Materials and methods

Experimental tests were performed on SmartFlex NiTi wires with diameter 0.2 mm, produced by the company SAES Getters (Lainate, MI, Italy). A graphical explanation of the electrical actuation of SMA wires can be found in Figure B.1.

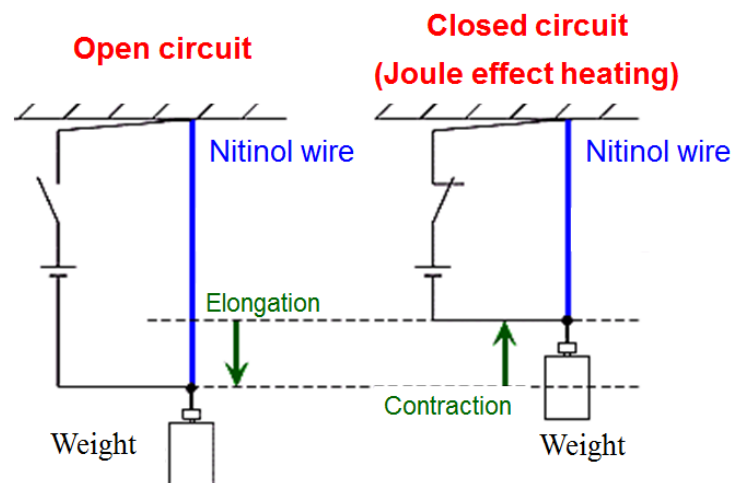


Figure B.1: SMA electrical actuation: when the circuit is closed, the wire is heated through Joule effect and it contracts, pulling the weight.

Technical data for the wires are reported in Figure B.2. The testing setup is displayed in Figure B.3. A frame was assembled in order to hang the Nitinol wire, cut about 150 mm long, which in turn held a variable weight, consisting of a cylindrical box containing lead spheres. In correspondence of the bottom surface of the box, a potentiometer was fastened

to the frame and adjusted vertically to catch the vertical displacement of the box, led by the wire contraction/extension. A counter-spring allowed the slider of the potentiometer to always remain in contact with the bottom surface of the box. An electrical circuit was built as reported in Figure B.4; a precision resistance, with a  $\pm 1\%$ , was used to calculate the electrical current circulating. A power supplier Elektro-Automatik PS 3000b was used to activate the NiTi wire and to provide potential difference for the electrical measurements. A DAQ USB-6210 by National Instruments was used for data acquisition, along with the software Labview.

Prodotto	Diametro [μm]	Forza Massima [N]	Elongazione Massima	Forza Applicata Suggesta [N]	Elongazione Applicata Suggesta
SmartFlex02	200	19	5%	5	<3,5%
SmartFlex03	300	42		12	
SmartFlex04	400	75		21	
SmartFlex05	500	118		33	

Figure B.2: Smartflex (SAES Getters) wires technical data.

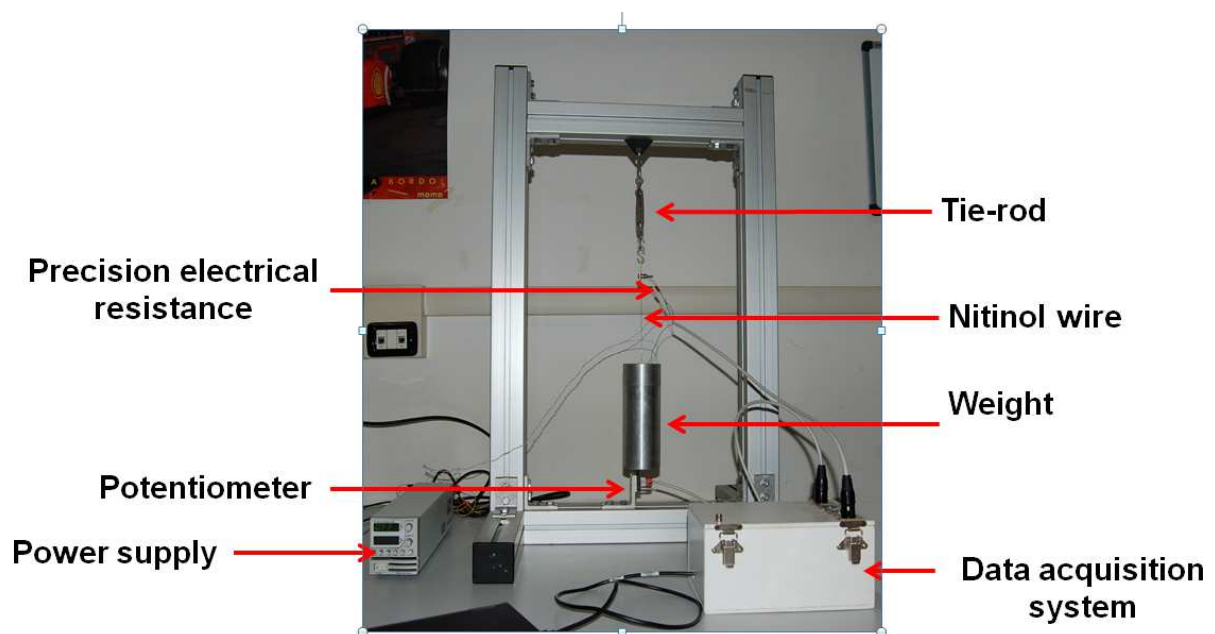


Figure B.3: Testing equipment.

A sufficient voltage was applied to the circuit, so that wire contraction was achieved thanks to the heat produced by Joule effect; after that, the voltage was dropped to a low

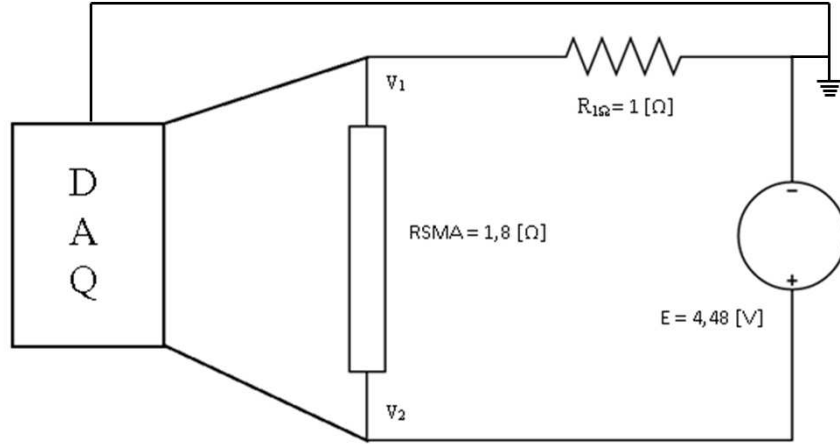


Figure B.4: Electrical circuit: voltage supply and data acquisition.

level in order to allow cooling (and so extension) of the wire, but still provide enough potential difference for the DAQ to measure the voltage drops in the circuit. Different weights were hang to the wires, in order to investigate the effect of load variation on the relationship between wire contraction/extension and electrical resistance.

## B.3 Experimental results

In the present section, a summary of the numerous experimental curves obtained will be presented.

In general, three different regions can be individuated in the plots. A bottom region where electrical resistance increases, along with a small extension of the wire due to thermal expansion: this phase corresponds to an initial heating of the wire, when the heat is yet not enough to produce phase transformation. In the central region of the plots, the phase transformation takes place, and the electrical resistance experiences a big decrease, nearly linearly proportional to the wire contraction. Finally, an upper region can be noted, where the phase transformation has ended, and the resistance increases; again, a small elongation takes place due to thermal expansion. It can be noted that the resistance variation due to the phase transformation is much higher than the one due to temperature change.

It can be noted that as higher weights are applied to the wire, the contraction versus resistance curve shifts to the right.



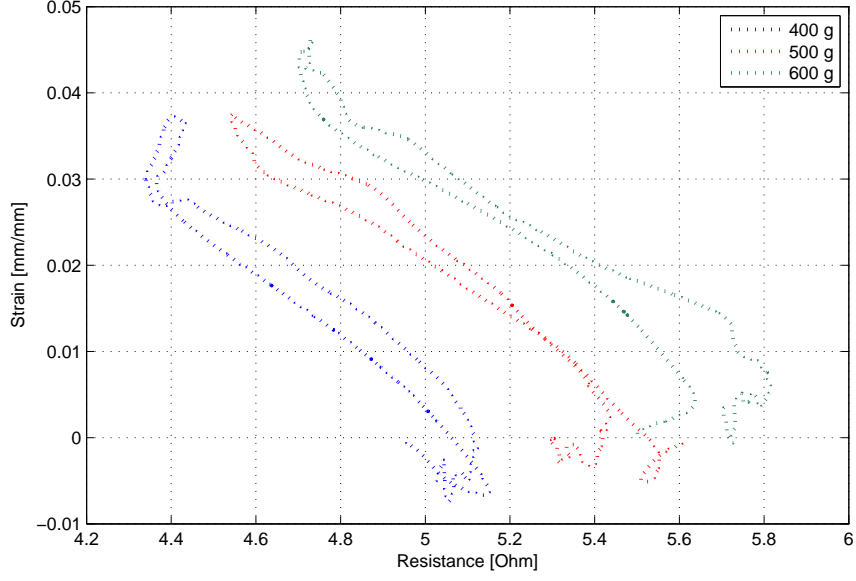


Figure B.5: Experimental data obtained from three trials, with different applied weight.

The rough data obtained by acquisition have been filtered in Matlab [200], in order to derive smoother curves. The obtained data match well with the trend of the experimental data which can be found in literature [177, 346].

## B.4 Constitutive model

In order to simulate the self-sensing behavior, the following constitutive material model is proposed.

The total electrical resistance of the actuator is derived from a rule of mixture, which reads:

$$R = R_M \frac{\varepsilon^{tr}}{\epsilon_L} + R_A \left( 1 - \frac{\varepsilon^{tr}}{\epsilon_L} \right). \quad (\text{B.1})$$

$R_M$  is the resistance of the martensite fraction,  $R_A$  is the resistance of the austenite fraction,  $\varepsilon^{tr}$  is the transformation strain and  $\epsilon_L$  is the maximum limit for the transformation strain. The  $\frac{\varepsilon^{tr}}{\epsilon_L}$  ratio represents the martensite fraction.

The model considered is one-dimensional, because it refers to actuators presenting one preferential actuation direction (e.g. wires or springs).

While  $\epsilon_L$  is given as a material parameter,  $\epsilon^{tr}$  can be derived from the one-dimensional version of the Souza-Auricchio model (detailed in Reference [25]).

Regarding  $R_M$  and  $R_A$ , the following expressions are chosen:

$$R_M = R_{M0} + \partial_T R_M (T - T_{M0}) + \partial_\sigma R_M \sigma \quad (\text{B.2})$$

$$R_A = R_{A0} + \partial_T R_A (T - T_{MA}) + \partial_\sigma R_A \sigma. \quad (\text{B.3})$$

where  $R_{M0}$ ,  $R_{A0}$ ,  $\partial_T R_M$ ,  $\partial_T R_A$ ,  $\partial_\sigma R_M$  and  $\partial_\sigma R_A$  are appropriately chosen constants.

The temperature of the wire can be calculated at every (acquisition) instant using the following energy balance:

$$\frac{c \cdot m}{\Delta t} (T - T_{old}) + h_{conv} (T - T_{ext}) = I \cdot V_{SMA}, \quad (\text{B.4})$$

where  $c$  is the specific heat of NiTi,  $m$  is the mass of the actuator,  $T$  and  $T_{old}$  are respectively the temperatures at the current and at the previous instant,  $h_{conv}$  is the convection coefficient defining the heat exchange with the external environment,  $T_{ext}$  is the external temperature,  $I$  is the electrical current flowing in the circuit, and  $V_{SMA}$  is the voltage drop on the NiTi wire.

# Bibliography

- [1] Abaqus, Analysis User's Manual, 2010, Dassault Systemes of America Corp, Woodland Hills, CA.
- [2] Abrahamson E.R., M.S. Lake, N.A. Munshi, and K. Gall, Shape memory mechanics of an elastic memory composite resin. *J. Intell. Mater. Syst. Struct.*, 2003, 14, 623–632.
- [3] Allium Medical Solutions Ltd. <[www.allium-medical.com](http://www.allium-medical.com)>. ( Consultation: may 2013).
- [4] Aortic Endografts Market. MedtechVentures. (2013).
- [5] J. Arghavani, F. Auricchio, R. Naghdabadi, A. Reali, S. Sohrabpour, A 3-d phenomenological constitutive model for shape memory alloys under multiaxial loadings, *International Journal of Plasticity* 26 (2010) 976–991.
- [6] B. Asgarian, S. Moradi, Seismic response of steel braced frames with shape memory alloy braces, *Journal of Constructional Steel Research* 67 (1) (2011) 65–74.
- [7] Assad, M., Chernyshov, A. V., Jarzem, P., Leroux, M. A., Coillard, C., Charette, S., Rivard, C. H. Porous Titanium-Nickel for Intervertebral Fusion in a Sheep Model: Part 2. Surface Analysis and Nickel Release Assessment. *Journal of Biomedical Materials Research Part B: Applied Biomaterials*, 64B, 121–129. (2003).
- [8] Auricchio, F., Taylor, R. Shape-memory alloys: Modelling and numerical simulations of the finite-strain superelastic behavior. *Computer Methods in Applied Mechanics and Engineering*, 143(1–2), 175–194. (1997).
- [9] Auricchio, F., Taylor, R., Lubliner, J. Shape-memory alloys: Macromodelling and numerical simulations of the superelastic behavior. *Computer Methods in Applied Mechanics and Engineering*, 146(3-4), 281–312. (1997).

- [10] Auricchio, F., Petrini, L., Pietrabissa, R., Sacco, E. Numerical modeling of shape-memory alloys in orthodontics. *CMES*, (2003), 4, 365–380.
- [11] Auricchio, F., Petrini, L. A three-dimensional model describing stress-temperature induced solid phase transformations: Solution algorithm and boundary value problems. *International Journal for Numerical Methods in Engineering*, 61(6), 807–836. (2004).
- [12] Auricchio, F., Conti, M. e., Morganti, S., Reali, A. Shape memory alloy: From constitutive modeling to finite element analysis of stent deployment. *CMES - Computer Modeling in Engineering and Sciences*, 57(3), 225–243. (2010).
- [13] F. Auricchio, J. Arghavani, M. Conti, S. Morganti, A. Reali, U. Stefanelli, Shape-memory alloys: effective 3d modeling, computational aspects and analysis of actuator and biomedical devices, in: *Proceedings of ACTUATOR10 - International Conference and Exhibition on New Actuators and Drive Systems*, 2010.
- [14] Auricchio, F., Conti, M., De Beule, M., De Santis, G., Verhegghe, B. Carotid artery stenting simulation: From patient-specific images to finite element analysis. *Medical Engineering and Physics*, 33(3), 281–289. (2011).
- [15] F. Auricchio, S. Morganti, A. Reali, M. Urbano, Theoretical and experimental study of the shape memory effect of beams in bending conditions, *Journal of Materials Engineering and Performance* 20 (2011) 712–718.
- [16] Auricchio, F., Conti, M., Ferraro, M., Reali, A. Evaluation of carotid stent scaffolding through patient-specific finite element analysis. *International Journal for Numerical Methods in Biomedical Engineering*, 28(10), 1043–1055. (2012).
- [17] Auricchio, F., Conti, M., Morganti, S. *Studies in Mechanobiology, Tissue Engineering and Biomaterials*. Springer. (2013).
- [18] Auricchio, F., Conti, M., Ferrara, A., Morganti, S., Reali, A. Patient-specific finite element analysis of carotid artery stenting: A focus on vessel modeling. *International Journal for Numerical Methods in Biomedical Engineering*, 29(6), 645–664. (2013).
- [19] Auricchio, F., Conti, M., Marconi, S., Reali, A., Tolenaar, J., Trimarchi, S. Patient-specific aortic endografting simulation: From diagnosis to prediction. *Computers in Biology and Medicine*, 43(4), 386–394. (2013).

- [20] F. Auricchio, A.-L. Bessoud, A. Reali, U. Stefanelli. A three-dimensional phenomenological models for magnetic shape memory alloys. *GAMM-Mitt.*, 34 (2011) 90–96.
- [21] F. Auricchio, A.-L. Bessoud, A. Reali, U. Stefanelli. A phenomenological model for the magneto-mechanical response of single-crystal Magnetic Shape Memory Alloys. *Eur. J. Mech. A/Solids*, 52 (2015) 1–11.
- [22] F. Auricchio, E. Bonetti, G. Scalet, F. Ubertini, Theoretical and numerical modeling of shape memory alloys accounting for multiple phase transformations and martensite reorientation, *International Journal of Plasticity* 59 (2014) 30–54.
- [23] F. Auricchio, A. Mielke, U. Stefanelli. A rate-independent model for the isothermal quasi-static evolution of shape-memory materials. *Math. Models Meth. Appl. Sci.*, 18 (2008) 125–164.
- [24] F. Auricchio, L. Petrini. Improvements and algorithmical considerations on a recent three-dimensional model describing stress-induced solid phase transformations. *Internat. J. Numer. Methods Engrg.*, 55 (2002) 1255–1284.
- [25] F. Auricchio, L. Petrini. A three-dimensional model describing stress-temperature induced solid phase transformations. Part I: Solution algorithm and boundary value problems. *Internat. J. Numer. Meth. Engrg.*, 61 (2004) 807–836.
- [26] F. Auricchio, L. Petrini. A three-dimensional model describing stress-temperature induced solid phase transformations. Part II: Thermomechanical coupling and hybrid composite applications. *Internat. J. Numer. Meth. Engrg.*, 61 (2004) 716–737.
- [27] F. Auricchio, A. Reali, U. Stefanelli. A three-dimensional model describing stress-induced solid phase transformation with residual plasticity. *Int. J. Plasticity*, 23 (2007) 207–226.
- [28] F. Auricchio, A. Reali, U. Stefanelli. A phenomenological 3D model describing stress-induced solid phase transformations with permanent inelasticity. In *Topics on Mathematics for Smart Systems*, B. Miara, G. Stavroulakis, and V. Valente (eds.), 1–14. World Sci. Publ., Hackensack, NJ, 2007.

- [29] F. Auricchio, A. Reali, U. Stefanelli. A macroscopic 1D model for shape memory alloys including asymmetric behaviors and transformation-dependent elastic properties. *Comput. Methods Appl. Mech. Engrg.*, 198 (2009) 1631–1637.
- [30] F. Auricchio, S. Morganti, A. Reali, SMA numerical modeling versus experimental results, in: Proceedings of European Symposium on Martensitic Transformations (ES-OMAT 2009), 2009, pp. 1–6.
- [31] Auricchio F., M. Conti, S. Morganti, A. Reali. "Shape Memory Alloy: from constitutive modelling to finite element analysis of stent deployment". *Computer Modeling in Engineering and Sciences*, 57 (2010) 225–243.
- [32] F. Auricchio, G. Scalet, M. Urbano. A Numerical/Experimental Study of Nitinol Actuator Springs. *J. Mater. Engrg. Perf.*, 23, 2014, 2420–2428.
- [33] Auricchio F., E. Boatti, M. Conti. SMA Biomedical Applications. In *Shape Memory Alloy engineering: for Aerospace, Structural and Biomedical Applications*. Editors: L. Lecce, A. Concilio, F. Auricchio. Elsevier, 307–341, (2014).
- [34] Auricchio F., E. Boatti, M. Conti. SMA Cardiovascular Applications and Computer-Based Design. In *Shape Memory Alloy engineering: for Aerospace, Structural and Biomedical Applications*. Editors: L. Lecce, A. Concilio, F. Auricchio. Elsevier, 343–367, (2014).
- [35] Auricchio F., E. Boatti, A. Reali, U. Stefanelli. Gradient structures for the thermomechanics of shape-memory materials. *CMAME*. Under review. (2015)
- [36] Azaouzi, M., Makradi, A., Belouettar, S. Deployment of a self-expanding stent inside an artery: A finite element analysis. *Materials and Design*, 41, 410–420. (2012).
- [37] Azaouzi, M., Lebaal, N., Makradi, A., Belouettar, S. Optimization based simulation of self-expanding Nitinol stent. *Materials and Design*, 50, 917–928. (2013).
- [38] [www.actuatorsolutions.de/](http://www.actuatorsolutions.de/), consultation: June 2014.
- [39] G. Babighian, M. Fontana, S. Caltran, M. Ciccolella, M. Amadori, M. De Zen, The heat-activated stapes prosthesis 'smart' piston: Technique and preliminary results, *Advances in Oto-Rhino-Laryngology* 65 (2007) 190–196.

- [40] Baer G., T. S. Wilson, D. L. Matthews, D. J. Maitland. Shape-memory behavior of thermally stimulated polyurethane for medical applications. *Journal of Applied Polymer Science*, 2007, 103, 3882–3892.
- [41] Baghani M., R. Naghdabadi, J. Arghavani, S. Sohrabpour, A thermodynamically-consistent 3D constitutive model for shape memory polymers, *International Journal of Plasticity*, 2012, 35, 13–30.
- [42] Baghani M., J. Arghavani, R. Naghdabadi, A finite deformation constitutive model for shape memory polymers based on Hencky strain, *Mechanics of Materials*, 2014, 73, 1–10.
- [43] Bansiddhi, A., Sargeant, T.D., Stupp, S.I., Dunand, D.C. Porous NiTi for bone implants: A review. *Acta Biomaterialia*, 4(4), 773–782. (2008).
- [44] Barcelos, A. M., A. S. Luna, N. de Assis Ferreira, A. V. Braga, D. C. do Lago, L. F.de Senna. Corrosion Evaluation of Orthodontic Wires in Artificial Saliva Solutions by Using Response Surface Methodology. *Materials Research*, (2012) 16, 50–64.
- [45] Barot G., I. Rao, K. Rajagopal. A thermodynamic framework for the modeling of crystallizable shape memory polymers, *Int. J. Eng. Sci.*, 2008, 46, 325–351.
- [46] Barras, C., K. Myers. Nitinol - Its use in vascular surgery and other applications. *EJVES Extra*, (2010), 19, 564–569.
- [47] A.-L. Bessoud, U. Stefanelli. Magnetic shape memory alloys: Three-dimensional modeling and analysis. *Math. Models Meth. Appl. Sci.*, 21 (2011) 1043–1069.
- [48] A.-L. Bessoud, M. Kružík, U. Stefanelli. A macroscopic model for magnetic shape memory alloys. *Z. Angew. Math. Phys.*, 64 (2013) 2:343–359.
- [49] R. Bharanidaran, T. Ramesh, Numerical simulation and experimental investigation of a topologically optimized compliant microgripper, *Sensors and Actuators A: Physical* 205 (2014) 156–163.
- [50] Bhattacharya, K., 2003. Microstructure of Martensite. Oxford University Press, Oxford.

- [51] bmctoday.net (Consultation: November 2013).
- [52] Boatti E., G. Scalet, F. Auricchio. A three-dimensional finite-strain phenomenological model for shape memory polymers. *IJP*. In preparation. (2015).
- [53] Bock, S. D., Iannaccone, F., Santis, G. D., Beule, M. D., Mortier, P., Verhegghe, B., Segers, P. Our capricious vessels: The influence of stent design and vessel geometry on the mechanics of intracranial aneurysm stent deployment . *Journal of Biomechanics*, 45(8), 1353–1359. (2012).
- [54] Bonet J., R.D. Wood. Nonlinear continuum mechanics for finite element analysis. *Cambridge University Press*, 2008.
- [55] Bonsignore, C. A decade of evolution in stent design. In A. R. Pelton, T. Duerig (Editor), *SMST 2003 - Proceedings of the International Conference on Shape Memory and Superelastic Technologies*. (2003).
- [56] C. Bouvet, C. Calloch, S.and Lexcellent, A phenomenological model for pseudoe-  
lasticity of shape memory alloys under multiaxial proportional and nonproportional  
loadings, *European Journal of Mechanics-A/Solids* 23 (1) (2004) 37–61.
- [57] H. Brézis. *Opérateurs Maximaux Monotones et Semi-Groupes de Contractions dans  
les Espaces de Hilbert*. Math Studies, Vol.5, North-Holland, Amsterdam/New York,  
1973.
- [58] F. Butera, Shape memory actuators for automotive applications, *Advanced Materials  
and Processes* - (2008) 37–40.
- [59] Carboni, B., W. Lacarbonara, F. Auricchio. Hysteresis of Multiconfiguration Assem-  
blies of Nitinol and Steel Strands: Experiments and Phenomenological Identification,  
*Journal of Engineering Mechanics*, 2015, 141(3).
- [60] Carotid Stent Systems Market: Current Status and Future Outlook. MedtechVentures.  
(2011).
- [61] Carpineto, N., W. Lacarbonara, F. Vestroni. Hysteretic tuned mass dampers for struc-  
tural vibration mitigation, *Journal of Sound and Vibration*, 2014, 333, 1302–1318



- [62] Cekirge, S., Weiss, J., Foster, R., Neiman, H., McLean, G. Percutaneous retrieval of foreign bodies: experience with the nitinol Goose Neck snare. *J Vasc Interv Radiol*, 4(6), 805–10. (1993).
- [63] Centofanti, P., Torre, M. L., Barbato, L., Verzini, A., Patané, F., di Summa, M. Sternal Closure Using Semirigid Fixation With Thermoreactive Clips, *Ann Thorac Surg*, 74, 943–5. (2002).
- [64] Chang, L., T. Read. Plastic deformation and diffusionless phase changes in metals - The gold-cadmium beta phase. *Trans. AIME*, 1951, 189, 47–52.
- [65] Chen Y.-C., D.C. Lagoudas. A constitutive theory for shape memory polymers. Part I Large deformations. *Journal of the Mechanics and Physics of Solids*, 2008, 56: 1752–1765.
- [66] Chen Y.-C., D.C. Lagoudas. A constitutive theory for shape memory polymers. Part II. A linearized model for small deformations. *Journal of the Mechanics and Physics of Solids*, 2008, 56, 1766–1778.
- [67] Cheng, X., Song, C. Mechanical design and finite element analysis of multi-degree-of-freedom transmission for single incision laparoscopic surgery. *4th International Conference on Biomedical Engineering and Informatics (BMEI)*, 2011, 1135–1138. Shanghai. (2011).
- [68] Chi, F., Wang, S., Liu, H. Auricle reconstruction with a nickel-titanium shape memory alloy as the framework. *Laryngoscope*, 117, 248–252. (2007).
- [69] Chuncai, Z., Shuogui, X., Jialin, W., Xuesong, Z., Jiaca, S., Jingfeng, L. Design and clinical application of Nitinol patellar concentrator. *SMST 2000 - Proceedings of the International Conference on Shape Memory and Superelastic Technologies*, 561–568, (2001).
- [70] Coda, A., L. Toia, G. Ischia, S. Gialanella. Effect of thermomechanical treatments on the microstructure of NiTi wires: A TEM study. *SMST-2006: Proceedings of the International Conference on Shape Memory and Superelastic Technologies*, 2006.
- [71] Coleman B. D., W. Noll. The thermodynamics of elastic materials with heat conduction and viscosity. *Arch. Ration. Mech. Anal.*, 1963, 13: 167–178.

- [72] Conti, M., Auricchio, F., De Beule, M., Verhegghe, B. Numerical simulation of Nitinol peripheral stents: from laser-cutting to deployment in a patient specific anatomy. *Proceedings of ESOMAT*. (2009).
- [73] Conti, M., Van Loo, D., Auricchio, F., De Beule, M., De Santis, G., Verhegghe, B., . . . Odero, A. Impact of carotid stent cell design on vessel scaffolding: A case study comparing experimental investigation and numerical simulations. *Journal of Endovascular Therapy*, 18(3), 397–406. (2011).
- [74] Conti, M., Marconi, M., Campanile, G., Reali, A., Adami, D., Berchiolli, R., Auricchio, F. Patient-specific finite element analysis of popliteal stenting. (2013 submitted).
- [75] Costamagna, G., Tringali, A., Spicak, J., Mutignani, M., Shaw, J., Roy, A., et al. Treatment of malignant gastroduodenal obstruction with a nitinol self-expanding metal stent: An international prospective multicentre registry. *Digestive and Liver Disease*, 44, 37–43. (2012).
- [76] A. Cuschieri, Variable curvature shape- memory spatula for laparoscopic surgery, *Surgical Endoscopy* 5 (1991) 179–181.
- [77] Dai KR, Hou XK, Sun YH, Tang RG, Qiu SJ, Ni C, Treatment of intra-articular fractures with shape memory compression staples. *Injury*, (1993), 24 (10), 651–5.
- [78] De Beule, M., Mortier, P., De Santis, G., Conti, M., Segers, P., Verdonck, P., Verhegghe, B. A virtual product development strategy for minimally invasive medical devices. *Trends in Biomaterials and Artificial Organs*, 24(1), 19–26. (2010).
- [79] De Bock S., Iannaccone F., De Santis G., De Beule M., Van Loo D., Devos D., Vermassen F., Segers P., Verhegghe B. Virtual evaluation of stent graft deployment: A validated modeling and simulation study. *Journal of the Mechanical Behavior of Biomedical Materials*, 13, 129–139. (2012).
- [80] De Bock S., Iannaccone F., De Santis G., De Beule M., Mortier P., Verhegghe B., Segers P. Our capricious vessels: The influence of stent design and vessel geometry on the mechanics of intracranial aneurysm stent deployment. *J Biomechanics*. Volume 45(8), 1353–1359. (2012).

- [81] DeHerrera M.A., Dang N. Finite Element Analysis of a Percutaneous Stent-Mounted Heart Valve. Abaqus User's Conference. (2004).
- [82] Demanget, N., Avril, S., Badel, P., OrgÃas, L., Geindreau, C., Albertini, J.-N., Favre, J.-P. Computational comparison of the bending behavior of aortic stent-grafts. *Journal of the Mechanical Behavior of Biomedical Materials*, 5(1), 272–282. (2012).
- [83] Demanget, N., Latil, P., OrgÃas, L., Badel, P., Avril, S., Geindreau, C., Albertini, J.-N., Favre, J.-P. Severe bending of two aortic stent-grafts: an experimental and numerical mechanical analysis. *Annals of biomedical engineering*, 40(12), 2674–2686. (2012).
- [84] Demanget, N., Duprey, A., Badel, P., OrgÃas, L., Avril, S., Geindreau, C., Albertini, J.-N., Favre, J.-P. Finite element analysis of the mechanical performances of 8 marketed aortic stent-grafts. *Journal of Endovascular Therapy*, 20(4), 523–535. (2013).
- [85] Demaria, R. G., Fortier, S., Malo, O., Carrier, M., Perrault, L. P. Interrupted Coalescent Nitinol Clip versus Continuous Suture Coronary Anastomosis: A Comparative Endothelial Function Study. *The Heart Surgery Forum*, 6(2), 72–76. (2003).
- [86] Dettmer W., S. Reese. On the theoretical and numerical modelling of Armstrong–Frederick kinematic hardening in the finite strain regime. *Comput. Methods Appl. Mech. Engrg.*, 2004, 193, 87–116.
- [87] DÃÃHoore, A., Cohen, S., Albert, M., Herbst, F., Senagore, A., Stamos, M. J., Pahlman, L., Wexner, S. D. COMPRES Final Results: Nitinol Compression Anastomosis Results in a Much Lower Than Expected Rate of Anastomotic Leak in Low Anterior Resection (LAR). Poster presented at: *Annual Scientific Meeting of the American Society of Colorectal Surgeons (ASCRS)*. (2012).
- [88] Diani J., Y. Liu, K. Gall. Finite Strain 3D Thermoviscoelastic Constitutive Model for Shape Memory Polymers. *Polymer engineering and Science*, 2006, 486–492
- [89] www.dicardiology.com (Consultation: November 2013).
- [90] T. Duerig, Applications of the shape memory, *Materials Science Forum* 56-58 (1990) 679–692.

- [91] Duerig, T., A. Pelton, D. Stoeckel. The use of supsuperelastic in medicine. *Biomed Mater Eng.*, (1996) 6(4), 255–266.
- [92] Duerig, T., A. Pelton, D. Stoeckel. An overview of nitinol medical applications. *Materials Science and Engineering A*, (1999), 273–275, 149–160.
- [93] V. Dunić, R. Slavković, N. Busarac, V. Slavković, M. Zivković, Implicit stress integration method of shape memory material model, *Proceedings in Applied Mathematics and Mechanics* 13 (1) (2013) 151–152.
- [94] Durville, D., Modélisation du comportement mécanique de cable métallique, *Revue européenne des Mécanismes finis*, 1998, Volume 7 (1–2).
- [95] M. Eleuteri, L. Lussardi. Thermal control of a rate-independent model for permanent inelastic effects in shape memory materials. *Evol. Equ. Control Theory*, 3 (2014) 411–427.
- [96] M. Eleuteri, L. Lussardi, U. Stefanelli. A rate-independent model for permanent inelastic effects in shape memory materials. *Netw. Heterog. Media*, 6 (2011) 145–165.
- [97] M. Eleuteri, L. Lussardi, U. Stefanelli. Thermal control of the Souza-Auricchio model for shape memory alloys. *Discrete Cont. Dyn. Syst.-S*, 6 (2013) 369–386.
- [98] Erdemir, A., Guess, T., Halloran, J., Tadepalli, S., Morrison, T. Considerations for reporting finite element analysis studies in biomechanics. *Journal of Biomechanics*, 45(4), 625–633. (2012).
- [99] Es-Souni, M., M. Es-Souni, H. Fischer-Brandies. Assessing the biocompatibility of NiTi shape memory alloys used for medical applications. *Analytical and Bioanalytical Chemistry*, (2005), 381, 557–567.
- [100] V. Evangelista, S. Marfia, E. Sacco. Phenomenological 3D and 1D consistent models for shape-memory alloy materials. *Comput. Mech.*, 44 (2009) 405–421.
- [101] V. Evangelista, S. Marfia, E. Sacco. A 3D SMA constitutive model in the framework of finite strain. *Internat. J. Numer. Methods Engrg.*, 81 (2010) 761–785.

- [102] V. Evangelista, S. Marfia, E. Sacco. A 3D SMA constitutive model in the framework of finite strain. *Internat. J. Numer. Methods Engrg.*, 81 (2010) 761–785.
- [103] Fernandes, D. J., Peres, R. V., M.Mendes, A., Elias, C. N. Understanding the Shape-Memory Alloys Used in Orthodontics. *ISRN Dent.*, (2011), 132408.
- [104] Ferraro M., Auricchio F., Boatti E., Scalet G., Conti M., Morganti S., Reali A., An efficient finite element framework to assess flexibility performances of SMA self-expandable carotid artery stents, *Journal of Functional Biomaterials*, 2015, 6(3), 585–597.
- [105] www.festo.com, consultation: August 2015.
- [106] S. Frigeri, U. Stefanelli. Existence and time-discretization for the finite-strain Souza-Auricchio constitutive model for shape-memory alloys. *Contin. Mech. Thermodyn.*, 24 (2012) 63–77.
- [107] Gall K., M. L. Dunn, Y. Liu, G. Stefanic, D. Balzar. Internal stress storage in shape memory polymer nanocomposites. *Applied Physics Letters*, 2004, 85(2) 290–292.
- [108] Gao, B., Baharoglu, M., Cohen, A., Malek, A. Stent-Assisted Coiling of Intracranial Bifurcation Aneurysms Leads to Immediate and Delayed Intracranial Vascular Angle Remodeling. *AJNR Am. J. Neuroradiol.*, 33, 649–654. (2012).
- [109] Garcia, A., Pena, E., Martinez, M. Influence of geometrical parameters on radial force during self-expanding stent deployment. Application for a variable radial stiffness stent. *Journal of the Mechanical Behavior of Biomedical Materials*, 10, 166–175. (2012).
- [110] Ge, Q., X. Luo, C. B. Iversen, H. B. Nejad, P. T. Mather, M. L. Dunn, H. J. Qi. A finite deformation thermomechanical constitutive model for triple shape polymeric composites based on dual thermal transitions. *International Journal of Solids and Structures*, 2014, 51, 2777–2790.
- [111] Ghosh P., A. Srinivasa. A two-network thermomechanical model of a shape memory polymer. *Int. J. Eng. Sci.*, 2011, 49, 823–838.

- [112] Ghosh P., A. Srinivasa. A two-network thermomechanical model and parametric study of the response of shape memory polymers. *Mech. Mater.*, 2013, 60, 1–17.
- [113] Giataganas, P., Evangeliou, N., Koveos, Y., Kelasidi, E., Tzes, A. Design and experimental evaluation of an innovative SMA-based tendon-driven redundant endoscopic robotic surgical tool. *19th Mediterranean Conference on Control and Automation*, 1071–1075. Corfu. (2011).
- [114] Global Markets for Coronary Stent Devices. BCC Research. (2012).
- [115] Gong, X.-Y. Nitinol: The Flexible Friend. <http://www.medicaldevice-network.com>. (2010).
- [116] Greninger, A., V. Mooradian. Strain transformation in metastable beta copper-zinc and beta copper-tin alloys. *Trans. AIME*, 1938, 128, 337–368.
- [117] Guber, Giordano, Schlusser, Baldinus, Loser, Wieneke. Nitinol-based microinstruments for neurosurgery. *Actuator 96: 5th Internat.Conf.on New Actuators*. (1996).
- [118] Guidoin, R., Z. Zhang, G. Dionne, Y. Douville, M. King, A. Legrand, P. Doppelt. Corrosion of the nitinol wire of endovascular prostheses: Does nickel ion impair the devices performance? In *Medical Device Materials II - Proceedings of the Materials and Processes for Medical Devices Conference 2004*, 284–289, St. Paul, MN.
- [119] Gurtin, M. An Introduction to Continuum Mechanics *Academic Press*, New York, 1981
- [120] D. Grandi, U. Stefanelli. A phenomenological model for microstructure-dependent inelasticity in shape-memory alloys. *Meccanica*, 49 (2014) 9:2265–2283.
- [121] D. Grandi, U. Stefanelli. The Souza-Auricchio model for shape-memory alloys. *Discr. Contin. Dyn. Syst. S.*, 8 (2015), 4:727–743.
- [122] M. Grmela, H. C. Öttinger, *Dynamics and thermodynamics of complex fluids. I. Development of a general formalism*, *Phys. Rev. E.* (3), 56 (1997), 6:6620–6632.
- [123] Haasters, J., Salis-Solio, G., Bensmann, G. The use of Ni-Ti as an implant material in orthopedics. In *Engineering aspects of shape memory alloys*. Butterworth-Heinemann, (1990).

- [124] C. Haberland, H. M. . I. M. Elahinia, J. Walker, Visions, concepts and strategies for smart nitinol actuators and complex nitinol structures produced by additive manufacturing, in: ASME 2013 Conference on Smart Materials, Adaptive Structures and Intelligent Systems (SMASIS 2013), 2013, pp. 1–8.
- [125] Haga, Y., Mineta, T., Makishi, W., Matsunaga, T., Esashi, M. Shape Memory Alloys. In C. Cismasiu (Editor). Sciyo. (2010).
- [126] Hager M. D., S. Bode, C. Weber, U. S. Schubert. Shape memory polymers: Past, present and future developments. *Progress in Polymer Science*, 2015.
- [127] D. Hartl, D. Lagoudas, Aerospace applications of shape memory alloys, in: Proceedings of the Institution of Mechanical Engineers, Part G: Journal of Aerospace Engineering, Vol. 221 of 4, 2007, pp. 535–552.
- [128] Harvey, S. M. Nitinol Stent Fatigue in a Peripheral Human Artery Subjected to Pulsatile and Articulation Loading. *JMEPEG*, 20, 697–705. (2011).
- [129] Hauck, F., Wendt, D., Stühle, S., Kawa, E., Wendt, H., Müller, W., Thielmann, M., Kipfmüller, B., Vogel, B., Jakob, H. Use of Circular Foldable Nitinol Blades for Resecting Calcified Aortic Heart Valves. *JMEPEG*, 18, 463–469. (2009).
- [130] Hill, A. C., Maroney, T. P., Virmani, R. Facilitated coronary anastomosis using a nitinol U-clip device: Bovine model. *J Thorac Cardiovasc Surg*, 121, 859–870. (2001).
- [131] Ho, M., Desai, J. Characterization of SMA actuator for applications in robotic neurosurgery. *Conference proceedings: Annual International Conference of the IEEE Engineering in Medicine and Biology Society. IEEE Engineering in Medicine and Biology Society. Conference*, 6856–6859. (2009).
- [132] Ho, M., Desai, J. Towards the development of a SMA-actuated MRI-compatible tendon-driven neurosurgical robot. *Proceedings - IEEE International Conference on Robotics and Automation*, 683–688. (2012).
- [133] Hornbogen, E. Review Thermo-mechanical fatigue of shape memory alloys. *J. Mater. Sci.*, (2004) 39(2), 385–399.

- [134] Hornung, J., Brase, C., Bozzato, A., Zenk, J., Schick, B., Iro, H. Retrospective analysis of the results of implanting Nitinol pistons with heat-crimping piston loops in stapes surgery. *European Archives of Oto-Rhino-Laryngology*, 267, 27–34. (2010).
- [135] Hsiao, H.-M., M.-T. Yin, M.-T. An intriguing design concept to enhance the pulsatile fatigue life of self-expanding stents. *Biomed Microdevices*, (2013).
- [136] Hu J., Y. Zhu, H. Huang, J. Lu. Recent advances in shape-memory polymers: Structure, mechanism, functionality, modeling and applications. *Progress in Polymer Science*, 2012, 37, 1720–1763.
- [137] Iko M, Tsutsumi M, Aikawa H, Matsumoto Y, Go Y, Nii K, Abe G, Ye I, Nomoto Y, Kazekawa K. Distal protection filter device efficacy with carotid artery stenting: comparison between a distal protection filter and a distal protection balloon. *Jpn J Radiol*, 31(1): 45–9. (2012).
- [138] Innomedicus < [www.innomedicus.com](http://www.innomedicus.com) >. (Consultation: february 2013).
- [139] Intramedullary nail to be inserted into a fractured long bone. Patent EP 2133034 A1, (2008).
- [140] Intrauterine Contraceptive Device. Patent USA 3.620.212. (1970).
- [141] R. Jähne, Multiaxial mechanical characterization and constitutive modeling of superelastic sheets for solid-state hinges, Ph.D. thesis, ETH Zurich (2012).
- [142] J. Jani, M. Leary, A. Subic, M. Gibson, A review of shape memory alloy research, applications and opportunities, *Materials & Design* 56 (2014) 1078–1113.
- [143] Jayatilake, D., Isezaki, T., Gruebler, A., Teramoto, Y., Eguchi, K., Suzuki, K. A wearable Robot Mask to support rehabilitation of facial paralysis. *Proceedings of the IEEE RAS and EMBS International Conference on Biomedical Robotics and Biomechatronics*, 1549–1554. Rome. (2012).
- [144] Jin, S., Y. Zhang, Q. Wang, D. Zhang, S. Zhang. Influence of TiN coating on the biocompatibility of medical NiTi alloy. *Colloids and Surfaces B: Biointerfaces*, (2013) 101, 343–349.



- [145] Jung, Y., Papadopoulos, P., Ritchie, R. Constitutive modelling and numerical simulation of multivariant phase transformation in superelastic shape-memory alloys. *International Journal for Numerical Methods in Engineering*, 60(2), 429–460. (2004).
- [146] Kaplanoglu, E. Design of shape memory alloy-based and tendon-driven actuated fingers towards a hybrid anthropomorphic prosthetic hand. *International Journal of Advanced Robotic Systems*, 9, 1–6. (2012).
- [147] Kasano, F., Morimitsu, T. Utilization of nickel-titanium shape memory alloy for stapes prosthesis. *Auris Nasus Larynx*, 24, 137–142. (1997).
- [148] Kasirajan, K., Schneider, P., Kent, K. Filter Devices for Cerebral Protection during Carotid Angioplasty and Stenting. *Journal of Endovascular Therapy*, 10(6), 1039–1045. (2003).
- [149] Kastratović, G.M., N.D. Vidanović. Some aspects of 3D finite element modeling of independent wire rope core, *FME Transactions*, 2011, 39, 37–40.
- [150] Kaul, U., Agarwal, R., Sharma, S., Jain, P., Goswami, K., Wasir, H. Our experience with Palmaz-Schatz coronary stent. *Indian Heart J.*, 46(6), 291–296. (1994).
- [151] A. Khandelwal, V. Buravalla, Models for shape memory alloy behavior: An overview of modeling approaches, *International Journals for Structural Changes in Solids* 1 (1) (2009) 111–148.
- [152] Kheirikhah, M., Khodayari, A., Nikpey, S. Design and modeling of a new biomimetic earthworm robot for endoscopy actuated by SMA wires. *Proceedings - IEEE-EMBS International Conference on Biomedical and Health Informatics: Global Grand Challenge of Health Informatics, BHI 2012*, 148–151. Hong Kong and Shenzhen. (2012).
- [153] Khmelevskaya, I., Ryklina, E., Prokoshkin, S., Markossian, G., Tarutta, E., Iomdina, E. A shape memory device for the treatment of high myopia. *Materials Science and Engineering A*, 481–482, 651–653. (2008).
- [154] Kianzad, S., Amini, A., Karkouti, S. Force control of laparoscopy grasper using antagonistic shape memory alloy. *2011 1st Middle East Conference on Biomedical Engineering, MECBME 2011*, 335–338. Sharjah. (2011).

- [155] Kim, J., Kang, T., Yu, W.-R. Mechanical modeling of self-expandable stent fabricated using braiding technology. *Journal of Biomechanics*, 41(15), 3202–3212. (2008).
- [156] Kim J., T. Kang, W. Yu. Thermo-mechanical constitutive modeling of shape memory polyurethanes using a phenomenological approach. *Int. J. Plast.*, 2010, 26, 204–218.
- [157] Kim, D., Eun, J., Park, J. Posterior cervical fixation with a nitinol shape memory loop for primary surgical stabilization of atlantoaxial instability: A preliminary report. *Journal of Korean Neurosurgical Society*, (2012), 52, 21–26.
- [158] Kitamura, K., Tobushi, H., Yoshimi, Y., Sugimoto, Y. Evaluation of mechanical characteristics of shape memory alloy for brain spatula. Nihon Kikai Gakkai Ronbunshu, A Hen, *Transactions of the Japan Society of Mechanical Engineers*, Part A, 75, 439–445. (2009).
- [159] Kleinstreuer, C., Li, Z., Basciano, C., Seelecke, S., Farber, M. Computational mechanics of Nitinol stent grafts. *Journal of Biomechanics*, 41(11), 2370–2378. (2008).
- [160] Knox, G., Reitan, H. Shape-memory stapes prosthesis for otosclerosis surgery. *Laryngoscope*, 115, 1340–1346. (2005).
- [161] Kode, V., Çavusoglu, M. Design and characterization of a novel hybrid actuator using shape memory alloy and DC micromotor for minimally invasive surgery applications. *IEEE/ASME Transactions on Mechatronics*, 12, 455–464. (2007).
- [162] M. Kohl, Shape Memory Microactuators, Springer, 2004.
- [163] J. Korelc, Multi-language and multi-environment generation of nonlinear finite element codes, *Engineering with Computers* 18 (4) (2002) 312–327.
- [164] Korelc J., Automatic generation of finite-element code by simultaneous optimization of expressions, 1997, *Theoretical Computer Science* 187(1-2): 231–248.
- [165] Krairi A., I. Doghri. A thermodynamically-based constitutive model for thermoplastic polymers coupling viscoelasticity, viscoplasticity and ductile damage. *International Journal of Plasticity*, 2014, 60, 163–181.

- [166] P. Krejčí, U. Stefanelli. Existence and nonexistence for the full thermomechanical Souza-Auricchio model of shape memory wires. *Math. Mech. Solids*, 16 (2011) 349–365.
- [167] P. Krejčí, U. Stefanelli. Well-posedness of a thermo-mechanical model for shape memory alloys under tension. *M2AN Math. Model. Numer. Anal.*, 44 (2010) 6:1239–1253.
- [168] Kucukyildirim, B., A. Eker. Surface roughness changes and corrosion on nickel titanium orthodontic wires compared to stainless steel wires in various artificial salivas. *Materialpruefung/Materials Testing*, (2012) 54, 261–265.
- [169] Kujala, S., Ryhänen, J., Jämsä, T., Danilov, A., Saaranen, J., Pramila, A., Tuukka-nen, J. Bone modeling controlled by a nickel-titanium shape memory alloy in-tramedullary nail. *Biomaterials*, 23(12), 2535–2543. (2002).
- [170] Kujawski, K., Stasiak, M., Rysz, J. The evaluation of esophageal stenting complica-tions in palliative treatment of dysphagia related to esophageal cancer. *Medical Science Monitor*, 18, CR323–CR329. (2012).
- [171] Kuo, C., Wang, M., Shiao, A. Superiority of Nitinol Piston Over Conventional Pros-theses in Stapes Surgery: First Comparative Results in the Chinese Population in Taiwan. *Journal of the Chinese Medical Association*, 73, 241–247. (2010).
- [172] Kuong, E., Cheung, K., Samartzis, D., Yeung, K., Luk, K. Superelastic rods: the future of scoliosis curve correction. *J Bone Joint Surg Br*, 94(B), no. SUPP XXXIX 102. (2012).
- [173] Kurdjumov G.V. , L.G. Khandros, First reports of the thermoelastic behaviour of the martensitic phase of Au-Cd alloys. *Doklady Akademii Nauk SSSR*, 1949, 66, 211–213.
- [174] D. C. Lagoudas, D. J. Hartl, Y. Chemisky, L. Machado, P. Popov, Constitutive model for the numerical analysis of phase transformation in polycrystalline shape memory alloys, *International Journal of Plasticity* 32-33 (2012) 155–183.
- [175] D. C. Lagoudas, K. Ravi-Chandar, K. Sarh, P. Popov, Dynamic loading of polycrys-talline shape memory alloy rods, *Mechanics of Materials* 35 (2003) 689–716.

- [176] Lampe, P., Kuanierz, K., Zhavoronkov, D., Morawiec, H. Use of compression clips made of shape memory material in the gastrointestinal surgery - A preliminary report. *Polski Przegląd Chirurgiczny*, 80, 544–550. (2008).
- [177] Lan C.C., C.H. Fan. An accurate self-sensing method for the control of shape memory alloy actuated flexures. *Sensors and Actuators A*, 2010, 163: 323–332.
- [178] Lekston, Z., Stroz, D., Drusik-Pawlowska, M. Preparation and characterization of nitinol bone staples for cranio-maxillofacial surgery. *Journal of Materials Engineering and Performance*, 21, 2650–2656. (2012).
- [179] Lendlein A., S. Kelch. Shape-Memory Polymers, *Angew. Chem. Int. Ed.*, 2002, 41: 2034–2057
- [180] Leng J., S. Du. Shape-Memory Polymers and Multifunctional Composites. CRC Press, 2010.
- [181] LExcellent, C., S. Leclercq; B. Gabry, G. Bourbon. The two way shape memory effect of shape memory alloys: an experimental study and a phenomenological model, *International Journal of Plasticity*, 2000, 16, 1155–1168.
- [182] Li G., W. Xu. Thermomechanical behavior of thermoset shape memory polymer programmed by cold-compression: Testing and constitutive modeling. *Journal of the Mechanics and Physics of Solids*, 2011, 59, 1231–1250.
- [183] Likibi, F., Assad, M., Coillard, C., Chabot, G., Rivard, C. Bone integration and apposition of porous and non porous metallic orthopaedic biomaterials. *Annales de Chirurgie*, 130, 235–241. (2005).
- [184] Lirici, M., Salerno, F., Califano, A. The use of superelastic suture clips in laparoscopic gastric banding. *Minimally Invasive Therapy and Allied Technologies*, 17, 176–180. (2008).
- [185] Liu, X., Luo, H., Liu, S., Wang, D. Pilot study of SMA-based expansion device for transanal endoscopic microsurgery. *Proceedings - International Conference on Machine Learning and Cybernetics*, 3, 1420–1424. Guilin, Guangxi. (2011).

- [186] Liu Y., K. Gall, M.L. Dunn, A.R. Greenberg, J. Diani. Thermomechanics of shape memory polymers: Uniaxial experiments and constitutive modeling. *International Journal of Plasticity*, 2006, 22: 279–313.
- [187] Liu C., H. Qinb, P.T. Mather. Review of progress in shape-memory polymers. *J. Mater. Chem.*, 2007, 17, 1543–1558.
- [188] Lubliner, J., Auricchio, F. Generalized plasticity and shape-memory alloys. *International Journal of Solids and Structures*, 33(7), 991–1003. (1996).
- [189] Luehrs, K. F. DESIGNING WITH NITINOL FOR THE COMMONER. *SMST-2003: Proceedings of the International Conference on Shape Memory and Superelastic Technologies*. (2003).
- [190] Lung J., Du S. (editors). Shape-Memory Polymers and Multifunctional Composites. *CRC Press, Taylor & Francis Group*, 2010
- [191] Luo, Y., M. Higa, S. Amae, T. Yambe, T. Okuyama, T. Takagi, H. Matsuki. The possibility of muscle tissue reconstruction using shape memory alloys. *Organogenesis*, 2005, 2, 2–5.
- [192] Luo, J., Cui, P., Gao, P., Nan, H., Liu, Z., Sun, Y. Reconstruction of tracheal wall defect with a mesh patch of nickel-titanium shape-memory alloy. *Annals of Otology, Rhinology and Laryngology*, 120, 198–203. (2011).
- [193] MacDonald, S. New embolic protection devices: a review. *The Journal of Cardiovascular Surgery*, 52(6):821–7. (2011)
- [194] Machado, L. G., Savi, M. A. Medical applications of shape memory alloys. *Brazilian Journal of Medical and Biological Research*, (2003), 36(6), 683–691.
- [195] Makishi W., Matunaga T., Haga Y., Esashi M. Active Bending Electric Endoscope Using Shape Memory Alloy Coil Actuators. *Biomedical Robotics and Biomechatronics*. (2006).
- [196] Maldovan M., E.L. Thomas . Periodic Materials and Interference Lithography: For Photonics, Phononics and Mechanics. *Wiley-VCH*, 2008.

- [197] Masoumi Khalil Abad, E., Pasini, D., Cecere, R. Shape optimization of stress concentration-free lattice for self-expandable Nitinol stent-grafts. *Journal of Biomechanics*, 45(6), 1028–1035. (2012).
- [198] Masoomi, H., Luo, R., Mills, S., Carmichael, J., Senagore, A., Stamos, M. Compression anastomosis ring device in colorectal anastomosis: a review of 1,180 patients. *American Journal of Surgery*, 205(4): 447–51. (2013).
- [199] Mathematica, Version 8.0, *Wolfram Research, Inc.*, Champaign, IL, 2010.
- [200] Matlab, The MathWorks Inc., Natick, MA, 2000.
- [201] Matsubara, S., Okamoto, S., Lee, J. Prosthetic hand using shape memory alloy type artificial muscle. *Lecture Notes in Engineering and Computer Science*, 2, 873–876. Kowloon. (2012).
- [202] Matsuzaki, A., Morita, T., Tokue, A., Kobayashi, Y. Clinical study of intraurethral stent (MEMOKATH<sup>®</sup>) for prostatic hyperplasia - Study of the changes in uroflowmetry and international prostate symptom score in the early phase after insertion of the stent. *Nishinihon Journal of Urology*, 66, 637–643. (2004).
- [203] Mavroidis, C., C. Pfeiffer, C., M. Mosley. Conventional actuators, shape memory alloys, and electrorheological fluids. In Y. Bar-Cohen (Editor). *American Society for Nondestructive Testing*, 2000.
- [204] MedShape <www.medshape.com>. (Consultation: february 2013).
- [205] www.medtronic.com (consultation: November 2013)
- [206] Melzer, A., Stoeckel, D. Function and Performance of Nitinol Vascular Implants. *The Open Medical Devices Journal*, 2, 32–41. (2010).
- [207] Meoli A., Dordoni E., Petrini L., Migliavacca F., Dubini G., Pennati G., Computational modelling of in vitro set-ups for peripheral self-expanding nitinol stents: The importance of stentwall interaction in the assessment of the fatigue resistance, *Cardiovascular Engineering and Technology*, 1–11. (2013).
- [208] Method and system for orthodontic moving of teeth. Patent US 4037324. (1973).

- [209] Wolfram Research, Inc., Mathematica, Version 8.0, Champaign, IL (2010).
- [210] M. Mertmann, G. Vergani, Design and application of shape memory actuators, *The European Physical Journal Special Topics* 158 (2008) 221–230.
- [211] A. Mielke. Formulation of thermoelastic dissipative material behavior using GENERIC. *Contin. Mech. Thermodyn.*, 23 (2011) 3:233–256.
- [212] A. Mielke. On thermodynamically consistent models and gradient structures for thermoplasticity. *GAMM Mitt.*, 34 (2011) 1:51–58.
- [213] A. Mielke. Dissipative quantum mechanics using GENERIC, Proc. of the conference on Recent Trends in Dynamical Systems, vol. 35 of *Proceedings in Mathematics & Statistics*, Springer, 2013, pp. 555–585.
- [214] A. Mielke, L. Paoli, A. Petrov. On existence and approximation for a 3D model of thermally induced phase transformations in shape-memory alloys. *SIAM J. Math. Anal.*, 41 (2009) 1388–1414.
- [215] A. Mielke, L. Paoli, A. Petrov, U. Stefanelli. Error estimates for space-time discretizations of a rate-independent variational inequality. *SIAM J. Numer. Anal.*, 48 (2010) 1625–1646.
- [216] A. Mielke, L. Paoli, A. Petrov, U. Stefanelli. Error bounds for space-time discretizations of a 3d model for shape-memory materials. In *IUTAM Symposium on Variational Concepts with Applications to the Mechanics of Materials*, K. Hackl (ed.), 185–197. Springer, 2010. Proceedings of the IUTAM Symposium on Variational Concepts, Bochum, Germany, Sept. 22–26, 2008.
- [217] A. Mielke, A. Petrov. Thermally driven phase transformation in shape-memory alloys, *Adv. Math. Sci. Appl.*, 17 (2007) 667–685.
- [218] Mikulewicz, M., K. Chojnacka. Release of metal ions from orthodontic appliances by in vitro studies: A systematic literature review. *Biological Trace Element Research*, (2011), 139, 241–256.
- [219] R. Mirzaeifar, R. Des Roches, A. Yavari, A combined analytical, numerical, and experimental study of shape-memory-alloy helical springs, *International Journal of Solids and Structures* 48 (2011) 611–624.

- [220] Montenegro-Santillán R., Alegre-Domingo T., Faus-Matoses V., Faus-Llópez, V. An in vitro comparison of cyclic fatigue resistance of ProTaper universal and GT series X files. *Med Oral Patol Oral Cir Bucal*, (2013), 1;18(3), e533–6.
- [221] Moon S., F. Cui, I. Rao. Constitutive modeling of the mechanics associated with triple shape memory polymers. *International Journal of Engineering Science*, 2015, 96, 86 - 110
- [222] Morawiec, H. Z., Lekston, Z. H., Kobus, K. F., Wegrzyn, M. C., Zdrzał, P., Drugacz, J. T. Superelasticity of NiTi Ring-Shaped Springs Induced by Aging for Cranioplasty Applications. *SMST-2008*. (2009).
- [223] Morgan, N. Medical shape memory alloy applications - The market and its products. *Materials Science and Engineering A*, 2004, 378, 16–23.
- [224] Müller, B., Deyhle, H., Mushkolaj, S., Wieland, M. The challenges in artificial muscle research to treat incontinence. *Swiss Medical Weekly*, 139, 591–595. (2009).
- [225] Müller-Hülsbeck S., Schäfer P.J., Hümme T.H., Charalambous N., Elhöft H., Heller M., Jahnke T. Embolic Protection Devices for Peripheral Application: Wasteful or Useful?. *Journal of Endovascular Therapy: February 2009*, Vol. 16, No. Supplement I, pp. I-163–I-169. (2009).
- [226] Müller-Hülsbeck S., Schäfer P., Charalambous N., Yagi H., Heller M., Jahnke T. Comparison of second generation stents for application in the superficial femoral artery: An in vitro evaluation focusing on stent design, *Journal of Endovascular Therapy*, 17(6), 767–776. (2010).
- [227] Nakamura, Y., Matsui, A., Saito, T., Yoshimoto, K. Shape-memory-alloy active forceps for laparoscopic surgery. *Proceedings - IEEE International Conference on Robotics and Automation*, 3, 2320–2327. Nagoya, Jpn. (1995).
- [228] Negri, A., Manfredi, J., Terrini, A., Rodella, G., Bisleri, G., Quarra, S. E., Muneretto, C. Prospective evaluation of new sternal closure method with termoreactive clips. *European Journal of Cardio-thoracic Surgery*, 22, 571-575. (2002).



- [229] Nematzadeh, F., Sadrnezhaad, S. Effects of Crimping on Mechanical Performance of Nitinol Stent Designed for Femoral Artery: Finite Element Analysis. *Journal of Materials Engineering and Performance*, 1–9. (2013).
- [230] Nguyen T.D., H.J. Qi, F. Castro, K.N. Long, A thermoviscoelastic model for amorphous shape memory polymers: Incorporating structural and stress relaxation, *Journal of the Mechanics and Physics of Solids*, 2008, 56: 2792–2814.
- [231] Nguyen T., C. Yakacki, P. Brahmabhatt, M. Chambers. Modeling the relaxation mechanisms of amorphous shape memory polymers. *Adv. Mater.*, 2010, 22, 3411–3423.
- [232] Nichols, M., Townsend, N., Scarborough, P., Luengo-Fernandez, R., Leal, J., Gray, A., Rayner, M. European Cardiovascular Disease Statistics 2012. European Heart Network, Brussels, European Society of Cardiology, Sophia Antipolis. (2012).
- [233] Nikanorov A., Smouse H., Osman K., Bialas M., Shrivastava S., Schwartz L. Fracture of self- expanding nitinol stents stressed in vitro under simulated intravascular conditions, *Journal of vascular surgery* 48(2) 435–440. (2008)
- [234] Nikolaidis, N., Tsang, G., Ohri, S. K. The Use of Nitinol Clips in Cardiac Surgery: A New Method of Sternal Closure. *CTSNet - The cardiothoracic surgery network*. (2009).
- [235] Norwich, D.W.. A Study of the Properties of a Room Temperature Martensitic Binary Nitinol Alloy Above and Below its Martensite to Austenite Transformation Temperature. *Journal of Materials Engineering and Performance*, 2011, 20, 529–534.
- [236] Ohkata, I. Shape memory and superelastic alloys - Technologies and applications. In K. Yamauchi, I. Ohkata, K. Tsuchiya, S. Miyazaki (Editors). Woodhead Publishing. (2011).
- [237] Olsen, J., Z. Zhang, H. Lu, C. van der Eijk. Fracture of notched round-bar NiTi-specimens, *Engineering Fracture Mechanics*, 2012, 1–14.
- [238] Olson, J., Shandas, R., Erlanger, M. Development of a minimally invasive, injectable, shape memory suture and delivery system. *Annals of Biomedical Engineering*, 40, 1520–1529. (2012).

- [239] Olson, J., Velez-Montoya, R., Erlanger, M. Ocular biocompatibility of nitinol intraocular clips. *Investigative Ophthalmology and Visual Science*, 53, 354-360. (2012).
- [240] OneMedPlace. Orthopedics Focus - Emerging Companies to Watch. Orthopedics Focus - Emerging Companies to Watch. (2007).
- [241] Open stent design. [www.nitinol.com](http://www.nitinol.com). (Consultation: November 2013).
- [242] H. C. Öttinger, *Beyond Equilibrium Thermodynamics*, John Wiley, New Jersey, 2005.
- [243] Overvelde J. T.B., K. Bertoldi. Relating pore shape to the non-linear response of periodic elastomeric structures. *Journal of the Mechanics and Physics of Solids*, 2014, 64, 351–366.
- [244] Pakula T., M. Trznadel. Thermally stimulated shrinkage forces in oriented polymers: 1. Temperature dependence. *Polymer*, 1985, 26, 1011–1018.
- [245] H. Pan, P. Thamburaja, F. Chau, An isotropic-plasticity-based constitutive model for martensitic reorientation and shape-memory effect in shape-memory alloys, *International Journal of Solids and Structures* 44 (22-23) (2007) 7688–7712.
- [246] Pandini S., S. Passera, M. Messori, K. Paderni, M. Toselli, A. Gianoncelli, E. Bon-tempi, T. Ricco. Two-way reversible shape memory behaviour of crosslinked poly( $\epsilon$ -caprolactone). *Polymer*, 2012, 53, 1915–1924.
- [247] M. Panico, L. Brinson, A three-dimensional phenomenological model for martensite reorientation in shape memory alloys, *Journal of the Mechanics and Physics of Solids* 55 (11) (2007) 2491.
- [248] Patoor, E., Lagoudas, D.C., Entchev, P.B., Brinson, L.C., Gao, X., 2006. Shape memory alloys. Part I: General properties and modeling of single crystals. *Mechanics of Materials* 38 (5–6), 391–429.
- [249] M. Peigney. A time-integration scheme for thermomechanical evolutions of shape-memory alloys. *C.R. Mecanique*, 334 (2006), 266–271.
- [250] M. Peigney, J.P. Seguin. An incremental variational approach to coupled thermo-mechanical problems in anelastic solids. Application to shape-memory alloys. *Int. J. Solids Struc.*, 50 (2013), 4043–4054.

- [251] M.H. Duong, M.A. Peletier, J. Zimmer. GENERIC formalism of a Vlasov-Fokker-Planck equation and connection to large-deviation principles, *Nonlinearity*, 26 (2013), 2951–2971.
- [252] Pelton, Stöckel, Duerig. Medical Uses of Nitinol. *Material Science Forum*, (2000), 327–328, 63–70.
- [253] Pelton, A.R., Gong, X.-Y., Duerig, T. Fatigue testing of diamond-shaped specimens. In S. S. (Editor), *Medical Device Materials - Proceedings of the Materials and Processes for Medical Devices Conference 2003*, 199–204. Anaheim, CA. (2003).
- [254] Pelton, A., V. Schroeder, M. Mitchell, X.-Y. Gong, M. Barney, S. Robertson. Fatigue and durability of Nitinol stents. *J. Mech. Behav. Biomed*, (2008) 1, 153–164.
- [255] Pelton, A. Nitinol Fatigue: A Review of Microstructures and Mechanisms. *J. Mater. Eng. Perform.*, (2011) 20(4–5), 613–617.
- [256] D. Peraza-Hernandez, E. and Hartl, R. Galvan, E. and Malak, Design and optimization of a shape memory alloy-based self-folding sheet, *Journal of Mechanical Design*, Transactions of the ASME 135 (11) (2013) 1–11.
- [257] Perry, M., Oktay, S., Muskivitch, J. Finite element analysis and fatigue of stents. *Minimally Invasive Therapy and Allied Technologies*, 11(4), 165–171. (2002).
- [258] Petrini, L., Migliavacca, F., Massarotti, P., Schievano, S., Dubini, G., Auricchio, F. Computational studies of shape memory alloy behavior in biomedical applications. *Journal of Biomechanical Engineering*, 127(4), 716–725. (2005).
- [259] Petrini, L., Migliavacca, F. Biomedical Applications of Shape Memory Alloys. *Journal of Metallurgy*, (2011), 1–15.
- [260] Petrini, L., Wu W., Dordoni E., Meoli A., Migliavacca F., Pennati G. Fatigue behavior characterization of nitinol for peripheral stents. *Funct. Mater. Lett.* (2012).
- [261] Petrini, L., E. Dordoni, W. Wu, C. Guala, C. Silvestro, F. Migliavacca, G. Pennati. FATIGUE RESISTANCE OF NITINOL PERIPHERAL STENTS. *6th ECCOMAS Conference on Smart Structures and Materials (SMART2013)*, Politecnico di Torino, 24–26 June 2013.

- [262] R. Peyroux, A. Chrysochoos, Ch. Licht, M. Löbel. Thermomechanical couplings and pseudoelasticity of shape memory alloys. *Int. J. Eng. Sci.*, 36 (1998) 489–509.
- [263] R. Peyroux, A. Chrysochoos, Ch. Licht, M. Löbel. Phenomenological constitutive equations for numerical simulations of SMA's structures. Effect of thermomechanical couplings. *J. Phys. C4 Suppl.*, 6 (1996) 347–356.
- [264] Pfeifer, R., Hustedt, M., Wesling, V., Hurschler, C., Olender, G., Mach, M., GÄußling T., Muller, C. Noninvasive induction implant heating: An approach for contactless altering of mechanical properties of shape memory implants. *Medical Engineering and Physics*, 35, 54–62. (2013).
- [265] Pieczyska, E. A., M. Maj, K. Kowalczyk-Gajewska, M. Staszczak, A. Gradys, M. Majewski, M. Cristea, H. Tobushi, S. Hayashi. Thermomechanical properties of polyurethane shape memory polymer: experiment and modelling. *Smart Materials and Structures*, 2015, 24, 045043.
- [266] J. Pilch, L. Heller, P. Sittner, <http://department.fzu.cz/ofm/roundrobin> (2009).
- [267] Pittaccio, S., Viscuso, S. Shape Memory Actuators for Medical Rehabilitation and Neuroscience. In G. Berselli, R. Vertechy, G. Vassura (Editor). *InTech*. (2012).
- [268] Poncet, P.P. Applications of superelastic Nitinol tubing. *SMST 1994 - Proceedings of the International Conference on Shape Memory and Superelastic Technologies 1994*. (1994).
- [269] Popa C., R. Fleischhauer, K. Schneider, M. Kaliske. Formulation and implementation of a constitutive model for semicrystalline polymers. *International Journal of Plasticity*, 2014, 61, 128–156.
- [270] Praveen Kumar G, Fangsen C, Asawinee D, Boyang S, Hon J.K.F., Liang L H.. Design and finite element based fatigue prediction of a new self-expandable percutaneous mitral valve stent. *Computer-Aided Design*. (2013).
- [271] Prosthetic Pump. Patent USA 3.827.426. Year 1971.
- [272] Purser, M. F., Richards, A. L., Cook, R. C., Osborne, J. A., Cormier, D. R., Buckner, G. D. Evaluation of a Shape Memory Alloy Reinforced Annuloplasty Band for Minimally Invasive Mitral Valve Repair. *Ann Thorac Surg*, 88, 1312–6. (2009).

- [273] Purser, M., Richards, A., Cook, R., Osborne, J., Cormier, D., Buckner, G. A novel shape memory alloy annuloplasty ring for minimally invasive surgery: Design, fabrication, and evaluation. *Annals of Biomedical Engineering*, 39(1), 367–377. (2011).
- [274] A. Quarteroni, R. Sacco, F. Saleri, Numerical Mathematics, Springer, 2nd ed. 2007.
- [275] Qi H., T. Nguyen, F. Castro, C. Yakacki, R. Shandas. Finite deformation thermo-mechanical behavior of thermally-induced shape memory polymers. *J. Mech. Phys. Solids*, 2008, 56, 1730–1751.
- [276] Rabani G., H. Luftmann, A. Kraft. Synthesis and characterization of two shape-memory polymers containing short aramid hard segments and poly( $\epsilon$ -caprolactone) soft segments, *Polymer*, 2006, 47, 4251–4260.
- [277] Rajan, G., Eikelboom, R., Anandacoomaraswamy, K., Atlas, M. In vivo performance of the nitinol shape-memory stapes prosthesis during hearing restoration surgery in otosclerosis: A first report. *Journal of Biomedical Materials Research - Part B Applied Biomaterials*, 72, 305–309. (2005).
- [278] Rajasekhar A., Streiff M.B., Vena cava filters for management of venous thromboembolism: A clinical review, *Blood Reviews*, 27(5), 2013, 225–241.
- [279] Rebelo, N., Perry, M. Finite element analysis for the design of Nitinol medical devices. *Minimally Invasive Therapy and Allied Technologies*, 9(2), 75–80. (2000).
- [280] Rebelo, N., X.-Y. Gong, M. Connally. Finite Element Analysis Of Plastic Behavior, In *Nitinol SMST-2003: Proceedings of the International Conference on Shape Memory and Superelastic Technologies (ASM International)*, 2004, 501–507.
- [281] Rebelo, N., Fu, R., Lawrenchuk, M. Study of a Nitinol Stent Deployed into Anatomically Accurate Artery Geometry and Subjected to Realistic Service Loading. *JMEPEG*, 18, 655–663. (2009).
- [282] Rebelo, N., Radford, R., Zipse, A., Schlun, M., Dreher, G. On modeling assumptions in finite element analysis of stents. *Journal of Medical Devices, Transactions of the ASME*, 5(3). (2011).

- [283] Reedlunn B., S. Daly, J. Shaw, Superelastic shape memory alloy cables: Part I - Isothermal tension experiments. *International Journal of Solids and Structures*, 2013, 50(20–21): 3009–3026.
- [284] Reese S., M. Böl, D. Christ. Finite element-based multi-phase modelling of shape memory polymer stents. *Comput. Methods Appl. Mech. Engrg.*, 2010, 199: 1276–1286
- [285] Robertson, S. W. Advances in Fatigue Characterization of Nitinol. *SMST-2013: The International Conference on Shape Memory and Superelastic Technologies (SMST)*, ASM International, (2013).
- [286] Robertson, S., A. Pelton, R. Ritchie. Mechanical fatigue and fracture of Nitinol. *Int. Mater. Rev.*, (2012) 57(1), 1–37.
- [287] Rodriguez J.N., F.J. Clubb, T.S. Wilson, M.W. Miller, T.W. Fossum, J. Hartman, E. Tuzun, P. Singhal, D.J. Maitland. In vivo response to an implanted shape memory polyurethane foam in a porcine aneurysm model. *J. Biomed. Mater. Res. A*, 2014, 102(5): 1231–42.
- [288] Roguin, A. Historical Perspectives in Cardiology. *Circulation: Cardiovascular Interventions*, 4, 206–209. (2011).
- [289] Rossi, P., Bezzi, M., Rossi, M., Adam, A., Chetty, N., Roddie, M., Iacari V, Cwikiel W, Zollikofer CL, Antonucci, F. et al. Metallic stents in malignant biliary obstruction: results of a multicenter European study of 240 patients. *Journal of vascular and interventional radiology*, 5, 279–285. (1994).
- [290] Roubíček T., U. Stefanelli. Magnetic shape-memory alloys: thermomechanical modeling and analysis. *Contin. Mech. Thermodyn.*, 26 (2014) 783–810.
- [291] Ryhänen, J. Biocompatibility evaluation of nickel-titanium shape memory metal alloy. Ph.D. dissertation, Faculty of Medicine, Department of Surgery, University of Oulu, (2000).
- [292] Sánchez Márquez, J., Sánchez Pérez-Grueso, F., Fernández-Baíllo, N., Gil Garay, E. Gradual scoliosis correction over time with shape-memory metal: a preliminary report of an experimental study. *Scoliosis*, 7(1). (2012).

- [293] Scalet G., F. Auricchio, E. Bonetti, L. Castellani, D. Ferri, M. Pachera, F. Scavello. An experimental, theoretical and numerical investigation of shape memory polymers. *International Journal of Plasticity*, 2015, 67: 127–147.
- [294] Scalet G., F. Auricchio, D. Hartl. Efficiency and effectiveness of implicit and explicit approaches for the analysis of shape-memory alloy bodies. *Journal of Intelligent Material Systems and Structures*, 2015.
- [295] Scalet G., E. Boatti, M. Ferraro, V. Mercuri, D. Hartl, F. Auricchio. Explicit finite element implementation of a shape memory alloy constitutive model and associated analyses. In preparation. (2015).
- [296] Schüssler A. Micro-machining and joining of NiTi-alloys using Nd: YAG lasers: status and prospects. *SMST-97: Proceedings of the Second International Conference on Shape Memory and Superelastic Technologies*, 2-6 March 1997, Asilomar Conference Centre, Pacific Grove, California, USA
- [297] Schüssler, A., Melzer, A. Nitinol - Smart material for vascular interventions. *Medizintechnik in Bayern*, 24–28. (2002).
- [298] Simo J.C., T.J.R. Hughes. Computational Inelasticity. *Springer-Verlag*, 1998.
- [299] P. Sedláč, M. Frost, B. Benesová, T. B. Zineb, P. Sittner, Thermomechanical model for niti-based shape memory alloys including r-phase and material anisotropy under multi-axial loadings, *International Journal of Plasticity* 39 (2012) 132–151.
- [300] Shabalovskaya, S., J. Anderegg, J. Van Humbeeck. Critical overview of Nitinol surfaces and their modifications for medical applications. *Acta Biomaterialia*, (2008) 4, 447–467.
- [301] Shan S., S.H. Kang, P. Wang, C. Qu, S. Shian, E.R. Chen, K. Bertoldi. Harnessing Multiple Folding Mechanisms in Soft Periodic Structures for Tunable Control of Elastic Waves. *Adv. Funct. Mater.*, 2014, 24(31), 4935–4942.
- [302] Shape memory alloy staple. Patent EP 1173102 B1. (1999).
- [303] Shen, Y., W. Qian, H. Abtin, Y. Gao, M. Haapasalo. Fatigue Testing of Controlled Memory Wire Nickel-Titanium Rotary Instruments. *JOE*, (2011) 37(7), 997–1001.

- [304] Shi, Z., Liu, D., Ma, C., Zhao, D. Accurate controlled shape memory alloy actuator for minimally invasive surgery. *2011 IEEE International Conference on Mechatronics and Automation*, ICMA 2011, 817–822. Beijing. (2011).
- [305] Shobayashi Y., Tanoue T., Tateshima S., Tanishita K. Mechanical design of an intracranial stent for treating cerebral aneurysms, *Medical Engineering and Physics*, 32(9), 1015–1024. (2010).
- [306] Simon, M., Kaplan, R., Salzman, E., Freiman, D. A vena cava filter using thermal shape memory alloy: experimental aspects. *Radiology*, 125 (1), 89–94. (1977).
- [307] Simske, S., Sachdeva, R. Cranial bone apposition and ingrowth in a porous nickel-titanium implant. *Journal of Biomedical Materials Research*, 29, 527–533. (1995).
- [308] J. Simo, T. Hughes, Computational Inelasticity, Springer-Verlag, 1998.
- [309] SMP Technologies Inc., Catalogue 2014.
- [310] Soares, A., Brash, H. B., Gow, D. The application of SMA in the design of prosthetic devices. *SMST-1997: Proceedings of the Second International Conference on Shape Memory and Superelastic Technologies*. (1997).
- [311] SolidWorks 2014, Dassault Systèmes, Vélizy-Villacoublay, France.
- [312] A. C. Souza, E. N. Mamiya, N. Zouain. Three-dimensional model for solids undergoing stress-induced transformations. *Eur. J. Mech. A Solids*, 17 (1998) 789–806.
- [313] A. Stebner, L. Brinson, Explicit finite element implementation of an improved three dimensional constitutive model for shape memory alloys, *Computer Methods in Applied Mechanics and Engineering* 257 (2013) 17–35.
- [314] U. Stefanelli. Magnetic control of magnetic shape-memory single crystals. *Phys. B*, 407 (2012) 1316–1321.
- [315] [www.stentys.com](http://www.stentys.com) (Consultation: November 2013).
- [316] Steven, A. Getting a microgrip in the operating room. *Mechanical Engineering - CIME*, 118, 91–93. (1996).



- [317] Stoeckel, D., Pelton, A., Duerig, T. Self-expanding nitinol stents: material and design considerations. *Eur Radiol*, 14, 292–301. (2004).
- [318] D. Stoeckel, T. Borden, Actuation and fastening with shape memory alloys in the automotive industry, *Metall Wissenschaft + Technik* 46 (1992) 668–672.
- [319] S. Stupkiewicz, H. Petryk, A robust model of pseudoelasticity in shape memory alloys, *International Journal of Numerical Methods in Engineering* 93 (2013) 747–769.
- [320] Sujithra R., S. Srinivasan, A. Arockiarajan. Shape recovery studies for coupled deformations in an epoxy based amorphous shape memory polymers. *Polymer Testing*, 2015, 48, 1–6.
- [321] Sun W., E.L. Chaikof, M.E. Levenston. Numerical Approximation of Tangent Moduli for Finite Element Implementations of Nonlinear Hyperelastic Material Models. *Biomech Eng.*, 2008, 130(6): 061003.
- [322] Talreja, J., Eloubeidi, M., Sauer, B., Al-Awabdy, B., Lopes, T., Kahaleh, M., Shami, V. Fully covered removable nitinol self-expandable metal stents (SEMS) in malignant strictures of the esophagus: A multicenter analysis. *Surgical Endoscopy and Other Interventional Techniques*, 26, 1664–1669. (2012).
- [323] Tang S., C.-Y. Zhang, M.-N. Huang, Y.-F. Luo, Z.-Q. Liang. Fallopian tube occlusion with a shape memory polymer device: evaluation in a rabbit model. *Contraception*, 2013, 87: 235–241.
- [324] Tarnita, D., Tarnita, D., Bolcu, D. Biomedical engineering - From theory to applications. In R. Fazel-Rezai (Editor), (2011).
- [325] P. Thamburaja, N. Nikabdullah, A macroscopic constitutive model for shape-memory alloys: Theory and finite-element simulations, *Computer Methods in Applied Mechanics and Engineering* 198 (2009) 1074–1086.
- [326] Theriault, P., Terriault, P., Brailovski, V., Gallo, R. Finite element modeling of a progressively expanding shape memory stent. *Journal of Biomechanics*, 39(15), 2837–2844. (2006).

- [327] Thompson, S. A. An overview of nickel-titanium alloys used in dentistry. *International Endodontic Journal*, (1999), 33, 297–310.
- [328] Tinker, M.L., M.A. Cutchins. Damping phenomena in a wire rope vibration isolation system, *Journal of Sound and Vibration*, 1992, 157, 7–18.
- [329] Tobushi, H., T. Hashimoto, S. Hayashi, E. Yamada, Thermomechanical Constitutive Modeling in Shape Memory Polymer of Polyurethane Series, *J. Intell. Mater. Syst. Struct.*, 1997, 8, 711–718.
- [330] Tobushi H., K. Okumura, S. Hayashi, N. Ito, Thermomechanical constitutive model of shape memory polymer, *Mechanics of Materials*, 2001, 33: 10, 545–554.
- [331] Tobushi H., R. Matsui, S. Hayashi, D. Shimada. The influence of shape-holding conditions on shape recovery of polyurethane-shape memory polymer foams. *Smart Materials and Structures*, 2004, 13, 881.
- [332] Tobushi H., S. Hayashi, K. Hoshio, N. Miwa. Influence of strain-holding conditions on shape recovery and secondary-shape forming in polyurethane-shape memory polymer. *Smart Materials and Structures*, 2006, 15, 1033.
- [333] Tognarelli, S., Salerno, M., Tortora, G., Quaglia, C., Dario, P., Menciassi, A. An endoluminal robotic platform for Minimally Invasive Surgery. *Proceedings of the IEEE RAS and EMBS International Conference on Biomedical Robotics and Biomechatronics*, (p. 7–12). Rome. (2012).
- [334] Tolomeo, D., S. Davidson, M. Santinoranout. Cyclic properties of superelastic nitinol: design implications. *Proc. Int. Conf. on SMST*, 409–417, Pacific Grove, CA, USA, April-May 2000.
- [335] Tzamtzis S., Viquerat J., Yap J., Mullen M.J., Burriesci G. Numerical analysis of the radial force produced by the Medtronic-CoreValve and Edwards-SAPIEN after transcatheter aortic valve implantation (TAVI), *Medical Engineering and Physics*, 35(1), 125–130. (2013).
- [336] Viscuso, S., Pittaccio, S., Caimmi, M., Gasperini, G., Pirovano, S., Villa, E., Besseghini, S., Molteni, F. Pseudoelastic Nitinol-Based Device for Relaxation of Spastic Elbow in Stroke Patients. *JMEPEG*, 18, 805–813. (2009).

- [337] B.L. Volk, D.C. Lagoudas, D.J. Maitland. Characterizing and modeling the free recovery and constrained recovery behavior of a polyurethane shape memory polymer. *Smart Mater Struct.*, 2011, 20(9): 094004–1–094004–18.
- [338] VV.AA. Engineering aspects of shape memory alloys. (T. W. Duerig, Editor) Butterworth-Heinemann Limited, (1990).
- [339] VV.AA. Heart Disease and Stroke Statistics - 2011 Update. Tech. rep., American Heart Association. (2011).
- [340] VV.AA. Perio root implant and medical application of shape memory alloy. In S. Fukuyo, R. Sachdeva, Y. Oshida (Editor). International Academy of Shape Memory Material for Medical Use, Japan Medical Culture Center, Tokio, Japan, (1992).
- [341] VV.AA., Shape memory polymers, editor: Lendlein A., Springer-Verlag Berlin Heidelberg, 2010
- [342] VV.AA., Shape-Memory Polymers and Multifunctional Composites, editors: Leng J., Du S., CRC Press, 2010.
- [343] VV.AA. Shape Memory Polymers for Biomedical Applications, editor: Yahia L., Woodhead Publishing, 2015, ix - x.
- [344] VV.AA. Surface Engineered Surgical Tools and Medical Devices. (M. J. Jackson, W. Ahmed, Editors) Springer, (2007).
- [345] Wang, Y., Zheng, G., Zhang, X., Zhang, Y., Xiao, S., Wang, Z. Temporary use of shape memory spinal rod in the treatment of scoliosis. *European Spine Journal*, 20, 118–122. (2011).
- [346] Wang T.M., Z.Y. Shi, D. Liu, C. Ma, Z.H. Zhang. An Accurately Controlled Antagonistic Shape Memory Alloy Actuator with Self-Sensing. *Sensors*, 2012, 12, 7682–7700.
- [347] Wayman, C. Shape memory and related phenomena. *Progress in Materials Science*, 36, 1992, 203–224
- [348] Wensing P., Scholten F., Buijs P., Hartkamp M., Mali W., Hillen B. Arterial tortuosity in the femoropopliteal region during knee flexion: a magnetic resonance angiographic study, *Journal of Anatomy* 187 (1) (1995) 133–139. (1995).

- [349] Westbrook K., P. Kao, F. Castro, Y. Ding, H. Qi. A 3d finite deformation constitutive model for amorphous shape memory polymers: a multi-branch modeling approach for nonequilibrium relaxation processes. *Mech. Mater.*, 2011, 43, 853–869.
- [350] Wever, D., A. Veldhuizen, M. Sanders, J. Schakenraad, J. Van Horn. Cytotoxic, allergic and genotoxic activity of a nickel-titanium alloy. *Biomaterials*, (1997), 18, 1115–1120.
- [351] Whitcher, F. Simulation of in vivo loading conditions of nitinol vascular stent structures. *Computers and Structures*, 64(5–6), 1005–1011. (1997).
- [352] Wilkinson, P., Dysart, P., Hood, J., Herbison, G. Load-deflection characteristics of superelastic nickel-titanium orthodontic wires. *American Journal of Orthodontics and Dentofacial Orthopedics*, (2002), 121, 483–495.
- [353] Wriggers P. Nonlinear Finite Element Methods. *Springer*, 2008.
- [354] Wu, W., Qi, M., Liu, X.-P., Yang, D.-Z., Wang, W.-Q. Delivery and release of nitinol stent in carotid artery and their interactions: A finite element analysis. *Journal of Biomechanics*, 40(13), 3034–3040. (2007).
- [355] Wu, Y., Wang, M., Luo, Y. A novel artificial sphincter for functional assist to human puborectalis. *International Journal of Applied Electromagnetics and Mechanics*, 39, 457–462. (2012).
- [356] Xie T. Recent advances in polymer shape memory. *Polymer*, 2011, 52, 4985–5000.
- [357] Xu W., G. Li. Constitutive modeling of shape memory polymer based self-healing syntactic foam. *Int. J. Solids Struct.*, 2010, 47, 1306–1316.
- [358] Yahia, A., Gordon, V., Whapham, J., Malek, A., Rehman, M., Fessler, R. Sapphire(R) platinum detachable coil experience in a tertiary-care facility. *Neurocritical Care*, 7(2), 128–135. (2007).
- [359] Yakacki C.M., R. Shandas, C. Lanning, B. Rech, A. Eckstein, K. Gall. Unconstrained recovery characterization of shape-memory polymer networks for cardiovascular applications. *Biomaterials*, 2007, 8(14), 2255–63.

- [360] Yamakawa, T., Yamakawa, T., Aou, S., Ishizuka, S., Suzuki, M., Fujii, M., Aoki, T. Subdural electrocorticogram measurement with a minimally-invasive procedure using an SMA-manipulated microelectrode array. *Advanced Materials Research*, 222, 313–317. (2011).
- [361] Youyi, C. Orthopedic application of NiTi shape memory alloys in China. *SMST-2000: Proceedings of the International Conference on Shape Memory and Superelastic Technologies*, (2001).
- [362] W. Zaki, Time integration of a model for martensite detwinning and reorientation under non-proportional loading using Lagrange multipliers, *International Journal of Solids and Structures* 49 (21) (2012) 2951–2961.
- [363] Zbar, A., Nir, Y., Weizman, A., Rabau, M., Senagore, A. Compression anastomoses in colorectal surgery: A review. *Techniques in Coloproctology*, 16, 187–199. (2012).
- [364] Zhang, Y., Luo, Y., Kodaira, S., Takagi, T. Application of shape memory alloy pressure-controlled vascular clamp for atraumatic vessel occlusion. *Annals of Vascular Surgery*, 23(6), 813–820. (2009).
- [365] Zhu, S., Yang, X., Chen, M., Li, C., Cui, Z. Effect of porous NiTi alloy on bone formation: A comparative investigation with bulk NiTi alloy for 15 weeks in vivo. *Materials Science and Engineering C*, 28, 1271–1275. (2008).
- [366] Zienkiewicz, O. The birth of the finite element method and of computational mechanics. *International Journal for Numerical Methods in Engineering*, 60(1), 3–10. (2004).
- [367] Zipse, A., M. Schlun, G. Dreher, J. Z. Gahr, N. Rebelo. Accelerated Fatigue Testing of Stent-Like Diamond Specimens. *J. Mater. Eng. Perform.*, (2011) 20(4-5), 579–583.

